Interactions between kelvin and tropical instability waves in the equatorial pacific ocean

Maria Gabriela Escobar Franco

THÈSE

En vue de l'obtention du

DOCTORAT DE L'UNIVERSITÉ DE TOULOUSE

Délivré par : *l'Université Toulouse 3 Paul Sabatier (UT3 Paul Sabatier)*

Présentée et soutenue le *21/03/2023* **par :**

Maria Gabriela ESCOBAR FRANCO

Interactions entre les ondes de Kelvin et les ondes d'instabilité tropicale dans l'océan pacifique équatorial

---

JURY

Jérôme Vialard	Directeur de recherche, IRD	Rapporteur
Xavier Carton	Professeur d'université. LOPS/IUEM.	Rapporteur
Véronique Garçon	Directrice de recherche, CNRS	Examinatrice
Dasha Gushchina	Professeur, Moscow State University (MSU)	Examinatrice
Karina von Schuckmann	Chargé de recherche, Mercator	Invitée
Julien BOUCHAREL	Chargé de recherche, IRD	Directeur de thèse
Boris DEWITTE	Directeur de recherche, IRD	Co-directeur de thèse

---

École doctorale et spécialité :
SDU2E : Océan, Atmosphère, Climat
Unité de Recherche :
LEGOS (UMR 5566)
Directeur(s) de Thèse :
Julien BOUCHAREL et *Boris DEWITTE*
Rapporteurs :
Jérôme VIALARD et *Xavier CARTON*

Résumé — Le climat tropical moyen est le résultat d'une interaction étroite entre l'océan et l'atmosphère. Toute perturbation de cet équilibre subtil peut déclencher d'intenses réponses océaniques et atmosphériques, entraînant une forte variabilité climatique sur une large gamme d'échelles de temps. En particulier, le Pacifique equatorial est (EEP) siège de l'Oscillation Australe El Niño (ENSO), la plus forte fluctuation climatique interannuelle avec des effets généralisés sur le climat mondial, les phénomènes météorologiques et les sociétés. Malgré les progrès considérables réalisés dans la recherche sur ENSO au cours des deux dernières décennies, de nombreux défis subsitent pour comprendre sa diversité et sa complexité temporelle nouvellement reconnues. Au coeur de cette complexité, les processus océaniques à haute fréquence sont susceptibles de jouer un role important.

En particulier, les ondes de kelvin intrasaisonnières (IEKWs) et les ondes d'instabilité tropicales (TIWs) sont des composantes essentielles de la variabilité climatique couplée du Pacifique tropical. Alors que les IEKWs de downwelling sont des précurseurs d'ENSO, les TIWs peuvent contribuer à son asymétrie en mélangeant les eaux plus/moins chaudes hors équatoriale avec les eaux de la cold tongue pendant La Niña/El Niño. Bien que le role des ondes de Kelvin et des TIWs sur ENSO aient été largement étudié de manière séparée, la question de leur interaction reste peu abordée dans la litterature. Outre l'intérêt d'étudier cette question pour mieux comprendre les intéractions d'échelles dans le Pacifique tropical, documenter les processus associés à la dissipation des ondes de Kelvin équatorial represente aussi un objectif pertinent pour l'étude de la teleconnection océanique aux échelles intrasaisonnière le long de la côte ouest de l'Amérique du Sud.

Cette thèse vise à mieux comprendre les mécanismes d'interactions non linéaires aux échelles de temps intrasaisonnières entre l'activité mésoéchelle des TIWs et les ondes de Kelvin équatoriales. Elle tire partie de prés de 30 ans de données altimétrique. Nous montrons en particulier que 42% de la variance des anomalies intrasaisonnières du niveau de la mer induites par les TIWs sont associées à l'activité des ondes de Kelvin. En combinant données altimétrique et de température de surface de la mer, nous montrons par ailleurs que ce mode est associé à des niveaux d'advection non-lineaire de chaleur comparable à ceux produits pendant El Niño. Afin de documenter les mécanismes en jeux lors de ces interactions, des simulations numériques sont réalisées à l'aide d'un modèle océanique du Pacifique tropical. L'activité mésoéchelle des TIWs est atténué dans les simulations ou les termes non-linéaires des équations de moments sont remplacés par un terme de diffusion horizontal. En Comparant aux simulations de controle pour lesquelles le niveau d'activité des TIWs est réaliste, il est possible de diagnostiquer l'effet du mode d'intéraction sur les processus à partir de l'analyse d'un budget d'énergie cinétique turbulente. Les résultats montrent une asymmetrie marquée de la contribution des instabilités barotropes et baroclines entre les IEKWs d' upwellings et de downwelling. En outre, nous montrons que l'interaction entre les TIWs et les IEKWs peut favoriser des changements significatifs de l'advection non linéaire de chaleur dans le Pacifique équatorial oriental, en accord avec les observations. Nous discutons les implications de nos

résultats pour la compréhension de la téléconnexion océanique entre le Pacifique occidental et oriental, ainsi que sur la dynamique ENSO.

Mots clés : *Ondes d'instabilité tropicales ; ondes de Kelvin océaniques ; variabilité climatique ; El Niño - Oscillation Australe ; cycle saisonnier ; modélisation océanique régionale ; interactions entre les échelles de temps*

Abstract —

The tropical mean climate is the result of a tight interplay between the ocean and overlaying atmosphere. Any perturbations of this subtle balance can trigger intense oceanic and atmospheric responses, resulting in a strong climate variability over a wide range of time scales. In particular, the Eastern Equatorial Pacific (EEP) is home to the El Niño/Southern Oscillation (ENSO), the strongest year-to-year climate fluctuation with widespread effects on global climate, weather patterns and societies. Despite tremendous progress in ENSO research over the last two decades, considerable challenges remain to understand its newly recognized pattern diversity and temporal complexity. Nonlinear processes and associated time scales interactions have been pointed out as a source of irregularity for ENSO and the climate variability in general. Among others, high frequency oceanic processes such as the intraseasonal tropical variability have been suggested to play a significant role in ENSO onset, evolution, termination, spatial diversity and temporal complexity.

In particular, intraseasonal Kelvin waves (IEKWs) and Tropical Instability Waves (TIWs) are essential components of the tropical Pacific coupled climate variability. While downwelling IKWs are precursors of ENSO, TIWs can contribute to its asymmetry by mixing more/less warm off-equatorial and cold tongue waters during La Niña/El Niño. While both Kelvin waves and TIWs have long been recognized to be part of a complex interplay of time scales interactions in the equatorial Pacific, far fewer studies have highlighted the potential for interactions between them. Yet the few studies that have addressed this issue have suggested that their interaction can lead to strong impacts in the eastern equatorial Pacific.

The purpose of this thesis is to provide a better picture of the nonlinear interactions occurring at intraseasonal time scales between the transient TIWs mesoscale activity and equatorial Kelvin Waves. By documenting for the first time their interaction from satellite observations over a period spanning almost 30 years, we evidence that 42% of the variance of TIWs-induced intraseasonal sea level anomalies are associated with Kelvin Waves activity. Then, the analysis of two types of simulations' ensembles of the tropical Pacific basin, one with the full mesoscale activity associated with the presence of TIWs, the other without non-linear terms in the momentum equation to damp the TIWs variability, reveals a strongly asymmetric response of TIWs to the passage of IEKWs between their two different phases. In particular, we observe that the passage of upwelling IEKWs induces a much larger increase in the barotropic instabilities in the upper-ocean and baroclinic instabilities in the subsurface layer than of downwelling IEKWs. In addition, we show that the interaction between TIWs and IEKWs can promote substantial changes in nonlinear heat advection in the eastern equatorial Pacific, which may have strong implications for the oceanic teleconnection between the western and eastern Pacific and the low-frequency variability in this key region for the ENSO and global carbon cycle.

Keywords: *Tropical Instability Waves; Oceanic Kelvin Waves; Climate Variability; El Niño – Southern Oscillation; Seasonal Cycle; Regional Ocean Modeling; Time scale Interactions*

Remerciements

À la fin de mes trois années et demie, un beau parcours remplit d'anecdotes, de connaissances scientifiques et d'apprentissage personnel. Une grande aventure familiale. C'était mon projet depuis 2014 de venir en France pour mes études, qui dirait que j'ai eu la chance d'apprendre que des chercheurs français recherchent un étudiant pour travailler avec la modélisation (merci Dr. Santos de m'avoir en parlé et à Ángel Muñoz, de m'avoir introduit au monde de la modélisation en 2011).

Tout d'abord, je tiens à remercier mes deux directeurs de thèse, Julien Boucharel et Boris Dewitte, qui sont très productifs d'une façon scientifique. Julien, merci d'avoir laissé ta porte toujours ouverte pour mes milliards de questions scientifiques, pour m'avoir aidé avec des financements (Projet MOPGA) afin que je puisse faire une belle thèse et arriver à la fin. Pour la patience de m'expliquer chaque étape, pour des centaines de diagrammes que tu faisais chaque fois que j'arrivais à ton bureau, également pour les moments difficiles de la thèse (mon stress deux fois plus élevé), j'ai réussi à avoir un directeur de thèse présent à 100% et comme tu l'as dit, "una tesis caliente". Boris, merci de m'avoir dirigé jusqu'ici depuis 2014, c'était un beau projet. J'avais tellement de difficulté à trouver le financement et c'est grâce à toi et à Julien que c'était possible. Tu es un excellent directeur de thèse avec un bon côté humain. Pour toi, tes étudiants sont des collègues, tu as toujours de bons retours même si on doit tout refaire, on est motivés à les faire. Merci pour les moments amicaux et familiaux que nous avons pu partager, pour ta disponibilité, pour la culture scientifique, et tu sais que la liste est immense, mais en bref, merci de me faire confiance. Merci à vous deux pour vos encouragements, vos conseils, votre présence constante en ces temps difficiles, et votre soutien à la Mission équatorienne et de Lima. Là, je suis remplie de motivation (les incontournables questions du Pacifique Sudest, mes collègues d'INAMHI, INOCAR, ESPOL et ma chère famille). Cette mission m'a donné l'énergie nécessaire pour continuer à avancer au cours des derniers mois. Nombreux échanges scientifiques « Kelvin et TIW » sur des sujets difficiles à comprendre au premier coup.

À mon jury de thèse: Véronique Garçon qui a distance elle a pu être la présidente, Jêrome Vialard pour ces bons questions et d'avoir lu toute ma thèse. À Xavier Carton pour la gentillesse d'être passé au Legos et de m'avoir félicité avant le jour J. À Dasha Guschina et Karina Von Schucmman pour ces questions constructives.

Je continue: à mon ex-groupe Sysco2, Aurélien et Véronique Garçon, deux collègues qui m'ont accueilli bien et que toujours sont présents avec des échanges de collaboration avec mon réseau équatorien où bien pour partager un repas en famille. Véro merci pour tous tes conseils.

Je tiens aussi à remercier les collegues du Legos avec qui j'ai eu des échanges scientifiques des codes CROCO et la science: Rachid Benshila (merci pour les heures sur Olympe), Guillaume Morvan, Marco Larranaga, Carlos Conejero, Alexandra Parrouffe, Wassim et Lisa Maillard.

Merci à tout le personnel LEGOS/OMP, de m'avoir donné de m'avoir accueilli et les démarches

administratives (Briggitte, Nadine, Agathe, Catherine, Nicolas), et de résoudre mes problèmes techniques de badget (Christine), coup de main avec le serveur SI (Geoffray, Caroline et surtout toi, Loïc). Je remercie également au CERFACs aussi pour les répétitions que j'ai pu faire et aussi au groupe de systeme d'avoir m'aidé à transmettre ma défense en direct.

Je m'approche à la partie plus douce de cette aventure: les amis et la famille. Très sympa d'avoir passé avec vous, Pierre et Lisa, toute la thèse, pour le français appris, café, thé et pour les soirées repas. J'ai appris quelques recettes françaises avec vous, et avec toi Lisa c'était plutôt recette CROCO. Romain, merci pour nous montrer pour première fois la neige, Génesis l'a aimé et elle se rappelle toujours. Manon, Flo, Adè, Alexandra, Quentien, Marion et Hanh, pour votre amitié, franchement j'ai jamais cru pouvoir faire tellement d'amis comme vous si facilement, merci de m'avoir integré au vie du labo même si de fois j'ai aimé d'être dans mon coin.

A tous me chères collegues du Labo, Lise, Benjamin, Arne, Simon, Elisa, Adrien, Benjamin, Margot, Camille, Alice, Antonin, Juliette, Micaël, desolée si je ne mets pas toute la liste, mais c'est enorme, merci à tous.

Mon team Latin LEGOS, a flor de piel, gracias amigos por compartir sus momentos familiares y por supuesto de ciencia: mis mejores amigos Carlitos y Marco, ustedes saben cuanto les agradezco las discusiones científicas, los momentos de risa y degustación gastronómica, pero también por haber estado ahí por Génesis. A Alessandra, Jessica, Marquito, Roberto, Mayanin, Diego, Dante, Marcela, Emilio, Camila, Sly, Rosmery, Aaron, y Sirel por ser parte de esta gran amistad, por ese corazón tan grande y el cariño que nos comparten siempre. Todos ustedes son un espejo de la lucha diaria.

A los amigos que por casualidad pude hacer sea por una coincidencia de maleta Totto o por compartir un parque, Mara, Alonso, Emmanuel, Claudia, Aurora, Sara. Mara y Claudia, gracias por tener tiempo siempre para nuestra amistad, las admiro mucho chicas de hierro. Y a mis amigos fuera del Legos Jean-Denis, Sylvie y Jean Louis.

A todos mis amigos y colegas de Ecuador (José, Jonathan, Maritza, Nadia, Telmo, Patricia, Mario), con quienes pude compartir momentos a distancia o cuando pasé por Ecuador en mi último año de la tesis, me contagiaron de su energía. Para usted Raul, por su sabios consejo, siempre lo recordaré.

A mi familia en Ecuador, mis amados padres Cruz María y Victor, gracias por ese empuje a la distancia, por los valores, por su ejemplo de perseverancia y educación que recibí. Nada habría sido posible sin ustedes y el apoyo de mi querida abuelita Panchita, gracias tía. A mi hermano Ernesto por el ejemplo de que siempre me diste. A Normita y mis sobrinos, mi pedacito en Ecuador, que junto a todos mis primos estuvieron cerca de las personas que más falta me hacen.

Mis suegros Margarita, Guillermo y cuñadas Paola, Jessica y por supuesto José quienes siempre nos tuvieron en su círculo de familia, por los mensajes de nuestros sobrinos que hicieron sentir en Ecuador.

Mis tíos de Barcelona, no podían faltar Olguita y Camilo, quienes no dudaron en venir a Toulouse a visitarme cada vez que podían y recibirnos en su casa durante esta aventura. No tengo palabras para agradecer tanto amor, mis padres lejos y ustedes tan cerca. A toda mi familia de Barcelona, Madrid, Génova y Torino que desde esos puntos me enviaron todo su cariño y motivación en la recta final.

Finalmente, llego a la parte más bonita de toda esta aventura, gracias Guillermo por tu amor incondicional y empuje, siempre fuimos soñadores y los pilotos de esta etapa de nuestras vidas. Quién diría que empezamos pensando en Australia y aterrizaríamos en Francia, felicidades a ti por tus logros académicos. A mi chiquita Génesis, mi princesa, has sido mi mejor amiga, has soportado mis peores momentos, disculpa por las veces que estuve en mi burbuja, no fue fácil pero intenté dar lo mejor por mi. Estoy orgullosa de cada paso y logro que das, tu eres mi motivación y mi razón de mirar hacia adelante sin importar la condición, me diste esa energía de super heroína que no se encuentra fácilmente.

Contents

List of Figures

Acronyms

C3S	*Copernicus Marine Climate Change Service*
CEOF	*Complex Empirical Orthogonal functions*
CMEMS	*Copernicus Marine Environment Monitoring Service*
CR	*Control run*
CROCO	*Coastal and Regional Oceanic Community Model*
ECMWF	*European Centre for Medium-Range Weather Forecasts*
EEP	*Eastern Equatorial Pacific*
EKE	*Eddy Kinetic Energy*
ENSO	*El Niño-Southern Oscillation*
ERA5	*Fifth Generation of the Atmosphere Reanalysis of the Global Climate*
EUC	*Equatorial Undercurrent*
EWBs/EWEs	*Easterly Wind Burts/Easterly Wind Events*
GLORYS2V4	*Global Ocean Reanalysis and Simulation version 4*
IEKWs	*Intraseasonal Equatorial Kelvin Waves*
IRWs	*Intraseasonal Rossby Waves*
ITCZ	*Intertropical Convergence Zone*
NECC	*North Equatorial Countercurrent*
ITV	*Intraseasonal Tropical Variability*
KmKe/BTR	*Barotrophic instability*
LIN	*Linear*
MJO	*Madden–Julian oscillation*
NDH	*Non-linear dynamical heating*
NEC	*North Equatorial Current*
NECC	*North Equatorial Counter Current*
OISST	*NOAA Optimum Interpolation SST*

PeKe(BCL) *Baroclinic instability*

SEC *South Equatorial current*

SLA *Sea level anomalies*

SODA *Simple Ocean Data Assimilation*

SSH *Sea surface height*

SST *Sea surface temperature*

TIWKE *TIW Kinetic energy*

TIWs *Tropical Instability Waves*

TOGA *Tropical Ocean-Global Atmosphere*

Tx *Zonal wind stress*

WWBs/WWEs *Westerly Wind Bursts/Westerly Wind Events*

Z20 *20° C isotherm depth*

General introduction

Tropical oceans (30°S – 30°N) are characterized by a tight coupling between the ocean and overlaying atmosphere resulting in a weakly stable balance making them sensitive to perturbations of oceanic or atmospheric origins. In the Pacific, easterly or trade winds drive a westward surface current confining warm surface water in the west and an equatorial upwelling in the east. This induces a shoaling of the thermocline in the east creating a pressure gradient that generates an eastward flowing equatorial undercurrent. Any perturbations of this subtle steady state can trigger intense oceanic and atmospheric responses, resulting in a strong climate variability over a wide range of time scales.

In particular, the Eastern Equatorial Pacific (EEP) is home to the El Niño/Southern Oscillation (ENSO), the strongest year-to-year climate fluctuation with widespread effects on global climate, weather patterns, and societies. Extreme ENSO events are becoming more frequent and increasingly disrupt ecosystems in the context of climate change. Despite the recent great progress in ENSO theory, modeling and prediction, considerable challenges remain to understand, simulate, and predict its pattern diversity and temporal complexity. For example, only a few of the current generation Earth System Models, including those used for long-term climate change projections and short-term operational forecasts, can capture with reasonable skill the observed ENSO pattern diversity and amplitude asymmetry.

A large body of literature pointed out the effects of nonlinear dynamics can have on the ENSO cycle, the EEP mean state and the overall climate variability. Nonlinearity in the climate system can operate at a wide range of time scales, which represents a source of irregularity for ENSO and the climate variability in general. On the other hand, oceanic processes in the tropics at high frequency such as the intraseasonal tropical variability have been suggested to play a significant role in ENSO onset, evolution, termination, spatial diversity and temporal complexity.

For instance, the wave dynamics and in particular intraseasonal oceanic Kelvin waves propagating eastward along the equator have long been acknowledged as a triggering mechanism for El Niño events. More recently, Tropical Instability Waves (TIWs), intraseasonal synoptic oceanic wave features that form in the EEP, have been recognized as a potential source of modulation for the EEP mean state, seasonal cycle amplitude and ENSO asymmetry. While individually these two wave types have been well studied, there is still a lot of uncertainties on how they interact, and how this interaction can influence longer timescales of variability (e.g. ENSO).

While both Kelvin waves and TIWs are at the heart of complex time scales interactions in the equatorial Pacific, far fewer studies have highlighted the potential for interactions between them (shown schematically in Figure 2). Yet the few observational, theoretical, and modeling studies that have addressed this issue have suggested that their interaction has the potential to modulate the energy budget in the eastern equatorial Pacific. In addition intraseasonal oceanic equatorial variability is also influential on coastal upwelling dynamics along the west

coast of South America that hosts very productive ecosystems, which also motivates to better understand the complex of processes that influence the characteristics of the equatorial Kelvin wave.

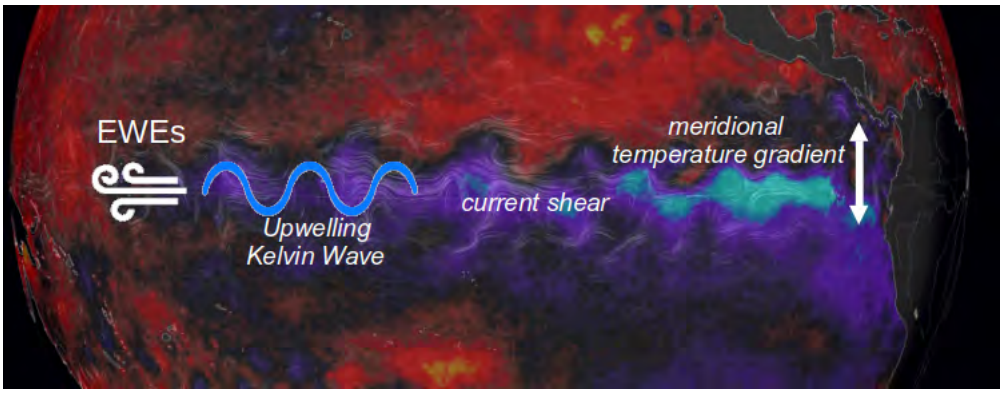

Figure 1: Illustration of the sea surface temperature anomaly on 20 December 2017 (blue/orange for the negative/positive values). The white contours on the ocean show the surface currents(From `https://earth.nullschool.net`).

The purpose of this thesis is to improve our understanding of the nonlinear interactions occurring at intraseasonal time scales between the transient TIWs mesoscale activity and equatorial Kelvin Waves. The manuscript is organized as follows:

The **first chapter** presents the main characteristics of the tropical Pacific climate, from its mean thermal state to the basin-scale circulation and the different coupled air-sea processes that govern their long-term balance. Then, the different time scales of the tropical Pacific climate variability will be described with a particular focus on the intraseasonal to interannual bands. Finally, we highlight the different nonlinear interactions occurring between these different temporal and spatial scales and their effect on the climate background and variability, which introduces the specific motivations of this work.

In the **second chapter**, we provide a detailed description of the different data sets and methodological framework used throughout the manuscript. In particular, we describe the different methods applied for assessing the variability related to TIW and Kelvin waves and diagnosing their interaction. We also describe the Coastal and Regional Ocean Community Model (CROCO) used in this thesis work and how sensitivity experiments are set up.

In the **third chapter**, we document for the first time the interaction between TIWs and equatorial Kelvin Waves from satellite observations over a period spanning almost 30 years (1993–2018). From complex empirical orthogonal functions analysis and sea level decomposition into meridional modes, we evidence that 42% of the variance of TIWs-induced intraseasonal sea level anomalies are associated with Kelvin Waves activity. We show also that non-linear dynamical heating (NDH) in the Eastern equatorial Pacific associated with this intraseasonal mode can be as large as that for interannual time scales, highlighting the importance of this interaction for better understanding ENSO.

In the **fourth chapter**, we seek to shed more light on the interaction by evaluating and quantifying the TIWs energetic and dynamics to the passage of different IEKWs phases (*i.e.*, downwelling *vs.* upwelling) using different sensitivity experiments of the high−resolution regional oceanic model CROCO. Two types of simulations' ensembles of the tropical Pacific basin are performed, one considering realistic level of mesoscale activity associated with the presence of TIWs, the so-called "Control Runs (CR)", the other without non-linear terms in the momentum equation ("Linear Runs (LIN)") in order to damp the TIWs mesoscale activity while also keeping the linear intraseasonal Kelvin Waves (IEKWs) mostly untouched. An eddy kinetic energy (EKE) budget performed on the two ensembles reveals a strongly asymmetric response of TIWs to the passage of IEKWs between their two different phases. In particular, we observe that the passage of upwelling IEKWs induces a much larger increase in the barotropic instabilities in the upper-ocean (0-50m) and baroclinic instabilities in the subsurface (50-100m) layer than of downwelling IEKWs. In addition, we show that the interaction between TIWs and IEKWs can promote substantial changes in nonlinear heat advection in the eastern equatorial Pacific, which may have strong implications for the oceanic teleconnection between the western and eastern Pacific and the low-frequency variability in this key region for the ENSO and global carbon cycle.

The **final chapter** provides a summary of this PhD work and describes a few perspectives envisioned for subsequent studies on this nonlinear intraseasonal interaction.

Introduction (Français)

Les océans tropicaux (30°S – 30°N) sont caractérisés par un couplage fort entre l'océan et l'atmosphère, ce qui les placent dans un équilibre relativement stable sujet à des perturbations d'origine océanique ou atmosphérique. Dans le Pacifique, les vents d'est ou alizés entraînent un courant de surface vers l'ouest qui confine les eaux chaudes de surface à l'ouest et une remontée d'eau équatoriale à l'est. Cela provoque une remontée de la thermocline à l'est, créant un gradient de pression qui génère un sous-courant équatorial s'écoulant vers l'est. Toute perturbation de ce subtil état d'équilibre peut déclencher d'intenses réactions océaniques et atmosphériques, entraînant une forte variabilité climatique sur une large gamme d'échelles de temps.

En particulier, le Pacifique équatorial oriental (EEP) est le siège d'El Niño/oscillation Sur (ENSO), la plus forte fluctuation climatique annuelle ayant des effets considérables sur le climat mondial, les régimes climatiques et les sociétés. Les événements ENSO extrêmes sont de plus en plus fréquents et perturbent de plus en plus les écosystèmes dans le contexte du changement climatique. Malgré les grands progrès réalisés récemment au niveau théorique, en modélisation et en terme de prévision, des défis considérables restent à relever pour comprendre, simuler et prévoir la diversité d'ENSO. Par exemple, peu de modèles du système terrestre de la génération actuelle, y compris ceux utilisés pour les projections à long terme du changement climatique et les prévisions opérationnelles à court terme, peuvent simuler de manière réaliste la diversité spatiale et temporelle ENSO, en en particulier son asymétrie

positive.

De nombreux ouvrages ont souligné les effets que la dynamique non linéaire peut avoir sur le cycle ENSO, l'état moyen EEP et la variabilité climatique globale. La non-linéarité du système climatique peut amplifier les interactions océan-atmosphère et agir comme une source d'irrégularité pour ENSO et la variabilité climatique en général. Il a été suggéré, entre autres, que les processus océaniques opérant dans les tropiques à la fréquence intrasaisonnière, tels que la variabilité tropicale intrasaisonnière, jouent un rôle important dans le déclenchement, l'évolution, la diversité spatiale et la complexité temporelle d'ENSO.

Par exemple, la dynamique des vagues, et en particulier les ondes océaniques intrasaisonnières de Kelvin se propageant vers l'est le long de l'équateur, est reconnue depuis longtemps comme un mécanisme de déclenchement des événements El Niño. Plus récemment, les ondes d'instabilité tropicale (TIWs), des ondes océaniques synoptiques intrasaisonnières qui se forment dans l'EEP, ont été reconnues comme une source potentielle de modulation de l'état moyen de l'EEP, de l'amplitude du cycle saisonnier et de l'asymétrie ENSO. Alors que ces deux types d'ondes ont été extensivement étudiées dans la littérature de manière séparée, il reste encore beaucoup d'incertituds concernant leur intéraction, et sur les processus qui pourraient faire qu'elle influence les échelles de temps de variabilité plus longue (e.g. ENSO).

Alors que les ondes de Kelvin et les TIWs sont toutes deux au cœur d'interactions complexes d'échelles temporelles dans le Pacifique équatorial, beaucoup moins d'études ont mis en évidence le potentiel d'interactions entre elles (illustré schématiquement dans la figure 2). Pourtant, les quelques études observationnelles, théoriques et de modélisation qui ont abordé cette question ont suggéré que leur interaction peut modifier le bilan energétique de surface dans le Pacifique équatorial oriental. De plus la variabilité intrasasionnière océanique le long de l'équateur influence aussi la dynamique d'upwelling côtier le long de la cote ouest de l'Amérique, laquelle acceuille des écosystèmes trés productifs. Cela motive aussi notre étude des intéractions entre onde de Kelvin et TIWs.

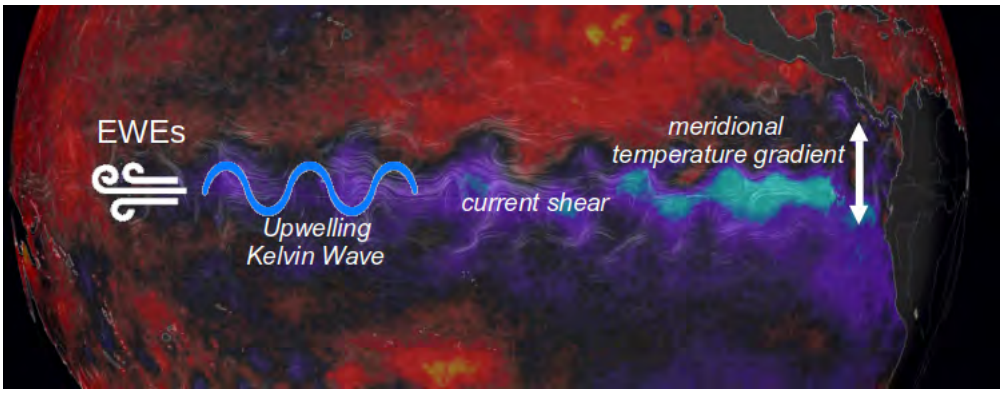

Figure 2: Illustration de l'anomalie de température de surface de la mer le 20 décembre 2017 (bleu/orange pour les valeurs négatives/positives). Les contours blancs sur l'océan montrent les courants de surface (Après `https://earth.nullschool.net`).

L'objectif de cette thèse est de mieux comprendre les mécanismes d'intéraction

non linéaires qui se produisent aux échelles de temps intrasaisonnières entre l'activité mésoéchelle des TIWs transitoires et les ondes de Kelvin équatoriales..
Le manuscrit est organisé comme suit:

Le **premier chapitre** présente les principales caractéristiques du climat tropical du Pacifique, depuis son état thermique moyen jusqu'à la circulation à l'échelle du bassin et les différents processus couplés air-mer qui régissent leur équilibre à long terme. Ensuite, les différentes échelles de temps de la variabilité du climat du Pacifique tropical seront décrites avec un accent particulier sur la bande intrasaisonnière à interannuelle. Enfin, nous mettons en évidence les différentes interactions non linéaires qui se produisent entre ces différentes échelles temporelles et spatiales et leur effet sur le fond et la variabilité du climat, ce qui permet d'introduire les motivations spécifiques de notre étude.

Dans le **deuxième chapitre**, nous fournissons une description détaillée des différents ensembles de données et du cadre méthodologique utilisé tout au long du manuscrit. En particulier, nous décrivons les différentes méthodes appliquées pour évaluer la variabilité liée aux TIWs et aux ondes Kelvin et diagnostiquer leur interaction. Nous décrivons également le modèle CROCO (Coastal and Regional Ocean Community Model) utilisé dans ce travail de thèse et la manière dont les expériences de sensibilité sont mises en place.

Dans le **troisième chapitre**, nous documentons pour la première fois l'interaction entre les TIWs et les ondes de Kelvin équatoriales à partir d'observations satellitaires sur une période de près de 30 ans (1993-2018). À partir d'une analyse complexe des fonctions orthogonales empiriques et de la décomposition du niveau de la mer en modes méridionaux, nous mettons en évidence que 42% de la variance des anomalies intrasaisonnières du niveau de la mer induites par les TIWs sont associés à l'activité des ondes de Kelvin. Nous montrons également que le réchauffement dynamique non linéaire (NDH) dans le Pacifique équatorial oriental associé à ce mode intrasaisonnier peut être aussi important que celui des échelles de temps interannuelles, soulignant l'importance de cette interaction pour mieux comprendre ENSO.

Dans le **quatrième chapitre**, nous cherchons à mieux comprendre cette interaction en évaluant et en quantifiant l'énergie et la dynamique des TIWs au passage de différentes phases de IEKWs (*i.*, downwelling *vs.* upwelling) en utilisant différentes expériences de sensibilité du modèle océanique régional à haute−résolution CROCO. Deux types d'ensembles de simulations du bassin tropical du Pacifique sont réalisés, l'un avec l'activité mésoéchelle complète associée à la présence de TIWs, appelé "Control Runs (CR)", l'autre sans termes non linéaires dans l'équation de la quantité de mouvement ("Linear Runs (LIN)") afin de réduire l'activité mésoéchelle des TIWs tout en gardant les ondes Kelvin intrasaisonnières (IEKWs) principalement linéaires intactes. Un bilan d'énergie cinétique de tourbillon (EKE) réalisé sur les deux ensembles révèle une réponse fortement asymétrique des TIWs au passage des IEKWs entre leurs deux phases différentes. En particulier, nous observons que le passage des IEKWs ascendants induit une augmentation beaucoup plus importante des instabilités barotropes dans la couche supérieure de l'océan (0-50m) et des instabilités baroclines dans la couche de subsurface (50-100m) que les IEKWs descendants. En outre, nous montrons que l'interaction entre les TIWs et les IEKWs peut promouvoir des changements substantiels dans l'advection non linéaire de la chaleur dans le Pacifique équatorial oriental, ce qui peut avoir de fortes

implications pour la téléconnexion océanique entre le Pacifique occidental et oriental et la variabilité à basse fréquence dans cette région clé pour l'ENSO et le cycle global du carbone.

Le **chapitre final** fournit un résumé de ce travail de thèse et décrit quelques perspectives envisagées pour des études ultérieures sur cette interaction intrasaisonnière non linéaire.

Chapter 1

Background

Contents

1.1 Equatorial Pacific mean state

1.1.1 Mean Thermal structure

The tropical climate is determined by the complex interactions between the large-scale atmospheric and oceanic circulations, the solar and terrestrial radiative transfer, the boundary layer, clouds, and atmospheric convection (Betts and Ridgway (1988)). In particular, we can decompose the large-scale tropical atmospheric circulation into the mean meridional and zonal overturning circulations, the Hadley and Walker circulations respectively.

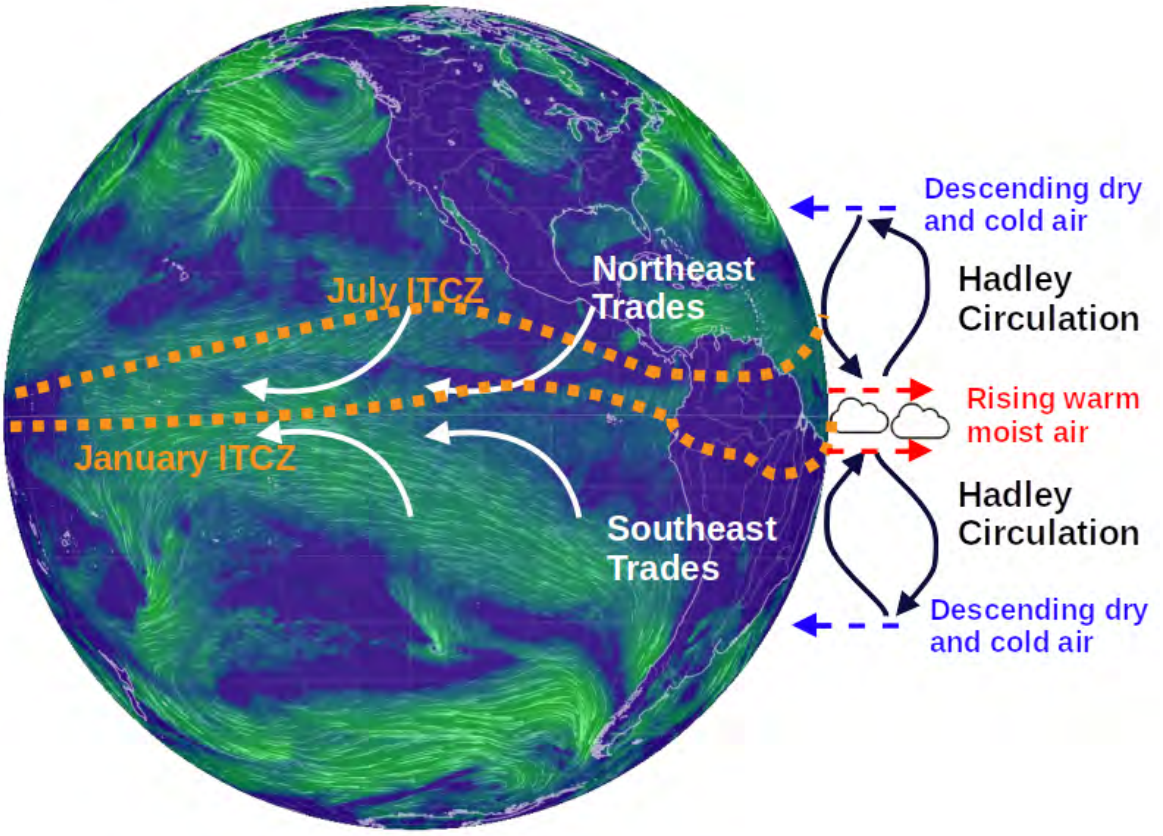

Figure 1.1: Schematic of the Hadley circulation and the mean atmospheric surface circulation in the tropics (*i.e.*, the trades winds).

The Hadley cell is due to the difference of incoming solar energy between the equator and the subtropics, with the air rising around the equator, moving towards the poles in the troposphere, and then descending back into the subtropics. This causes important differences in the surface pressure gradient, with low pressure at the equator and high pressure towards the poles, which induce movements of air parcels from the subtropics to the equator. This mechanism results in particular in tropical easterly trade winds as shown in Figure 1.1. Because the air parcels are deflected to the right in the northern hemisphere and to the left in the southern hemisphere, due to the Coriolis effect (through the conservation of the angular

momentum), this creates northeast and southeast trades winds in the northern and southern hemispheres, respectively. As a result, a low-pressure center called the Intertropical Convergence Zone (ITCZ) is located in the equatorial region (10°S-10°N) and characterized by strong convective movements from the arising warm and moist surface air.

The nearly zonal easterly surface winds (*i.e.*, Northeast and Southeast trades) blowing westward above the tropical Pacific, play an important role in the distribution of ocean water mass and heat. Because of this circulation, warm surface waters pile up in the western Pacific, defining the warm pool (SST> 28°C) (Figure 1.2a). By conservation of mass, this promotes deep cold water to be upwelled in the tropical Eastern Pacific, defining the cold tongue (SST< 25°C). These warm waters to the west and cold waters to the east shape the zonal slope of the thermocline. This results in particular in a thermocline depth of about 150 to 200 meters in the west and around 40 meters deep on average in the eastern Pacific (Figure 1.2b). Similar but reversed zonal characteristics of the thermocline are also observed on the sea level, which slopes up by about 60 cm from east to west along the equatorial band.

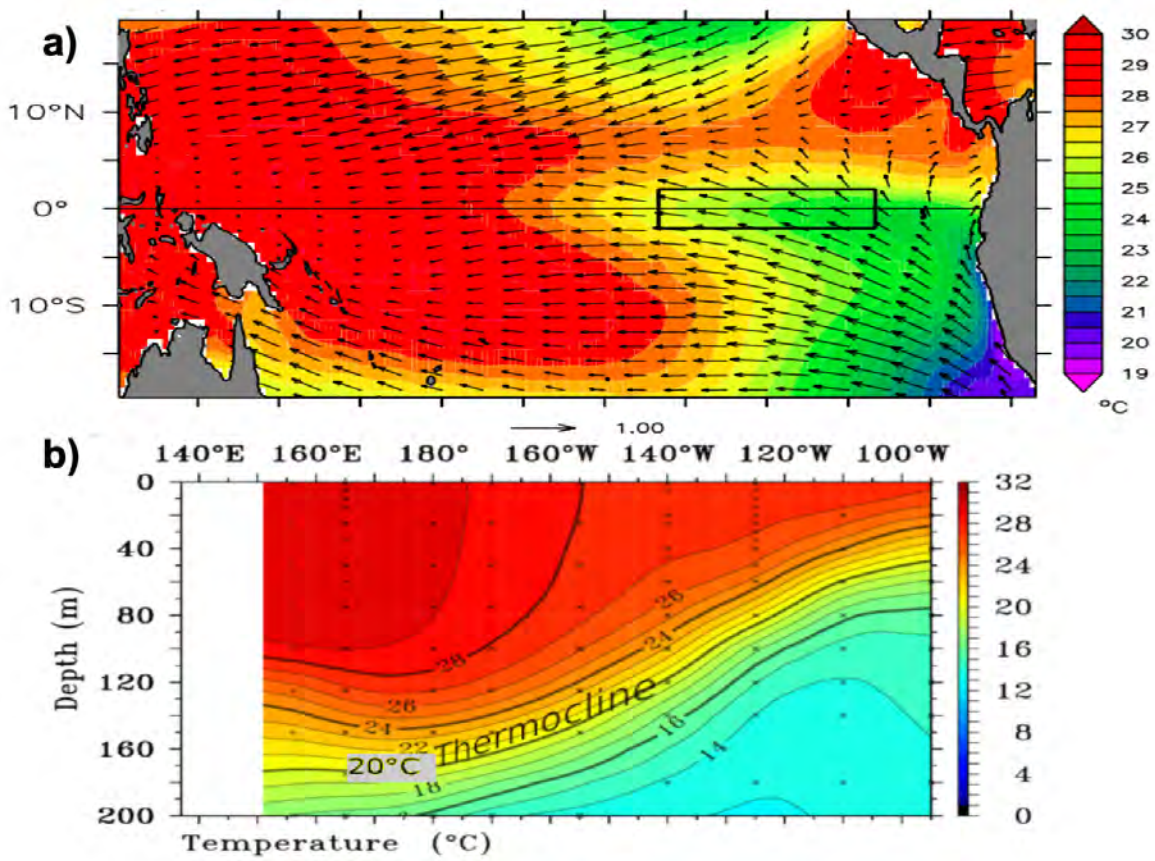

Figure 1.2: (a) Mean SST (shading) from HadISST observations and surface wind stress (arrows) from ERA-Interim in the tropical Pacific over the period 1981–2010. (b) Mean temperature section along the equator (February-April 2019) with the position of the thermocline defined as the depth of the isotherm 20°C indicated. Data provided by GTMBA Project Office of NOAA/PMEL, `https://www.pmel.noaa.gov/tao/drupal/disdel/`.

As they cross the equatorial Pacific, the easterlies gradually charge in moisture and heat through evaporation, reinforcing the warming of the western Pacific. This mechanism strengthens the salient feature of the tropical Pacific mean state described above alongside an equatorial gradient between the warm pool and the cold tongue (Figure 1.2). This zonal circulation along the equatorial Pacific is known as the Walker circulation (Walker (1923), Walker (1924), Walker and Bliss (1928), Walker and Bliss (1932), Bjerknes (1969) and results in a pressure difference between the western (low) and the eastern (high) Pacific, as shown in Figure 1.3. Over the eastern Pacific, the cold tongue is well-established, with the transport of cold water upward from the ocean interior, and the air above it is too cold and heavy to be raised with the ascending branch of the Hadley circulation, causing the air flows towards the warm pool where it will be heated sufficiently to ascend through convective towers. This upper air would then flow eastwards and descend back to the surface over the eastern Pacific when it cools (Wang et al. (2017)).

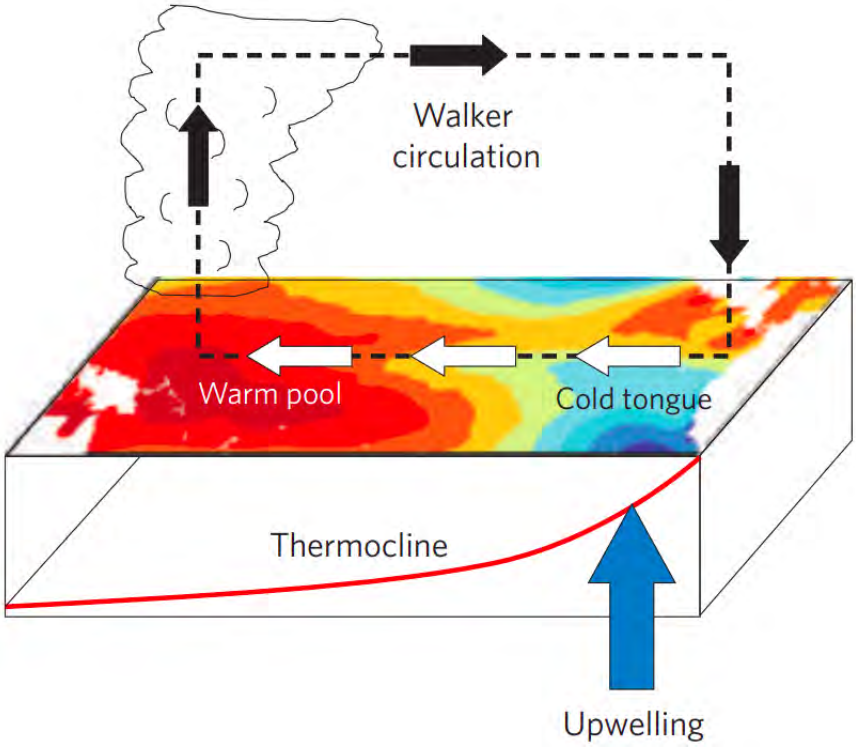

Figure 1.3: Schematic of the mean climate conditions in the tropical Pacific, indicating SSTs, surface wind stress and the associated Walker circulation, the mean position of convection, and the mean upwelling and position of the thermocline. From Collins et al. (2010).

1.1.2 Mean ocean circulation

The zonal circulation of trade winds creates a local divergence on the surface currents at the Equator (the South Equatorial Current, the North Equatorial Current, and the North Equatorial Countercurrent) owing to the Earth's rotation. These zonal equatorial currents

are fundamental to the Earth's climate system because they play an important role in the distribution of heat, salt, and biogeochemical properties between the warm pool and the cold tongue across the Pacific Ocean.

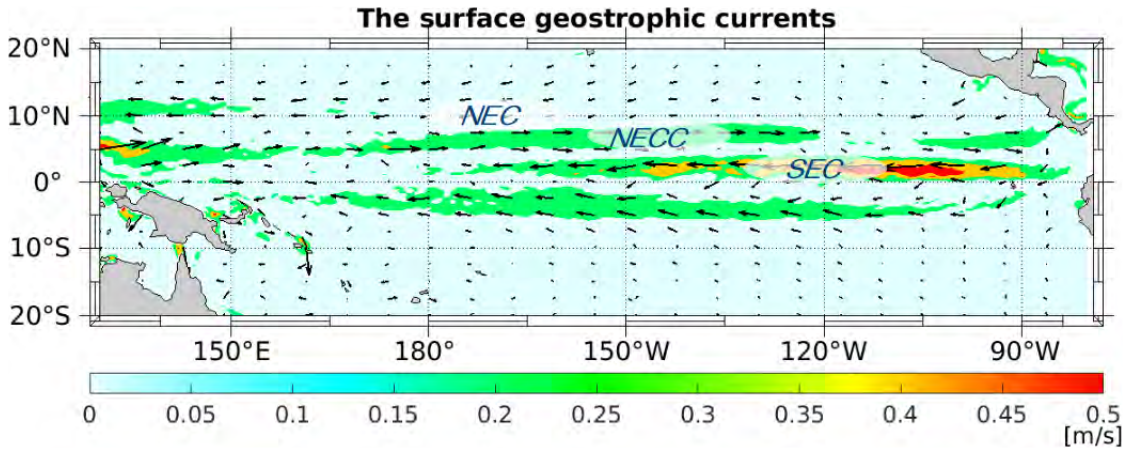

Figure 1.4: The surface geostrophic currents averaged for the period 1993-2018 (unit: [m/s]), from the Copernicus Marine Environment Monitoring Service (CMEMS) and the Copernicus Climate Change Service (C3S) Taburet et al. (2019). SEC: South Equatorial Current; NECC: North Equatorial Countercurrent; NEC: North Equatorial Current. The geostrophic velocity magnitudes are in shading pattern and direction in arrows.

The equatorial currents comprise:

Surface westward currents:

- The South Equatorial current (SEC) is a system of ocean currents that flow east-to-west between the equator and about 20° degrees south that also extends across the equator to about 5°N. It is essentially split into three main branches: the north (2°S-5°N), middle (7°S-3°S), and south (20°S-8°S) branches (Yang et al. (2022)). It is characterized by a maximum zonal velocity of 55 cms^{-1} and total volume transport of 49.8 Sv in the central-east Pacific with some spatial specificities. The SEC northern branch is situated in the SST front and is faster in the central Pacific at 3°N than in the western Pacific. The weakest part of the SEC is the southern branch located at 4°S-5°S with its maximum in the central-western Pacific (Yang et al. (2022)). The SEC is driven by the zonal and alongshore winds, which induce the upwelling along the equator and the southeastern coast of the basin respectively. Intensification in the winds provokes a strengthening of the SEC and an expansion of the upwelling zone. Conversely when the winds relax the reverse happens, causing a zonal redistribution of heat in the southeastern Pacific (Philander and Pacanowski (1981)). Because it serves to recharge or discharge the western Pacific warm pool (Fine et al. (1994); Grenier et al. (2011); Davis et al. (2012); Gasparin et al. (2012); Ganachaud et al. (2014); Hu et al. (2015)) and also connects the Pacific and Indian oceans via the Indonesian Throughflow, the SEC plays a major role in the global climate variability.

- The North Equatorial Current (NEC) is a similarly wind-driven current located between 8°N and 18°N with an annual mean transport in the western Pacific between 41.3 Sv and 62.3 SV (Qu et al. (1998) and Qiu and Joyce (1992)). It connects the subtropics with the tropics in the Pacific through its bifurcation into the Kuroshio Current and the Mindanao Current that contributes to the tropical and subtropical gyres (Fine et al. (1994); Qiu and Lukas (1996)). The NEC plays an important role in the evolution of the western warm pool (Qiu et al. (1997)). It also has an impact on the variability of biological properties in the western Pacific (Kimura et al. (2001), Amedo et al. (2002)) and in the modulation of the thermohaline circulation (Gordon (1986)).

Eastward currents:

- The North Equatorial Counter Current (NECC) is a wind-driven eastward flowing current which extends to depths of 100–150 meters and from 2°N to 10°N, shifting its main body to 5°N in the western Pacific and to 7°N (Donguy and Meyers (1996)) in the central Pacific. It is shallower in the western than the eastern Pacific (Donguy and Meyers (1996); Johnson et al. (2002); Wyrtki and Kendall (1967)). The NECC transports water against the mean westward wind stress in the tropics. This west-east transport is governed by the north-south change in the wind stress curl as explained by the Sverdrup theory (Sverdrup (1947)). The NECC can transport 10–30 Sv eastward, contributing to warm the eastern Pacific, therefore having an important role in the heat budget of this region (Clement et al. (2005); Meyers and Donguy (1984); Picaut and Delcroix (1995)). It can reach a zonal velocity of 0.4 ms^{-1} near 220°E (Gouriou and Toole (1993); Johnson et al. (2002); Wyrtki and Kendall (1967)).
- The Equatorial Undercurrent (EUC) is an eastward subsurface countercurrent in the Pacific, confined between 2°N-2°S by the Coriolis force with a maximum velocity of 1 ms^{-1} near 95°W (Johnson et al. (2002); Rudnick et al. (2021)) that transports about 30 Sv in the central Pacific (Lukas and Firing (1984); Wyrtki and Kilonsky (1984)). It is the result of the zonal pressure gradient induced by the easterly winds (Qiao and Weisberg (1997)). In particular, the zonal pressure gradient force, related to the zonal sea level slope, is maintained by the trade winds and the westward surface current and constitutes a dominant acceleration term in the EUC momentum budget (Knauss (1959); Knauss (1966)). The balance between the eastward zonal pressure gradient force and westward surface stress determines the EUC strength as well as its zonal and vertical structure (Philander (1973); McPhaden and Taft (1988)). This mechanism forces it to shoal from 200m in the west to 50m in the east near 95°W (Knauss and KING (1958); Wyrtki (1974b); Johnson et al. (2002)), and to sometimes outcrop in the far eastern equatorial Pacific. Figure 1.5 illustrates the position of the EUC along the equatorial thermocline and provides a simplified diagram of its generation due to the sea level difference between the western (high pressure) and eastern Pacific (low pressure). The EUC, which can also recirculate into the SEC (Lukas (1986)), has an important role in the variability of the eastern Pacific by modulating the equatorial Pacific thermal structure and feeding the equatorial upwelling in the cold tongue region (Bryden and Brady (1985)) and along the coast of Peru (Wyrtki and Bennett (1963)).

It has been shown that the EUC can control the position and the variability of the upper oxygen minimum zone (OMZ)'s shape and depth in the eastern Pacific (Busecke et al. (2019)), highlighting its key role in the biogeochemistry and dynamics of one of the most productive ecosystem and in the global carbon cycle.

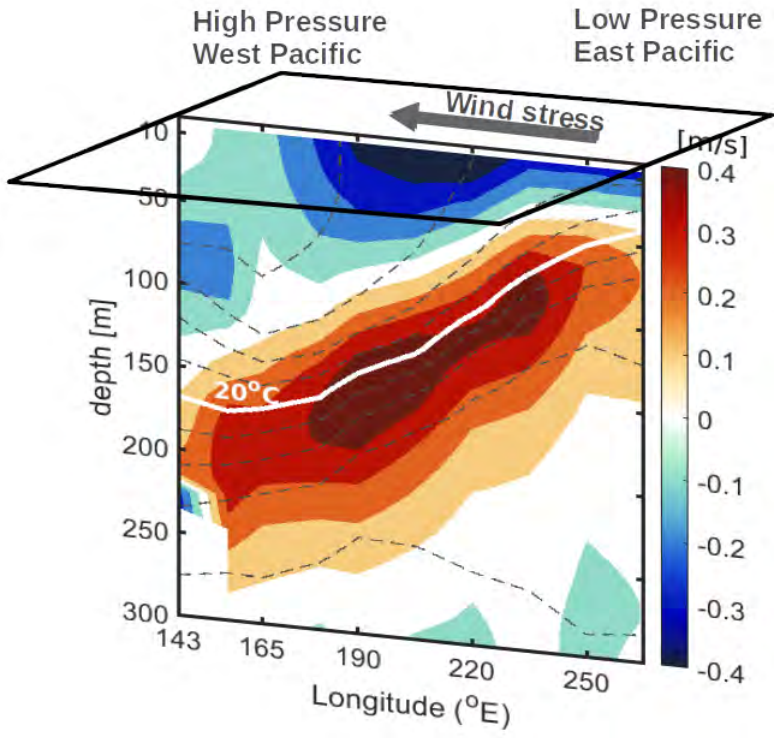

Figure 1.5: Longitude-depth section (2.5°S - 2.5°N average) of mean zonal velocity (shading) and temperature (dashed contours (2°C increments). The thick white line represents the equatorial thermocline as the 20°C isotherm. Data come from *in situ* observations collected in the 1990s by (Johnson et al. (2002)).

1.2 Equatorial Pacific climate variability

1.2.1 Seasonal variability

The sun crosses the equator twice a year, at the end of the boreal winter in March and summer in September. In addition, the ITCZ undergoes shifts its latitudinal position due to the annual variation of the incoming radiation, reaching its maximum northern (southern) position in July (January) (Figure 1.1). This results in a zonal asymmetry in the seasonal variability of equatorial oceanic features, which tend to exhibit annual and semiannual harmonics (Fiedler and Talley (2006)) depending on the region and the different combinations of external forcing (*i.e.*, winds and heat fluxes), and other oceanic processes (*i.e.*, upwelling strength, vertical mixing, wind mixing). This zonal asymmetry in the seasonal variability of

equatorial climate variables is illustrated in Figure 1.6 with essentially weak/strong annual cycle in the central/eastern Pacific.

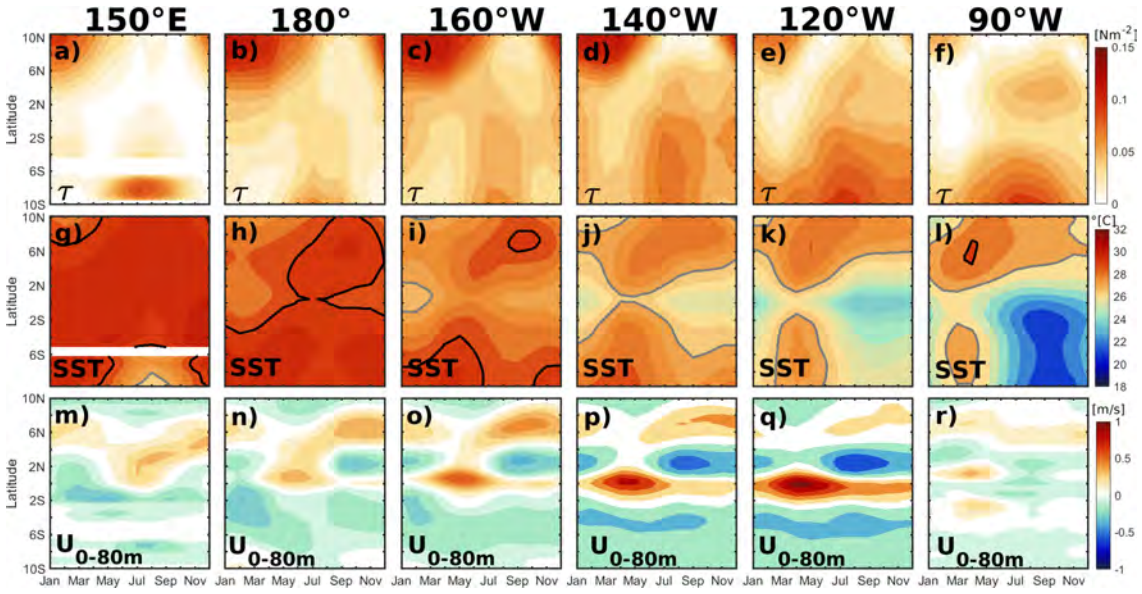

Figure 1.6: The monthly climatology of (a,b,c,d,e,f) the zonal wind stress, (g,h,i,j,k,l) sea surface temperature (averaged in the upper 15 meters), (m,n,o,p,q,r) and zonal currents (averaged in the upper 80 meters) averaged between 10°N and 10°S at three different longitudes: 150°E,180°,160°W, 140°W, 120°W, and 90°W. Data are derived from the SODA version 3.4.2 reanalysis product. The climatology is calculated as the monthly mean over the period 1993 to 2019. The 27°C (29°C) isotherm is shown by the gray (black) contour in the sea surface temperature.

At the equator, it shows that wind stress τ has an annual cycle and fluctuates from weak (Mars-May) to intense (July-November) when the ITCZ position is its farthest south, north respectively (Figure 1.6 a,b,c,d,e,f). When the trade winds are intense (July-September), they cool the Eastern Tropical Pacific from about 27°C (February-March) to 21°C (June-September) by enhancing evaporation and driving coastal upwelling (Figure 1.6 g,h,i,j,k,l and Figure 9, middle from Kessler (2006a)). In addition, an increased strato-cumulus formation over the cold SST in the far eastern Pacific tends to damp solar radiation and reduce the SST even further (Mitchell and Wallace (1992); Klein and Hartmann (1993)) leading to a strong/weak SST annual cycle in the eastern/central Pacific (Horel (1982)).

The strength of the equatorial currents (Figure 1.6 m,n,o,p,q,r) responds also to this seasonal wind variations. In the northern part of the Eastern Pacific, the NEC (about 8°N-10°N) intensifies from February to June and weakens during July-September, and the NECC intensifies (weakens) during the boreal autumn (spring) due to the strong wind-forcing fluctuations associated with the ITCZ (e.g., Wyrtki (1974a); Wyrtki (1974c); Qiu and Lukas (1996); Hsin and Qiu (2012);Liu and Zhou (2020); Liu et al. (2021)). On both sides of the equator, the two branches of the SEC also exhibit a seasonal cycle although a little weaker: the northern position at 2°N (about 50cms^{-1}) which intensifies during the boreal summer (Yang et al. (2022)) and weakens from February to March (Johnson et al. (2002)), and the middle branch

at 5°S (close to 30 cms^{-1}) that maintains its strength in the central Pacific (140°W and 120°W) and intensifies between July and November. The seasonal variations of the SEC are also dominated by wind stress driven annual Rossby waves along 5°N (Yang et al. (2022)). The annual cycle of the EUC reaches its maximum around April-May when the trade winds weaken and reduce the sea level difference between the western and eastern Pacific as well as the westward momentum imparted on the EUC through nonlinear effects (Keenlyside and Kleeman (2002), Johnson et al. (2002)), Kessler (2006b)) Note also the split of EUC into two branches of slower eastward-moving water (Stevenson and Taft (1971)) observed in the section at 90°W when it encounters the topographic barrier of the Galapagos Archipelago (Jakoboski et al. (2020)).

1.2.2 Interannual variability - ENSO

1.2.2.1 General description

The El Niño/Southern Oscillation (ENSO) is the dominant climate mode of variability in the tropical Pacific Ocean, which arises from ocean-atmosphere interactions and impacts the global climate (McPhaden et al. (2006)), weather events, ecosystems, agriculture, and fisheries worldwide via atmospheric and oceanic teleconnections (Lin et al. (2020); Sprintall et al. (2020); Taschetto et al. (2020); Sprintall et al. (2020)). The dominant air-sea interaction leading to the interannual variations of oceanic and atmospheric conditions is called the Bjerknes feedback, which can be seen as a "chain reaction" simply summarized as: "an intensifying Walker Circulation provides for an increase of east-west temperature contrast that is the cause of the Walker Circulation in the first place" (Bjerknes (1969)). In other words, ENSO can be simply seen as a disruption or intensification of the Walker zonal circulation. During El Niño (Fig. 1.7a), the easing of the trade winds is associated with an eastward extension of the Warm Pool (*i.e.*, the Bjerknes feedback). The equatorial and coastal upwelling weakens (or even disappears in the case of strong El Niño events), inducing a deepening of the thermocline and an eastward shift of warm waters. These reinforcements of the initial warming are called respectively the upwelling, thermocline, and zonal advective feedbacks (*e.g.*, Kim and Jin (2011a), Kim and Jin (2011b), Hu et al. (2016)). The eastward shift of warm water is associated with a shift of the atmospheric convective cell leading to droughts in the west and heavy rainfall in the eastern part of the basin. El Niño events can be followed by cold episodes called La Niña, corresponding to cold conditions in the central Pacific (Fig. 1.7c). This phase of the oscillation is actually considered a strengthening of normal conditions (Fig. 1.7b), with an intensification and extension of the trade winds into the center of the basin and a Cold Tongue penetrating further west. As a summary, Figure 1.7 presents schematics of the climate conditions encountered across the tropical Pacific basin during El Niño (October-December 2015, Fig. 1.7a), La Niña (October-December 2019, Fig. 1.7b) and neutral (October-December 2021, Fig. 1.7c) conditions.

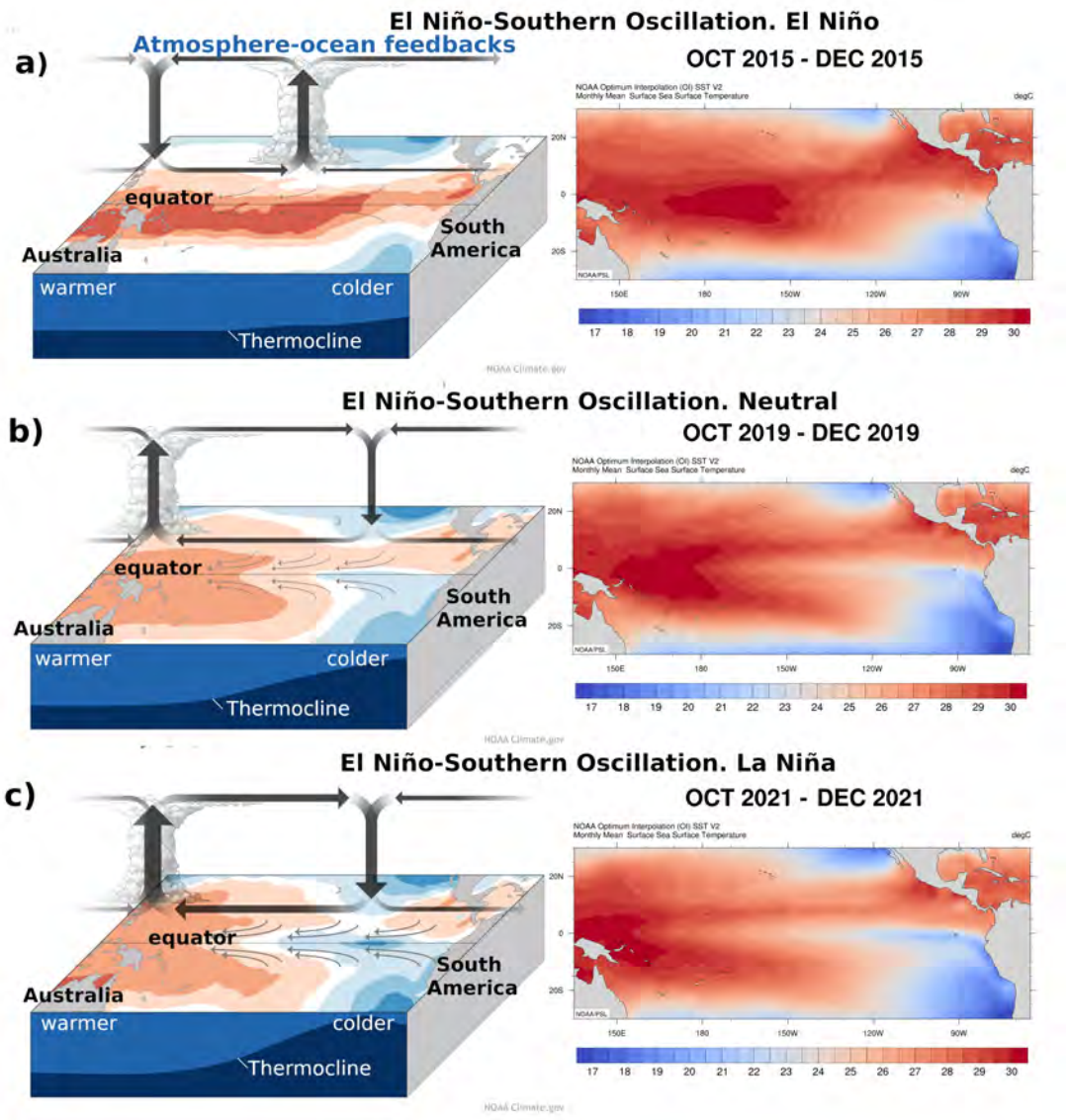

Figure 1.7: Schematic of climate conditions in the tropical Pacific associated with El Niño (a), Neutral (b) and La Niña (c) conditions (left panels); and the sea surface temperatures (SST) (right panels) during the corresponding El Niño (October-December 2015), Neutral (October-December 2019) and La Niña (October-December 2021) peak season. The orange (blue) shading pattern at the top of the schema is when the sea surface temperature is warmer (cooler) than the average; the equatorial section (depth, longitude) shows the changes in the thermocline depth; and the thin (thick) and surface arrows represent the trades winds (Walker Circulation). This figure is adapted from the schematics from Climate.gov (by Emily Eng, and inspired by NOAA PMEL). SST is derived from the NOAA Optimum Interpolation SST version 2 and obtained from `https://psl.noaa.gov/data/gridded/data.noaa.oisst.v2.html`.

1.2.2.2 Diversity and complexity of ENSO events

The ENSO cycle evolution is tightly liked to the seasonal cycle of the tropical Pacific. Typically, El Niño and La Niña episodes develop during the boreal summer, peak early winter, and decay rapidly during the following spring, lasting about 9–12 months although El Niño events tend to be shorter lived and stronger than La Niña events, which can occur over 2 successive years (McPhaden et al. (2020)). However, not all ENSO events are the same, as they exhibit very diverse features in terms of their amplitude, temporal evolution, and spatial patterns that may arise from nonlinearities in the ocean, atmosphere, coupled feedbacks or external forcings to the tropical Pacific (Capotondi et al. (2015), Timmermann et al. (2018)). This has been recently referred to as the "ENSO diversity and complexity" (Capotondi et al. (2015), Timmermann et al. (2018)).

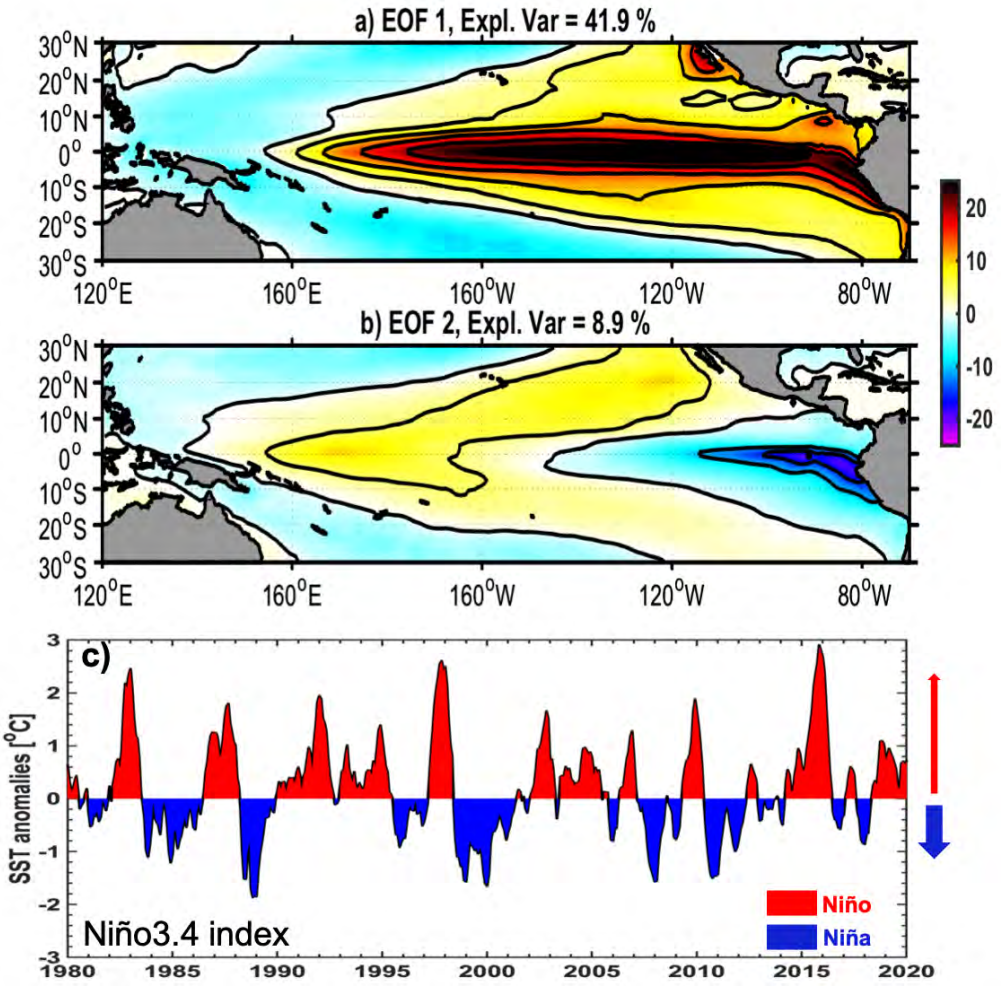

Figure 1.8: Spatial pattern of the first (a) and second (d) mode from the decomposition of SST interannual anomalies into Empirical Orthogonal Functions (EOF). (c) Time-series of SST anomalies averaged in the Niño3.4 region (5°N-5°S, 170°W-120°W). Contribution by Julien Boucharel.

The term "ENSO diversity" originates from the concept that SST anomaly patterns exhibit marked variations. The repeated occurrence of SST warming in the central Pacific in the 2000s suggested in particular that ENSO events may be grouped into two flavors: the conventional El Niño, with SST anomalies concentrated in the Eastern Pacific (EP), and the Central Pacific (CP) El Niño, with SST anomalies located around the dateline (Kao and Yu (2009); Kug et al. (2009)), which roughly correspond to the first and second most dominant modes of SST anomalies variability from a decomposition into Empirical Orthogonal Functions (EOF), (cf. Figure 1.8a and b).

The complexity refers to its intricate temporal behavior characterized by large variations in amplitude, and duration that is expressed mostly through the strong asymmetry between El Niño and La Niña events (cf. Figure 1.8c), with differences in spatial patterns, amplitude and temporal evolution between the two phases of ENSO.

This asymmetry can originate from nonlinearity in atmospheric processes in particular the asymmetrical response of wind stress to SST anomalies (Kang and Kug (2002)) and a nonlinear shortwave feedback (Im et al. (2015)). It can also arise from nonlinear oceanic processes, such as the nonlinear advection of anomalous temperature by anomalous currents (*i.e.*, the Nonlinear Dynamical Heating (NDH), An and Jin (2004)), the nonlinear oceanic wave response (Im et al. (2015)) or an asymmetrical biophysical feedback (Marzeion et al. (2005)) among others.

Another source of ENSO asymmetry resides in the impact of processes operating in the tropics at a higher frequency and in particular the intraseasonal tropical variability that will be described in detail in the following section.

1.2.3 Intraseasonal Tropical Variability - ITV

The Intraseasonal Tropical Variability (ITV) can be defined as seasonal variations, shorter than a season, that impact the weather but can also drive strong multi-scale interactions (Wang and Liu (2011), Liu and Wang (2012), Liu et al. (2012), Liu and Wang (2013)), Kim et al. (2011)). The ITV is produced by perturbations in the upper troposphere and sea level pressure, causing changes in the winds, humidity, sea surface and subsurface temperature, surface heat fluxes, as well as air-sea temperature. It can also have its source in the ocean circulation as will be described hereafter.

1.2.3.1 Atmospheric ITV

The atmospheric ITV can be divided into three hierarchic categories (Wheeler and Kiladis (1999)): (*i*) first the most dominant mode of variability is the Madden-Julian Oscillation (MJO) (Madden and Julian (1971);Madden and Julian (1972)) characterized by an eastward propagation along the equator with quasi-periodicity of 30 to 60 days and planetary scales of about 20000 km (Zhang (2005)); which is an envelope of (*ii*) the Convectively Coupled

equatorial Waves (CCWs) that have an equatorial synoptic scales of 2000 km and 4 days (Kiladis et al. (2009)); which is also an envelope of smaller fluctuations of (*iii*) Mesoscale Convective Systems (MCSs) that have a mesoscale of 200 km and 0.4 days (Houze Jr (2004)).

Convectively coupled equatorial wave and mesoscale convective systems

- The MCSs are regions of convective and stratiform clouds clusters that persist for several hours with deep convection, causing continuous and heavy precipitation. In the tropics, the ITV activity centers from the Indian Ocean to the Western Pacific and most of the deep convection comes from the MCSs (Houze Jr (2004) and Lin (2007)).
- The CCWs are the most important mode of convection variability in the tropics, with important impacts on climate variations such as the genesis of tropical cyclones (e.g., Ventrice et al. (2012a);Ventrice et al. (2012b)) and the MJO (e.g., Roundy et al. (2009)) and monsoon (e.g., Straub et al. (2006); Janicot et al. (2010); DeMott et al. (2011)). In the tropics, the rainfall responds to the movement of equatorially trapped waves in the atmosphere to which the deep convection is coupled: the Kelvin, equatorial Rossby, mixed Rossby-gravity and westward and eastward inertia-gravity waves (described by Matsuno (1966)'s solution of the shallow water equation) (Kiladis et al. (2009)).

An example of the observed outgoing longwave radiation (a classic proxy for convection) associated with the MJO, convective coupled Kelvin and equatorial Rossby wave of January 3, 2023 is shown in Figure 1.9, where the blue regions which indicate MJO-induced convection are located in the western Pacific.

Madden–Julian oscillation-MJO The MJO was first documented by Madden and Julian (1971) and Madden and Julian (1972). Its eastward propagation with an average speed of 5ms^{-1} (e.g., Weickmann et al. (1985); Knutson and Weickmann (1987); Zhang (2005))influences regions from the Indian ocean, the maritime continent, Australia all the way to the American continent. The MJO is characterized by two phases: the so-called "convective phase" which enhances the clouds generation and the rainfall; and the "suppressed convective phase" with the reverse impact. Figure 1.10 shows the large-scale wind structure associated with the MJO when the convective center is located over the Indian Ocean. At the low level of the atmosphere, the winds converge and the air rises up to higher levels, increasing the moisture and the rainfall (see green arrows). Then at the top of the atmosphere, the winds diverge and propagate eastward. Conversely, the suppressed convective phase is characterized by convergent winds at the top of the atmosphere leading to sinking air motion towards the surface, warming and drying the air masses (see brown arrows), therefore inhibiting rainfall.

The MJO has been shown to trigger and modulate high-frequency wind variability and in particular episodes of anomalous, strong, and short-lived wind bursts characterized by either westerlies or easterlies anomalies, also known as Westerly Wind Events (WWEs) and Easterlies Wind Events (EWEs) respectively.

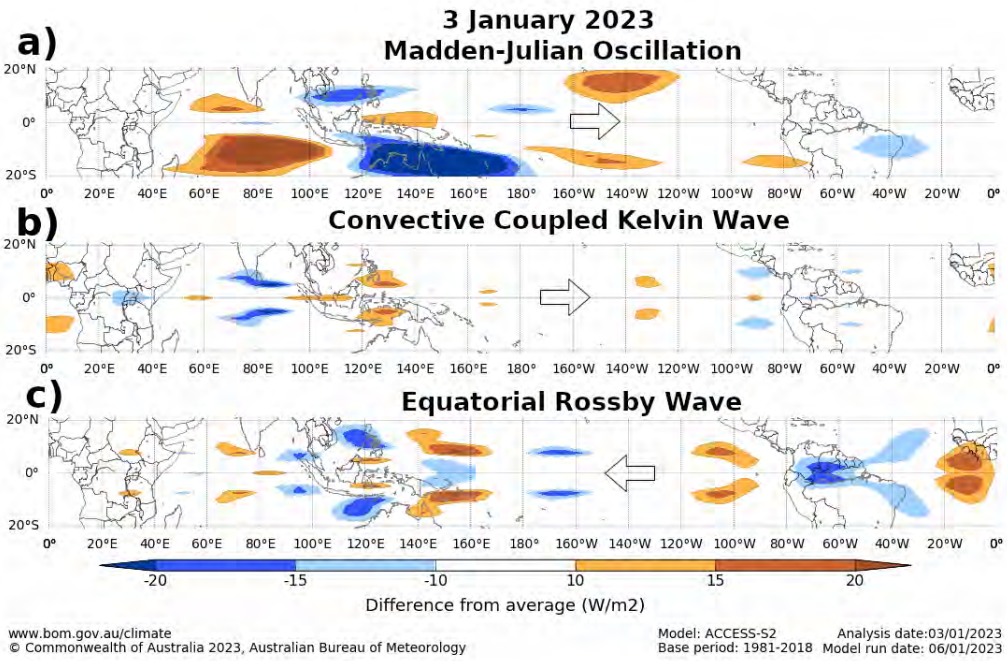

Figure 1.9: Maps of outgoing longwave radiation anomalies associated with (a) MJO, and the CCWs: (b) convective coupled Kelvin wave and (c) Equatorial Rossby Wave, on January 3, 2023. Blue/orange shading indicates enhanced/suppressed convection. The arrows indicate the direction of the tropical waves. (Figure obtained from Climate Driver Update `http://www.bom.gov.au/`).

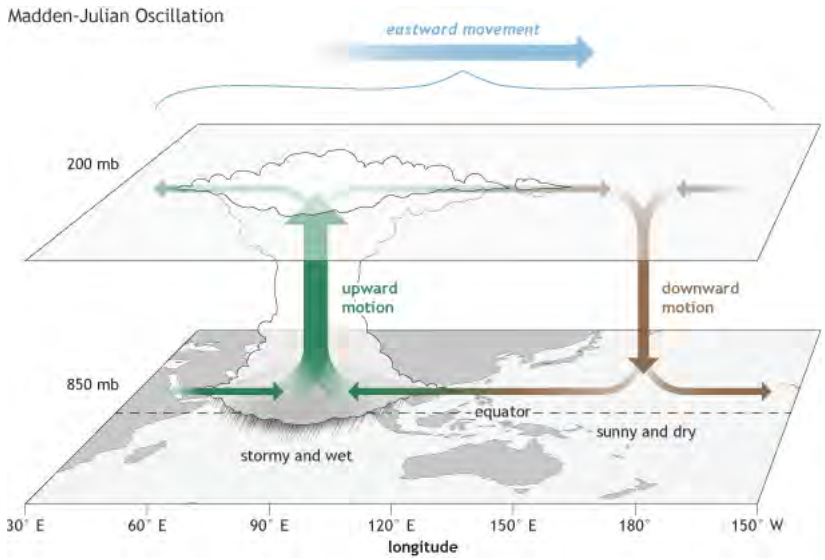

Figure 1.10: Schema of the upper-atmosphere structure of the MJO for a period characterized by a convective phase centered in the Indian ocean. The arrows pointing left (right) illustrate the easterly (westerly) wind anomalies. (Figure obtained from Climate.gov).

WWEs, also known as Westerly Wind Bursts (WWBs), occur over the warm pool with typical amplitudes of 7ms/1 and a zonal fetch of 20° with 8 days of duration (Lengaigne et al. (2004a), Harrison and Vecchi (1997)).

EWEs are the counterpart of the WWEs, although less frequent, and can be described as episodic reinforcements of the trade winds in the central and western Pacific, (*i.e.*, located further east than WWEs (Puy et al. (2016)).

Their composite spatio-temporal evolution is shown in Figure 1.11.

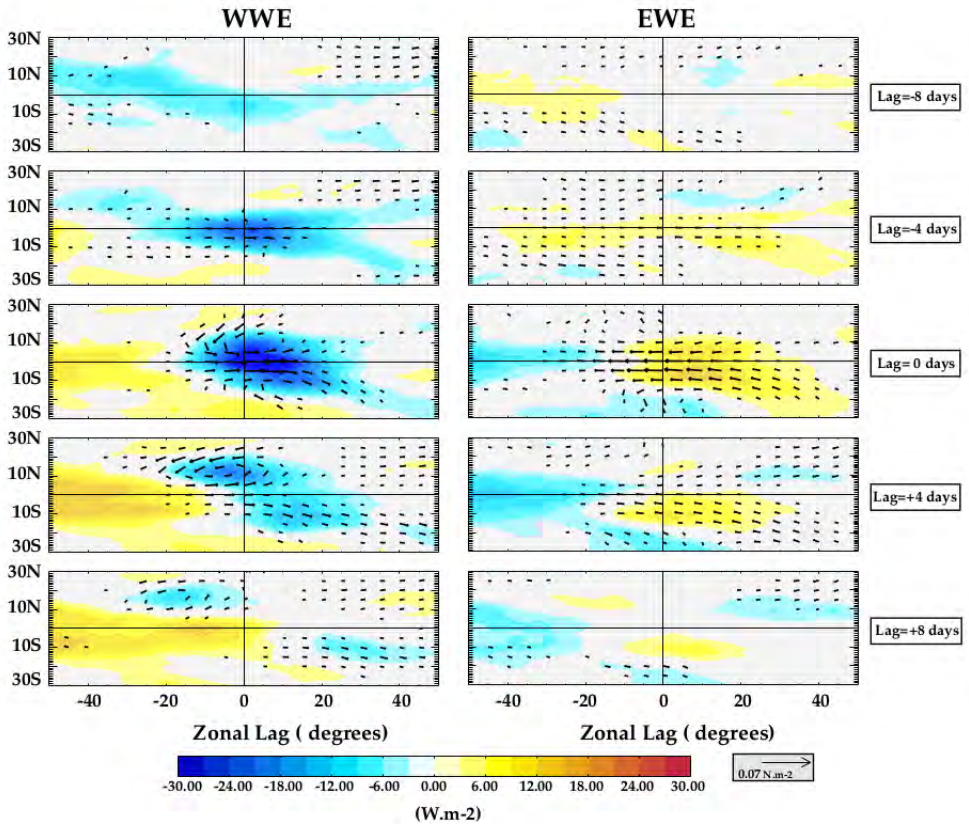

Figure 1.11: Lead-lag temporal and zonal composites of the WWEs (left panels) and EWEs (right panels). The vectors represent the speed and direction of wind anomalies and the shading shows the intraseasonal outgoing longwave radiation anomalies (blue/yellow shading associated with enhanced/suppressed convection), 5 days before and 8 days after the peak of the event. (Figure 4 and selection of events by Puy et al. (2016)).

It has been long known since the seminal study of Enfield (1987), who evidenced intraseasonal SLA propagation coherent with the MJO-related 850 mb winds, that the atmospheric ITV in the western Pacific could excite equatorial oceanic long-wavelength waves, in particular the first baroclinic Kelvin waves, suggesting a strong connection between atmospheric and oceanic ITV and in particular with equatorial waves. The next section is dedicated to the detailed description of the oceanic ITV, especially related to intraseasonal equatorial Kelvin

and Rossby waves (IEKWs, IRWs) tied to the atmospheric ITV through air-sea interactions (*e.g.*, Gushchina and Dewitte (2012); Gushchina and Dewitte (2019)) and on the Tropical Instability Waves (TIWs) resulting from current instabilities in the shear zone between the SEC and EUC.

1.2.3.2 Oceanic ITV

Equatorial Kelvin and Rossby waves In the equatorial region, the Coriolis parameter vanishes, which allows the equatorial band to act as a wave guide or natural boundary for the propagation of oceanic waves as a response of the ocean to the atmospheric ITV. This response can be described in terms of the natural modes of the ocean: baroclinic modes and barotropic modes for the oceanic vertical structure and the equatorial Kelvin (KWs) and Rossby (RWs) waves for the horizontal structure (Philander (1978)) which are obtained as solutions of the linearized shallow-water equations on the equatorial β-plane (Cane et al. (1981)). The theory of the decomposition of the equatorial variability into horizontal (meridional) modes will be thoroughly described in the next chapter. Figure 1.12 shows the idealized oceanic response in terms of Kelvin and Rossby waves from a shallow-water ocean model forced by a wind stress perturbation (such as WWEs or EWEs) with the typical eastward propagation of SLA along the equator and westward propagation of opposite SLA on both sides of the equator (3°N and 3°S) respectively.

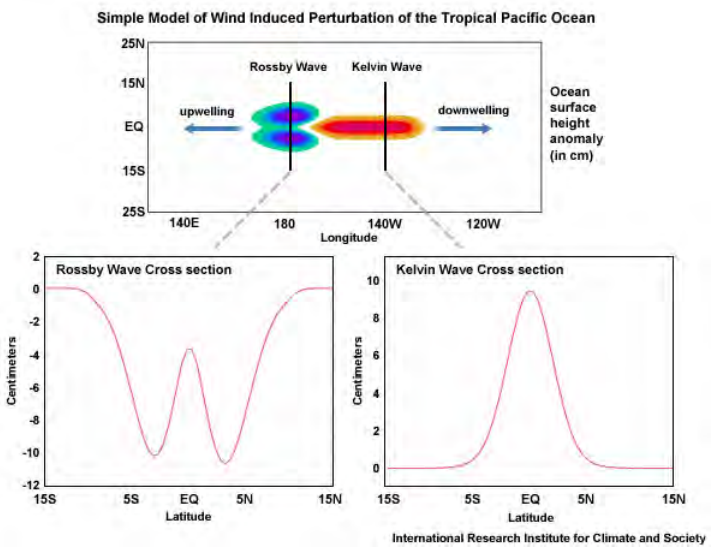

Figure 1.12: Illustration of the eastward propagation of a Kelvin wave and westward propagation of a Rossby wave from an idealized linear shallow water ocean model forced by a wind stress perturbation. Red and blue shading show their opposite signature on sea surface height anomalies. The bottom panels display the SLA meridional structure associated with the Rossby (left) and Kelvin (right) waves. (Figure `http://www.chanthaburi.buu.ac.th/~wirote/met/tropical/textbook_2nd_edition/navmenu.php_tab_5_page_2.1.3.htm`)

KWs are usually triggered in the western Pacific where atmospheric ITV-related wind bursts

occur, propagate eastward and cross the Pacific basin in about 2.5 months (Wang et al. (2016)) which corresponds to time it takes at a phase speed of around 2.7ms^{-1}(Busalacchi et al. (1983); Cravatte et al. (2003); Enfield (1987); Hendon et al. (1998); Kessler and McPhaden (1995); Knox and Halpern (1982); Kutsuwada and McPhaden (2002);Lukas and Firing (1984);McPhaden (2002b); Roundy and Kiladis (2006); Shinoda et al. (2009); Zhang (2001)). Depending on the type of wind episodes, a downwelling (upwelling) equatorial KW is generated as a response to the WWEs (EWEs) and deepen (rise) the thermocline. Figure 1.14 illustrates the eastward propagation of a downwelling KW and its signature on the sea level, currents and ocean heat content anomalies. After its initiation in the western Pacific, the amplitude of the KW reaches its maximum near 150°W, with an enhancement of the eastward zonal currents and increase in heat content. Near 120°W, the surface amplitude of the downwelling KW weakens as it propagates towards the South American coast. Concurrently, RWs of the opposite phase propagates westward crossing the Pacific basin in about 7 months (Wang et al. (2016)). After a downwelling RW has reached the western boundary of the Pacific Ocean, it is reflected back as an upwelling KW. However, at intraseasonal timescales, both RW and KW tend to dissipate in the surface layer much more than at interannual timescales due to the vertical propagation of their energy. In particular the higher frequency the steeper the energy beam (McCreary Jr (1984)). Owing to the sloping thermocline that produces a zonal density front, the KW can also partially reflect near the location of the maximum zonal gradient in density ($\sim$ 120°W) (Mosquera-Vásquez et al. (2014)). Other processes of dissipation include the scattering of energy (Busalacchi and Cane (1988);Giese and Harrison (1991), Dewitte et al. (1999)), Doppler shifting by the equatorial undercurrent (McPhaden (1986)), local wind forcing in the far eastern Pacific (Dewitte and Takahashi (2019)).

The dissipation of the IEKW energy (Figure 1.13) is evidenced in the decrease of the variability of the sea temperature to the east of 120 °W. Mosquera-Vásquez et al. (2014) suggest that the dissipation may result from the shallowing thermocline that induces changes on the phase speed from 2.2 to 1.5 ms^{-1} for TAO data.

In the tropical Pacific ocean, the second major source of intraseasonal variability is related to the Tropical Instabilities Waves, described in the next section.

Tropical Instability Waves (TIWs) first observed in the 1970s from satellite as the cusp-shaped meanders of the SST near 2°N (Legeckis (1977)) along the SST front (Wallace et al. (1989)), are the dominant form of oceanic mesoscale activity in the equatorial Pacific (Hansen and Paul (1984)). They are particularly observed in the SST pattern (eg. Chelton et al. (2001); Contreras (2002)), but their signature can also be seen in many oceanic, atmospheric and biogeochemical variables like sea surface height (Musman (1989); Weidman et al. (1999); Lawrence and Angell (2000); Benestad et al. (2001); Polito et al. (2001); Lyman et al. (2005); Shinoda et al. (2009)), meridional and zonal velocity (Qiao and Weisberg (1995); Flament et al. (1996); Inoue et al. (2012)), salinity (Lee et al. (2012)), chlorophyll (Yoder et al. (1994); Strutton et al. (2001); McClain et al. (2002);Legeckis et al. (2004); Evans et al. (2009)), subsurface temperature (Flament et al. (1996); McPhaden (1996); Kennan and Flament (2000)) and low-level wind and wind stress (Xie et al. (1998); Chelton et al. (2001);

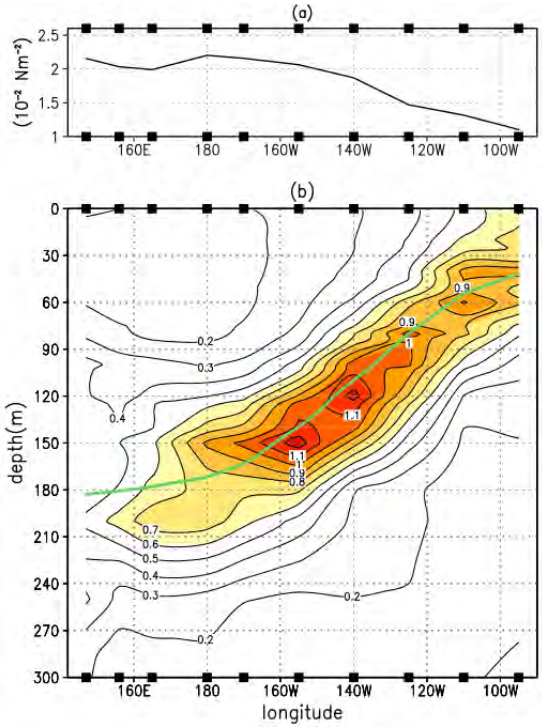

Figure 1.13: Depth-longitude section of the root mean square along the equatorial band (2°N-2°S) of the intraseasonal anomalies of (a) zonal wind stress and (b) sea temperature derived from TAO-TOGA data and for the period 2000-2011. From Mosquera-Vásquez et al. (2014) (Figure 1).

Hashizume et al. (2001)). TIWs are characterized by a westward propagation with a phase speed between 30 cms^{-1} and 60 cms^{-1}, frequencies of 17-day^{-1} near 2°N and 33-day^{-1} in the latitudinal band 2°-6°N (Lyman et al. (2007)) and wavelengths of 1000-3000 km (Qiao and Weisberg (1995)) over a typical depth comprised between 30 and 110 m, although they have been shown to generate intraseasonal variability down to 2000 meters (Tuchen et al. (2018)) which could potentially be related to the generation of deep jets (Delpech et al. (2020). Lyman et al. (2007) has evidenced that the 17-day^{-1} and 33-day^{-1} TIWs variability have characteristics similar to a mixed planetary-gravity Yanai wave and the unstable first meridional mode of Rossby waves respectively.

Figure 1.15 shows the cusp-shaped form of TIWs generated along the northern and southern equatorial fronts illustrating how these eddies can stir and transport water masses through anticyclonic vortices in a form of cold cusps that are warm in the troughs (Warner et al. (2018)). TIWs, which are the dominant form of oceanic mesoscale activity in the Tropical Pacific, draw their eddy kinetic energy (EKE) from the background state through two main conversion processes:

- the *barotropic instability* that arises from the meridional shear between the SEC and the EUC or the NECC (Philander (1978); Cox (1980); Qiao and Weisberg (1998)). This corresponds to an energy conversion from the mean kinetic energy into EKE.

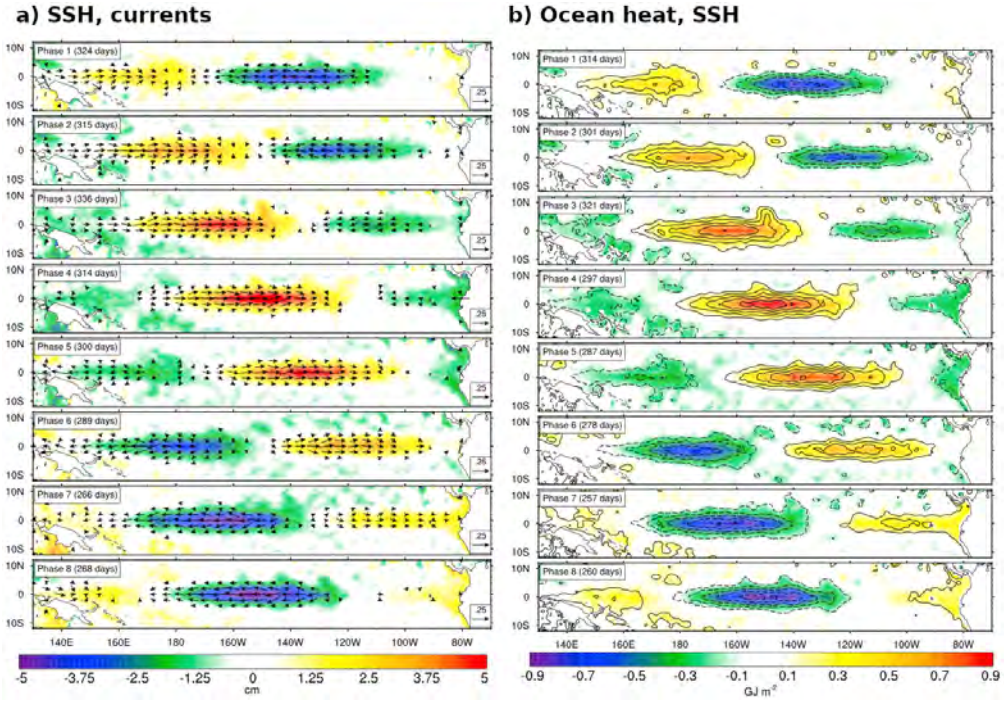

Figure 1.14: Composites of 30–120 day band-pass-filtered sea surface height (line contours, cm) and 0–700 m ocean heat content (shading, GJ/m^2) anomalies regressed on the Kelvin wave index defined in Rydbeck et al. (2019). The number of days in each composite is shown in the upper left. Figure adapted from Figure 8 and 10 of Rydbeck et al. (2019)).

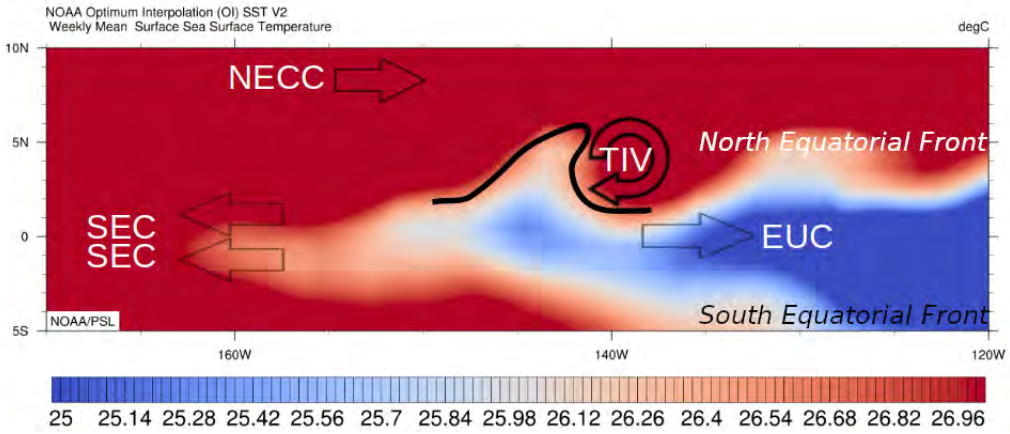

Figure 1.15: Schematic illustration of the cusp-shaped features of TIWs (plain and black line) observed from satellite in the weekly averaged SST on the week of 24 September 2017. The main equatorial zonal currents are shown by the straight arrows and the clockwise arrow illustrates the anticyclonic Tropical Instability Vortex (TIV). The SST is derived from the NOAA Optimum Interpolation SST version 2 and obtained from `https://psl.noaa.gov/data/gridded/data.noaa.oisst.v2.html`

- the *baroclinic instability* due to the meridional density front between the cold tongue and

the off-equatorial warmer water (McCreary Jr and Yu (1992); Yu et al. (1995); Masina et al. (1999)). In particular, the meridional temperature gradient acts as a reservoir of available potential energy, that can be converted into kinetic energy (Masina et al. (1999)).

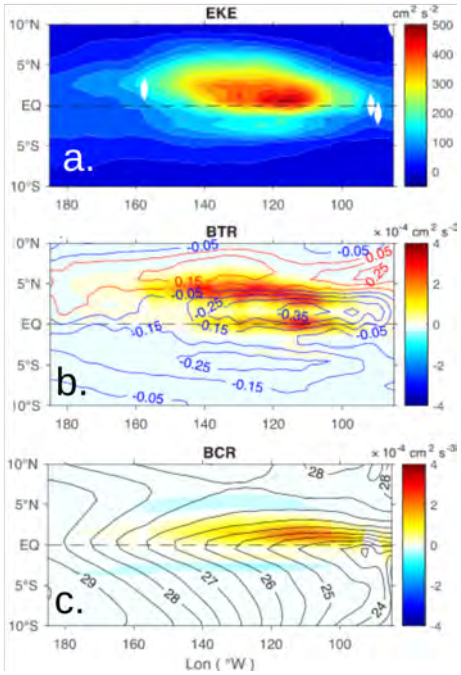

Figure 1.16: Observed (a) EKE, (b) barotropic conversion rate (shading) and zonal currents (contours), and (c) baroclinic conversion rate (shading) and SST (contours), averaged over the period 1993–2018. Adapted from Wang et al. (2019).

Figure 1.16a shows the mean pattern of intraseasonal EKE with high values concentrated in the eastern equatorial Pacific [0°N-8°N; 140°W-120°W] that corresponds to the location of maximum TIWs activity. This pattern is the result of the relative contributions from the two main conversions terms described above with the baroclinic instability occurring primarily along the northern SST front between 0°N–5°N (Figure 1.16c) and the barotropic instability stronger at the equator and near 5°N (where the shear between zonal currents is the strongest, Figure 1.16c). The EKE budget at the intraseasonal TIWs scale will be described in more detail in the next chapter.

1.3 Time scales interactions in the Equatorial Pacific

Since the tropical Pacific's background state, *i.e.*, the SST meridional gradient or the strength of the zonal currents' shear, is responsible for the strength of the baroclinic and barotropic instabilities that generate TIWs, its temporal evolution (*e.g.*, seasonal or interannual) will therefore contribute to modulating TIWs features (*e.g.*, their amplitude). More generally,

a change in the mean position of the equatorial thermocline or in the zonal or meridional gradients of surface temperature (linked to the slow evolution of the system) is likely to significantly modify the mean conditions of the tropical Pacific and thus its temporal variability, from intraseasonal to interannual and even longer (decadal) timescales. In this sense, Meehl et al. (2001) proposed an 'integrative' concept that encourages the understanding of all scales of variability, both spatial and temporal, for the study of the climate system. This concept can be summarized as follows: "Large temporal scales (associated with low-frequency changes), as well as large spatial scales, define a baseline state, a 'climate background', for processes acting at finer scales, which may feed back to these larger scales in a continuum of interactions". Figure 1.17 illustrates this continuum of temporal scales, their characteristic temporal and spatial dimensions, and an overview of this intricate web of interactions in the ocean.

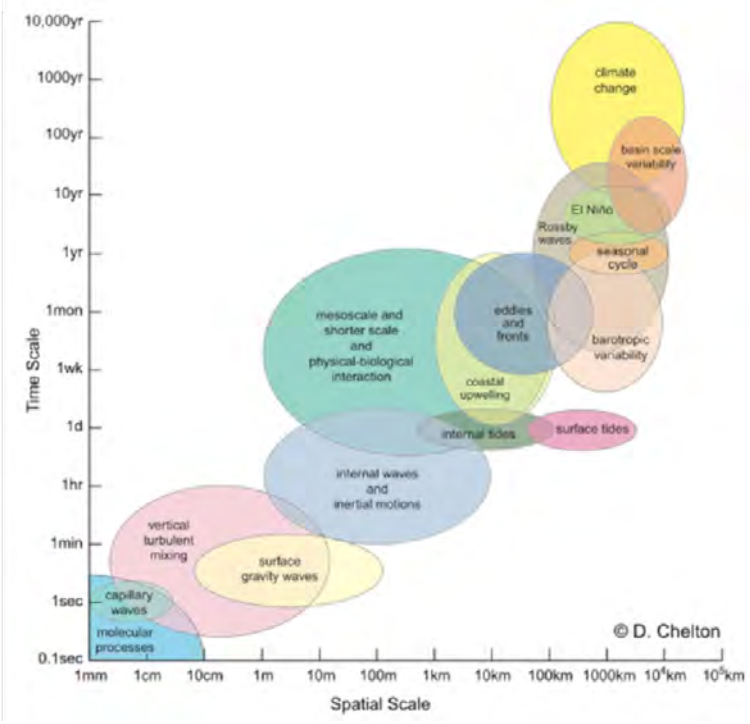

Figure 1.17: Sets of spatial and temporal scales of variability present in the ocean and their interactions. According to Chelton.

In what follows, we provide some examples of the major time-scale interactions at play in the tropical Pacific basin, and then review the few studies that took a look specifically at the interaction between IEKW and TIWs.

1.3.1 Interactions between the (decadal) mean state and ENSO

Decadal variability in the tropical Pacific, characterized among other things by abrupt shifts in the timeseries of climate variables, reflects long-term changes in the mean state of the

Pacific. Such "background" climate changes can induce (or *modulate*) changes in the statistical properties and dynamics of ENSO (Boucharel et al. (2009); Boucharel (2010)). For example, An and Wang (2000) noted differences in the propagation and development of SST anomalies before and after the abrupt climate shift of 1976/77. Before 1976, positive SST anomalies began to develop east of the Pacific basin and then progressed westward. This was reversed following the climate shift, with anomalies moving from the center of the basin to the east (An (2004)). The frequency of events has also changed: the period has increased since the late 1970s from about 2-4 years to 4-6 years (Wang and Wang (1996); Setoh et al. (1999); An and Wang (2000)).

Earlier, we mentioned the strong asymmetry between the two phases of ENSO, which has been shown to be explained mostly through two different approaches/theories: either via deterministic nonlinear dynamics or via the effect of external stochastic forcing. An example of nonlinearity potentially responsible for ENSO asymmetry is the nonlinear dynamical heating (NDH, advection of anomalous temperature by anomalous currents, cf. An and Jin (2004)) because this term is always positive whatever the phase of the oscillation. This implies a strongly increased warming during El Niño period (pushing the positive anomaly to grow) as well as a weak damping of the cooling in La Niña period (preventing the negative anomaly from growing too much). On decadal time scales, the heat budget is therefore not zero as there remains a residual from the compensation between warm and cold events, that can *rectify* into the mean state (*e.g.*, Dewitte et al. (2007); Choi et al. (2011); Sun et al. (2014)).

1.3.2 Interactions between seasonal and interannual time scales

ENSO events usually tend to peak at the end of the calendar year (Figure 1.18), which leads to a phenomenon called "ENSO phase locking", that could be attributed to the nonlinear interaction between the annual cycle and ENSO cycle (*e.g.*, Tziperman et al. (1994); Jin et al. (1996); Neelin et al. (2000). Several studies (Jin et al. (1994); Tziperman et al. (1994); Galanti and Tziperman (2000)) have described the role of the seasonal cycle on ENSO as a resonance between these two frequencies leading to deterministic chaos and helping to explain the aperiodicity of ENSO in observations. Recent progresses on the ENSO frequency cascade demonstrated that this nonlinear interaction can actually generate a low-frequency instability producing a deterministic variability on timescales much shorter than ENSO's main interannual band, the "Annual cycle-ENSO combination mode" (Stuecker et al. (2013)). This relatively fast variability at near annual timescale has great implications on its impacts on the climate system (*e.g.*, Stuecker et al. (2017); Boucharel and Jin (2020); Boucharel et al. (2021)).

1.3.3 Interactions between intraseasonal KWs and seasonal to interannual time scales

It has been suggested in many studies that the ITV in the western Pacific may be a triggering mechanism for El Niño or at least may affect its duration or intensity (Fedorov (2002); Fedorov

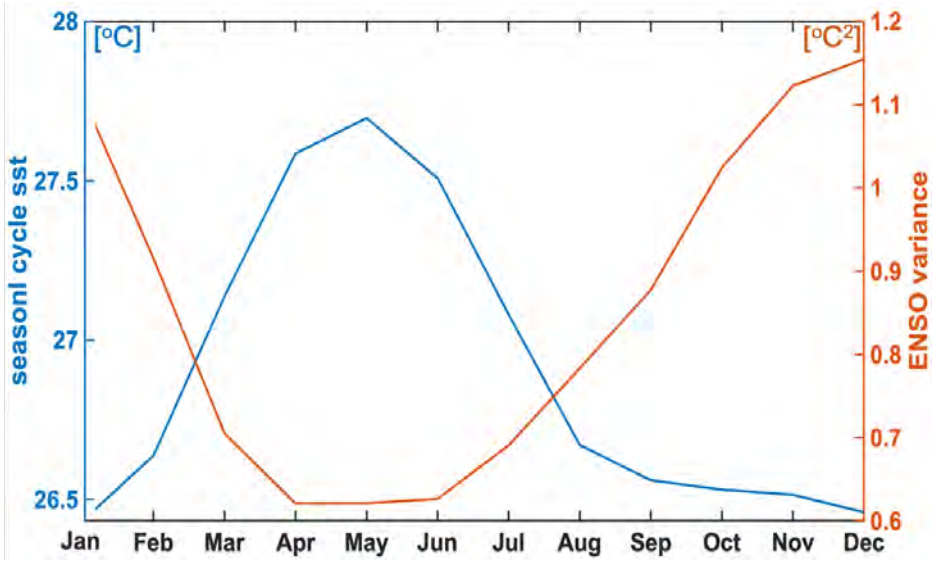

Figure 1.18: Monthly mean climatology (blue line) and variance (orange line) of the Niño3.4 index. Contribution by Julien Boucharel.

et al. (2003); Kessler (2002); Lengaigne et al. (2004b); McPhaden (1999); McPhaden and Yu (1999)). For instance, because the active phase of the MJO in the western and central Pacific is associated with long periods of WWEs, it may influence the onset and the evolution of El Niño events (Zhang (2005), Takayabu et al. (1999); Bergman et al. (2001); Kessler (2001)) through the generation of downwelling IEKWs. These can induce the eastward extension of the warm pool (Hendon et al. (1999); Kessler (2001)) via the deepening of the thermocline throughout their propagation and contribute to the initial anomalous warming in the eastern Pacific (Kutsuwada and McPhaden (2002)). It is through this mechanism that the 1997/98 El Niño started (Lengaigne et al. (2002)) as shown on Figure 1.19. This leads to a modification of the background oceanic circulation and thermal state in this central-eastern Pacific and thus to changes in air–sea interactions critical for the subsequent development of El Niño events (McPhaden and Taft (1988); Lien et al. (1995); Bergman et al. (2001); McPhaden (2002a); Picaut et al. (1997);Suarez and Schopf (1988)). Depending on the ocean initial state;Hu et al. (2014) showed that WWB can lead to either a Central Pacific (CP) or an Eastern Pacific (EP) warming, highlighting the role played by ITV on ENSO diversity. The termination of El Niño event has also been suggested to originate from the negative feedback of the delayed oscillator, *i.e.* from the combination of Rossby wave reflection (Boulanger and Menkes (1999)) into an upwelling EKW and the wind-forcing (Boulanger et al. (2003)).

On the other hand, IEKWs can also be modulated by the phase of ENSO, with much more damped waves during La Niña conditions than during El Niño, due in particular to the increased viscous dissipation resulting from an enhanced vertical shear (Benestad et al. (2002)). This mechanism can potentially represent a significant source of nonlinearity between El Niño and La Niña, with potential influence on the onset, lifetime, and amplitude of SST and subsurface temperature anomalies.

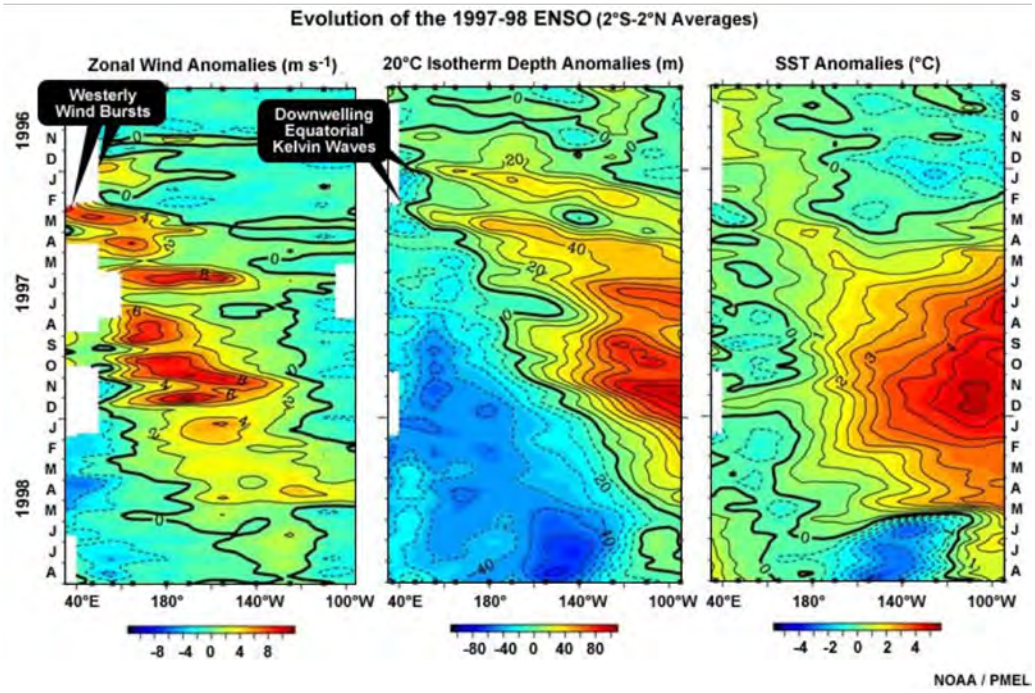

Figure 1.19: Hovmöller diagrams of equatorial (2°S-2°N averages) zonal wind (left panel), 20°C isotherm depth (middle panel) and SST (right panel) anomalies. Data from TAO-TOGA, Figure from NOAA /PMEL

IEKWs can also be modulated by mean state, particularly in the eastern Pacific where changes in mean thermocline depth can produce energy scattering or dissipation (Dewitte et al. (1999);Mosquera-Vásquez et al. (2014); others). IEKWs are also strongly modulated at seasonal timescales, with increased activity in boreal winter and fall (Kessler et al. (1995); Hayes et al. (1991)). In turn, the Kelvin waves that are continuously generated by the intraseasonal wind forcing, can also rectify nonlinearly the mean state and contribute to an overall net warming in the Eastern equatorial Pacific (Dewitte et al. (2012)).

Overall, because the IEKW (and its related WWBs) can be modulated by mean state change during the evolution of ENSO, it can act as a state-dependent noise to ENSO, which favors ENSO bursting behavior (Jin et al. (2007)).

1.3.4 Interactions between TIWs and seasonal to interannual time scales

TIWs are generated by barotropic energy conversions related to the meridional shear of zonal equatorial currents (Philander (1976);Philander (1978)) and through the baroclinic instability related to the meridional SST gradient between the cold equatorial water and the warmer off-equatorial waters (Yu et al. (1995)). As such, the TIW activity is strongly modulated by changes in the background of the equatorial circulation and meridional temperature gradient over a wide range of timescales. For example, Figure 1.20a illustrates the strengthening of the cold tongue due to the intensification of trade winds and the increase in SSH that leads

to an intensification of the SEC and therefore to a strong currents' shear north of the equator (0-5°N) during the second half of the year. These conditions favor a seasonal increase in TIWs activity (*i.e.*, as diagnosed by the intraseasonal EKE, Figure 1.20b) from July through the beginning of the following year (*e.g.*, Contreras (2002)); Von Schuckmann et al. (2008); Wang et al. (2017); Wang et al. (2019)).

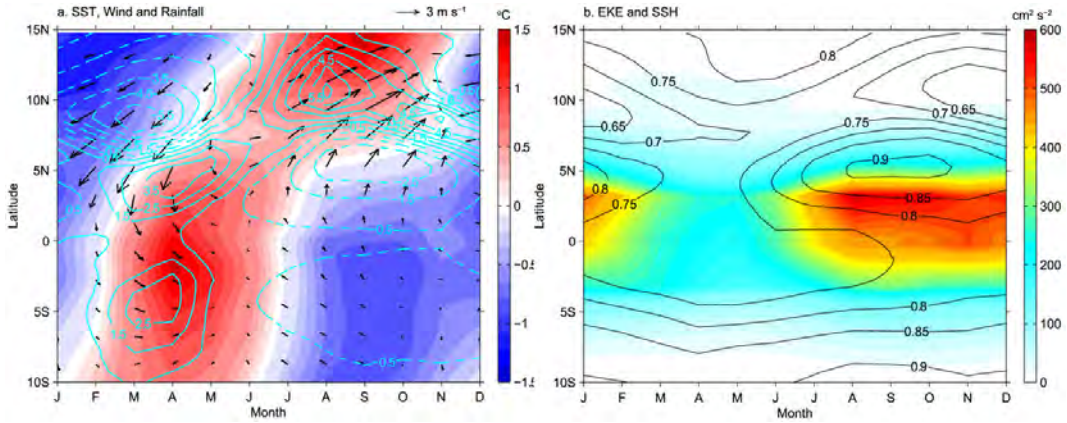

Figure 1.20: (a) Latitude-time plots of SST (shading), wind direction and speed (vectors) and daily rainfall (cyan contours; mm day^{-1}) anomalies. (b) Latitude-time plots of sea surface height (black contours; m) and surface EKE (shading). SSH based on AVISO and the equatorial 35-m-depth EKE from ADCPs. All are averaged between 155° and 110°W. (Adapted from Figure 13 of Wang et al. (2019))

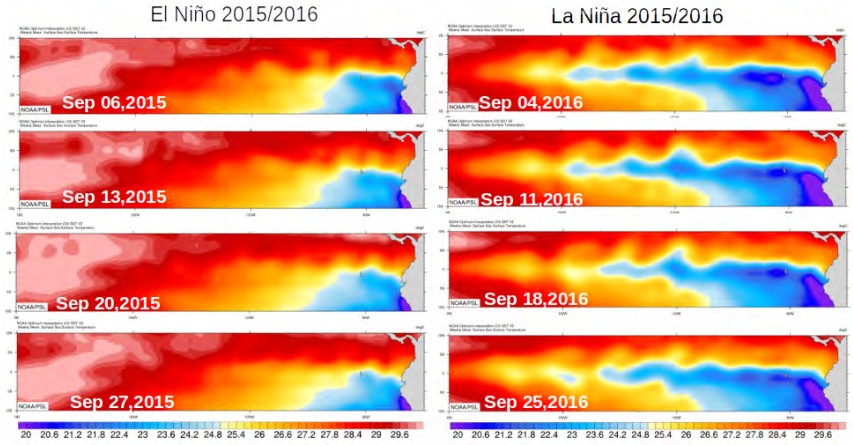

Figure 1.21: Snapshots of weekly averaged SST (mean centered around the date indicated on each panel) in September 2015 (left panels) and September 2016 (right panels) characterized by El Niño and La Niña conditions respectively. Derived from the NOAA Optimum Interpolation SST version 2.

TIWs are also modulated by the interannual variability associated with ENSO, characterized by an increased (decreased) activity during El Niña (La Niño) when the meridional SST gradient and equatorial zonal circulation are increased (reduced) (Hashizume et al. (2001); Yu and Liu (2003); Philander (1990); Vialard et al. (2001)). This is illustrated in Figure 1.21 that shows the TIWs meandering features in the weekly averaged SST of September (*i.e.*, a

typically active month of TIWs) that is absent in 2015 characterized by El Niño while they are visible the following year (September 2016) when La Niña conditions prevail in the Pacific.

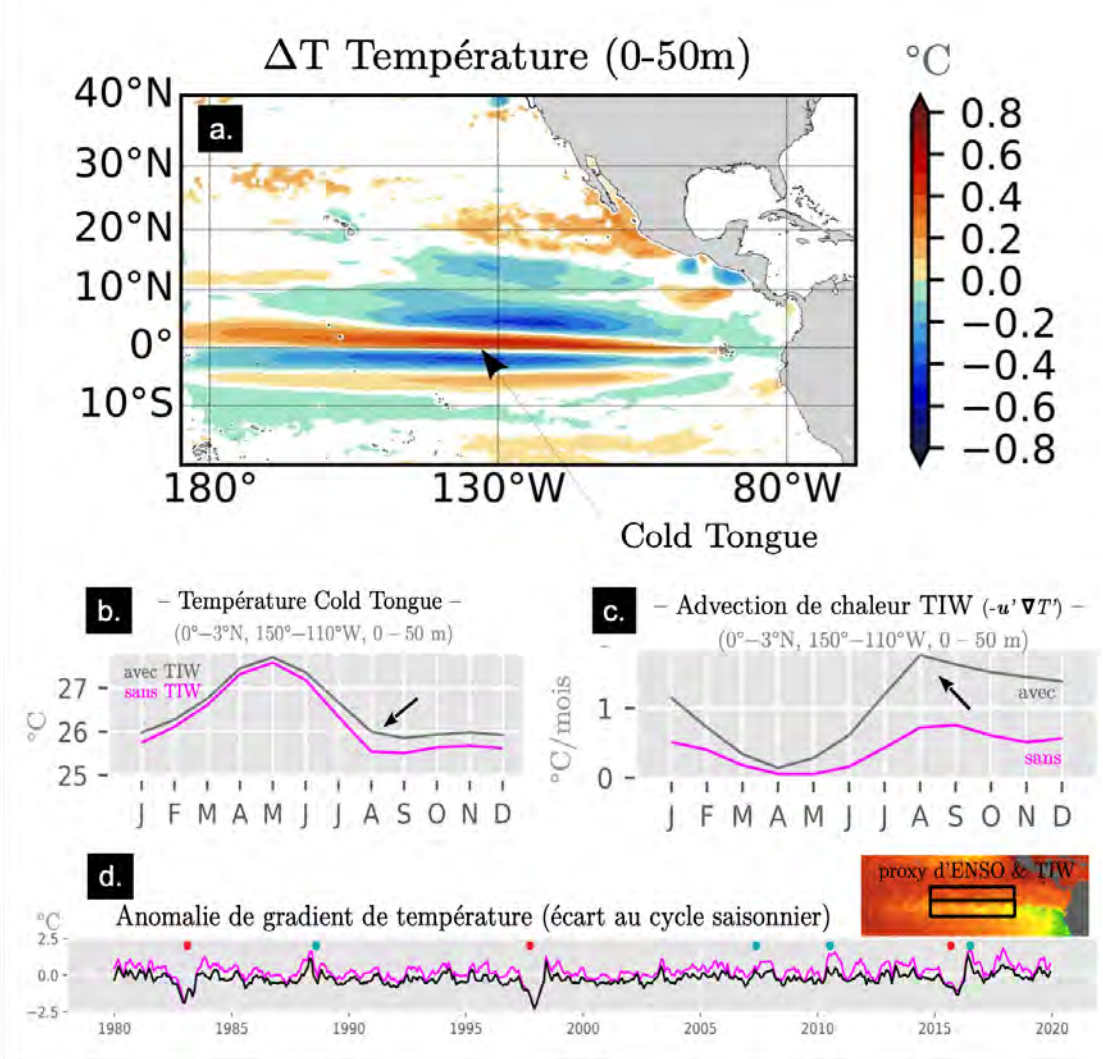

Figure 1.22: (a) Map of the 50-m averaged temperature difference between the run with and without TIWs. (b) Seasonal cycle calculated as the monthly mean climatology (from the 40 years simulations) of ocean temperature averaged in the region [0°-3°N, 150°-110°W, 0 - 50 m] for the simulation with (solid black line) and without (solid magenta line) TIWs. (c) Same as (b) but for NDH. (d) Time series of the NiñoD index (Xue et al. (2021)) calculated as the difference in interannual SST anomalies between the northern and southern box delineated in the map on the upper right corner of the panel, for the run with (solid black line) and without (solid magenta line) TIWs. Red (blue) dots indicate El Niño (La Niña) events. Figure adapted from Maillard (2023); Maillard et al. (2022b); Maillard et al. (2022a).

On the other hand, TIWs can also feedback onto low-frequency climate variability mostly through Nonlinear Dynamical Heating (NDH, e.g., Holmes and Thomas (2015); Jin et al. (2003)). For instance, TIWs have been shown to warm the Cold Tongue via direct meridional NDH (Menkes et al. (2006); Graham (2014)) and reduce the EUC strength leading to both a

direct and rectified effect on the mean Eastern equatorial Pacific heat budget (Maillard et al. (2022a)). These feedbacks being stronger during La Niña and in summer than during El Niño and in winter, TIWs can therefore also modulate the amplitude of both the seasonal (*e.g.*, Im et al. (2012); Maillard et al. (2022b)) and ENSO cycle, potentially participating in ENSO asymmetry (Im et al. (2012); Graham (2014); Boucharel and Jin (2020); Xue et al. (2020); Xue et al. (2021), An (2008); Vialard et al. (2001)).

Recently Maillard et al. (2022a) from modeling experiments that TIWs activity can reduce by $\sim 0.4°C$ month^{-1}°C the Austral spring SST over the cold tongue, which is associated with substantial increase of non-linear advection of heat in the TIWs region (1.22).

- First, TIWs modify the near-surface mean equatorial temperature through (1) a direct nonlinear dynamical warming at a rate of 0.4°C month^{-1} in the Cold Tongue (Figure 1.22a, note also the off equatorial cooling) and (2) an indirect/rectified cooling effect of -0.10°C month^{-1} produced by the weakening and deepening of the EUC induced by TIWs (not shown).
- Second, due to their seasonal phase-locking, TIWs can rectify into the annual cycle of the basin. In particular, the amplitude of the equatorial ocean temperature seasonal cycle is decreased by 0.4°C (Figure 1.22b), due to the TIWs-induced NDH in boreal fall and summer (Figure 1.22c). TIWs also alter the EUC seasonal cycle year round, by stabilizing and weakening the current throughout the year (not shown).
- Third, the presence of TIWs tend to increase the asymmetry of the NiñoD index (Xue et al. (2020), defined as the difference in sea surface temperature anomalies between the region 3°N-8°N,150°W-110°W and the region 3°S-3°N, 150°W-110°W), (Figure 1.22d).

1.3.5 Interaction between TIWs and IEKWs

While IEKWs and TIWs are both at the heart of complex low-frequency interactions in the equatorial Pacific (summarized schematically in Figure 1.23), far fewer studies have highlighted the potential for interactions between them. Yet, the few observational, theoretical, and modeling studies that have addressed this issue have suggested that their interaction can lead to strong impacts in terms of SST, circulation, and energy variability in the eastern equatorial Pacific, potentially itself participating in rectification processes affecting the slower climate variability.

Here is a summary of these few seminal studies:

- Harrison and Giese (1988) considered a single model experiment with the Geophysical Fluid Dynamics Laboratory (GFDL) ocean model and examined the response to an episode of surface westerly winds in the western Pacific, concluding that any perturbation of the shear field associated with the passage of a kelvin wave can modify the strength of TIWs.

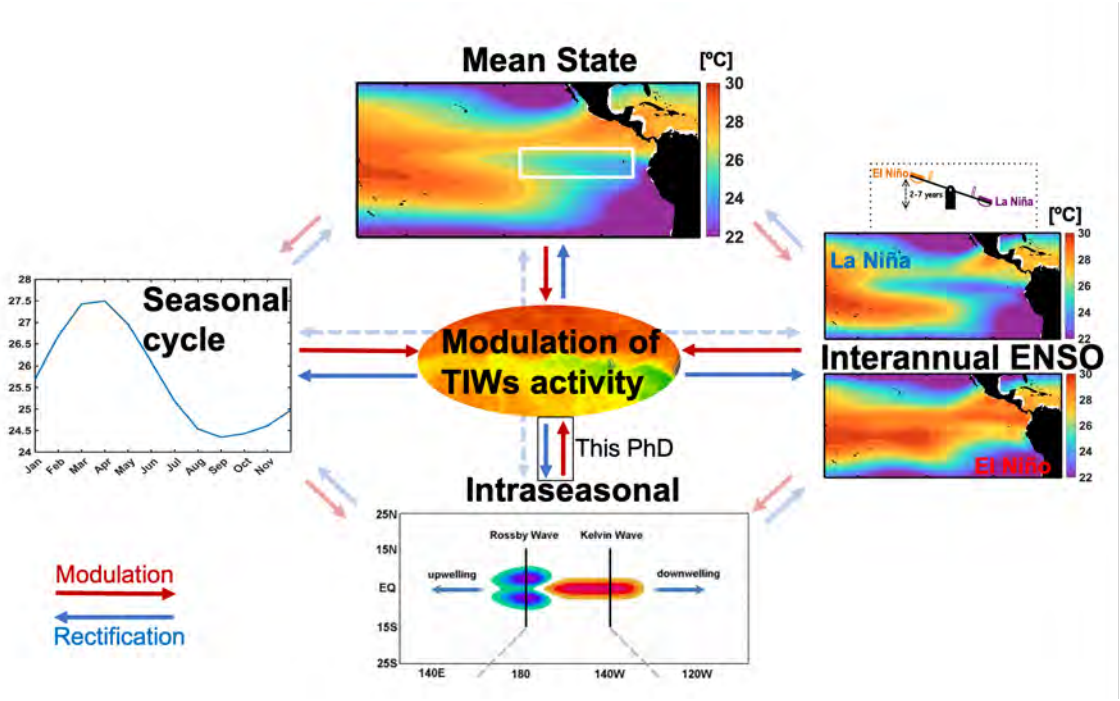

Figure 1.23: Schematic illustration of the main time scales interactions operating in the equatorial Pacific. The modulation by low-frequency time scales of processes acting at finer scales is indicated by red arrows. The rectification of high frequency variability into larger temporal scales is indicated by blue arrows. Contribution by Julien Boucharel.

- Giese and Harrison (1991) used the same ocean model and forced it with three idealized wind types. They concluded that westerly winds events can trigger kelvin waves and therefore the eastward heat advection, altering the TIWs through modifications in the horizontal shear of equatorial currents.

- Allen et al. (1995) forced a standard primitive-equation ocean model with wind stress, suggesting that the TIWs could be also the response to a phase-locking of the Rossby waves (the result of a reflection of the Kelvin waves at the South American coast) which interact with the current shear in the eastern Pacific.

- Qiao and Weisberg (1998) used in-situ ocean velocity data and found that the end of the TIWs season observed from August to December 1990 coincided with the propagation of a large intraseasonal Kelvin Wave responsible for a decrease in the meridional shear between the SEC and EUC, in the associated barotropic energy conversion rate and therefore in the TIW activity. They also reported that the baroclinic instability due to the mean meridional density gradient was small compared to the barotropic instability during this period.

- Angell et al. (1998) used sea surface heights from altimetry and reported the passage of several pulses of Kelvin waves, specifically one in March, 1993 that reached the South American coast and reflected as two Rossby waves at 5°N and 5°S, exciting TIWs.

- Shinoda et al. (2009) examined satellite-derived SSH, SST, and surface velocity to identify the frequency of the TIWs, Kelvin, and Rossby waves and confirmed that the prominent peak at 33 days of the TIWs corresponds to that of the first meridional mode of equatorial Rossby waves.
- Holmes and Thomas (2016) used a high-resolution regional oceanic model with a temporally constant atmospheric forcing and an idealized first-baroclinic-mode Kelvin wave to illustrate that the passage of a single IEKW can modify the background zonal currents, barotropic energy conversion rate and consequently TIWs activity. In particular, they highlighted an asymmetric response of TIWs to different phases of IEKWs, characterized by a decrease (increase) of the TIWs-induced EKE during the passage of a downwelling (upwelling) IEKWs.

1.4 Motivation and Scientific objectives

Because KWs play a key role in propagating signals of intraseasonal atmospheric variability across the Pacific basin through the field of TIWs and because both types of equatorial waves are involved in a complex interplay of dynamical processes impacting among others the development and properties of ENSO, their so-far relatively overlooked interaction is likely to affect the energy balance, momentum transport and therefore the oceanic teleconnection between the western and eastern equatorial Pacific, one of the most productive ecosystems on the planet.

The principal motivations of this PhD work are to document and better understand the dynamics of the intraseasonal interaction occurring between KWs and TIWs. In particular, we take advantage of now available long-spanning altimetry and reanalysis data sets to revisit the few past studies that initially described this interaction using sparse observations. Then, in order to extend previous modeling studies that relied either on low resolution global models or idealized regional configurations, we propose a numerical approach with different sensitivity experiments of a realistic eddy-rich oceanic model to better characterize the dynamical processes involved in this nonlinear interaction.

Chapter 2

Data set and Methodology

Contents

2.1 Preamble

In this chapter, we present the observational products and methodological frameworks used throughout this thesis to study the interaction between Tropical Instability Waves (TIWs) and intraseasonal equatorial Kelvin Waves (IEKWs). The first part "Observation and reanalysis products" details the different datasets used to characterize this interaction from an observational approach in chapter 3 and from a numerical approach and especially for the validation of the simulations in chapter 4. The second part "Decomposition of Equatorial Waves in meridional modes" describes the mathematical method used to project sea level, zonal currents, and zonal wind stress onto the Kelvin and Rossby waves theoretical meridional structures from the linear approximation of the equatorial dynamics. This diagnostic is used to characterize the intraseasonal variability associated with the propagating equatorial waves in the observational study of this thesis. This section is followed by the description of the different indices used to characterize TIWs activity in the observational data and numerical simulations. The last section "Numerical model" is devoted to the general description of the primitive equations of the ocean model and of the tropical Pacific configuration used to study the interaction between the two types of waves via a sensitivity experiment approach performed in chapter 4.

We use a variety of *in situ*, satellite observational data, and reanalyses products to evaluate the tropical Pacific mean state, its dynamic and variability as well as to force/constrain and validate our numerical simulations.

2.2 Data sets

2.2.1 Observational Data

To evaluate the effects from IEKWs and TIWs on the sub-surface oceanic conditions and circulation and in particular on the thermocline depth, here classically evaluated as the depth of the 20° isotherm at the equator, and on the zonal currents, we have used *in situ* observations from The Tropical Ocean-Global Atmosphere (TOGA) (`https://www.pmel.noaa.gov/`) (Figure 2.1a where the moorings within [165°E-95°W, 8°S-9°N] are denoted by the small squares), available (sometimes sparsely) on the period January 1993 - July 2019. In our study, we are focused on the equatorial region and the off-equatorial region between 4°N and 10°N, where the TIWs activity is the strongest. We also used seasonal zonal currents from the Johnson's climatology (Johnson et al. (2002), that includes meridional sections of upper ocean zonal currents of Conductivity Temperature Depth and Acoustic Doppler Current Profiler data from 172 synoptic sections taken mostly in the 1990s in the tropical Pacific.

To evaluate the effects from IEKWs and TIWs at the surface, we used sea surface height (SSH) and the derived geostrophic currents from the multi-satellite Data Unification and Altimeter Combination System datasets available through the Copernicus Marine Environment Monitoring Service (CMEMS) and the Copernicus Marine Climate Change Service (C3S) (Taburet

et al. (2019)) over the period 1993-2018 (and until July 2019 to validate the model in chapter 4) and the region [10°N-10°S, 130°E-80°W] at a spatial resolution of 0.25°x0.25°. CMEMS is a merged product from multiple satellite missions such as Sentinel-3A, Cryosat-2, Jason-1,2 and 3, Topex/Poseidon, Envisat, and ERS-1 and -2. Figure 2.1a (from Wang et al. (2019)) is a snapshot of intraseasonal anomalies of SSH (or sea level anomalies, SLA) from October 6th, 2010 from the CMEMS product, which shows the anticyclonic vortices of TIWs on SLA between 5°N and 10°N in the central Pacific. The TIWs signature can also be observed in the temperature records from the TOGA mooring at 5°N, 140°W, between 100 and 150 meters depth with perturbations on the thermocline depth highlighted by the black line, as well as in the anomalies of meridional currents and also the raw zonal currents at the same longitude but on the Equator for the years 2010 and 2011 (Figure 2.1b,c,d).

We also used Sea Surface Temperatures (SST) derived from the daily Optimum Interpolation Sea Surface Temperature version 2.1 product (Huang et al. (2020)) at a horizontal resolution of 0.25°x0.25° over the same domain and period as the SSH data. Observed SST data will be in particular used to estimate the non-linear meridional oceanic heat transport associated with TIWs and their interaction with Kelvin waves in chapter 3.

2.2.2 Reanalysis Products

2.2.2.1 Atmospheric datasets

We used three atmospheric reanalysis products to characterize the atmospheric circulation associated with the TIWs-IEKWs interaction and to force and validate the numerical simulations in chapter 4:

1. The 10-meter zonal winds from the Fifth Generation of the Atmosphere Reanalysis of the Global Climate (ERA5, Hersbach et al. (2020)) produced by the European Centre for Medium-Range Weather Forecasts (ECMWF) were used to calculate the wind stress and quantify the IEKWs forcing (i.e., the zonal wind stress projected onto the theoretical meridional structures of the Kelvin and Rossby modes).

2. The radiation fluxes (surface thermal radiation, surface downward thermal radiation, and surface solar radiation), 2-meter air temperature and specific humidity, precipitation rate, and 10-meter winds from the ERA-Interim reanalysis product (an earlier version than ERA5) produced by ECMWF were used to force the numerical model (chapter 4).

3. The radiation fluxes obtained from the TropFlux project, which is derived from the corrected ERA-Interim product (Dee et al. (2011)), International Satellite Cloud Climatology (ISCCP), and the NOAA outgoing Longwave Radiation product (Praveen Kumar et al. (2012)) with 1° horizontal resolution and from 1993 to 2018 were used to validate the short and long-wave radiation calculated from the COARE bulk formula (Fairall et al. (2003)) in the numerical simulations.

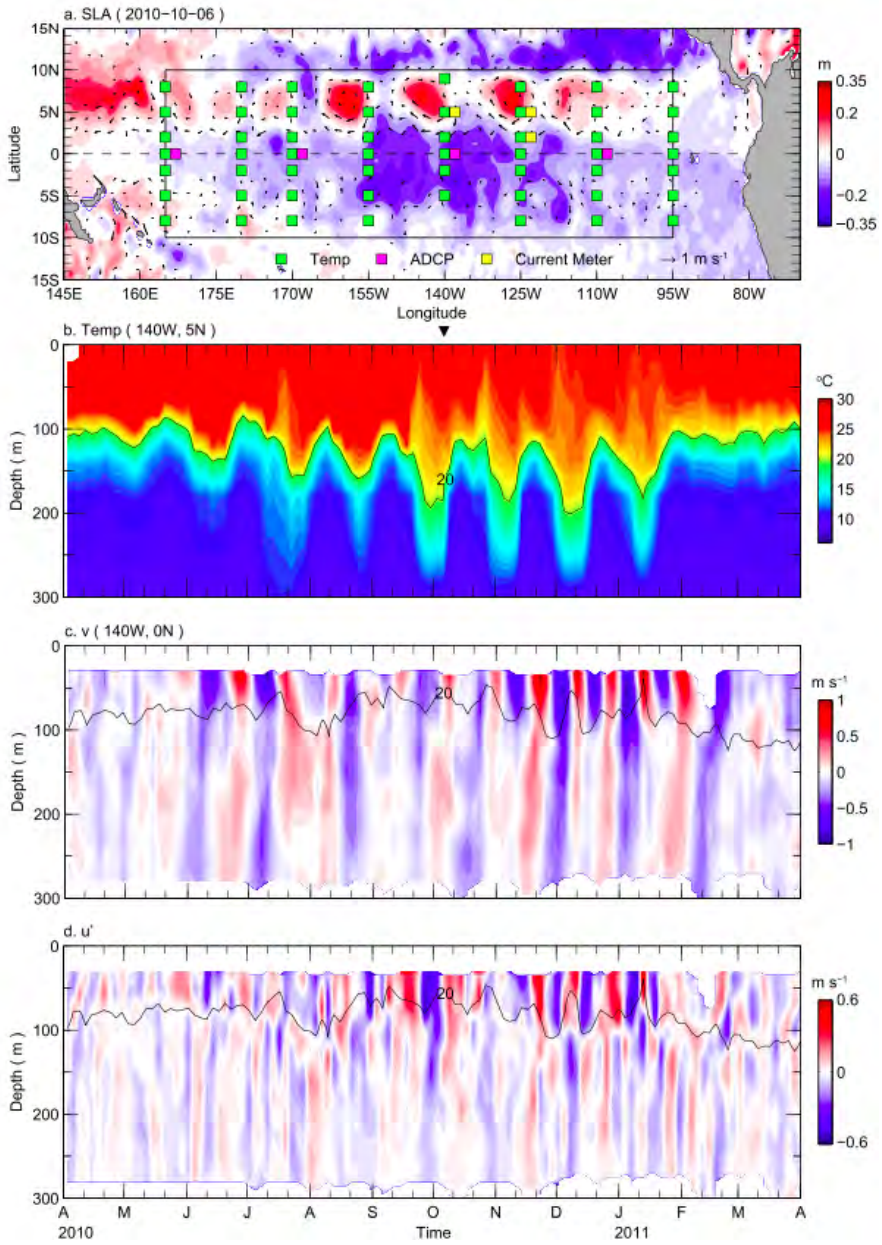

Figure 2.1: (a) Snapshot (6 Oct 2010) of Sea Level Anomalies (SLA) from the CMEMS product. The squares denote the locations of the moorings from the TOGA TAO array and the green, magenta, and yellow colors of the different instruments and associated variables recorded. (b) Sea Temperature at 5°N, 140°W and (c) meridional current anomalies and (d) total zonal velocities at 0°, 140°W, where the zonal velocity (u') is the anomaly after removing the 33-day running mean. The black curves in (b)–(d) denote the 20°C isotherm. Figure 1 from Wang et al. (2019)).

2.2.2.2 Oceanic datasets

Two reanalysis products were used in this thesis: one to extract the lateral open boundary and initial conditions for the numerical simulations and the other to validate the simulated 20°C isotherm depth in chapter 4:

1. The 20°C isotherm depth (Z20) is derived from the Simple Ocean Data Assimilation (SODA) version 3.4.2 reanalysis product(Carton and Giese (2008)) at a 0.25° horizontal resolution.
2. The numerical simulations' initial and lateral open boundaries conditions (temperature, salinity, sea surface height, zonal and meridional velocity) were derived from the Global Ocean Reanalyses and Simulations CMEMS global reanalysis product GLORYS (Global Ocean Reanalysis and Simulation) version 4 (hereinafter GLORYS2V4) at a 3 days temporal resolution and a 0.25° horizontal resolution, provided by `https://catalogue.marine.copernicus.eu/documents/PUM/CMEMS-GLO-PUM-001-031.pdf`.

The bottom bathymetry and topography in the model were obtained from the 1/15 arc-second high-resolution bathymetric dataset GEBCO, provided by `https://www.gebco.net/`.

2.2.3 Intraseasonal and Interannual anomalies

All variables (ocean temperature, zonal and meridional currents, zonal wind stress, and sea surface height) whether from observational products or from the model's outputs were linearly detrended beforehand. The intraseasonal anomalies are computed as the departure of the instantaneous daily data from the monthly mean following the method by Lin et al. (2000). This method is somewhat equivalent to applying a high-pass Lanczos filter with a frequency cut-off at (1/90) days-1 (Dewitte et al. (2011)). The daily intraseasonal anomalies of model's outputs (chapter 4) were calculated with respect to a 30-days running, which is equivalent to the method applied to the observations. Interannual monthly mean anomalies are computed by removing the mean monthly climatology.

2.2.4 Statistical significance analysis

In chapter 4, two types of ensemble simulations are compared in order to study the interaction between the TIWs and the Kelvin Waves. By using a set of independent model runs (so-called ensemble simulations) that can be averaged as a whole (ensemble mean), we can reduce and quantify the impact of the model's internal variability. We use a Student's t-test (two-samples) to quantify the significance of the model output average relative to the variability of the average. In particular, the two types of simulations are assumed to be significantly distinct when the differences between the sensitivity experiment's ensemble mean exceed the 95% confidence level based on a two-tailed Student's t-test.

2.3 Decomposition of Equatorial Waves into Meridional Modes

As was discussed in the previous chapter, close to the equator, the Coriolis parameter f = $2\Omega \sin \Theta$ (Ω being the Earth angular rotation speed and Θ the latitude) decreases in amplitude, becomes null at the equator and its sign reverses in the other hemisphere. This singularity of the Coriolis parameter makes the equatorial thermocline a waveguide for waves propagating eastward (equatorial Kelvin waves) or westward (off-equatorial Rossby waves) (Figure 2.2). As such, all changes in the thermocline depth and hence in the heat content are directly reflected in sea surface height (Rebert et al. (1985)). This can be observed in Figure 2.3, with a deeper thermocline (20°C isotherm) associated with positive anomalies of mean sea level anomalies at 140°W and 0°) during the El Niño event of December 2015 (Figure 2.3a and b). The opposite behavior is observed during the La Niña event of October 2017, with a shallower thermocline above the 100 meters and negative SLA (Figure 2.3a and c).

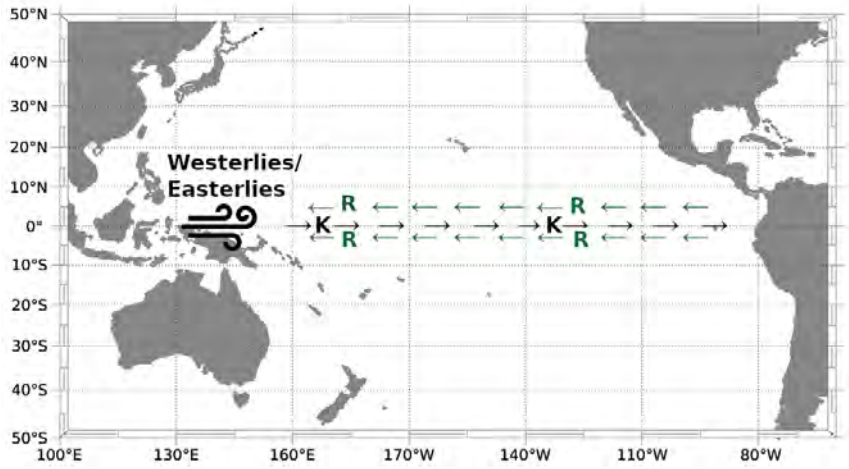

Figure 2.2: Schema of the oceanic Kelvin (K) and Rossby (R) Waves

In the equatorial linear theory, when it is assumed that the oceanic vertical structure along the equator can be accounted for by just the first baroclinic mode in the long-wave approximation, the total sea level (h) and zonal current (u) anomalies can be expressed as a linear combination of meridional mode functions accounting for the Kelvin and Rossby waves contributions (*e.g.*, Cane and Sarachik (1976), Boulanger and Menkes (1995), Perigaud and Dewitte (1996), Delcroix et al. (1994)).

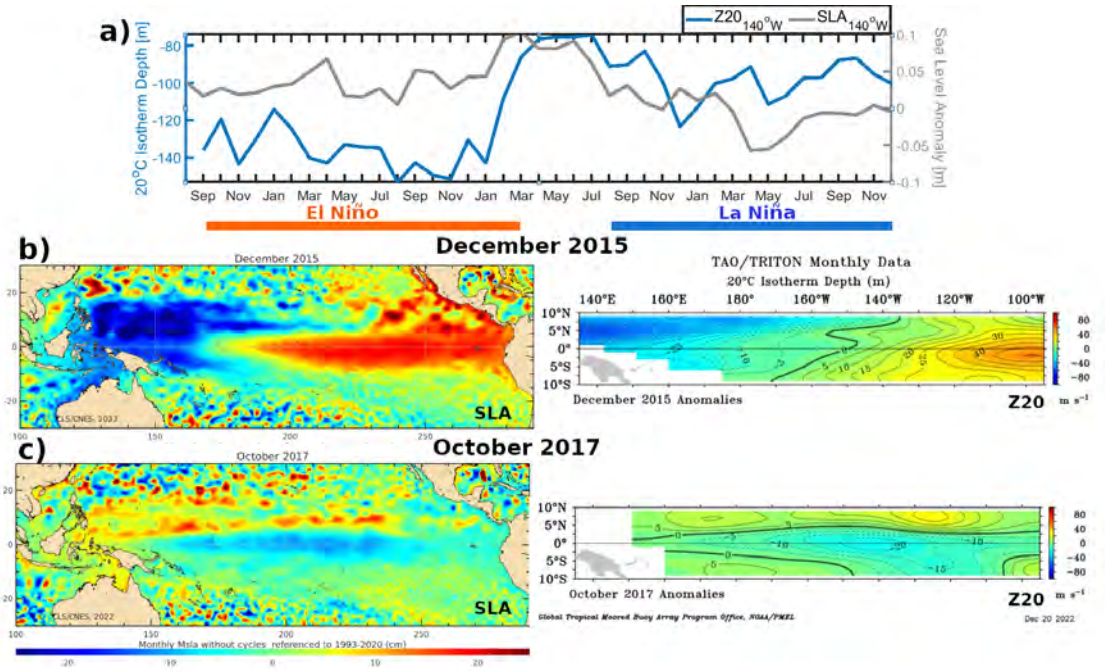

Figure 2.3: (a) Time series of the 20°C Isotherm depth monthly mean [m] (blue line) and interannual monthly sea level anomalies [m] (grey line) at 140°W,0° from September 2014 to December 2017. The El Niño conditions of December 2015 are illustrated in (b) for the SLA (left panel) and the 20°C Isotherm depth interannual anomalies [m] (right panel). The La Niña conditions of October 2017 are shown in (c). The isotherm depth and the sea level data are derived from the TOGA-TAO array project and AVISO respectively (`https://bulletin.aviso.altimetry.fr/html/produits/indic/enso/welcome_uk.php`). Note that positive/negative thermocline depth anomalies mean a deeper/shallower thermocline than climatology, respectively.

Let's consider an idealized ocean stably stratified and flat-bottomed with a right-handed system of axes with an x-axis eastward, a y-axis northward (y=0 at the equator), and a z-axis vertically upward (z=0 the sea surface at rest). To facilitate the examination of sea level and currents variability in terms of equatorial waves, it is convenient to adimensionalize the variables as such: $u = cu'$; $v = cv'$; $h = \frac{c^2 h'}{g}$; $x = \sqrt{\frac{c}{\beta}}x'$;$y = \sqrt{\frac{c}{\beta}}y'$;$t = \frac{t'}{\sqrt{\beta c}}$. The prime is associated with the raw variables, g is the gravity equal to 9.81 m/s, c the baroclinic mode phase speed, u, v and h are the zonal current, meridional current and the sea level, respectively. The non-dimensionalized shallow-water momentum and continuity equations on the β-plane are shown in 2.1.

$$\begin{aligned} \partial_t u - yv + \partial_x h &= 0 \\ \partial_t v + yu + \partial_y h &= 0 \\ \partial_t h + \partial_x u + \partial_y v &= 0 \end{aligned} \tag{2.1}$$

Since we are studying the equatorial band, where the zonal scale is very long and the ocean is meridionally unbounded, we can apply the long wave approximation to simplify the basic formulas of equatorial dynamics. Then, the solutions of the momentum equations can be

expanded into Kelvin and long Rossby waves whose components (u, v and h) are linear combinations of Hermite functions as an orthogonal set of vectors (Cane and Sarachik (1976)).

We can solve these equations with the assumption that all the waves depend on x and t in the form $exp[ik(x-ct)]$.

$$\begin{pmatrix} u \\ v \\ h \end{pmatrix} = \begin{pmatrix} \widetilde{u} \\ \widetilde{v} \\ \widetilde{h} \end{pmatrix} e^{i(kx-wt)} \tag{2.2}$$

Where ω is the frequency and k is the wave number. Substituting equation 2.2 into equation 2.1 and eliminating the u variable, the solution for the meridional velocity v that decays to zero for large y can be expressed as:

$$\frac{\partial^2 \widetilde{v}}{\partial y^2} + (\omega^2 - k^2 - \frac{k}{\omega} - y^2)\widetilde{v} = 0 \tag{2.3}$$

The solution of the equation 2.3 exists only when the relation of equation 2.4 is satisfied.

$$\omega^2 - k^2 - \frac{k}{\omega} = (2n+1) \tag{2.4}$$

Where n denotes the meridional modes being 0 for the Kelvin wave (where the meridional velocity v=0) and $n \geq 1$ for the Rossby modes. The equation 2.3 can be written as the harmonic oscillator equation or *Schrödinger* equation, where v has the form $\tilde{v} = exp(ikx - i\omega t)\psi(y)$ and can be expressed in terms of the Hermite polynomial equations:

$$\frac{\partial^2 \psi_n}{\partial y^2} - y^2\psi_n = -(2n+1)\psi_n \tag{2.5}$$

Where the Hermite function $\psi_n(y)$ is of the form of equation 2.6 and $H_n(y)$ is the n-th Hermite polynomial.

$$\psi_n(y) = \frac{exp(-\lambda^2/2)H_n(y)}{\sqrt{2^n \cdot n!\sqrt{\pi}}} \tag{2.6}$$

The first few Hermite polynomials are (Clarke (2008)):

$$\begin{aligned} H_0(y) &= 1 \\ H_1(y) &= 2y \\ H_2(y) &= 4y^2 - 2 \\ H_3(y) &= 8y^3 - 12y \\ H_4(y) &= 16y^4 - 48y^2 + 12 \end{aligned} \tag{2.7}$$

Since we are interested in the low-frequency equatorial waves, the vector solution for u and h can be written as (Boulanger and Menkes (1995)):

$$\begin{pmatrix} u(x,y,t) \\ h(x,y,t) \end{pmatrix} = \begin{pmatrix} u \\ h \end{pmatrix} = r_0(x,t)\begin{pmatrix} R_0^u(y) \\ R_0^h(y) \end{pmatrix} + \sum_{n>=1} r_n(x,t)\begin{pmatrix} R_n^u(y) \\ R_n^h(y) \end{pmatrix} \tag{2.8}$$

$$r_n = uR_n = \int_{Y_N}^{Y_S} (uR_n^u + hR_n^h)dy \tag{2.9}$$

Where $R_0^u(y)$, $R_0^h(y)$ and $R_n^u(y)$, $R_h^n(y)$ are the normalized Kelvin and $n-th$ normalized Rossby waves meridional structures and can be written as combinations of Hermite functions ψ_n. The wave coefficients are calculated with r_n that fits well for an open ocean, in our case we project the sea level and zonal current anomalies onto the meridional modes between 10°N (Y_N) and 10°S (Y_S) in order to capture the decrease of the Kelvin and Rossby wave meridional structures from the equator. See the meridional profiles for the first 4 modes in Figure 2.4.

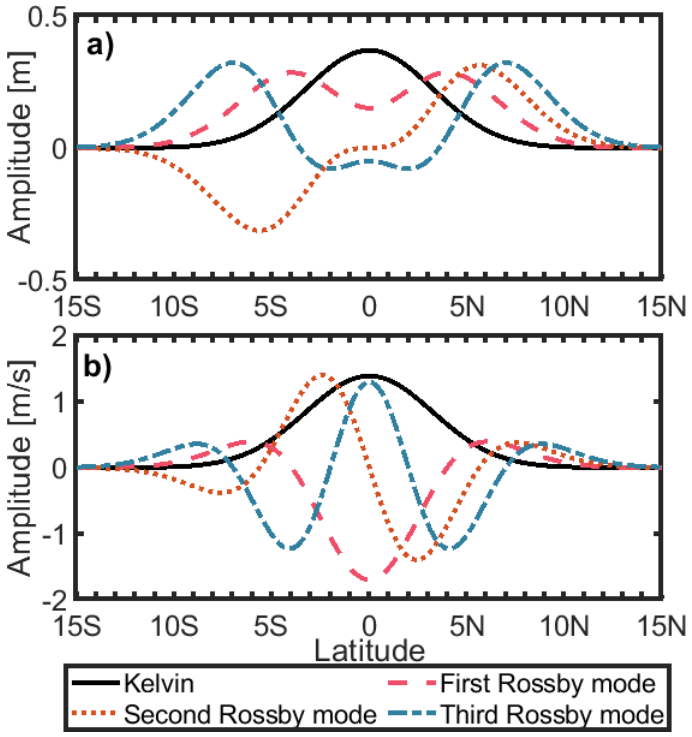

Figure 2.4: Meridional structures of (a) sea level and (b) zonal currents for the Kelvin and first to third Rossby modes (calculated using a 2.6m/s Kelvin wave phase speed).

$$\begin{pmatrix} R_0^u(y) \\ R_0^h(y) \end{pmatrix} = \begin{pmatrix} \frac{\psi_0^u(y)}{\sqrt{2}} \\ \frac{\psi_0^h(y)}{\sqrt{2}} \end{pmatrix};$$
$$\begin{pmatrix} R_0^u(y) \\ R_0^h(y) \end{pmatrix} = \sqrt{\frac{n(n+1)}{2(2n+1)}} \begin{pmatrix} \frac{\psi_{n+1}(y)}{\sqrt{n+1}} - \frac{\psi_{n-1}(y)}{\sqrt{n}} \\ \frac{\psi_{n+1}(y)}{\sqrt{n+1}} + \frac{\psi_{n-1}(y)}{\sqrt{n}} \end{pmatrix} \tag{2.10}$$

The phase speed $c(x)$ of the equatorial waves varies zonally and is governed by the zonal

changes in stratification at the equator (Picaut and Sombardier (1993) and Dewitte et al. (1999)). In order to provide a more realistic $c(x)$ to our analysis (see chapter 3), we apply the following approximation $c(x) = c_{(x=170°W)}\sqrt{\frac{\overline{Z_{eq}}}{\overline{Z_{170°W}}}}$, where Z_{eq} is the mean depth of the 20°C isotherm at 170°W at equator (averaged between 2.5°N and 2.5°S).

As a "proof of concept", Figure 2.5 shows Hovmöller diagrams of intraseasonal SLA (U) averaged around the equator (between 2.5°N and 2.5°S) as well as the SLA(U) contribution from (*i.e.*, projected onto) different combinations of meridional modes derived from the sea level and zonal currents. Overall, the sum of the contributions from the Kelvin and 1st, 2nd and 3rd Rossby modes to the SLA (U) accounts $\sim$ 88% ($\sim$ 90%) for almost the total SLA intraseasonal variability (Figure 2.5e and Figure 2.6e). See for example the downwelling Kelvin wave that propagated eastward at the beginning of 2016 (during the El Niño event).

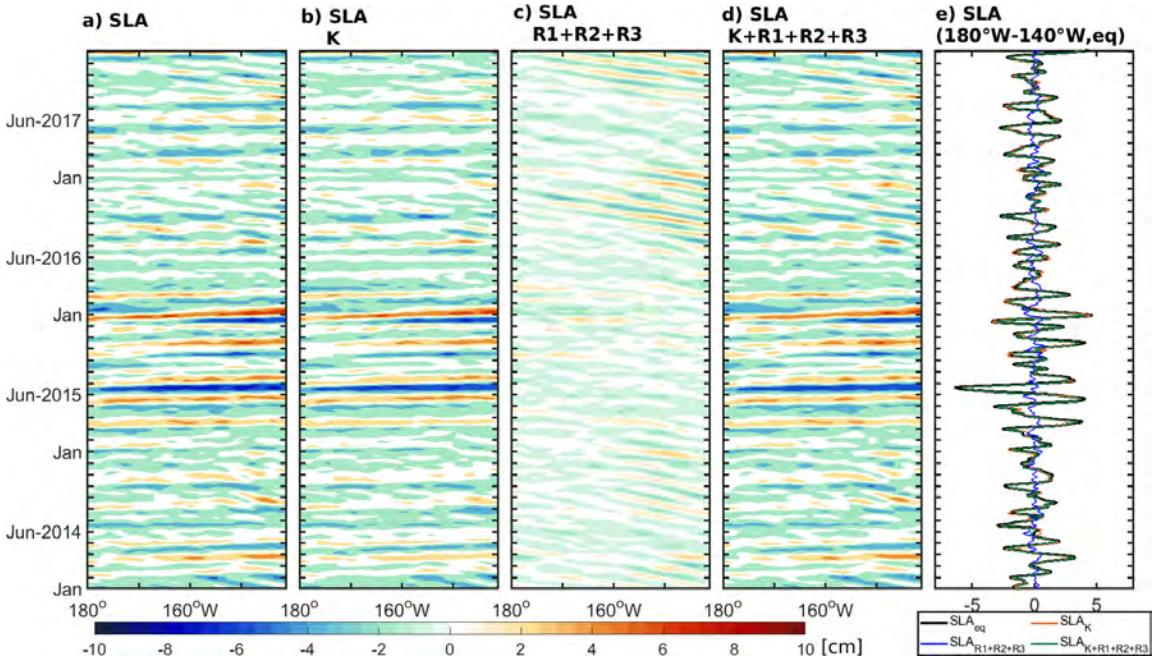

Figure 2.5: Intraseasonal sea level anomalies (SLA) averaged at the equator (2.5°N-2.5°S) from AVISO (a), projected onto the Kelvin mode (b), onto the sum of the first 3 Rossby modes (c) and onto the sum of the Kelvin mode and the Rossby modes (1+2+3) (d). (e) Time series of SLA and the contributions from different combination of meridional modes averaged between 180°and 120°W.

The meridional decomposition of the sea level can also be computed when the sea level is the only variable available by using the approach of Boulanger and Menkes (1995) (see Boulanger and Menkes (1995) appendix B).

Similarly, we can also quantify how the wind forcing contributes to the waves' generation, by projecting the zonal wind stress (τ_x) also onto the theoretical meridional structure of the first baroclinic mode. The contribution of the zonal wind forcing to the generation of the Kelvin mode is then inferred from the following approximation:

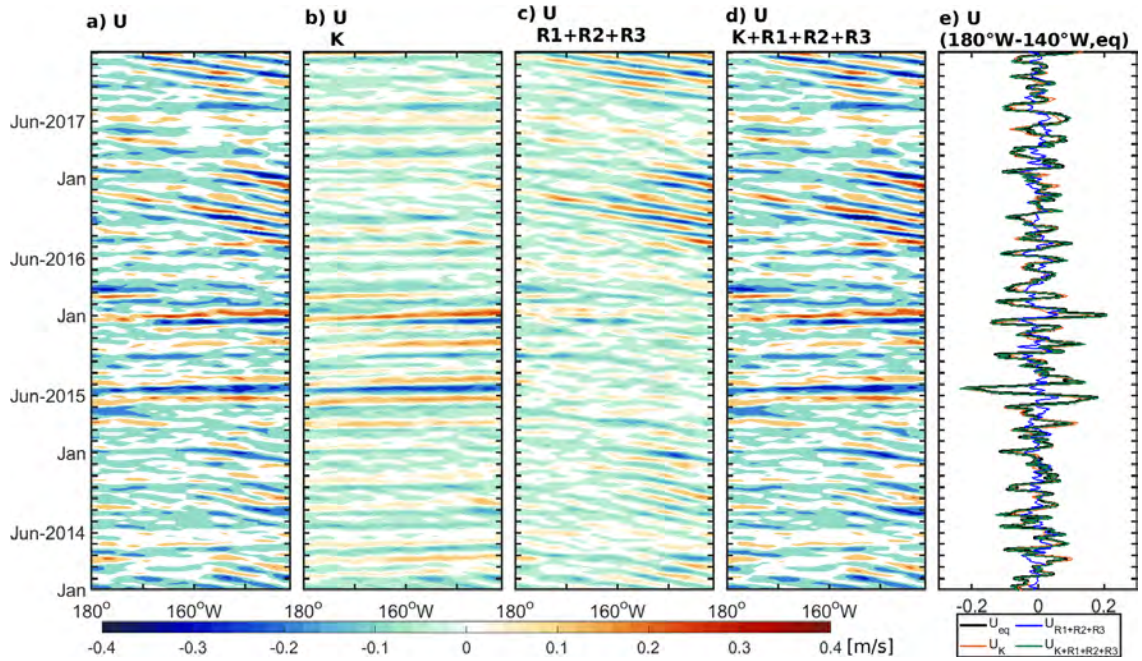

Figure 2.6: Intraseasonal zonal current anomalies (U) averaged at the equator (2.5°N-2.5°S). From AVISO (a), projected onto the Kelvin mode (b), onto the sum of the first 3 Rossby modes (c) and onto the sum of the Kelvin mode and the Rossby modes (1+2+3) (d). (e) Time series of SLA and the contributions from different combination of meridional modes averaged between 180°and 140°W.

$$\begin{aligned} \tau_x(x,y,t) &= F_o(x,t)R_n(y) \\ F_o(x,t) &= \int_{Y_N}^{Y_S} \tau_x(x,y,t)R_0^u(x,y)dy \end{aligned} \tag{2.11}$$

In chapter 3, this approach of decomposition into meridional wave structures is applied to observational data in order to quantify the Kelvin Wave contribution to the variance of TIWs-induced intraseasonal sea level anomalies and thus evaluate the nonlinear interaction between TIWs and IEKWs.

2.4 Characterization of Tropical Instability Waves activity

As it was mentioned in the previous chapter, TIWs are characterized by meanders in the SST front just north of the equator. These cusp-shaped features have been widely observed in oceanic, atmospheric and biogeochemical variables from *in situ*, satellite observations and modeling experiments. As an illustration, Figure 2.7 shows their signature in a snapshot of satellite SST from 14 November 2022.

TIWs have been known to be stronger during the second half of the year since the seminal

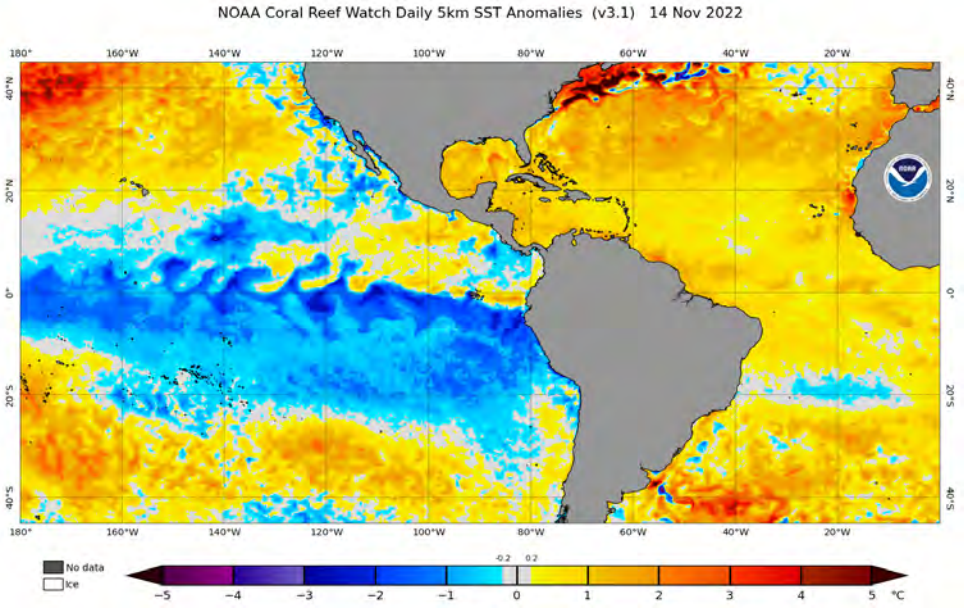

Figure 2.7: Snapshot (14 November 2022) of daily SST anomaly from the NOAA Coral Reef Watch (CRW) global 5km product. (`https://coralreefwatch.noaa.gov/product/5km/index_5km_ssta.php`)

study by Legeckis (1977), however no quantitative indicator of their activity was developed until 1997 when Baturin and Niiler (1997) and Johnson and Proehl (2004) proposed to assess it on the basis of meridional velocity measurements from moorings positioned along the equator (0°N,140°W) and (0°N,110°W). In particular, Baturin and Niiler (1997) used a multitaper procedure to define a TIWs index as a time-varying amount of energy in the 15-30-day period band. They turned on/off the index when the amount of energy was greater/smaller than +/- 0.5 standard deviation from the mean to differentiate high and low TIW activity periods. Johnson and Proehl (2004) isolated the TIWs activity by using filtering of the meridional velocity in the 13 to 30 days period range. Both studies confirmed that the increased strength of the SEC northern branch and NECC generates high TIWs energy in the boreal fall through barotropic energy conversion.

Since these seminal studies, several others have developed different frameworks and indices to characterize TIWs activity, their seasonality and amplitude modulation at intraseasonal to interannual timescales. This section is dedicated to describe the main contributions.

2.4.1 TIWs as a measure of SST and currents intraseasonal variability

Yu and Liu (2003) measured the TIWs activity as the root-mean-square of the 50-day high-pass filtered SST in a 28-year long coupled atmosphere-ocean general circulation model simulation. An (2008) characterized TIWs activity as the monthly variations of SST, where the variation is calculated as the deviation from the monthly mean of SST obtained from TOGA-TAO data at 2°N, 140°W. Figure 2.8 (adapted from An (2008)) shows the monthly

TIWs variability from two datasets: the TOGA-TAO *in situ* observations and the SODA reanalysis product, which overall agree well, in particular displaying the increased/decreased TIWs activity during La Niña/El Niño periods.

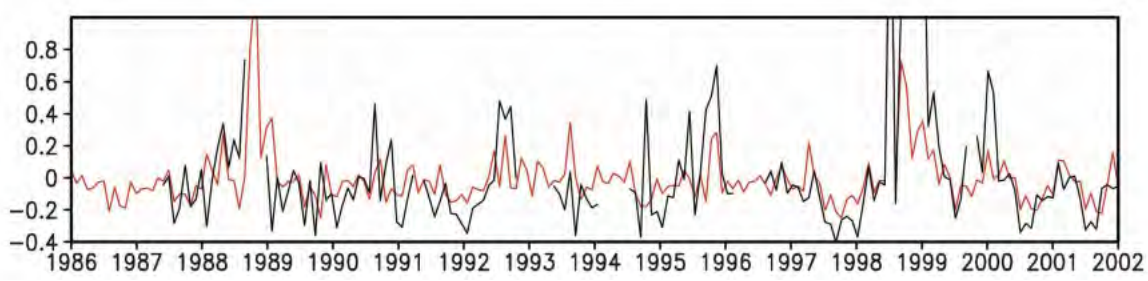

Figure 2.8: Monthly time series of SST variability from TOGA-TAO data at 2°N,140°W (black curve) and from the SODA reanalysis product at 2.25°N, 140.25°W (red curve). (Figure 1 bottom panel from An (2008))

Recently, Maillard et al. (2022b) and Xue et al. (2023) used the variance of SST and meridional currents intraseasonal anomalies to evaluate the ability of different configurations of a regional ocean model and different oceanic reanalysis products to simulate TIWs variability.

Overall, TIWs activity exhibits similar double-peak patterns in models characterized by high horizontal resolutions such as CROCO at a 1/12° horizontal resolution in Maillard et al 2022b (cf. Figure 2.9), although their intensity and locations are model-dependent (not shown). However, TIWs are shown to be seriously underestimated in datasets with coarse spatial resolutions (e.g., GODAS and ECCO2) (Xue et al. (2023)).

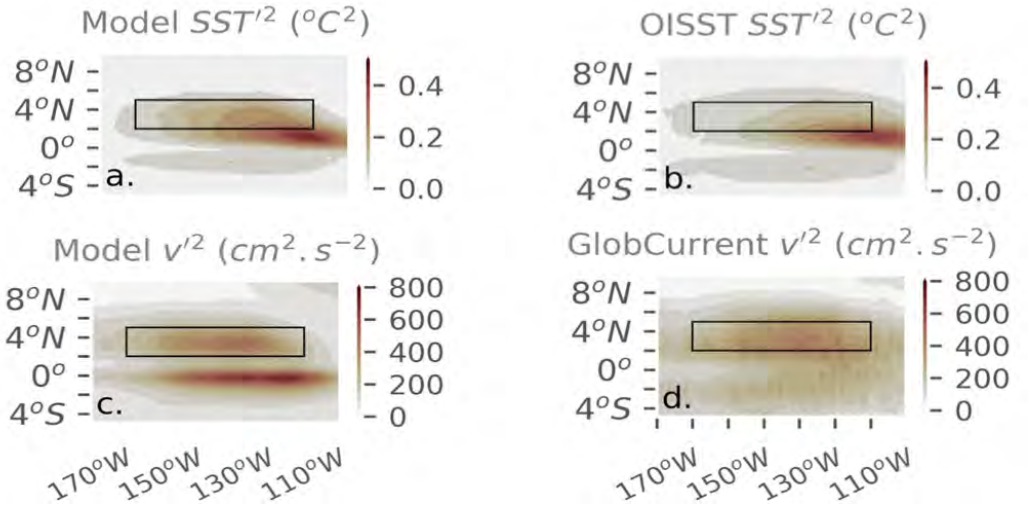

Figure 2.9: Maps of TIWs annual variance SST'^2 in (a) a realistic high-resolution regional ocean model (CROCO at a 1/12° horizontal resolution over the period 1980–2019), and (b) satellite OISST (1981–2019), (c, d) Same as (a, b) but for the TIW variance v'^2, in (c) CROCO and (d) the GlobCurrent product (1993–2017) (adapted from Maillard et al. (2022b)).

2.4.2 TIWs index as the sum of nodes

Recently, Boucharel and Jin (2020) proposed a complex TIWs index to characterize the temporal variations of TIWs activity. The real part of this complex TIWs index (TIW_1) is simply extracted as the equally spaced and weighted (but with alternating signs) summation of unfiltered SST anomalies at 8 fixed points along 0-6°N. This new index is capable to capture the amplitude and phase without doing any mathematical transformation such as temporal filtering. The index is calculated as:

$$\begin{aligned} TIW_1(t) &= \sum \pm SST'(t, nodes) \\ TIW_2(t) &= \sum \pm SST'(t, nodes + 6.25°) \end{aligned} \tag{2.12}$$

TIW_2(t) is calculated similarly as TIW_1(t) except the base points are all shifted by a fixed distance representing a 90 degree zonal phase shift (i.e. roughly 6.25 degrees in longitude). The final TIWs amplitude (A) can be calculated as:

$$A = \sqrt{TIW_1(t)^2 + iTIW_2(t)^2} \tag{2.13}$$

To illustrate the positions of the nodes, Figure 2.10 shows the regression of daily SST intraseasonal anomalies onto TIW_1 index and displays the typical equatorial TIWs cusps at the right locations as compared with the spatial pattern of the daily SST intraseasonal anomalies decomposition into Empirical Orthogonal Functions (see Boucharel and Jin (2020)'s supplementary material). Choosing different numbers and locations of the nodes (such 4, 6 or 10) and shifting them all together in the zonal direction have been shown to give similar results.

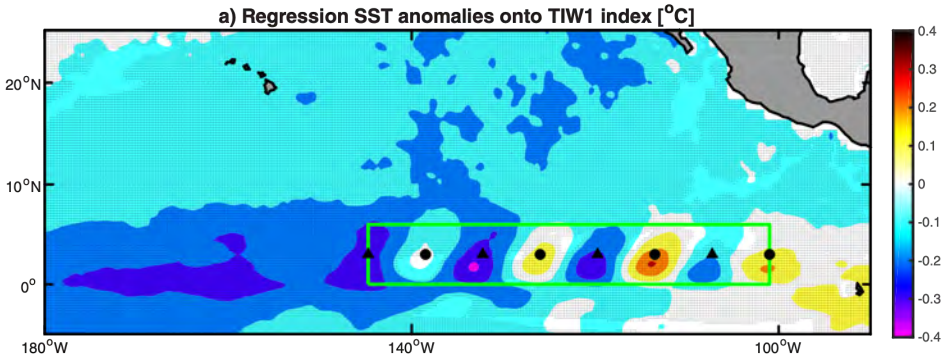

Figure 2.10: (a) Regression of daily SST anomalies onto TIW_1 index (1997–2015). Dots denote the 95% statistical significance level. Black filled triangles and circles show the positions of longitudinal nodes (adapted from Boucharel and Jin (2020)).

2.4.3 Demodulation of the TIWs activity using Complex Empirical Orthogonal Functions (CEOF)

As shown for instance by Stein et al. (2011), Boucharel et al. (2013), or Boucharel et al. (2016a) complex empirical orthogonal functions (CEOFs) can be an efficient tool to disentangle the spatiotemporal signals of the equatorial dynamics. In addition, because it provides amplitude and phase information, the CEOF analysis is in particular well suited to capture and characterize propagating features, such as those from equatorial waves.

The method was first introduced by Barnett (1983) to detect the propagation features of wind systems in the equatorial Pacific. This approach is based on the Fourier theory which requires information about the propagation provided by a complex representation of the variable.

Let's present an example of CEOF decomposition of the daily sea surface height (SSH) variable that will be used in both chapters 3 and 4. First, SSH is detrended and then intraseasonal sea level anomalies (SLA) are calculated as the departure of daily SSH from the monthly mean. To produce the complex field of SLA, we apply the Hilbert transform as a linear operator that computes the real ($\mathcal{R}$) and imaginary ($\mathcal{I}$) part of the signal. If the scalar SLA field can be represented by:

$$sla_{jt} = \sum_{w} a_j(\omega t)\cos(\omega t) + b_j(\omega)\sin(\omega t) \tag{2.14}$$

then, the propagation feature can be described by:

$$\begin{aligned} SLA_j(t) &= \textstyle\sum_w [\underbrace{a_j(\omega t)\cos(\omega t) + b_j(\omega)\sin(\omega t)}_{sla_j(t)}] + i[\underbrace{b_j(\omega t)\cos(\omega t) - a_j(\omega)\sin(\omega t)}_{\widehat{sla_j(t)}}] \\ SLA_j(t) &= sla_j(t) + i\widehat{sla_j(t)} \end{aligned} \tag{2.15}$$

Where sla_{jt} is the original data and $\widehat{sla_{jt}}$ is the Hilbert transformation, which is identical to the original time series except for a quarter ($\pi/2$) phase-shift. This approach allows to have a reasonable measure of the momentum of the variable when its temporal variations are confined to a relative narrow timescale before applying a classic Empirical Orthogonal Functions (EOF) analysis. The EOF, also called Principal Component Analysis is a technique that determines the dominant spatial patterns of variability by rearranging the data into "eigenmodes" that evolve with time following a specific function. The EOF analysis is also considered as an eigenvalue problem and this method consists in computing first the covariance matrix of the filtered and complex $SLA_j(t)$ field is $C_{jk} = \langle SLA_j(t)^* SLA_k(t) \rangle_t$, where $*$ denotes the complex conjugation, $\langle .. \rangle$ indicates the time average. The covariance matrix being symmetric and diagonalizable, the eigenvalue problem ($C_{j,k}e_n = \lambda e_n$) can be resolved and $C_{j,k}$ can be decomposed into a set of orthogonal eigenvectors and eigenvalues. Then, the observed SLA field can be represented as a sum of the contributions from the N principal components P_n multiplied by the complex and eigenvectors e_n (sorted in decreasing order):

$$SLA(x,t) = \textstyle\sum_{n=1}^{N} e_n(x)^* P_n(t) \tag{2.16}$$

The time-dependent principal components are given by

$$P_n(t) = \sum_x SLA(x,t)e_n(x) \tag{2.17}$$

The fraction of the total field variance associated with the n-th complex eigenvector is given by $\lambda_n / \sum_{n=1}^{N} \lambda_n$.

The extraction of the eigenmodes of this complex covariance matrix permits to study the propagation features of (in our case) SLA, using the spatial and temporal distribution of the amplitude and phase of the eigenmodes. The spatial phase function $\theta_n(x)$ shows the relative phase of fluctuations among the spatial domain and amplitude functions $S_n(x)$ provide the spatial distribution of the variability associated with each eigenmode of our new field SLA(x,t):

$$\begin{aligned} \theta_n(x) &= arctan\Big[\frac{\mathcal{I}e_n(x)^*}{\mathcal{R}e_n(x)^*}\Big] \\ S_n(x) &= [e_n(x)e_n^*(x)]^{1/2} \end{aligned} \tag{2.18}$$

The temporal phase $\phi_n(t)$ and amplitude $R_n(t)$ allow characterizing as time-dependent each eigenmode, permitting to identify dominant periods of increased anomalies that can be related for instance to major signatures of climate modes variability such as ENSO (Barnett (1983)).

$$\begin{aligned} \phi_n(t) &= arctan\Big[\frac{\mathcal{I}P_n(t)^*}{\mathcal{R}P_n(t)^*}\Big] \\ R_n(t) &= [P_n(t)P_n^*(t)]^{1/2} \end{aligned} \tag{2.19}$$

Examples of CEOF analysis for TIWs characterization:

- By applying the CEOF decomposition on the 10-60 days band-pass filtered currents velocity and temperature from the TAO mooring at 140°W, Lyman et al. (2007) evidenced two distinct modes of TIWs with periods near 33 and 17 days, and commonly referred to as the Rossby and Yanai modes, respectively contained in the first and second CEOF mode. The observed period of 17 and 33 days are near-multiple of each other, which prompted Lyman et al. (2007) to suggest a possible nonlinear interaction between the two types of waves.
- Xue et al. (2021) Xue et al. (2021) used the CEOF analysis on SST anomalies and demonstrated that the first mode account for TIWs propagation which represents ∼30% of the total intraseasonal variability. In addition, they showed that the time series associated with the real and imaginary part of the first mode's principal component were highly correlated with Boucharel and Jin (2020)'s TIW_1 and TIW_2 indices respectively (Figure 2.11).

Note also that Boucharel et al. (2016b) applied this diagnostic on the intraseasonal anomalies of thermocline depth in the tropical Pacific to extract the eastward propagating signal associ-

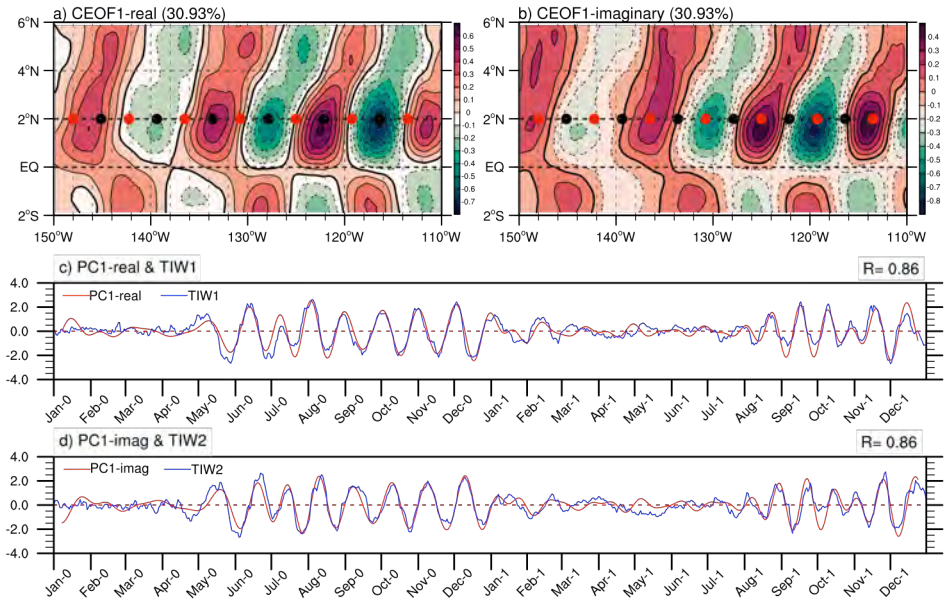

Figure 2.11: Spatial patterns of the leading CEOF modes of SSTAs over the TIW region (2°S–6°N, 110°–150°W) for the (a) real and (b) imaginary parts obtained through a linear regression of SSTAs onto the normalized real part ($PC1 - real$) and imaginary part ($PC1 - imag$) of the leading PC time series over the 2016–17 period. Red (black) dots show the positions of longitudinal nodes used to calculate TIW_1 (TIW_2). Corresponding normalized PC time series real (c) and imaginary (d) part of leading CEOF mode (red lines) and complex TIW index (blue lines), respectively. Adapted from Figure 2 from Xue et al. (2021).

ated with intraseasonal equatorial Kelvin waves. Therefore, the CEOF analysis is a suitable tool to disentangle the propagation features of TIWs and IEKWs.

Overall, these different indices allow capturing the spatio-temporal variability associated with TIWs-propagating features and in particular their seasonal variability with an increased (decreased) activity in boreal summer and fall (winter and spring) as well as their interannual variability characterized by decreased (increased) activity during El Niño (La Niña) events (cf. Figure 2.12).

2.4.4 Eddy Kinetic Energy (EKE) budget

In an effort to understand the energy conversions occurring during the IEKWs-TIWs interaction, we estimate in the different sensitivity experiments of the regional ocean model (4) the contribution of the tendency terms of the Eddy Kinetic Energy (EKE) budget obtained from the momentum equations following (Masina et al. (1999); Qiao and Weisberg (1998); Holmes and Thomas (2016); Conejero (2021)). Here, instead of using the long-term mean or the climatological state as a baseline to derive anomalies, as usually done, the EKE budget is done for the intraseasonal anomalies, so that the baseline is the 30-days running mean and anomalies are the departure from it. Conversion terms (see below) thus vary in time. The en-

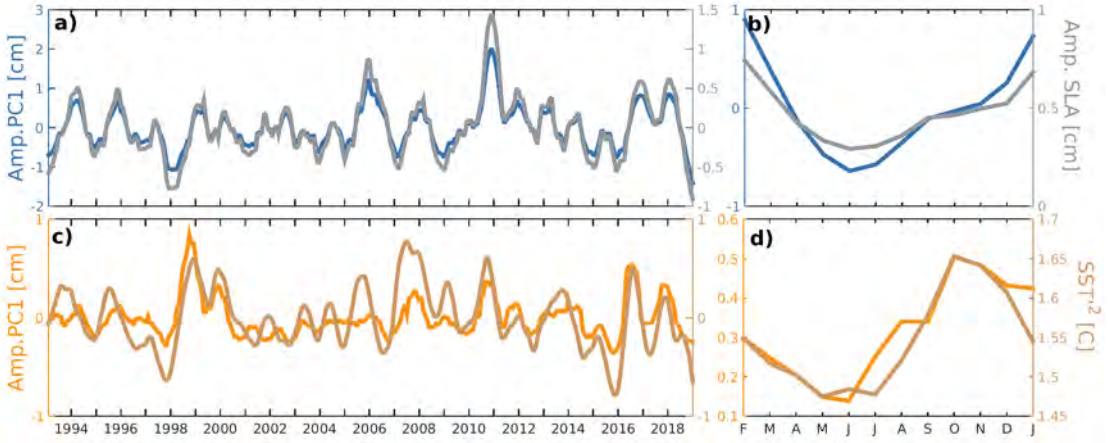

Figure 2.12: Interannual anomalies of some indices of TIWs activity : (a) Amplitude of the First Principal Component from the SLA (blue line) and TIWs amplitude calculated from the SLA reconstructed from CEOF1 (gray line). (c) SST monthly variability (SST'^2) from OISST product at 2°N, 140°W (brown curve) and TIWs amplitude derived from the SSTA observations (brown curve). Seasonal cycles of the different indices of TIWs activity(a and c) are shown in the right panels (b and d) with the same color code. A 3-months running mean is applied to all TIWs indices.

ergy variation in terms of conversion terms and flux vector gives us the approximation of the available energy transformation to the generation of eddies. The equation for the variation of EKE $K_e = (1/2)\rho_0 * ((u'u') + (v'v'))$ is finally given by (Masina et al. (1999)):

$$\begin{aligned}\frac{\partial K_e}{\partial t} + U \cdot \nabla \mathbf{K}_e + \overline{W} K_{ez} + u' \cdot \nabla \mathbf{K}_e + w' K_{ez} = \\ -u' \cdot \nabla p' + \rho_o[-u' \cdot (u' \cdot \nabla U) - u' \cdot (w' V_z) \\ + u' \cdot \overline{(u' \cdot \nabla u')} + u' \cdot \overline{w' u'_z} \\ + K_{Mh}(u' \cdot \nabla^2) u') + u' \cdot (K_{Mv} u'_z)].\end{aligned} \tag{2.20}$$

The EKE budget includes in particular the two main conversion terms: the kinetic and potential energy contributions in the Ke equation:

- *Barotropic conversion* ($K_m K_e$) corresponds to the conversion of mean Kinetic energy (K_m) into EKE (K_e) when the horizontal deformation work terms are positives $K_m \rightarrow K_e$.

$$K_m K_e = \langle \frac{-1}{H} \int_H^0 \Big(u'u' \frac{\partial \overline{u}}{\partial x} + u'v' \frac{\partial \overline{u}}{\partial y} + u'w' \frac{\partial \overline{u}}{\partial z} + v'u' \frac{\partial \overline{v}}{\partial x} + v'v' \frac{\partial \overline{v}}{\partial y} + v'w' \frac{\partial \overline{v}}{\partial z} \Big) \rangle \tag{2.21}$$

- *Baroclinic conversion* ($P_e K_e$) corresponds to the conversion of the available eddy potential energy (P_e) of the mean state into EKE $P_e \rightarrow K_e$, when its value is positive.

$$P_e K_e = \langle \frac{-g}{H\rho_o} \int_H^0 (\rho' w') dz \rangle \tag{2.22}$$

where the velocity field is (u, v, w) and the density is ρ. The brackets stand for the mean over 40 days to capture the transient effect of the passage of the IEKWs on the TIWs energetics. The constant variables are the gravitational acceleration $g = 9.8ms^{-2}$ and the reference water density $\rho_0 = 1025km/m^3$.

2.5 Numerical model: the Coastal and Regional Oceanic Community Model: CROCO

2.5.1 General description

In this thesis, the numerical simulations were performed with the Coastal and Regional Ocean Community model (CROCO) version 1.2 developed around the kernel of the Regional Oceanic Modeling System (ROMS) (Shchepetkin and McWilliams (2005) and Debreu et al. (2012)). CROCO is a free-surface, terrain-following coordinate model with split-explicit time stepping and with Boussinesq and hydrostatic approximations that solves the primitive equations as ROMS. The ocean model configuration also uses the K-profile parameterization in the vertical mixing of tracers and momentum (Large et al. (1994)) that is a parameterization for convective and wind-driven mixing in the ocean surface boundary layer, and the stress-correction parameterization approach for the effect of surface currents on the wind stress (known as "current feedback", Renault et al. (2016) and Renault et al. (2020)). The surface freshwater, heat, and momentum fluxes are estimated using the COARE bulk formulae (Fairall et al. (2003)).

The primitive equations in CROCO are solved using the following approximations:

- The variations in the seawater density are neglected except in their vertical contribution to the buoyancy force, also known as the "Boussinesq hypothesis".
- The hydrostatic approximation assumes that the vertical acceleration of the momentum is neglected in the ocean, then the vertical momentum equation is reduced to a balance between the buoyancy force and the vertical pressure gradient.
- Incompressibility hypothesis supposes that the volumetric mass of the fluid's particle does not vary with the pressure, then the non-divergence of the continuity equation.
- The spherical earth approximation, where the geopotential surfaces are assumed to be spheres and the gravity parallel to the earth's radius.
- The ocean depth is neglected compared to the earth's radius.
- The turbulent fluxes can be expressed in terms of large-scale features.

The primitive equations solved by CROCO are:

$$\frac{\partial u}{dt} + \overrightarrow{\nabla} \cdot (\overrightarrow{\mathbf{v}} u) - fv = \frac{-1}{\rho_o}\frac{\partial P}{\partial x} + \nabla_h(K_{Mh} \cdot \nabla_h u) + \frac{\partial}{\partial z}\left(K_{Mv}\frac{\partial u}{\partial z}\right) \quad u \text{ momentum eq.}$$

$$\frac{\partial v}{dt} + \underbrace{\overrightarrow{\nabla} \cdot (\overrightarrow{\mathbf{u}} v)}_{\text{advection}} - \underbrace{fu}_{\text{Coriolis}} = \underbrace{\frac{-1}{\rho_o}\frac{\partial P}{\partial y}}_{\text{Pressure gradient}} + \underbrace{\nabla_h(K_{Mh} \cdot \nabla_h v)}_{\text{Horizontal diffusion}} + \underbrace{\frac{\partial}{\partial z}\left(K_{Mv}\frac{\partial v}{\partial z}\right)}_{\text{Vertical diffusion}} \quad v \text{ momentum eq.} \tag{2.23}$$

$$0 = -\frac{\partial P}{\partial z} - \rho g \quad \text{hydrostatic equation} \tag{2.24}$$

$$0 = \frac{\partial u}{\partial x} + \frac{\partial v}{\partial y} + \frac{\partial w}{\partial z} \quad \text{continuity equation} \tag{2.25}$$

$$\rho = \rho(T, S, P) \quad \text{equation of state} \tag{2.26}$$

$$\begin{aligned} \frac{\partial T}{\partial t} + \overrightarrow{u} \cdot \nabla T &= \nabla_h(K_{Th} \cdot \nabla_h T) + \frac{\partial}{\partial z}\left(K_{Tv}\frac{\partial T}{\partial z}\right) \\ \frac{\partial S}{\partial t} + \overrightarrow{u} \cdot \nabla S &= \nabla_h(K_{Sh} \cdot \nabla_h S) + \frac{\partial}{\partial z}\left(K_{Sv}\frac{\partial S}{\partial z}\right) \quad \text{Tracer conservation eq.} \end{aligned} \tag{2.27}$$

Where u, v, w are the (x, y, z) components of the velocity vector $\overrightarrow{\mathbf{v}}$, g is the acceleration of gravity, and P is the total pressure. The total *in situ* density is equal to $\rho_o + \rho(x, y, z, t)$. K_{Mh} and K_{Mv} are the horizontal and vertical coefficients of turbulent diffusivity, respectively. S and T are the salinity and temperature, respectively.

2.5.2 Model Set Up

The domain covers the tropical Pacific from 135°E to the American coast and from 18°S to 18°N with a horizontal resolution of 0.25°, which is considered sufficient to resolve the equatorial mesoscale activity since the typical wavelength of TIWs is about 1500 km.

The vertical grid has 54 vertical levels, stretched in the upper layers ($hcline = 300m$) with the parameter $\sigma_s = 7$, and in the bottom layer with the parameter $\sigma_b = 2$.

The model is run from January 1st 1993 to June 2019 preceeded by a 3 years long spin-up consisting in repeating the year 1993.

The open boundaries and initial conditions for tracers, SSH and horizontal velocity are derived from GLORYS2V4 (Garric et al. (2017)) with 3 days temporal resolution, a 0.25° spatial

resolution and 75 vertical levels.

GLORYS2V4 is produced with the numerical ocean model NEMO (Nucleus for European Modelling of the Ocean, Madec et al. (1997)) and is constrained with data assimilation of satellite and *in situ* observations. The reanalysis product uses a tripolar ORCA grid type at 0.25° horizontal resolution (ORCA025), with 75 vertical levels, that is interpolated on a regular grid. As an example of GLORYS2V4's ability to simulate the tropical Pacific's dynamics, Figure 2.13(c) shows the mean zonal circulation simulated in GLORYS2V4 and inferred from drifters. GLORYS2V4 displays a realistic representation of the main zonal currents in the tropical Pacific: the eastward North Equatorial Counter Current (NECC) and the South Equatorial Current (SEC) (Figure 2.13a). The anomalous zonal current observed in 2015 is also well reproduced by the reanalysis product (Figure 2.13d).

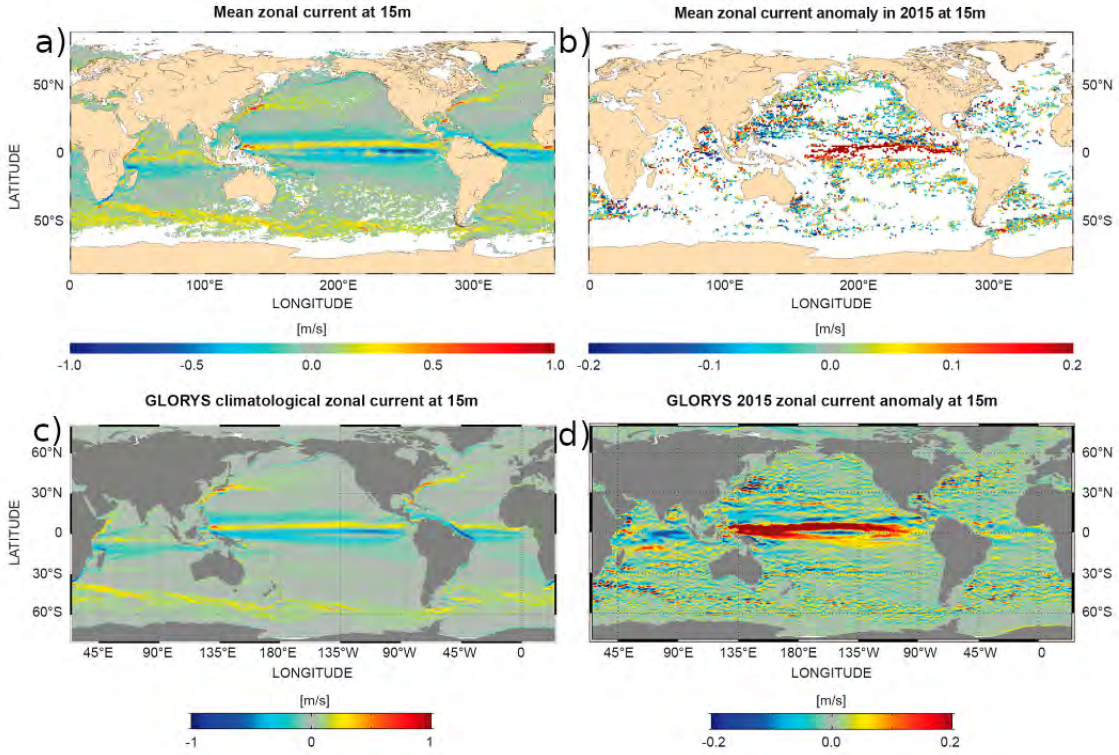

Figure 2.13: 1993–2014 average near-surface (0-15 m average) zonal current (a) and zonal current anomaly in 2015 (relative to 1993–2014 mean) (b) computed from drifter observations obtained from the *in situ* Global ocean product (`https://catalogue.marine.copernicus.eu/documents/PUM/CMEMS-INS-PUM-013-044.pdf`). (c) and (d) identical to (a) and (b) but computed from GLORYS2V4. Positive values indicate eastward, and negative values westward currents. Figure 18 from Von Schuckmann et al. (2016).

The simulation is forced at the surface with ERA-Interim fluxes (Dee et al. (2011)), from the same reanalysis product that forced GLORYS2V4.

The bottom topography is derived from the 1/15 arc-second high-resolution bathymetric dataset GEBCO, provided by `https://www.gebco.net/`.

2.5.3 Sensitivity to the domain's size and topography

Because of the complicated bathymetry and topography in the western tropical Pacific and the lack of observations available for data assimilation (*e.g.*, see the near absence of drifters in the equatorial Pacific west of the dateline in 2015 on Figure 2.13b), GLORYS2V4 suffers from several biases in the representation of the mean circulation and dynamics in this region (Jean-Michel et al. (2021)). For instance, spurious strong currents off New Guinea have been reported by Von Schuckmann et al. (2016) in the GLORYS2V4 reanalysis, originating from a known sea surface height bias in the Mercator Ocean monitoring system (Lellouche et al. (2013). Lellouche et al. (2018) also reported that sea level errors in the Indonesian archipelago and tropical western Pacific can be attributed to uncertainties in mean dynamic topography (MDT) due to the complicated bathymetric characteristics of the islands. Grenier et al. (2011) also encountered similar problems in their modeling study with in particular mean zonal currents not well simulated at 147°E along the equator and in the core of the EUC concurrently with a thermocline shallower than in the observations. They attributed such biases in their simulation to the unrealistic (because too coarse) topography/bathymetry of the small islands and straits in the southwestern tropical Pacific.

Because such biases are likely to propagate into our domain through the western lateral OBC and even could be amplified due to the interpolation of GLORYS2V4 data at the OBCs on the CROCO grid, we performed numerous tests using grids with different positions for the western boundary and different interpolation methods, in order to come up with a configuration that simulate realistically the mean equatorial circulation, in particular the mean equatorial thermocline.

- Grid 1 ($G1$) covers the spatial domain [125°E-292°E, 20°N-20°S], and includes the complex topography in the western Pacific.
- Grid 2 ($G2$) covers a smaller domain [135°E-292°E, 18°S-18°N], with less islands and narrow straits in the domain's western part than G1.
- The same Grid $G2$ was also applied a Gaussian smoothing ($G2_{smooth}$) near the remaining complicated western islands at the western boundary in order to reduce inconsistencies and aliasing between variables from GLORYS2V4 product and their interpolation on the CROCO grid to generate OBCs and initial conditions.
- An even smaller grid ($G3$) is also tested [140°E-290°E, 14°S-14°N], in order to cut most of the western islands off the domain.
- Finally, a grid GF covering the same domains as $G2$ but that includes a mask between Papua New Guinea and the North of Australia is tested. This mask is applied specifically to prevent unrealistic re-circulations between New Guinea and the northern part of Australia (Grenier et al. (2011)).

As an illustration, Figure 2.14 shows the bathymetry of the GLORYS2V4 (Figure 2.14a) and CROCO (Figure 2.14b) $G2$ grids, as well as their differences (Figure 2.14c). Strong

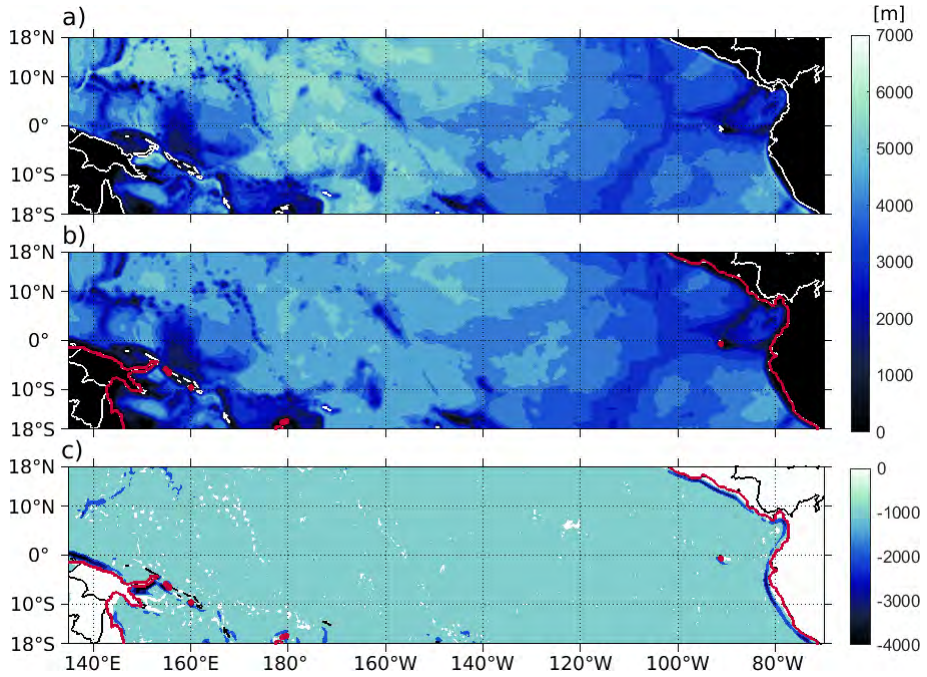

Figure 2.14: Bathymetry from the the GLORYSV2 reanalysis product (a) and CROCO G2 (b) grids. (c) Difference in bathymetry between the CROCO $G2$ and GLORYSV2 grids (CROCO-GLORYSV2). The red contour indicated the mask used in CROCO GF grid.

differences can be observed in particular near the western OBC along the Papua New Guinea coast due to the difference in resolution and mask between the two models. Note that some of these differences may also come from the first interpolation of variables from the original ORCA025 grid onto the regular grid used by Mercator to provide the GLORYS2V4 reanalysis product. Such bathymetrical differences between the two grids will generate inconsistencies when GLORYS2V4's data are interpolated on the CROCO grid as seen in Figure 2.15.

Figure 2.16a shows the mean position of the 20^{o}C isotherm depth during the first year of simulation after the spin-up for the different grids tested. Overall, while all grids lead to a too shallow equatorial thermocline and associated cold biases compared to observational products, these biases tend to be reduced when the westernmost part of the tropical Pacific is cut off the domain ($G3$) and in particular when the mask is applied to prevent recirculations between Papua New Guinea and the northern part of Australia (GF). This prompted us to use GF to run the CROCO simulation over the entire 1993-2019 period.

Figure 2.16 (b,c and d) show the position of the 20°C isotherm depth along different depth-longitude sections for the long simulation (1993-2018) run with the GF grid and the different observational products. While the shallow bias still persists in the equatorial region and in particular in the western part of the basin, most likely originating for the several problems mentioned above, they remain below 20m in the central Pacific and overall below 5m in the central-eastern Pacific, the region of strong TIWs activity, which gives us confidence in the ability of our simulation to reproduce the variability associated with both TIWs and IEKWs.

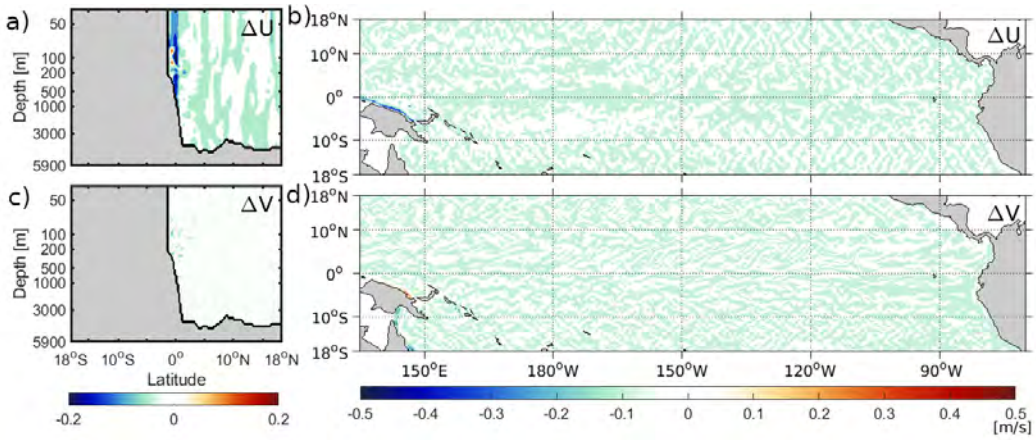

Figure 2.15: Differences in zonal (a,b) and meridional (c,d) velocity between the GLORYS2V4 product and its interpolation on the CROCO G2 grid for the initial condition of January 1,1993. (a) and (c) show latitude-depth sections of the differences in zonal (Δ U) and meridional (Δ V) currents respectively at the western OBC (135°E). (a) and (c) show maps at 15-meters of the differences in zonal (Δ U) and meridional (Δ V) currents respectively for the initial condition. (Δ=GLORYS2V4-CROCO).

More diagnostics will be performed to evaluate our simulation regarding these issues in chapter 4.

Overall, while more tests could have been done in order to reduce biases in the representation of the equatorial thermocline, these diagnostics highlight the strong sensitivity of tropical Pacific simulations by regional oceanic models to the position of the Western lateral OBC.

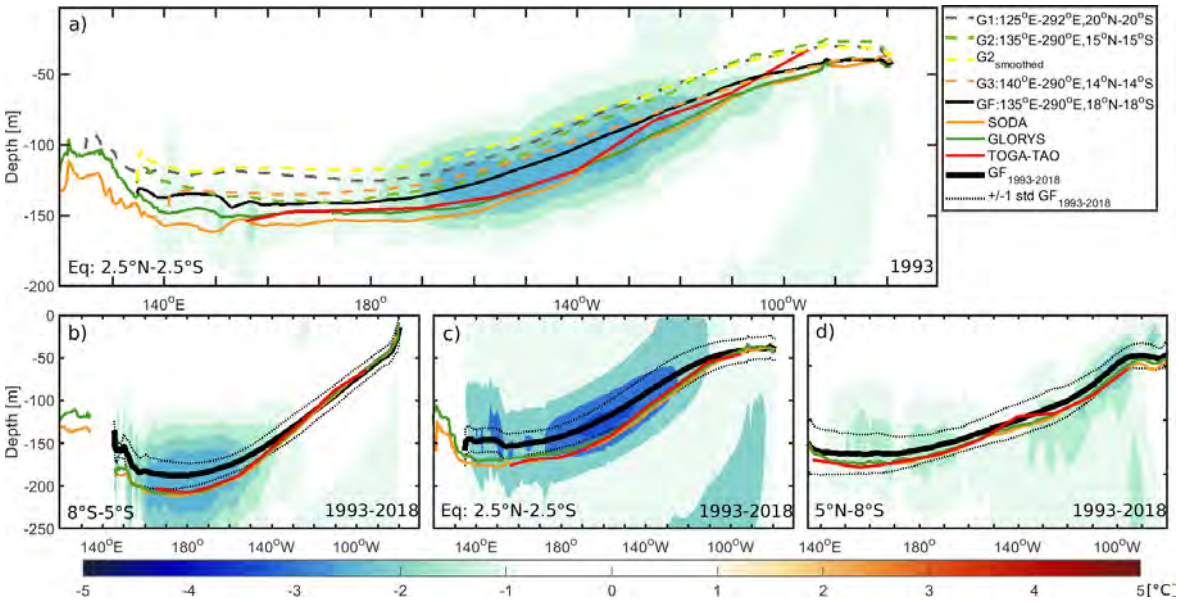

Figure 2.16: (a) Depth-longitude section at the equator (2.5°N - 2.5°S) of the mean temperature biases (shading) between GLORYS2V4 and the first year after spin up (1993) of the CROCO simulation using the *GF* grid. (b), (c) and (d) are depth-longitude sections averaged in (5°S - 8°S), (2.5°N - 2.5°S) and (5°N - 8°N) respectively of the mean temperature biases (shading) between GLORYS2V4 and CROCO *GF* for the entire 1993-2018 period. Plain lines represent the position of the isotherm 20°C in different observational and reanalyses products. Dashed lines represent the position of the isotherm 20°C simulated by CROCO using the different grids ($G1$,$G2$, $G2_{smooth}$,$G3$) and *GF* in thin black line (a) and thick black lines in (b), (c) and (d). The observations and reanalysis products are TOGA-TAO arrays (red line), SODA v3.4.2 (orange line) and GLORYS2V4 (green line) reanalysis products. The interannual variability of the long simulation (+/- 1 standard deviation) is represented by the thin dotted black lines) in (b, c and d).

Chapter 3

Observational evidence of consistent interactions between Intraseasonal Kelvin Waves and Tropical Instability Waves

Contents

3.1 Preamble

While both IEKWs and TIWs are at the heart of complex low-frequency interactions, with a large body of literature documenting how both can be rectified by mean states or vice-versa, only a few observational, theoretical, and modeling studies have suggested that they may also interact with each other, leading to potentially strong impacts in terms of SST, circulation and energetic variability in the eastern equatorial Pacific.

Using *in situ* ocean velocity data, Qiao and Weisberg (1998) found that the early end of the TIWs season observed in December 1990 coincided with the propagation of a large IEKW responsible for a decrease in the meridional shear between the SEC and EUC, in the associated barotropic energy conversion rate and therefore in the TIW activity. Several studies have also highlighted the possibility that IEKWs can be reflected from the eastern boundary (*i.e.*, the South American coast) into Rossby waves that can then modify the strength and phase of TIWs (Allen et al. (1995);Lawrence et al. (1998);Lawrence and Angell (2000);Benestad et al. (2001); Angell et al. (1998)). The seminal global modeling studies of Harrison and Giese (1988) and Giese and Harrison (1991) have demonstrated that kelvin waves triggered by westerly wind events can alter TIWs features by modifying the horizontal shear in the equatorial current field throughout their eastward equatorial propagation. Holmes and Thomas (2016)(HT16 hereafter) used a high-resolution regional oceanic model to further illustrate that the passage of a single idealized IEKW can modify the background zonal currents, barotropic energy conversion rate and consequently TIWs activity. In particular, they highlighted an asymmetric response of TIWs to different phases of IEKWs, characterized by a decrease (increase) of the TIWs-induced eddy kinetic energy (EKE) during the passage of a downwelling (upwelling) IEKW.

However, most of these studies have been conducted using idealized models or observations over limited time periods. Therefore, due to the chaotic nature of TIWs, it remains to be demonstrated that these interactions between the two types of waves occur consistently. In this chapter, we take advantage of nearly 30 years of altimetric data and the methodological framework described in the previous chapter, in particular a CEOF analysis and sea level decomposition into meridional modes, to document conjointly both TIWs and IEKWs as well as their potential interaction. This chapter corresponds to the content of the article "On the Relationship Between Tropical Instability Waves and Intraseasonal Equatorial Kelvin Waves in the Pacific From Satellite Observations (1993–2018)" published in "Frontiers in Marine Science" `https://doi.org/10.3389/fmars.2022.788908`.

3.2 Article published in *Frontiers in Marine Science*

Article edited by: Frédéric Cyr, Northwest Atlantic Fisheries Centre, Fisheries and Oceans Canada, Canada

Article reviewed by: - Ryan Holmes, The University of Sydney, Australia - Tong Lee,

NASA Jet Propulsion Laboratory (JPL), United States

frontiers in Marine Science

ORIGINAL RESEARCH
published: 09 February 2022
doi: 10.3389/fmars.2022.788908

On the Relationship Between Tropical Instability Waves and Intraseasonal Equatorial Kelvin Waves in the Pacific From Satellite Observations (1993–2018)

M. Gabriela Escobar-Franco[1], Julien Boucharel[1,2] and Boris Dewitte[3,4,5]*

[1] Laboratoire d'Études en Géophysique et Océanographie Spatiales, Université de Toulouse III, CNRS, Toulouse, France, [2] Department of Atmospheric Sciences, University of Hawai'i at Mānoa, Honolulu, HI, United States, [3] CECI, Université de Toulouse III, CERFACS/CNRS, Toulouse, France, [4] Centro de Estudios Avanzados en Zonas Áridas (CEAZA), Coquimbo, Chile, [5] Departamento de Biología Marina, Facultad de Ciencias del Mar, Universidad Católica del Norte, Coquimbo, Chile

OPEN ACCESS

Edited by:
Frédéric Cyr, Northwest Atlantic Fisheries Centre, Fisheries and Oceans Canada, Canada

Reviewed by:
Ryan Holmes, The University of Sydney, Australia
Tong Lee, NASA Jet Propulsion Laboratory (JPL), United States

***Correspondence:**
M. Gabriela Escobar-Franco
maria.gabriela.escobar.franco@legos.obs-mip.fr

Specialty section:
This article was submitted to Physical Oceanography, a section of the journal Frontiers in Marine Science

Received: *03 October 2021*
Accepted: *18 January 2022*
Published: *09 February 2022*

Citation:
Escobar-Franco MG, Boucharel J and Dewitte B (2022) On the Relationship Between Tropical Instability Waves and Intraseasonal Equatorial Kelvin Waves in the Pacific From Satellite Observations (1993–2018). Front. Mar. Sci. 9:788908. doi: 10.3389/fmars.2022.788908

Intraseasonal Kelvin waves (IKWs) and Tropical Instability Waves (TIWs) are essential components of the tropical Pacific coupled climate variability. While downwelling IKWs are precursors of ENSO (e.g., the El Niño Southern Oscillation), TIWs contribute to its asymmetry by mixing more/less warm off-equatorial and cold tongue waters during La Niña/El Niño. Theoretical studies and a few observational case studies also suggest that TIWs and IKWs can interact non-linearly. However, owing to the chaotic nature of TIWs, observational evidence that such a process occurs consistently has not been established thus far. Here, we document for the first time their interaction from satellite observations over a period spanning almost 30 years (1993–2018). From complex empirical orthogonal functions analysis and sea level decomposition into meridional modes, we evidence that a substantial share (∼42%) of the variance of TIWs-induced intraseasonal sea level anomalies are associated with IKWs activity. We show that non-linear dynamical heating (NDH) in the Eastern equatorial Pacific associated with this intraseasonal mode can be as large as that for interannual time scales. Implications for understanding the eastern tropical Pacific heat budget and ENSO variability are discussed.

Keywords: tropical instability waves, non-linear interaction, satellite observations, intraseasonal kelvin waves, non-linear dynamical heating, equatorial pacific

INTRODUCTION

Tropical instability waves (TIWs) are unique westward-moving cusp-shaped mesoscale features first observed via infrared satellite systems by Legeckis (1977) in particular along the strong meridional Sea Surface Temperature (SST) gradient in the eastern equatorial Pacific. Thereafter, TIWs signature has also been observed in many other ocean-surface variables such as sea surface height (Lawrence and Angell, 2000; Benestad et al., 2001; Polito et al., 2001; Lyman et al., 2005; Shinoda et al., 2009), meridional and zonal velocity (Qiao and Weisberg, 1995; Flament et al., 1996; Inoue et al., 2012), salinity (Lee et al., 2012), ocean color (Yoder et al., 1994; Strutton et al., 2001;

Legeckis et al., 2004; Evans et al., 2009), subsurface temperature (Flament et al., 1996; McPhaden, 1996; Kennan and Flament, 2000) and even atmospheric variables such as low-level wind and wind stress (Xie et al., 1998; Chelton et al., 2001; Hashizume et al., 2001).

This dominant form of eddy variability in the near equatorial region can modulate many aspects of the basin-scale equatorial circulation. For instance, TIWs-induced upwelling has been suggested to fertilize the central equatorial region (Yoder et al., 1994; Strutton et al., 2001; Menkes, 2002), which is related to the vigorous turbulent mixing and associated vertical heat flux they produce at their leading edges (Dutrieux et al., 2008; Lien et al., 2008; Moum et al., 2009; Inoue et al., 2012; Holmes and Thomas, 2015; Liu et al., 2016; Warner et al., 2018). TIWs are also thought to modulate the mixed-layer heat budget at seasonal to interannual time scales (Jochum and Murtugudde, 2006; Menkes et al., 2006), potentially affecting longer time scales of variability through the modulation of air–sea interactions at basin-scale. In particular, the enhanced meridional heat transport associated with TIWs during La Niña; compared to El Niño has been shown to contribute to the El Niño–Southern Oscillation (ENSO) asymmetry characterized by larger-amplitude El Niño than La Niña events (An, 2008; Imada and Kimoto, 2012; Boucharel and Jin, 2020; Xue et al., 2020, 2021), which can in turn feedback onto the Pacific decadal variability (Rodgers et al., 2004; Yeh and Kirtman, 2004, 2005; Choi et al., 2009, 2011, 2013; Ogata et al., 2013; Capotondi et al., 2020; Zhao et al., 2021). TIWs have also been suggested to modulate the subthermocline circulation by radiating internal waves downward (Jing et al., 2014; Holmes and Thomas, 2016; Tanaka and Hibiya, 2019; Delpech et al., 2020), which also represents a pathway by which TIWs could influence long-term climate variability. Despite their likely importance on the global climate, TIWs are still not simulated to the full extent of their observed characteristics in IPCC (Intergovernmental Panel on Climate Change)-like models, mostly due to their too coarse horizontal resolution. Most studies have thus focused on how mean state change can modulate TIWs activities from high-to-medium resolution simulations of ocean general circulation models (Pezzi, 2003; Zhang, 2014).

As they are generated in part by barotropic energy conversion associated with the large meridional shears between the North Equatorial Counter Current (NECC) and South Equatorial Current (Philander, 1978; Cox, 1980; Imada and Kimoto, 2012) and between the Equatorial Undercurrent (EUC) and South Equatorial Current (SEC) (Luther and Johnson, 1990; Lyman et al., 2007), TIWs activity depends on the state of these equatorial currents and the associated thermocline structure. Such large-scale equatorial circulation features are modulated among others by planetary equatorial waves. For instance, during a La Niña event, the equatorial upwelling Kelvin waves tend to sharpen/uplift the central equatorial thermocline and intensify the EUC (Izumo et al., 2002; Izumo, 2005; Roundy and Kiladis, 2006; Rydbeck et al., 2019) which favors the growth of an unstable linear mode associated with the coupling of two Rossby waves, that are trapped along the latitudinal bands of ∼1–3°N and ∼3–8°N, respectively (Tanaka and Hibiya, 2019). TIWs can thus be seen in part as the result of these two Rossby waves interacting with off-equatorial currents with a westward propagation and growth rate of TIWs (Lawrence et al., 1998; Tanaka and Hibiya, 2019). On the other hand, during the peak phase of strong El Niño events, reflected downwelling equatorial Rossby waves at the eastern boundary can reduce the NECC (Hsin and Qiu, 2012; Zhao et al., 2013; Webb et al., 2020), which can modulate barotropic instabilities associated with the meridional shear between the SEC and NECC and therefore TIWs activity. It is then clear that TIWs and long-wave length equatorial waves (in particular Kelvin waves, hereafter KWs) can interact non-linearly (Allen et al., 1995). Harrison and Giese (1988) and Giese and Harrison (1991) evidenced changes in TIWs amplitude in a numerical model as a response to the presence of KWs. The theoretical and modeling study by Holmes and Thomas (2016) (hereafter HT16) further confirmed their seminal work and showed that the passage of a single intraseasonal KWs (IKWs) can disrupt the background zonal currents and therefore the TIWs kinetic energy balance through lateral shear production. This in particular leads to a decay (increase) of TIWs kinetic energy during the downwelling (upwelling) IKWs phase. Such an interaction has also been suggested from observations, although limited to the period from August to December 1990 by Qiao and Weisberg (1998). They observed that the end of the TIWs season coincided with the arrival of strong IKWs from the western Pacific. They suggested that the passage of the IKWs decreased the meridional shear of background zonal currents, which resulted in the decay of TIWs strength.

In most studies, it is usually implicitly considered that the frequency of the KWs that influences TIWs is smaller than that of TIWs, since the KWs-induced changes in the circulation is assumed to set the background conditions that trigger the barotropic instability growth. However, because of their relative smaller frequencies (around (1/60) days^{-1}), IKWs are characterized by smaller wavelength than their interannual counterparts, and thus tend to dissipate faster at the surface due to vertical propagation of their energy along trajectories having steep downward slope (Mosquera-Vásquez et al., 2014). This results in a much weaker impact of IKWs on the basin-scale mean temperature/stratification/currents compared to interannual Kelvin waves. Due to the clearer signature of interannual Kelvin waves on surface properties, most observational and modeling studies have thus focused on changes in TIWs activity associated with the peak ENSO phase that takes place in boreal winter (Qiao and Weisberg, 1998; Zhang and Busalacchi, 2008; Evans et al., 2009; Boucharel and Jin, 2020) and in particular their intensification during La Niña events (Yu and Liu, 2003; see also **Figure 1** of An, 2008). However, most of the variance in TIWs activity cannot be explained by ENSO. For instance, the regression of the SST-based TIWs index of An (2008), which is the monthly variability of daily SST (i.e., standard deviation for each month) at the location (2.625°N, 140.125°W), onto the two independent ENSO indices representing the two flavors of El Niño defined by Takahashi et al. (2011) yields an approximated TIWs index that only accounts for ∼22% of the interannual variance of the original index over the period 1982–2018 (May–April average, see **Supplementary Figure 1**). In fact, the relationship between TIWs and ENSO has been emphasized

due to the enhancement of TIWs activity prior to the peak phase of strong La Niña event, and because IKWs activity has a peak climatological variance in boreal winter (Mosquera-Vásquez et al., 2014), similar to that of TIWs variance (Qiao and Weisberg, 1998; Zhang and Busalacchi, 2008; Evans et al., 2009; Boucharel and Jin, 2020).

Even though IKWs activity also tends to peak during the onset of El Niño events, in particular during strong Eastern Pacific El Niño events (McPhaden and Yu, 1999; Gushchina and Dewitte, 2012), it is still unclear whether IKWs could also modulate TIWs activity independently of whether or not an El Niño event occurs. In particular, IKWs can reflect as Rossby waves on the density front near 120°W (Mosquera-Vásquez et al., 2014) and trigger coupled Rossby-TIWs (Tanaka and Hibiya, 2019) without invoking changes in background circulation. This represents a strong incentive to investigate a potential consistent IKWs-TIWs interaction. Here, as a preliminary step toward understanding the mechanisms of this interaction at intraseasonal time scales, we analyze almost 30 years of altimetric data to document conjointly both types of waves and their interaction.

Our approach goes beyond the traditional one in that, rather than relating the envelope of TIWs activity to a particular change in the circulation due to an equatorial wave, we attempt to relate specific TIWs and IKWs events. We suggest in particular the existence of a statistically significant mode that couples IKWs and TIWs despite their differences in zonal wavelength and direction of group velocity. The paper is structured as follows: section "Data Sets and Methods" provides an overview of the dataset and methodology. Section "Results" is devoted to the analysis of results of the Complex Empirical Orthogonal Functions (CEOF) and meridional mode decompositions of sea level anomalies, and to the investigation of the forcing mechanism of the IKWs-TIWs coupled mode. In Section " Meridional Eddy Heat Flux Associated With the Intraseasonal Kelvin Waves-Tropical Instability Waves Mode and Implications for the Eastern Equatorial Pacific Heat Budget", we estimate the contribution of this mode to the non-linear advection in the Eastern Pacific and compare it to the one associated with ENSO time scales. Conclusions are presented in section "Conclusion."

DATA SETS AND METHODS

Satellite Data

To characterize the oceanic circulation associated with TIWs and IKWs, we use the daily sea level (SLA) and geostrophic currents (U,V) anomalies from the multi-satellite Data Unification and Altimeter Combination System datasets available through the Copernicus Marine Environment Monitoring Service (CMEMS) and the Copernicus Climate Change Service (C3S) (Taburet et al., 2019) at a spatial resolution of 0.25°× 0.25° over the region (10°S–10°N, 130°E–80°W) and the period 1993–2018.

To document the IKWs atmospheric forcing, we calculated the zonal wind stress (τ_x) considering the drag coefficient formulation of Trenberth et al. (1989) from the 10-m zonal winds from the Fifth Generation ECMWF Atmospheric Reanalysis of the Global Climate (ERA5) (Hersbach et al., 2018) at a 0.25°× 0.25° horizontal resolution over the same region and period than the sea level. Finally, to estimate the meridional oceanic advection associated with the TIWs-IKWs interaction mode, we use the daily sea surface temperatures (SST) from the NOAA 1/4° daily Optimum Interpolation Sea Surface Temperature version 2.1 product (Huang et al., 2020) at a 0.25°× 0.25° resolution over the same period and domain. All data were first linearly detrended. Then, we define the intraseasonal anomalies for all variables as the departure of the instantaneous daily data from the monthly mean following the method by Lin et al. (2000), which is somewhat equivalent to applying a high-pass Lanczos filter with a frequency cut-off at (1/90) days-1 (cf. Dewitte et al., 2011).

Complex Empirical Orthogonal Functions Analyses

Complex Empirical Orthogonal Functions (CEOF) are an efficient tool to disentangle the spatiotemporal characteristics of the intraseasonal variability related to TIWs and KWs as this analysis provides both amplitude and phase information, and is therefore well-suited to capture propagating features (Barnett, 1983; Stein et al., 2011; Boucharel et al., 2013, 2016).

Tropical Instability Waves Amplitude and Indices

To analyze the TIWs characteristics, we use the definition of the TIWs amplitude and index from Boucharel and Jin (2020). We take a simple equally spaced and weighted nodes (positive and negative SLA anomalies) index TIW_1. As stated in Boucharel and Jin (2020), the number of nodes and their longitudinal location within the (0°–6°N) band can be chosen arbitrarily. In this study, we chose 6 (SLA) nodes within the (3°N–7°N and 165°–107°W) band that essentially fit the TIWs cusps from the related CEOF mode's spatial pattern (see section "Satellite Data").

$$TIW_1\,(t) = \sum \pm SLA\,(t, nodes)$$

Where SLA refers to the sea level intraseasonal anomalies. Then, to grasp the TIWs propagation, we define TIW_2 similarly to TIW_1 except the nodes are now shifted by 90 degrees representing half the TIWs wavelength.

$$TIW_2\,(t) = \sum \pm SLA\,(t, nodes + 90°\,degrees\ zonal\ shift\ phase)$$

$$TIWindex\,(t) = TIW_1 + iTIW_2$$

$$TIWamp\,(t) = \sqrt{TIW_1^2 + TIW_2^2}$$

In this paper, we apply this methodology to derive the TIWs activity from the sea level.

Intraseasonal Kelvin Waves Meridional Mode Decomposition

To infer the IKWs contribution to sea level anomalies and interpret the results from the CEOF decomposition, we project the SLA and zonal wind stress anomalies onto the

Kelvin/Rossby meridional wave structures in the long wavelength approximation (see Cane and Sarachik, 1976). We assume like in former studies based on satellite sea level (Boulanger and Menkes, 1995; Perigaud and Dewitte, 1996) that the oceanic vertical structure along the equator can be accounted for by just the first baroclinic mode, so that, total sea level (h) and zonal current (u) anomalies can be expressed as a linear combination of meridional mode functions accounting for Kelvin and Rossby waves. This writes as follows:

$$\begin{pmatrix} u \\ h \end{pmatrix} = r_0\,(x,t) \begin{pmatrix} R_0^u\,(y) \\ R_0^h\,(y) \end{pmatrix} + \sum_{n\geq 1} r_n\,(x,t) \begin{pmatrix} R_n^u\,(y) \\ R_n^h\,(y) \end{pmatrix}$$

$$r_n = \mathrm{u}R_n = \int_{Y_N}^{Y_S} \left(uR_n^u + hR_n^h \right) dy$$

Where $R_0^u\,(y)$, $R_0^h\,(y)$ and $R_n^u\,(y)$, $R_n^h\,(y)$ are the normalized Kelvin and the n-th normalized Rossby waves meridional structures, n denotes the meridional modes being 0 for Kelvin waves and $\geq$ 1 for the Rossby modes. The r_n are the corresponding wave coefficients calculated at each grid point along the equator. The projection of sea level and zonal current anomalies onto the meridional modes is performed between the northern Y_N and southern limits Y_S (10°N–10°S in this study). This latitudinal range allows capturing the poleward exponential decrease of Kelvin and Rossby waves and ensuring an approximate orthogonality property between meridional modes.

$$\begin{pmatrix} R_0^u\,(y) \\ R_0^h\,(y) \end{pmatrix} = \begin{pmatrix} \frac{\psi_0^u(y)}{\sqrt{2}} \\ \frac{\psi_0^h(y)}{\sqrt{2}} \end{pmatrix};$$

$$\begin{pmatrix} R_n^u\,(y) \\ R_n^h\,(y) \end{pmatrix} = \sqrt{\frac{n\,(n+1)}{2\,(2n+1)}} \begin{pmatrix} \frac{\psi_{n+1}(y)}{\sqrt{n+1}} - \frac{\psi_{n-1}(y)}{\sqrt{n}} \\ \frac{\psi_{n+1}(y)}{\sqrt{n+1}} + \frac{\psi_{n-1}(y)}{\sqrt{n}} \end{pmatrix}$$

Where the ψ_n(y) are the Hermite functions, calculated using a value for phase speed that varies zonally. Its value is set to 3 m/s at 170°W, which corresponds to an average value used in the literature for the first baroclinic mode (Picaut and Sombardier, 1993; Dewitte et al., 1999). We then approximate C(x) as $C\,(x) = C\,(x = 170°\,W)\sqrt{\frac{\overline{Z_{eq}}}{\overline{Z_{170°\,W}}}}$ where Zeq is the mean depth of the 20°C isotherm at 170°W and between 2°S and 2°N. Zeq was derived from the global ocean data assimilation system (GODAS, Behringer and Xue, 2004) using the 20°C isotherm depth as a proxy and for the period 1980–2018. The total SLA as well as the SLA reconstructed from the individual CEOF modes are, unless stated otherwise, projected onto the meridional modes functions using the method by Boulanger and Menkes (1995) (see their Appendix B), which does not require the knowledge of zonal current anomalies and is comparable to assuming that Rossby wave coefficients are negligible from a certain rank (see also Perigaud and Dewitte, 1996).

The zonal wind stress is also projected onto the theoretical meridional mode structures of the first baroclinic mode, and its contribution to the Kelvin wave is inferred from the following formula: $\tau_x\,(x,y,t) = Fo\,(x,t)\,R_n\,(y)$, and

$$Fo\,(x,t) = \int_{Y_N}^{Y_S} \tau_x\,(x,y,t)\,R_0^u\,(x,y)\,dy$$

Where h, u and τ_x come from observations described in section" Satellite Data."

RESULTS

Complex Empirical Orthogonal Functions Analysis of Sea Level Anomalies

Results from the CEOF decomposition of the sea level intraseasonal anomalies are presented in **Figure 1**. The first two modes grasp 21% of the explained variance of the total sea level anomalies over the spatial domain shown in **Figure 1**, almost equally distributed. Since higher-order modes explain individually less than 5.4% of the variance, in the following we focused on the first two modes only. The first mode (CEOF1), characterized by a strong amplitude between 3–7°N and 120–165°W (**Figure 1A**), mostly captures the variability associated with TIWs (with an explained variance of 11%) although a relative maximum amplitude is also observed along the equator reminiscent of IKWs contribution to sea level anomalies. The real part of the spatial CEOF pattern (**Supplementary Figure 2A**) exhibits TIWs cusps similarly positioned as in Xue et al. (2020). The decreasing phase from east to west in this region shown on the CEOF spatial phase pattern (**Supplementary Figure 3A**) characterizes the TIWs westward propagation. The second mode (CEOF2), which explains a similar amount of variance, exhibits a comparable phase (**Supplementary Figure 3B**) and amplitude pattern although the amplitude along the equator is about twice as large as that of the first mode while the amplitude of the TIWs cups is smaller. Note also the exact same location of the TIWs cups but with opposite value of amplitude of the real part between CEOF1 and CEOF2 (**Supplementary Figure 2**), which results from the orthogonality of the two modes's patterns and suggests that they capture the same sequence of TIWs propagations. Their summed-up contribution explains 42% of the variance of the total sea level anomalies over the region (2°S–2°N, 170–120°W). The summed-up contribution from CEOF1 and CEOF2 over the TIWs active region (3–7°N and 165–107°W) was also found to be highly correlated with both TIWs index and TIWs amplitude from Boucharel and Jin (2020) (r = 0.5 and 0.7 respectively, not shown) which all together indicates that CEOF1 + 2 capture most of TIWs variability. In the equatorial band, the zonally elongated pattern symmetrical around the equator, more pronounced for CEOF2 than for CEOF1, is indicative of the IKWs activity and suggests that the two modes capture the non-linear interaction between IKWs and TIWs. The phase patterns of the two modes along the equator (**Supplementary Figure 3**) confirm the eastward propagation at a phase speed estimated to 2.6 m/s consistent with former studies based on altimetry data (Cravatte et al., 2003; Dewitte et al., 2003). Their projections onto the Kelvin wave structure indicate that CEOF2 explains 24% of the

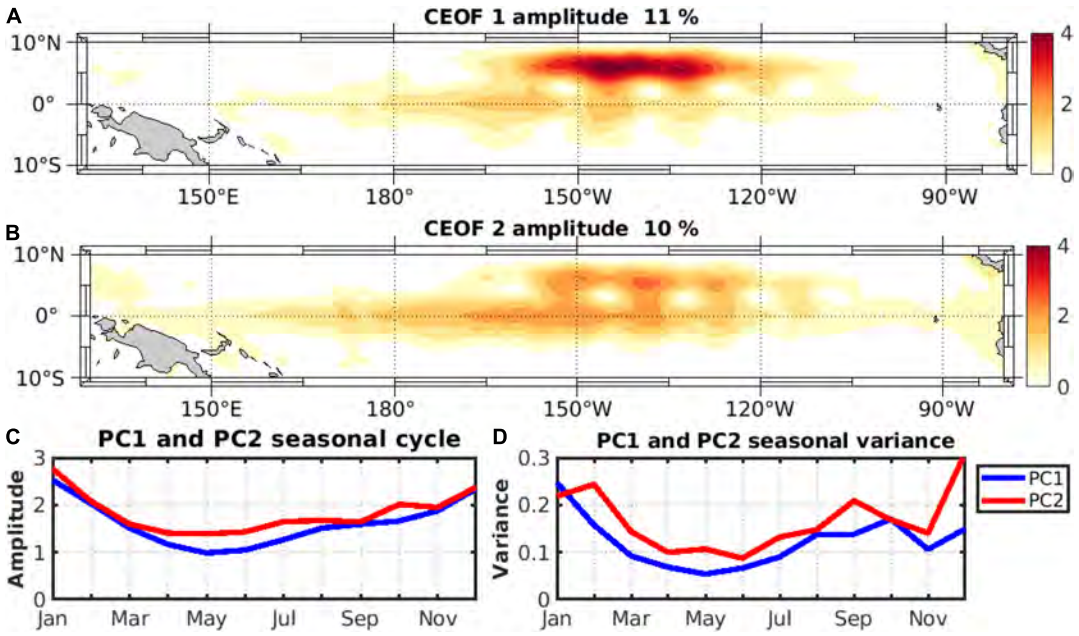

FIGURE 1 | Decomposition into Complex Empirical Orthogonal functions (CEOF) of intraseasonal sea level anomalies (over the period 1993–2018). Spatial patterns of the amplitude of the first CEOF1 **(A)** and second CEOF2 **(B)** mode. **(C)** Seasonal cycle of each mode's corresponding Principal Component (PC) amplitude, **(D)** seasonal cycle of each PC amplitude's monthly variance (PC1 in blue and PC2 in red).

variance of the Kelvin wave contribution to the full sea level anomalies average over (2°S–2°N, 170–120°W) while CEOF1 only explains 12.9% (see **Table 1**). The maximum correlation between sea level anomalies reconstructed from CEOF1 and CEOF2 is reached (r = 0.3 between 2°S–2°N and 170–120°W) at a positive lag of 14 days [Principal Component (PC) 1 lags PC2], corresponding to about a quarter of the main period of IKWs, which confirms that the two modes capture the same sequences of IKWs. In order to diagnose the seasonality of the PC timeseries, their climatology and climatological variance are shown in **Figures 1C,D**, respectively, which indicates they both have a peak amplitude during the boreal summer and fall, consistent with the expectation that they grasp the same seasonally synchronized interaction mode between IKWs and TIWs. Lastly, the correlation between the 3-month running variance of PC1 and PC2 reaches 0.84 which confirms that the two modes grasp the same physical mode of interaction between IKWs and TIWs.

TABLE 1 | Explained variance (%) of SLA and TIWs amplitude explained by the SLA reconstructed from CEOF 1, CEOF2 and CEOF1 + 2.

SLA reconstructed from	TIWs amplitude	TIWs amplitude without the La Niña events	SLA	SLA averaged without the La Niña events
CEOF 1	21.7%	20.1%	12.9%	3.0%
CEOF 2	27.2%	27.9%	24.0%	15.0%
CEOF 1 + 2	31.6%	33.1%	42.0%	26.0%

This table shows the explained variance of the sea level reconstructed from CEOF 1, CEOF 2 and CEOF 1 + 2 and averaged at the equator (2°S–2°N, 170–120°W) and the TIWs amplitude derived from the TIWs index calculated using sea level anomaly and following the methodology by Boucharel and Jin (2020). The explained variance is also compared without La Niña periods defined as the period when the C index is less than −0.5°C.

Composite Analysis

In order to document further the relationship between IKWs and TIWs, we perform a lead-lag composite analysis of strong events identified from the SLA timeseries reconstructed from CEOF2 and averaged in the equatorial region (2°S–2°N, 180–80°W). This choice is motivated by the fact that (i) CEOF2 grasps twice as much variance along the equator (see **Table 1**) and therefore can be interpreted as the portion of TIWs variability that relates to IKWs, and (ii) PC2 leads PC1 slightly (by ∼15 days). 25 downwelling and 28 upwelling events are identified for which the equatorial SLA reconstructed from CEOF2 is above or below 2 standard deviations, respectively (**Figure 2A**). **Figure 2** shows the composite evolution of the dominant EOF mode of equatorial zonal wind stress intraseasonal anomalies in the equatorial band (**Figure 2B**, see also its spatial pattern and temporal evolution in **Supplementary Figures 4**, **5** respectively), the equatorial Kelvin wave contribution to sea level anomalies, and the reconstructed sea level anomalies from CEOF2 (**Figures 2C**). In particular, **Figure 2B,C** indicate that the positive equatorial SLA events in the central Pacific characterize strong downwelling IKWs triggered by westerly wind bursts that occurred on average ∼10 days prior in the Western Pacific. These westerly wind anomalies spread toward the central-western Pacific and maintain the eastward propagation of IKWs, which take approximately 30 days to cross the entire basin, consistently with the IKWs phase speed. Similar composite patterns but with a

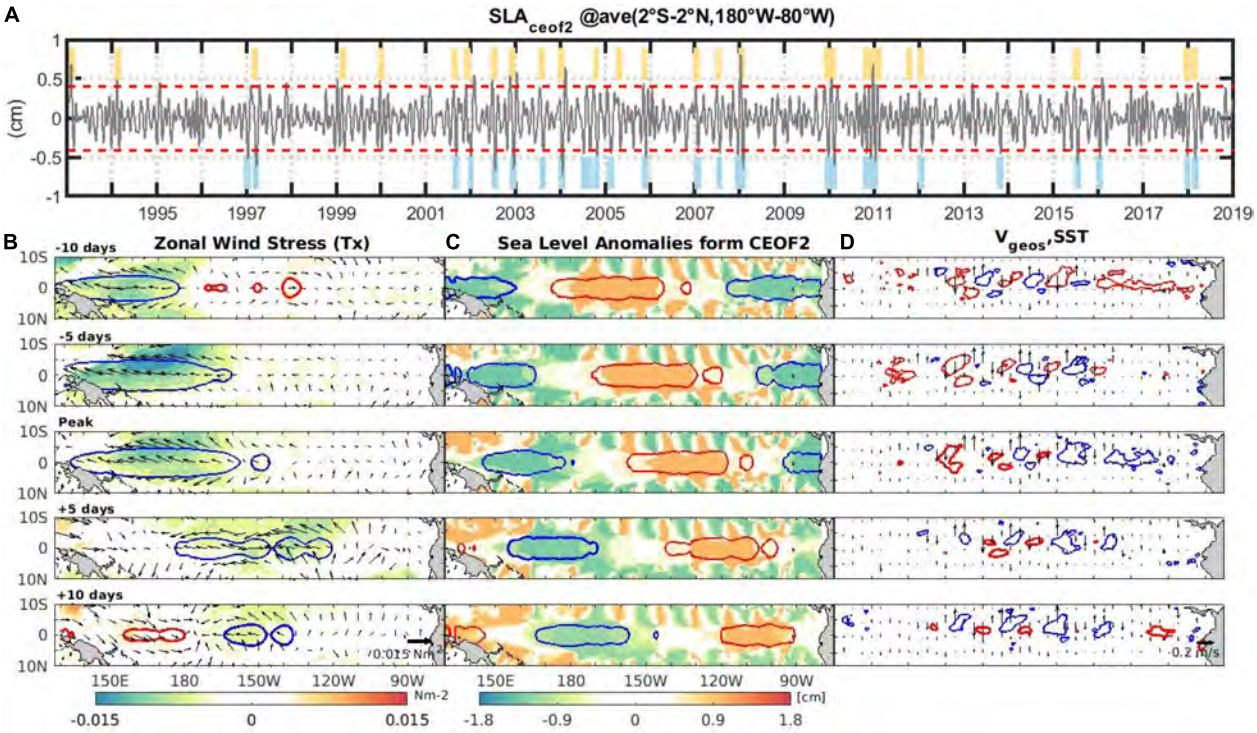

FIGURE 2 | (A) SLA reconstructed from CEOF2 and averaged in the region (2°S–2°N, 180°W–80°W). SLA events above (below) 2 standard deviations are highlighted in yellow (blue). (**B**, left panels) Composites of the corresponding intraseasonal wind stress anomalies (in Nm^{-2}) reconstructed from the first EOF mode at different leads/lags (centered, i.e., lag 0, at the SLA peak from **A**). The colored contours represent the intraseasonal zonal wind stress anomalies projected onto the theoretical Kelvin wave meridional structure; blue (red) contours correspond to -0.002 Nm^{-2} (+ 0.002 Nm^{-2}). (**C**, middle panels) Composites (shading in cm) of SLA reconstructed from CEOF2 at different leads/lags (in days) indicated on the top left of the leftmost panels and centered (i.e., lag 0) during the strong positive intraseasonal equatorial sea level anomalies events identified in **(A)** (i.e., the IKWs downwelling phases). The colored contours represent the intraseasonal SLA projected onto the theoretical Kelvin wave meridional structure; blue (red) contours are for values of -0.5 (+ 0.5) cm. (**D**, right panels) Composites of meridional geostrophic velocity anomalies (arrows), and SST anomalies [red (blue) contours corresponds to 0.2 (-0.2)°C].

reverse sign are observed during upwelling events sparked by easterly wind bursts (**Supplementary Figure 6**). Interestingly, most of the events used to conduct this lag-composite analysis can also be found in the upwelling IKWs either preceding or following the composite downwelling IKWs presented in **Figure 2**. This means that the basin scale CEOF analysis, which inherently encompasses most IKWs propagation features into a single mode does not allow disentangling quantitatively the IKWs phases but rather represents the succession of upwelling and downwelling pulses as an integrated pattern of IKWs variability. This is why we observe active TIWs in the northeastern tropical Pacific throughout the entire IKWs propagation cycle across the basin (**Figure 2C** and **Supplementary Figure 6B**). Their presence in the eastern Pacific, whereas the IKWs has yet to reach the area, has likely been triggered by the preceding IKWs (∼60 days prior).

Although the CEOF analysis is not designed to grasp asymmetry in the variability, still, we can observe that the amplitude of the CEOF2 SLA as well as the SST and meridional geostrophic velocity anomalies composite (superimposed on **Figure 2D** and **Supplementary Figure 6C**) in the region of TIWs activity is larger during the upwelling than the downwelling IKWs propagation cycle. In order to further quantify such asymmetrical response in TIWs amplitude to the IKWs phase, we present in **Figure 3**, a bar plot between total SLA averaged in the equatorial region (2°S–2°N, 150–80°W) and TIWs amplitude calculated from SLA using Boucharel and Jin's (2020) method for the strong upwelling and downwelling events identified previously. **Figure 3** indicates that upwelling IKWs tend to promote a larger TIWs amplitude than downwelling IKWs by ∼15%. Note that this is significant at the ∼90% level based on a Student's *t*-test. This is consistent with the theoretical and modeling study by HT16 who also evidenced an asymmetry in the amplitude of the TIWs activity between the passage of upwelling and downwelling IKWs, although in their case the TIWs response is somewhat stronger (in their experiments, the TIWs kinetic energy is decreased (increased) by 38% (42%) for downwelling (upwelling) IKWs compared to the background control). In addition, in their idealized setting, HT16 estimated a ∼60 days lagged TIWs response to the passage of IKWs, while we find a faster response (∼10–15 days). These differences can be attributed to the distinct methodological approaches between the two studies. In particular, while we diagnose the lag in SLA amplitude between the equatorial

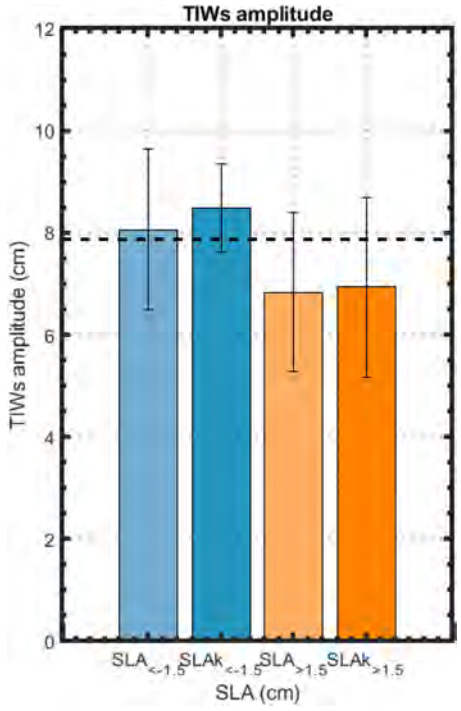

FIGURE 3 | Mean TIWs amplitude (calculated using the method described in Boucharel and Jin, 2020, applied on SLA reconstructed from CEOF1 + 2) during upwelling (blue) and downwelling (orange) events. Upwelling (Downwelling) events correspond to events identified in **Figure 2A** restricted to when the total sea level anomalies averaged in the region (2°S–2°N, 150–80°W) are below −1.5 cm (above +1.5 cm). Similarly, the dark blue and orange bars represent the average TIWs amplitude for upwelling (downwelling) events when the total sea level anomalies projected on the Kelvin wave mode (SLAk) are below −1.5 cm (above +1.5 cm). The error bars represent ± 1 standard deviation of TIWs amplitude amongst the retained events. The dashed black horizontal line indicates the annual mean of TIWs amplitude calculated from the method by Boucharel and Jin (2020) applied on the total sea level.

and TIWs regions, HT16 use the rate of volume averaged TIWs kinetic energy, which has a longer time scale adjustment due to its quadratic formulation and may encompass the contribution of high-order baroclinic modes due to the depth integration. In addition, unlike in HT16's idealized settings, the different Kelvin waves phases are not well differentiated in our CEOF observational analysis as most of the time they form a sequence a 2–3 pulses of waves (i.e., wave trains). So, it is expected that the lagged relationship between TIWs and IKWs in the data differs from that in their modeling study, because of the cumulative effect of consecutive IKWs on TIWs activity.

The composite patterns of sea level, SST and meridional geostrophic velocity anomalies at the peak of the passing IKWs (**Figure 4**) in the region of TIWs activity not only confirms the somewhat asymmetrical response in the TIWs amplitude but also showcase an in-phase signal between temperature and meridional currents anomalies likely leading to a TIWs-induced meridional heat flux convergence (Xue et al., 2020). This now raises the question of the contribution of these coupled IKWs-TIWs individual events to the Cold Tongue heat budget and in particular, to which extent they compare to the strong TIWs-induced non-linear dynamical heating evidenced at seasonal and interannual time scales in previous studies (e.g., Wang and McPhaden, 1999; Menkes et al., 2006; An, 2008; Xue et al., 2020, 2021).

Meridional Eddy Heat Flux Associated With the Intraseasonal Kelvin Waves-Tropical Instability Waves Mode and Implications for the Eastern Equatorial Pacific Heat Budget

While most focus has been drawn to TIWs-induced heat flux convergence associated with interannual fluctuations in the background state (i.e., ENSO) in earlier studies, our results call for the evaluation the TIWs-induced non-linear dynamical heating (NDH) at intraseasonal time scales. The seasonally varying TIWs has been shown to warm the equatorial cold tongue through meridional heat advection (Wang and McPhaden, 1999). Similarly, many studies have highlighted the TIWs effect at interannual time scales as a potential source for ENSO asymmetry (An, 2008; Boucharel and Jin, 2020; Xue et al., 2020, 2021) due to the rectified effect of anomalous temperature transport by anomalous currents referred to as oceanic eddy heat flux (e.g., Baturin and Niiler, 1997; Menkes et al., 2006; Jochum and Murtugudde, 2006; Jochum et al., 2007, 2008; Graham, 2014; Xue et al., 2020). In this section, we estimate the eddy heat flux spatial derivative composite of the specific events that correspond to periods of strong activity of the IKWs-TIWs interaction mode. This allows diagnosing the NDH of the eastern equatorial Pacific triggered by the passage of strong downwelling and upwelling IKWs. The intraseasonal NDH is approximated here by $NDH_{TIWs} = v'\partial yT'$ following Xue et al. (2020).

Figure 5 shows the TIWs-induced intraseasonal meridional NDH composite associated with the upwelling (a) and downwelling (b) phase of the IKWs-TIWs interaction mode. They both exhibit a warming pattern located just north of the equator along with a cooling pattern centered around 4°N indicating a rather similar TIWs-induced entrainment of warm equatorial water into the Cold Tongue region between the two IKWs phases. As an integrated measure of the warming effect of the IKWs-TIWs interaction mode on the eastern equatorial Pacific, we present in **Figure 5C** the intraseasonal NDH longitudinally averaged between 150°W and 110°W (the same region as in Xue et al., 2020). It confirms the rather similar magnitude of NDH_{TIWs} (∼0.8°C/month) during both the downwelling and upwelling IKWs phases, albeit slightly stronger during upwelling events due to the stronger TIWs activity (**Figure 3**). Note however that there is a significant spread (dotted line in **Figure 5C**) amongst the individual events, which reflects a large diversity in the response of NDH_{TIWs} to individual IKWs or IKWs trains. The spread tends to be larger among the upwelling events along the equator (see dashed turquoise thin line in **Figure 5C**). What is also

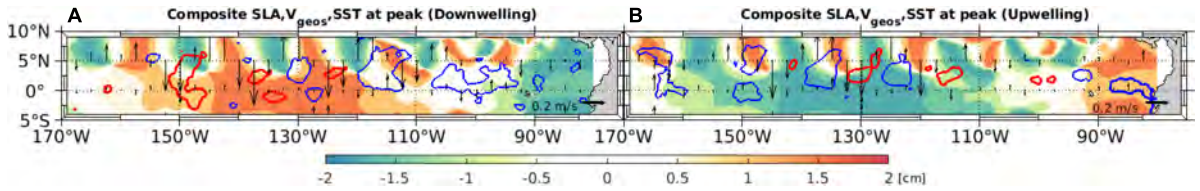

FIGURE 4 | Composites of SLA, meridional geostrophic velocity anomalies (arrows) and SST anomalies [red (blue) contours corresponds to 0.2 (-0.2)°C] at the peak of a strong events in sea level anomalies (i.e., IKW) along the equator (cf. **Figure 2A**) [**(A)** for downwelling, **(B)** for upwelling].

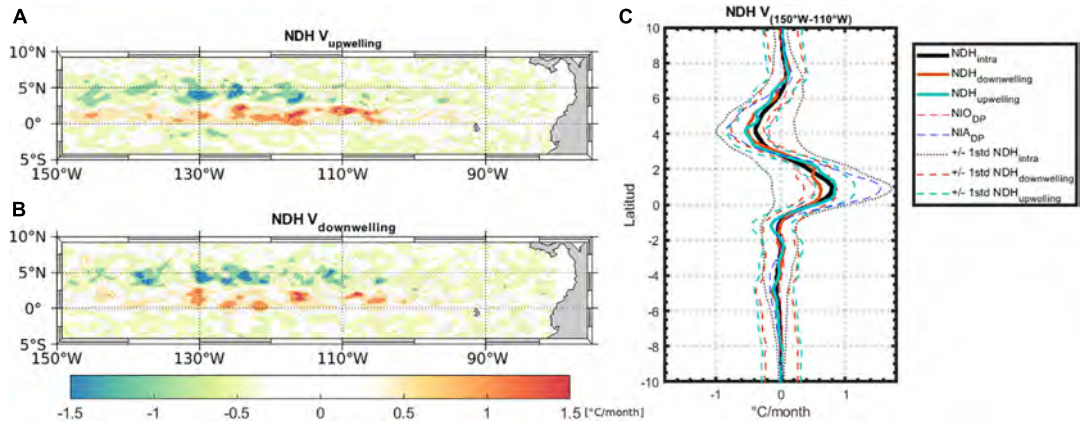

FIGURE 5 | Composites of meridional components of intraseasonal Non-linear Dynamical Heating (NDH) during upwelling **(A)** and downwelling **(B)** IKWs events identified in **Figure 2A**. **(C)** Longitudinal average (between 150 and 110°W) of intraseasonal NDH annual mean (thick black line), IKWs upwelling phases (thick turquoise line), IKWs downwelling phases (thick brown line), interannual El Niño (dashed red line) and La Niña (dashed blue line) developing phase (July–November) NDH composite. The thin black (orange/turquoise) dashed lines indicate ± 1 standard deviation of the total intraseasonal NDH (amongst the downwelling/upwelling events). Units are °C/month.

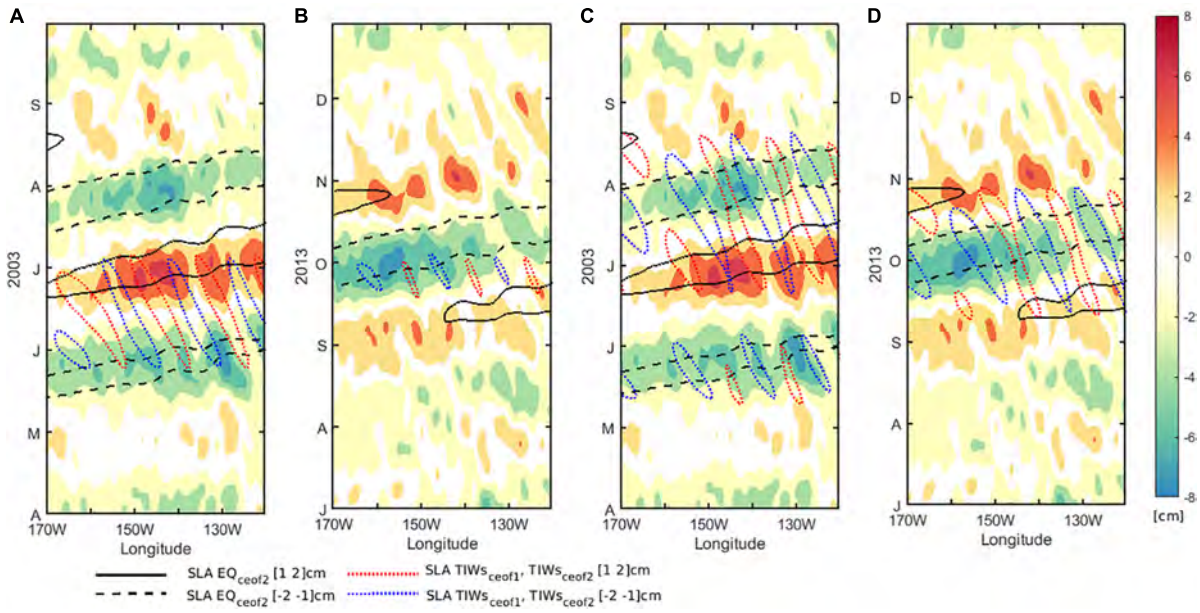

FIGURE 6 | IKWs and TIWs evolution during two periods (**A,C**. April-September 2003 and **B,D**. July–December 2013): Hovmoller of total SLA (color) at the equator (2°S–2°N), SLA reconstructed from CEOF2 projected onto the Kelvin mode (upwelling/downwelling in dashed/continuous black contours, at the equator) and SLA reconstructed from CEOF 1 **(A,B)** and from CEOF2 **(C,D)** in the TIWs region (3°N–7°N) [dashed blue (red) lines for negative (positive) SLA].

noticeable from **Figure 5C** is that NDH_{TIWs} falls within the range of warming induced by the interannual eddy heat flux convergence as indicated by the latitudinal profiles of the El Niño and La Niña meridional NDH composites during their developing phase (i.e., July–November average) over the same period (1993–2018). Note that the latter is mostly induced by the prolonged La Niña event (1998–2001) that followed the strong Eastern Pacific El Niño of 1997/98 (not shown). Although both triggered by TIWs-induced NDH, the Cold Tongue warming presumably originates from different dynamical mechanisms.

CONCLUSION

In this study, we have analyzed 26 years of altimetric data to document the interaction between TIWs and IKWs, observing that TIWs activity is only weakly linearly related to ENSO. Our statistical (complex EOF) analysis evidences a coupling between these equatorial waves contained in the first two dominant modes of the intraseasonal SLA decomposition that explain together 21% of the total variance. In detail, the first mode (11%) tends to dominantly capture the TIWs activity and is correlated to typical TIWs variance indices, while the second mode (10%) leading the first mode by ∼10 days, exhibits a comparable loading in the equatorial and TIWs region, best accounting for the interaction between IKWs and TIWs. The two modes have also similar seasonal modulation with a peak activity in the austral summer like ENSO. However, their interannual modulation is not linearly related to ENSO with in particular a peak activity taking place predominantly during non-El Niño or non-La Niña years (43 and 51% for modes 1 and 2, respectively). This is consistent with the interpretation that the intraseasonal Kelvin wave has the capacity to modulate the background conditions over which TIWs can grow, and that this does not necessarily require variations in mean conditions at low-frequency (e.g., ENSO). HT16 showed in particular that IKWs can disrupt the zonal currents background and thus the TIWs kinetic energy balance through lateral shear production, despite the fact TIWs and IKWs time scales are intertwined, making unclear to which extent individual IKWs can produce changes in background conditions sufficiently fast for this barotropic instability to develop. Our results are thus consistent with the experimental findings of HT16 suggesting that the statistical modes documented in this study could be interpreted as resulting from such a mechanism, although the distinct methodological approaches between the two studies lead to differences in the lagged and asymmetric response of the TIWs amplitude to the passage of different phases of IKWs. However, further investigations based on a regional ocean model are needed to confirm if the mechanism proposed by HT16 applies to observed events accounted for by the statistical modes documented here. Events taking place during "normal" years (i.e., non-ENSO) represent case studies to consider for our future investigation in order to rule out the influence of variability at time scales larger than that associated with episode of IKWs. For instance, the years 2003 and 2013 that correspond to "neutral" years in terms of interannual variability showcase a succession of events that are well accounted for by the statistical modes (**Figure 6**). **Figure 6** indicates in particular that TIWs (accounted for by CEOF1 for the June 2003 event and CEOF2 for the August 2003 and October 2013 events) start growing as an upwelling IKWs propagates across the central Pacific, suggesting that IKWs-induced modification in the circulation is sufficiently "slow" for the instability to grow despite the closeness of peak frequencies between the two waves. It is interesting to note that TIWs activity is increased (reduced) during the passage of upwelling (downwelling) IKWs, even though our analysis makes difficult to isolate the impact of individual IKWs events. Although this TIWs modulation occurs almost instantaneously, this is consistent with the asymmetric TIWs amplitude response to the passage of IKWs found in HT16 (yet with a weaker response). Note that previous studies have identified from observations two distinct modes of TIWs in the eastern equatorial Pacific with periods near 33 and 17 days, and commonly referred to as the Rossby and Yanai modes, respectively (Lyman et al., 2007; Cai et al., 2020). Here the CEOF2 mode has a dominant frequency at ∼(1/57) days-1, suggesting that it may encapsulate the rectified effect of instability processes associated with these Rossby and Yanai modes. This needs further investigation based on the experimentation with a high-resolution ocean model, which is our current plan.

DATA AVAILABILITY STATEMENT

The original contributions presented in the study are included in the article/**Supplementary Material**, further inquiries can be directed to the corresponding author/s.

AUTHOR CONTRIBUTIONS

JB and BD: conceptualization. ME-F: methodology, data curation, and writing—original draft preparation. All authors have discussed the results and contributed to writing the manuscript.

FUNDING

BD acknowledges support from ANID (Concurso de Fortalecimiento al Desarrollo Científico de Centros Regionales 2020-R20F0008-CEAZA, Grant 1190276 and COPAS COASTAL FB210021) and ANR (Grant ANR-18-CE01-0012). JB was funded by the French Agence Nationale de la Recherche project Make Our Planet Great Again (MOPGA) "Trocodyn" (ANR-17-MPGA-0018) and GE was funded by the Région Occitanie.

SUPPLEMENTARY MATERIAL

The Supplementary Material for this article can be found online at: https://www.frontiersin.org/articles/10.3389/fmars.2022.788908/full#supplementary-material

REFERENCES

Allen, M. R., Lawrence, S. P., Murray, M. J., Mutlow, C. T., Stockdale, T. N., Llewellyn-Jones, D. T., et al. (1995). Control of tropical instability waves in the Pacific. *Geophys. Res. Lett.* 22, 2581–2584. doi: 10.1029/95GL02653

An, S.-I. (2008). Interannual Variations of the Tropical Ocean Instability Wave and ENSO. *J. Clim.* 21, 3680–3686. doi: 10.1175/2008JCLI1701.1

Barnett, T. P. (1983). Interaction of the Monsoon and Pacific Trade Wind System at Interannual Time Scales Part I: The Equatorial Zone. *Monthly Weather Rev.* 111, 756–773. doi: 10.1175/1520-04931983111<0756:IOTMAP<2.0.CO;2

Baturin, N. G., and Niiler, P. P. (1997). Effects of instability waves in the mixed layer of the equatorial Pacific. *J. Geophys. Res.* 102, 27771–27793. doi: 10.1029/97JC02455

Behringer, D., and Xue, Y. (2004). "Evaluation of the global ocean data assimilation system at NCEP: The Pacific Ocean," in *AMS 84th Annual Meeting*, (Seattle, WA: AMS), 7.

Benestad, R. E., Sutton, R. T., Allen, M. R., and Anderson, D. L. T. (2001). The influence of subseasonal wind variability on tropical instability waves in the Pacific. *Geophys. Res. Lett.* 28, 2041–2044. doi: 10.1029/2000GL012563

Boucharel, J., and Jin, F.-F. (2020). A simple theory for the modulation of tropical instability waves by ENSO and the annual cycle. *Tellus Dynam. Meteorol. Oceanogr.* 72, 1–14. doi: 10.1080/16000870.2019.1700087

Boucharel, J., Jin, F.-F., England, M. H., Dewitte, B., Lin, I. I., Huang, H.-C., et al. (2016). Influence of Oceanic Intraseasonal Kelvin Waves on Eastern Pacific Hurricane Activity. *J. Clim.* 29, 7941–7955. doi: 10.1175/JCLI-D-16-0112.1

Boucharel, J., Timmermann, A., and Jin, F.-F. (2013). Zonal phase propagation of ENSO sea surface temperature anomalies: Revisited. *Geophys. Res. Lett.* 40, 4048–4053. doi: 10.1002/grl.50685

Boulanger, J.-P., and Menkes, C. (1995). Propagation and reflection of long equatorial waves in the Pacific Ocean during the 1992–1993 El Niño. *J. Geophys. Res.* 100:25041. doi: 10.1029/95JC02956

Cai, W., McPhaden, M. J., Grimm, A., Rodrigues, R. R., Taschetto, A. S. (2020). Climate impacts of the El Niño–Southern Oscillation on South America. *Nat. Rev. Earth Environ.* 1, 215–231. doi: 10.1038/s43017-020-0040-3

Cane, M., and Sarachik, E. (1976). Forced Baroclinic Ocean Motions .1. Linear Equatorial Unbounded Case. *J. Mar. Res.* 34, 629–665.

Capotondi, A., Deser, C., Phillips, A. S., Okumura, Y., and Larson, S. M. (2020). ENSO and Pacific Decadal Variability in the Community Earth System Model Version 2. *J. Adv. Model. Earth Syst.* 12:2019MS002022. doi: 10.1029/2019MS002022

Chelton, D. B., Esbensen, S. K., Schlax, M. G., Thum, N., Freilich, M. et al. (2001). Observations of Coupling between Surface Wind Stress and Sea Surface Temperature in the Eastern Tropical Pacific. *J. Clim.* 14, 1479–1498. doi: 10.1175/1520-04422001014<1479:OOCBSW<2.0.CO;2

Choi, J., An, S.-I., Dewitte, B., and Hsieh, W. W. (2009). Interactive Feedback between the Tropical Pacific Decadal Oscillation and ENSO in a Coupled General Circulation Model. *J. Clim.* 22, 6597–6611. doi: 10.1175/2009JCLI2782.1

Choi, J., An, S.-I., Kug, J.-S., and Yeh, S.-W. (2011). The role of mean state on changes in El Niño's flavor. *Clim. Dyn.* 37, 1205–1215. doi: 10.1007/s00382-010-0912-1

Choi, J., An, S.-I., Yeh, S.-W., and Yu, J.-Y. (2013). ENSO-Like and ENSO-Induced Tropical Paci?c Decadal Variability in CGCMs. *J. Clim.* 26:17.

Cox, M. D. (1980). Generation and Propagation of 30-Day Waves in a Numerical Model of the Pacific. *J. Physical Oceanogr.* 10, 1168–1186. doi: 10.1175/1520-04851980010<1168:GAPODW<2.0.CO;2

Cravatte, S., Eldin, G., and Picaut, J. (2003). Second and first baroclinic Kelvin modes in the equatorial Pacific at intraseasonal timescales. *J. Geophys. Res.* 108, 22–21. doi: 10.1029/2002JC001511

Delpech, A., Cravatte, S., Marin, F., Ménesguen, C., and Morel, Y. (2020). Deep Eddy Kinetic Energy in the Tropical Pacific From Lagrangian Floats. *J. Geophys. Res.* 125:23. doi: 10.1029/2020JC016313

Dewitte, B., Illig, S., Parent, L., duPenhoat, Y., Gourdeau, L., and Verron, J. (2003). Tropical Pacific baroclinic mode contribution and associated long waves for the 1994-1999 period from an assimilation experiment with altimetric data. *J. Geophys. Res.* 108, 3121–3138. doi: 10.1029/2002JC001362

Dewitte, B., Illig, S., Renault, L., Goubanova, K., Takahashi, K., Gushchina, D., et al. (2011). Modes of covariability between sea surface temperature and wind stress intraseasonal anomalies along the coast of Peru from satellite observations (2000–2008). *J. Geophys. Res.* 116:C04028. doi: 10.1029/2010JC006495

Dewitte, B., Reverdin, G., and Maes, C. (1999). Vertical Structure of an OGCM Simulation of the Equatorial Paci?c Ocean in 1985–94. *J. Physical Oceanogr.* 29:29.

Dutrieux, P., Menkes, C. E., Vialard, J., Flament, P., and Blanke, B. (2008). Lagrangian Study of Tropical Instability Vortices in the Atlantic. *J. Physical Oceanogr.* 38:18.

Evans, W., Strutton, P. G., and Chavez, F. P. (2009). Impact of tropical instability waves on nutrient and chlorophyll distributions in the equatorial Pacific. *Deep Sea Res. Part I Oceanogr. Res. Pap.* 56, 178–188. doi: 10.1016/j.dsr.2008.08.008

Flament, P. J., Kennan, S. C., Knox, R. A., Niiler, P. P., and Bernstein, R. L. (1996). The three-dimensional structure of an upper ocean vortex in the tropical Pacific Ocean. *Nature* 383, 610–613. doi: 10.1038/383610a0

Giese, B. S., and Harrison, D. E. (1991). Eastern equatorial Pacific response to three composite westerly wind types. *J. Geophys. Res.* 96:3239. doi: 10.1029/90JC01861

Graham, T. (2014). The importance of eddy permitting model resolution for simulation of the heat budget of tropical instability waves. *Ocean Model.* 79, 21–32. doi: 10.1016/j.ocemod.2014.04.005

Gushchina, D., and Dewitte, B. (2012). Intraseasonal Tropical Atmospheric Variability Associated with the Two Flavors of El Niño. *Monthly Weather Rev.* 140, 3669–3681. doi: 10.1175/MWR-D-11-00267.1

Harrison, D. E., and Giese, B. S. (1988). Remote westerly wind forcing of the eastern equatorial Pacific; Some model results. *Geophys. Res. Lett.* 15, 804–807. doi: 10.1029/GL015i008p00804

Hashizume, H., Xie, S.-P., Liu, W. T., and Takeuchi, K. (2001). Local and remote atmospheric response to tropical instability waves: A global view from space. *J. Geophys. Res.* 106, 10173–10185. doi: 10.1029/2000JD900684

Hersbach, H., Bell, B., Berrisford, P. et al. (2018). *ERA5 hourly data on pressure levels from 1979 to present*. Available online at: https://cds.climate.copernicus.eu/cdsapp#!/dataset/reanalysis-era5-pressure-levels?tab=overview (accessed January 1, 2020).

Holmes, R. M., and Thomas, L. N. (2015). The Modulation of Equatorial Turbulence by Tropical Instability Waves in a Regional Ocean Model. *J. Physical Oceanogr.* 45, 1155–1173. doi: 10.1175/JPO-D-14-0209.1

Holmes, R. M., and Thomas, L. N. (2016). Modulation of Tropical Instability Wave Intensity by Equatorial Kelvin Waves. *J. Physical Oceanogr.* 46, 2623–2643. doi: 10.1175/JPO-D-16-0064.1

Hsin, Y.-C., and Qiu, B. (2012). The impact of Eastern-Pacific versus Central-Pacific El Niños on the North Equatorial Countercurrent in the Pacific Ocean. *J. Geophys. Res.* 117:2012JC008362. doi: 10.1029/2012JC008362

Huang, B., Liu, C., Banzon, V. F., Freeman, E., Graham, G., Hankins, B., et al. (2020). NOAA 0.25-degree Daily Optimum Interpolation Sea Surface Temperature (OISST), Version 2.1. *NOAA Natl. Centers Environ. Informat.* 2020:T57. doi: 10.25921/RE9P-PT57

Imada, Y., and Kimoto, M. (2012). Parameterization of Tropical Instability Waves and Examination of Their Impact on ENSO Characteristics. *J. Clim.* 25, 4568–4581. doi: 10.1175/JCLI-D-11-00233.1

Inoue, R., Lien, R.-C., and Moum, J. N. (2012). Modulation of equatorial turbulence by a tropical instability wave: Equatorial Turbulence Modulated by a TIW. *J. Geophys. Res.* 117:2011JC007767. doi: 10.1029/2011JC007767

Izumo, T. (2005). The equatorial undercurrent, meridional overturning circulation, and their roles in mass and heat exchanges during El Niño events in the tropical Pacific ocean. *Ocean Dynam.* 55, 110–123. doi: 10.1007/s10236-005-0115-1

Izumo, T., Picaut, J., and Blanke, B. (2002). Tropical pathways, equatorial undercurrent variability and the 1998 La Niña. *Geophys. Res. Lett.* 29, 37–31. doi: 10.1029/2002GL015073

Jing, Z., Wu, L., Wu, D., and Qiu, B. (2014). Enhanced 2-h–8-day Oscillations Associated with Tropical Instability Waves. *J. Physic. Oceanogr.* 44, 1908–1918. doi: 10.1175/JPO-D-13-0189.1

Jochum, M., and Murtugudde, R. (2006). Temperature Advection by Tropical Instability Waves. *J. Physic. Oceanogr.* 36, 592–605. doi: 10.1175/JPO2870.1

Jochum, M., Cronin, M. F., Kessler, W. S., and Shea, D. (2007). Observed horizontal temperature advection by tropical instability waves. *Geophys. Res. Lett.* 34:2007GL029416. doi: 10.1029/2007GL029416

Jochum, M., Danabasoglu, G., Holland, M., Kwon, Y.-O., and Large, W. G. (2008). Ocean viscosity and climate. *J. Geophys. Res.* 113:C06017. doi: 10.1029/2007JC004515

Kennan, S. C., and Flament, P. J. (2000). Observations of a Tropical Instability Vortex *. *J. Phys. Oceanogr.* 30, 2277–2301. doi: 10.1175/1520-04852000030<2277:OOATIV<2.0.CO;2

Lawrence, S. P., Allen, M. R., Anderson, D. L. T., and Llewellyn-Jones, D. T. (1998). Effects of subsurface ocean dynamics on instability waves in the tropical Pacific. *J. Geophys. Res.* 103, 18649–18663. doi: 10.1029/98JC01684

Lawrence, S. P., and Angell, J. P. (2000). Evidence for Rossby wave control of tropical instability waves in the Pacific Ocean. *Geophys. Res. Lett.* 27, 2257–2260. doi: 10.1029/1999GL002363

Lee, T., Lagerloef, G., Gierach, M. M., Kao, H.-Y., Yueh, S., and Dohan, K. (2012). Aquarius reveals salinity structure of tropical instability waves. *Geophys. Res. Lett.* 39:2012GL052232. doi: 10.1029/2012GL052232

Legeckis, R. (1977). Long waves in the eastern equatorial Pacific Ocean: A view from a geostationary satellite. *Science* 197, 1179–1181. doi: 10.1126/science.197.4309.1179

Legeckis, R., Brown, C. W., Bonjean, F., and Johnson, E. S. (2004). The influence of tropical instability waves on phytoplankton blooms in the wake of the Marquesas Islands during 1998 and on the currents observed during the drift of the Kon-Tiki in 1947. *Geophys. Res. Lett.* 31:2004GL021637. doi: 10.1029/2004GL021637

Lien, R.-C., D'Asaro, E. A., and Menkes, C. E. (2008). Modulation of equatorial turbulence by tropical instability waves. *Geophys. Res. Lett.* 35:L24607. doi: 10.1029/2008GL035860

Lin, J. W.-B., Neelin, J. D., and Zeng, N. (2000). Maintenance of Tropical Intraseasonal Variability: Impact of Evaporation–Wind Feedback and Midlatitude Storms. *J. Atmospheric Sci.* 57:31.

Liu, C., Köhl, A., Liu, Z., Wang, F., and Stammer, D. (2016). Deep-reaching thermocline mixing in the equatorial pacific cold tongue. *Nat. Commun.* 7:11576. doi: 10.1038/ncomms11576

Luther, D. S., and Johnson, E. S. (1990). Eddy Energetics in the Upper Equatorial Pacific during the Hawaii-to-Tahiti Shuttle Experiment. *J. Physic. Oceanogr.* 20, 913–944. doi: 10.1175/1520-04851990020<0913:EEITUE<2.0.CO;2

Lyman, J. M., Chelton, D. B., deSzoeke, R. A., and Samelson, R. M. (2005). Tropical Instability Waves as a Resonance between Equatorial Rossby Waves*. *J. Physic. Oceanogr.* 35, 232–254. doi: 10.1175/JPO-2668.1

Lyman, J. M., Johnson, G. C., and Kessler, W. S. (2007). Distinct 17- and 33-Day Tropical Instability Waves in Subsurface Observations*. *J. Physic. Oceanogr.* 37, 855–872. doi: 10.1175/JPO3023.1

McPhaden, M. J. (1996). Monthly period oscillations in the Pacific North Equatorial Countercurrent. *J. Geophys. Res.* 101, 6337–6359. doi: 10.1029/95JC03620

McPhaden, M. J., and Yu, X. (1999). Equatorial waves and the 1997-98 El Niño. *Geophys. Res. Lett.* 26, 2961–2964. doi: 10.1029/1999GL004901

Menkes, C. E. (2002). A whirling ecosystem in the equatorial Atlantic. *Geophys. Res. Lett.* 29:1553. doi: 10.1029/2001GL014576

Menkes, C. E., Vialard, J. G., Kennan, S. C., Boulanger, J.-P., and Madec, G. V. (2006). A Modeling Study of the Impact of Tropical Instability Waves on the Heat Budget of the Eastern Equatorial Pacific. *J. Physic. Oceanogr.* 36, 847–865. doi: 10.1175/JPO2904.1

Mosquera-Vásquez, K., Dewitte, B., and Illig, S. (2014). The Central Pacific El Niño intraseasonal Kelvin wave. *J. Geophys. Res. Oceans* 119, 6605–6621. doi: 10.1002/2014JC010044

Moum, J. N., Lien, R.-C., Perlin, A., Nash, J. D., Gregg, M. C., and Wiles, P. J. (2009). Sea surface cooling at the Equator by subsurface mixing in tropical instability waves. *Nat. Geosci.* 2, 761–765. doi: 10.1038/ngeo657

Ogata, T., Xie, S.-P., Wittenberg, A., and Sun, D.-Z. (2013). Interdecadal Amplitude Modulation of El Nin˜o–Southern Oscillation and Its Impact on Tropical Paci?c Decadal Variability. *J. Clim.* 26:18.

Perigaud, C., and Dewitte, B. (1996). El Niño–La Niña Events Simulated with Cane and Zebiak's Model and Observed with Satellite or In Situ Data. Part I: Model Data Comparison. *J. Clim.* 9, 66–84. doi: 10.1175/1520-04421996009<0066:ENNESW<2.0.CO;2

Pezzi, L. P. (2003). Effects of lateral mixing on the mean state and eddy activity of an equatorial ocean. *J. Geophys. Res.* 108:3371. doi: 10.1029/2003JC001834

Philander, S. G. H. (1978). Instabilities of zonal equatorial currents, 2. *J. Geophys. Res.* 83:3679. doi: 10.1029/JC083iC07p03679

Picaut, J., and Sombardier, L. (1993). Influence of density stratificationand bottom depth on vertical mode structure functions in the tropical Pacific. *J. Geophys. Res.* 98, 727–714.

Polito, P. S., Ryan, J. P., Liu, W. T., and Chavez, F. P. (2001). Oceanic and atmospheric anomalies of tropical instability waves. *Geophys. Res. Lett.* 28, 2233–2236. doi: 10.1029/2000GL012400

Qiao, L., and Weisberg, R. H. (1995). Tropical instability wave kinematics: Observations from the Tropical Instability Wave Experiment. *J. Geophys. Res.* 100:8677. doi: 10.1029/95JC00305

Qiao, L., and Weisberg, R. H. (1998). Tropical Instability Wave Energetics: Observations from the Tropical Instability Wave Experiment. *J. Physical Oceanogr.* 28:16.

Rodgers, K. B., Friederichs, P., and Latif, M. (2004). Tropical Pacific Decadal Variability and Its Relation to Decadal Modulations of ENSO. *J. Clim.* 17:14.

Roundy, P. E., and Kiladis, G. N. (2006). Observed Relationships between Oceanic Kelvin Waves and Atmospheric Forcing. *J. Clim.* 19, 5253–5272. doi: 10.1175/JCLI3893.1

Rydbeck, A. V., Jensen, T. G., and Flatau, M. (2019). Characterization of Intraseasonal Kelvin Waves in the Equatorial Pacific Ocean. *J. Geophys. Res. Oceans* 124, 2028–2053. doi: 10.1029/2018JC014838

Shinoda, T., Kiladis, G. N., and Roundy, P. E. (2009). Statistical representation of equatorial waves and tropical instability waves in the Pacific Ocean. *Atmos. Res.* 94, 37–44. doi: 10.1016/j.atmosres.2008.06.002

Stein, K., Timmermann, A., and Schneider, N. (2011). Phase Synchronization of the El Niño-Southern Oscillation with the Annual Cycle. *Phys. Rev. Lett.* 107:128501. doi: 10.1103/PhysRevLett.107.128501

Strutton, P. G., Ryan, J. P., and Chavez, F. P. (2001). Enhanced chlorophyll associated with tropical instability waves in the equatorial Pacific. *Geophys. Res. Lett.* 28, 2005–2008. doi: 10.1029/2000GL012166

Taburet, G., Sanchez-Roman, A., Ballarotta, M., Pujol, M.-I., Legeais, J.-F., Fournier, F., et al. (2019). DUACS DT2018: 25 years of reprocessed sea level altimetry products. *Ocean Sci.* 15, 1207–1224. doi: 10.5194/os-15-1207-2019

Takahashi, K., Montecinos, A., Goubanova, K., and Dewitte, B. (2011). ENSO regimes: Reinterpreting the canonical and Modoki El Niño. *Geophys. Res. Lett.* 38:2011GL047364. doi: 10.1029/2011GL047364

Tanaka, Y., and Hibiya, T. (2019). Generation Mechanism of Tropical Instability Waves in the Equatorial Pacific Ocean. *J. Phys. Oceanogr.* 49, 2901–2915. doi: 10.1175/JPO-D-19-0094.1

Trenberth, K. E., Large, W. G., and Olson, J. G. (1989). The Effective Drag Coefficient for Evaluating Wind Stress over the Oceans. *J. Clim.* 2, 1507–1516. doi: 10.1175/1520-04421989002<1507:TEDCFE<2.0.CO;2

Wang, W., and McPhaden, M. J. (1999). The Surface-Layer Heat Balance in the Equatorial Paci?c Ocean. Part I: Mean Seasonal Cycle. *J. Physic. Oceanogr.* 29:20.

Warner, S. J., Holmes, R. M., Hawkins, E. H. M., Hoecker-Martínez, M. S., Savage, A. C., and Moum, J. N. (2018). Buoyant Gravity Currents Released from Tropical Instability Waves. *J. Physic. Oceanogr.* 48, 361–382. doi: 10.1175/JPO-D-17-0144.1

Webb, D. J., Coward, A. C., and Snaith, H. M. (2020). A comparison of ocean model data and satellite observations of features affecting the growth of the North Equatorial Counter Current during the strong 1997–1998 El Niño. *Ocean Sci.* 16, 565–574. doi: 10.5194/os-16-565-2020

Xie, S.-P., Ishiwatari, M., Hashizume, H., and Takeuchi, K. (1998). Coupled ocean-atmospheric waves on the equatorial front. *Geophys. Res. Lett.* 25, 3863–3866. doi: 10.1029/1998GL900014

Xue, A., Jin, F., Zhang, W., Boucharel, J., Zhao, S., and Yuan, X. (2020). Delineating the Seasonally Modulated Nonlinear Feedback Onto ENSO From Tropical Instability Waves. *Geophys. Res. Lett.* 47:2019GL085863. doi: 10.1029/2019GL085863

Xue, A., Zhang, W., Boucharel, J., and Jin, F.-F. (2021). Anomalous Tropical Instability Wave activity hindered the development of the 2016/2017 La Niña. *J. Clim.* 2021, 1–1. doi: 10.1175/JCLI-D-20-0399.1

Yeh, S.-W., and Kirtman, B. P. (2004). Tropical Pacific decadal variability and ENSO amplitude modulation in a CGCM. *J. Geophys. Res.* 109:C11009. doi: 10.1029/2004JC002442

Yeh, S.-W., and Kirtman, B. P. (2005). Pacific decadal variability and decadal ENSO amplitude modulation. *Geophys. Res. Lett.* 32:5. doi: 10.1029/2004GL021731

Yoder, J. A., Ackleson, S. G., Barber, R. T., Flament, P., and Balch, W. M. (1994). A line in the sea. *Nature* 371, 689–692.

Yu, J.-Y., and Liu, W. T. (2003). A linear relationship between ENSO intensity and tropical instability wave activity in the eastern Pacific Ocean. *Geophys. Res. Lett.* 30:2003GL017176. doi: 10.1029/2003GL017176

Zhang, R.-H. (2014). Effects of tropical instability wave (TIW)-induced surface wind feedback in the tropical Pacific Ocean. *Clim. Dynam.* 42, 467–485. doi: 10.1007/s00382-013-1878-6

Zhang, R.-H., and Busalacchi, A. J. (2008). Rectified effects of tropical instability wave (TIW)-induced atmospheric wind feedback in the tropical Pacific. *Geophys. Res. Lett.* 35:L05608. doi: 10.1029/2007GL033028

Zhao, J., Li, Y., and Wang, F. (2013). Dynamical responses of the west Pacific North Equatorial Countercurrent (NECC) system to El Niño events: Responses of Necc System to El NiÑos. *J. Geophys. Res. Oceans* 118, 2828–2844. doi: 10.1002/jgrc.20196

Zhao, Y., Lorenzo, E. D., Sun, D., and Stevenson, S. (2021). Tropical Pacific Decadal Variability and ENSO Precursor in CMIP5 Models. *J. Clim.* 34, 1023–1045. doi: 10.1175/JCLI-D-20-0158.1

Conflict of Interest: The authors declare that the research was conducted in the absence of any commercial or financial relationships that could be construed as a potential conflict of interest.

Publisher's Note: All claims expressed in this article are solely those of the authors and do not necessarily represent those of their affiliated organizations, or those of the publisher, the editors and the reviewers. Any product that may be evaluated in this article, or claim that may be made by its manufacturer, is not guaranteed or endorsed by the publisher.

3.3 Conclusion and perspective

3.3.1 Summary

We confirmed for the first time in long-term observational data (26 years of altimetry SSH data) the evidence of systematic nonlinear coupling between TIWs and IEKWs that accounts for 21% of the total intraseasonal variability in the Tropical Pacific.

We also reported the asymmetric TIWs response to the passage of different IEKWs phases, yet with a faster adjustment than that found in the idealized study by Holmes and Thomas (2016), suggesting the almost quasi-instantaneous TIWs response to the alteration of equatorial circulation induced by IEKWs.

3.3.2 EKE from observations

In order to provide material for a more quantitative comparison with HT16, we estimated lag composites of SLA and intraseasonal eddy kinetic energy (*i.e.*, EKE associated with TIWs, noted hereinafter TIWKE) for the same downwelling and upwelling events used for our Figure 2, and using the same region (7°S-10°N; 150°W-110°W) than in HT16 (their figures 8 and 9) for averaging (but not averaged with depth). We use the geostrophic velocity data derived from the AVISO products and assume that the vertical structure reduces to the gravest baroclinic mode. This diagnostic confirms that our CEOF analysis captures successive upwelling and downwelling kelvin waves, which inherently prevents a straightforward comparison with HT16 modeling case studies that allows differentiating both qualitatively and quantitatively the two phases of the IEKW. Yet, consistently with HT16, we do observe a decrease (increase) in TIWKE before the passage of a downwelling (upwelling) IEKWs although happening ∼20 days before as compare to 45-60 days as in HT16. While differences can be broadly interpreted as resulting from differences in mean state conditions (i.e. mean vertical stratification) impacting both wave characteristics and instability processes, it is also worth noting that we compare the lag between the sea surface height at the equator and in the TIWs region and not the kinetic energy in the broad equatorial region as in HT16.

However, our methodological approach based on the decomposition of SSH anomalies into complex empirical orthogonal functions (CEOFs) made it difficult to separate the impact of the different phases of individual IEKWs (mixed together in the CEOF modes) on the energetics of TIWs and thus to really confront the results of the HT16's idealized modeling study with the actually observed TIWs-IEKWs interaction events.

Therefore, in the next chapter and in order to evaluate the TIWs response to the passage of IEKWs in a more realistic large-scale environment, we set up sensitivity experiments using an eddy resolving regional oceanic model initialized before the onset of the different upwelling and downwelling IEKWs-TIWs interaction events identified in Escobar-Franco et al. (2022)'s observational analysis. By turning on or off the non-linear terms in the momentum equation, we can control the level of TIW's oceanic mesoscale activity without affecting the almost

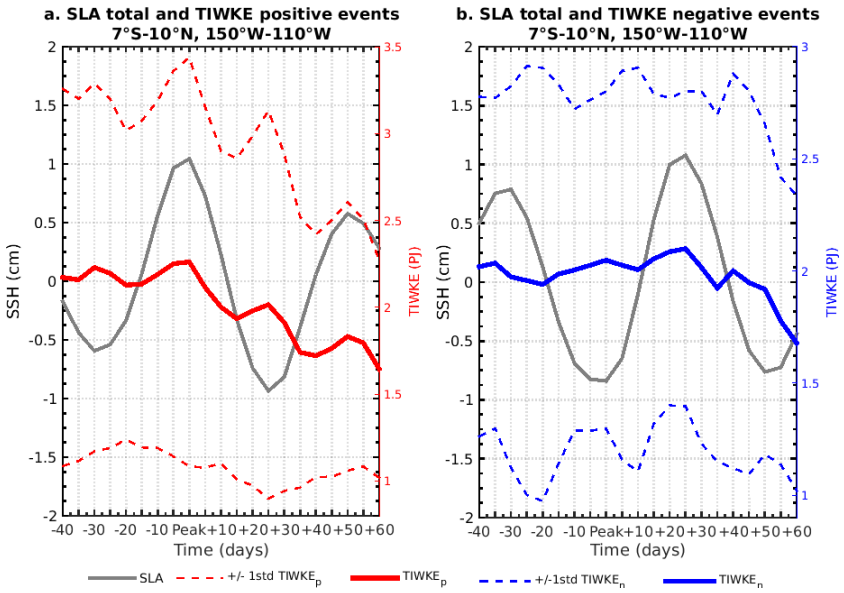

Figure 3.1: Comparable figures to Figures 8ab and Figures 9ab of HT16: Composites of (a.) total SLA (grey) and TIW kinetic energy (TIWKE) averaged over the region (150°W-110°W, 7°S-10°N) for (left, a) positive (downwelling, red) and (right, b) negative (upwelling, blue) events as defined from Fig. 2a of the manuscript. The averaging is done only horizontally but assuming that observed sea level anomalies account dominantly for the first baroclinic mode and that the latter can be approximated by a step function (1 above the thermocline, 0 below), this is equivalent to a vertical integration (as in HT16). The dashed lines show the departures of $+/-1$ standard deviation from TIWKE composites. Units of SLA are [cm] and of TIWKE [PJ].

completely linear IEKWs dynamics and therefore quantify in a different manner than in HT16's idealized model experiments, the changes in TIWs-related EKE induced by the passage of different phases of individual Kelvin waves.

Chapter 4

Energetic of the nonlinear interaction between Intraseasonal Kelvin Waves and Tropical Instability Waves

Contents

4.1 Draft of the article "Interaction between intraseasonal equatorial Kelvin waves and tropical instability waves in a tropical Pacific model simulation"

To be submitted to the Journal of Physical Oceanography. In this paper we investigate a process that has been somehow overlooked in the TIWs literature that concerns the interaction between equatorial Kelvin waves and TIWs at intraseasonal timescales. Most previous studies have focused on the relationship between ENSO and TIW activity, with either showing that TIW activity is modulated by ENSO through frequency entrainment or that TIW activity can influence ENSO development and contribute to its asymmetry.

This model study extends a previous one published in Frontiers in Marine Sciences based on observations where we revealed the existence of a mode associated to the interaction between IKWs and TIWs that is independent of ENSO. In the present paper the use of the regional modelallowsw us to investigate the processes at work based on sensitivity experiments. Our results provide a comprehensive description of the 3D structure of the barotropic and baroclinic conversion terms, showing that both conversion terms contribute rather equally to the increase(decrease) in the mean EKE during upwelling(downwelling) events, with corresponding changes in the meridional temperature gradient and meridional current shear between the EUC and NECC

Publisher: AMS; Journal:

Draft

Interaction between intraseasonal equatorial Kelvin waves and tropical instability waves in a tropical Pacific model simulation

M. Gabriela Escobar-Franco[a], Julien Boucharel[a,b], Boris Dewitte[c,d,e]

[a] Université de Toulouse III, Laboratoire d'Études en Géophysique et Océanographie Spatiales, CNRS/IRD, Toulouse, France

[b] *Department of Atmospheric Sciences, University of Hawai'i at Mānoa, Honolulu, HI, United States, 3 CECI, Université de Toulouse III, CERFACS/CNRS, Toulouse, France*

[c] *CECI, Université de Toulouse III, CERFACS/CNRS, Toulouse, France, 4 Centro de Estudios Avanzados en Zonas Áridas (CEAZA), Coquimbo, Chile*

[d] *Departamento de Biología Marina, Facultad de Ciencias del Mar, Universidad Católica del Norte, Coquimbo, Chile*

[e] *Departamento de Biología Marina, Facultad de Ciencias del Mar, Universidad Católica del Norte, Coquimbo, Chile*

Corresponding author: Maria Gabriela Escobar Franco, magaemge@gmail.com

ABSTRACT

The Kelvin wave is a dominant source of intraseasonal variability, transporting energy from the central equatorial Pacific up to the high latitudes along the west coast of the Americas. Along its path, it can interact with Tropical Instability Waves (TIWs), a process that has been little studied despite its potentially important role in influencing large-scale tropical dynamics (*e.g.*, the El Niño Southern Oscillation). Here we investigate the energetics of this interaction based on a tropical Pacific configuration of a regional ocean model over the period 1993-2019. It is first shown that the model's control run (CR) simulates realistically most aspects of the mean circulation, intraseasonal variability and the characteristics of the turbulent flow in the TIWs region. Sensitivity experiments consisted in rerunning the model for an ensemble of selected upwelling and downwelling Kelvin wave events with the TIWs activity strongly reduced through canceling out non-linear advection in the momentum equations (LIN). The LIN simulations thus serve as a baseline for diagnosing changes in the TIW kinetic energy (TIWKE) due to the passage of intraseasonal Kelvin waves (IEKWs) in CR. First, the results indicate an asymmetry between upwelling and downwelling events in terms of changes in TIWKE, with upwelling events causing a significant increase (27%) while downwelling events decrease it (20%). The analysis of the tendency terms of the TIWKE rate of change further reveals that both barotropic and baroclinic conversion terms contribute to the increase in mean EKE during upwelling events, with corresponding increase in the meridional current shear between the Equatorial Undercurrent and North Equatorial Countercurrent and in the meridional temperature gradient. Dispersion amongst events is however rather large reflecting a sensitivity to the IEKWs characteristics. Overall, our results indicate that the IEKW is effective in altering the balance of the EKE budget in the TIWs activity region, which has implications for the interpretation of the heat budget in the eastern equatorial Pacific on timescales beyond the season.

1. Introduction

The intraseasonal tropical variability (ITV) is a major component of both the atmospheric and oceanic circulation in the tropics. The atmosphere is mostly composed of the so-called coherent Madden–Julian Oscillation (MJO) with periods in the 30–90 day band and zonal wavenumbers of 1–3 (Madden and Julian (1972); Zhang (2005)) and the equatorial convectively coupled waves (CWs) (Wheeler and Kiladis (1999)) that include several modes themselves. The ocean key features of ITV include the intraseasonal equatorial Kelvin and Rossby waves (IEKWs, IRWs) that are forced by the atmospheric intraseasonal variability and wind bursts through air-sea interactions (Roundy (2006); Seiki and Takayabu (2007); Gushchina and Dewitte (2012) among others) and the Tropical Instability Waves (TIWs) resulting from instabilities in the shear zone between the South Equatorial Current (SEC) and the Equatorial Undercurrent (EUC) and the North Equatorial Countercurrent (NECC) (Philander (1978); Cox (1980); Qiao and Weisberg (1998)) and along the density front between the cold equatorial and warm off-equatorial waters (McCreary and Yu 1992; Yu et al. 1995; Masina et al. 1999).

Both aspects of ITV have been shown to be related to the El Niño Southern Oscillation (ENSO), the largest interannual variability in the climate system (McPhaden et al. (2006)). For example, MJO and CWs activity have been shown to modulate Westerly Wind Events, which are precursors of some El Niño events (Hendon et al. (2007); others), through forcing IEKWs and IRWs (Gushchina and Dewitte (2012)). TIWs activity contributes to ENSO asymmetry by dampening the development of La Niña (Im et al. (2015); An (2004); Xue et al. (2020); Xue et al. (2021); An (2008), Xue et al. (2021)) and could also lead to a

weakening of ENSO in the context of global warming (Wengel et al. (2021)). Overall, the different sources of ITV contribute to the modulation of ENSO and largely determine its predictability (L'Heureux et al. (2020)). This calls for a better understanding of the different facets of ITV interactions.

In this paper, we focus on two main oceanic components of the ITV, namely the IEKWs and the TIWs, which have mostly been documented independently in previous studies, with a large body of literature investigating how both can be rectified by the mean states or vice versa. For instance, studies have shown how TIWs can feedback onto low-frequency climate variability through Nonlinear Dynamical Heating (NDH, e.g., Holmes and Thomas (2015); Jin et al. (2003)). TIWs have been shown to warm the Cold Tongue via direct meridional NDH (Menkes et al. (2006); Graham (2014)) and reduce the EUC strength leading to a rectified effect on the mean Eastern equatorial Pacific heat budget (Maillard et al. (2022a)). These feedbacks being stronger during La Niña and in summer than during El Niño and in winter, TIWs can therefore also modulate the amplitude of both the seasonal (e.g., Im et al. (2012); Maillard et al. (2022b)) and ENSO cycle, participating in ENSO asymmetry (An (2008); Im et al. (2012); Graham (2014); Boucharel and Jin (2020); Xue et al. (2020); Xue et al. (2021); Xue et al. (2023)). On the other hand, IEKWs activity tends to peak prior to El Niño development, which has motivated studies to document its imprint on the surface heat-budget (Philander and Hurlin (1988); Huang et al. (2010); Huang et al. (2012); Mosquera-Vásquez et al. (2013)) and how they favor ENSO development. IEKWs can also be modulated by the background state, particularly in the eastern Pacific where changes in mean thermocline depth and stratification can produce energy scattering or dissipation (Dewitte et al. (1999); Mosquera-Vásquez et al. (2014) among others).

On the other hand, fewer studies have highlighted the potential for interactions between TIWs and IEKWs. Harrison and Giese (1988) and Giese and Harrison (1991) have demonstrated that Kelvin waves triggered by westerly wind events can alter TIWs features by modifying the meridional shear in the equatorial current field throughout their eastward equatorial propagation. Allen et al. (1995) and Angell et al. (1998), suggested the possibility that IEKWs can be reflected from the eastern boundary (i.e., the South American coast) into Rossby waves and then modify the strength and phase of TIWs. Qiao and Weisberg (1998) found that the early end of the TIWs season observed in December 1990 coincided with the propagation of a large IEKW responsible for a decrease in the meridional shear between the SEC and EUC, in the associated barotropic energy conversion rate and therefore in the TIWs activity. Shinoda et al. (2009) confirmed that the prominent peak at 33 days in the TIWs spectrum corresponds to that of the first meridional mode equatorial Rossby waves, by analyzing satellite data. To further understand and address the energy balance of this interaction, Holmes and Thomas (2016) (hereafter HT16) conducted idealized sensitivity experiments with a high-resolution regional ocean model of the eastern tropical Pacific to document the evolution of the eddy kinetic energy (EKE) of TIWs during the passage of IEKWs, and showed that IEKWs have the potential to modify the background zonal currents, barotropic energy conversion rates and consequently TIWs activity. In particular, they highlighted an asymmetric response of TIWs to different phases of IEKWs, characterized by a decrease (increase) of the TIWs-induced EKE during the passage of a downwelling (upwelling) IEKWs. While their study sheds light on key processes at work in the IEKWs-TIWs interaction, the idealized framework of HT16 remains a limitation when it comes to comparison with what happens in nature. In particular, IEKWs in the eastern Pacific have more energy in higher-order baroclinic modes (Dewitte et al. (1999)), which is not accounted for in the experiments of HT16 for which a first baroclinic mode vertical structure is imposed near the eastern boundary of their model domain (160°W). Also, IEKWs in

observations can vary in amplitude quite substantially with a marked seasonal dependence (Mosquera-Vásquez et al. (2014)). This is influential on the IEKWs-TIWs interaction as shown by Escobar-Franco et al. (2022) that evidenced from altimeter data a coupled mode between TIWs and IEKWs accounting for 21% of the explained variance of the total sea level anomalies between 10°N and 10°S in the equatorial Pacific and exhibiting a modulation at seasonal to interannual.

Here, our motivation is to gain insights into the role of the IEKWs-TIWs interaction on the energy balance in the eastern Pacific, extending the study of HT16 in a more realistic framework. A corollary motivation is also to better understand the processes that affect the IEKW propagation characteristics, considering its role in ENSO development and its impact on the highly productive ecosystems of the eastern tropical Pacific.

The paper is organized as follows: Section 2 describes the data and model configuration. In section 3, we evaluate the model's ability to simulate the tropical Pacific mean state, intraseasonal variability, mesoscale activity, and the nonlinear interaction between TIWs and IEKWs. In section 4, we perform an EKE budget to evaluate and quantify the origins of changes in instability in the eastern equatorial Pacific associated with the passage of different IEKW phases. The results are summarized and discussed in section 5 in terms of a possible rectification effect of the TIWs-IEKWs interaction in the equatorial mean thermal state and circulation, and its potential role in ENSO.

2. Data, Method and Model configuration

a. Ocean model set up and strategy for the sensitivity experiments

The oceanic simulations were performed using the Coastal and Regional Ocean Community model (CROCO), a free-surface, terrain-following coordinate model with split-explicit time-stepping and with Boussinesq and hydrostatic approximations (Shchepetkin and McWilliams (2005) and Debreu et al. (2012)). The domain covers the tropical Pacific from 135°E to the American coast and from 18°S to 18°N with a horizontal resolution of 0.25°, which is considered sufficient to resolve the equatorial mesoscale activity since the typical wavelength of TIWs is about 1500 km. A sponge layer is applied to enhance the viscosity and diffusivity and avoid spurious rim currents near the boundaries (Marchesiello et al. (2001)). The configuration has 54 vertical σ levels and the vertical grid is stretched for increased resolution at the surface (hcline = 300m) and bottom boundary layers using stretching parameters of θs=7, θb=2 respectively. The boundaries and initial conditions for tracers, SSH and horizontal velocity are derived from the Global Ocean Reanalyses and Simulations (GLORYS2V4) with 3 days temporal resolution, a 0.25° horizontal resolution and 75 vertical levels. The bottom topography is derived from the 1/15 arc-second high-resolution bathymetric dataset GEBCO (https://www.gebco.net/). We further apply a mask over the complicated western islands' coastlines in order to reduce inconsistencies and aliasing between the topography from CROCO and GLORYS2V4 grids. The vertical mixing of tracers and momentum is computed using the classic K-profile parameterization (KPP; Large et al. (1994)). The surface freshwater, heat, and momentum fluxes are estimated using the COARE bulk formulae (Fairall et al. (2003)). In order to have coherence between the atmospheric surface forcing and open boundary conditions, we use the same reanalysis product that forces GLORYS2V4 to force our simulations. The atmospheric surface fields are therefore derived from the 6-hourly ERA-Interim reanalysis produced by the European Centre for Medium-Range Weather Forecasts (ECMWF) that can be found at http://www.ecmwf.int/research/era at a horizontal resolution of 0.25°x0.25°. The atmospheric fields necessary to drive ocean-only models are the precipitation rate, the wind field at 10 m,

the shortwave and longwave radiation flux, and the temperature and specific humidity at 2 m. We also include the surface oceanic current feedback to the atmosphere (Renault et al. (2016)), using the stress-correction parameterization approach (Renault et al. (2020)) in order to have a realistic representation of the mesoscale activity and momentum exchange between the ocean and the atmosphere. A long control run ("CR-long") is run from January 1993 to July 2019 and is used in the next section to evaluate, the model's ability to realistically simulate the mean state and circulation as well as the intraseasonal variability and level of mesoscale activity. To quantify the changes in EKE associated with the TIWs-IEKWs interaction, we also perform sensitivity experiments that consider the same forcing than CR but with a modified physics, consisting in removing the nonlinear terms in the momentum equations and replacing them by a constant viscosity term with a viscosity coefficient set to 100 m^2s^{-1}. This approach for reducing eddy activity was first used by Gruber et al. (2011) to study the effect of mesoscale variability on the mean biological production in the California upwelling system, and applied subsequently for other problems in other studies (Vergara et al. (2017); Maillard et al. (2022b)). These latter experiments, referred to as LIN, are performed for short periods (90 days) when the TIWs-IEKWs interaction takes place. These periods are inferred from the statistical analysis of sea level anomalies of the CR-long simulation (see section "Composite Analysis: IEKWs-TIWs interaction") and start 6 days prior to 33 selected events using the restart from the CR-long simulation.

The difference between CR and LIN thus informs on the role of the TIWs-IEKWs interaction on any of the model variables and diagnostics (i.e. EKE budget). This assumes that the rectified effect of this interaction on the mean state during the 90 days-long simulations is only marginal and that the mean state of LIN and CR are therefore similar. This was verified a posteriori. On average the difference between CR and LIN is less than 0.03% for both temperature and zonal current over the domain (10°S-10°N; 0-200m, 140°W) for the ensemble mean of the 33 events (not shown).

b. Observational data

We use a variety of in situ and satellite observational data, as well as an ocean reanalysis, to validate the model long CR run:

- The satellite-derived SST from the NOAA 0.25° Daily Optimum Interpolation Sea Surface Temperature (OISST) product (Huang et al. (2021)), derived from satellite and in-situ observations from 1993 to 2019.
- The depth of isotherm 20°C (Z20), a good proxy for thermocline depth in the equatorial Pacific, is derived from the reanalysis product of the Simple Ocean Data Assimilation (SODA) version 3.4.2 (Carton and Giese (2008)) with 0.25° of spatial resolution. We have also considered the in-situ observations from the Tropical Ocean-Global Atmosphere (TOGA) (https://www.pmel.noaa.gov/) to validate the Z20 at the equator.
- The in-depth currents are validated at four cross sections (170°W, 140°W, 125°W and 110°W) from Johnson's climatology (Johnson et al. (2002)), that includes meridional sections of upper ocean zonal currents of Conductivity Temperature Depth and Acoustic Doppler Current Profiler data from 172 synoptic sections taken mostly in the 1990s in the tropical Pacific.
- The sea surface height (SSH) is obtained from the multi-satellite Data Unification and Altimeter Combination System datasets available through the Copernicus Marine Environment Monitoring Service (CMEMS) and the Copernicus Climate Change

Service (C3S) (Taburet et al. (2019)) at a spatial resolution of 0.25°×0.25° over the region (10°S–10°N, 130°E–80°W) and the period 1993–2019.

The radiation fluxes were obtained from the TropFlux project derived from corrected ERA Interim, International Satellite Cloud Climatology (ISCCP) and NOAA outgoing Longwave Radiation products (Praveen Kumar et al. (2012)) over the period 1993-2018 at a 1° horizontal resolution are analyzed.

c. Eddy Kinetic Energy (EKE) Budget

In an effort to understand the energy conversions occurring during the IEKWs-TIWs interaction, we perform in the different sensitivity experiments an EKE budget obtained from the momentum equations following (Masina et al. (1999); Qiao and Weisberg (1998); HT16; Conejero et al. (2021)). Here, since we are interested in intraseasonal timescales, our baseline to derive anomalies in the variables (3D velocities, density) consists of a 30-days running mean, which follows Lin et al. (2000). The energy variation in terms of conversion terms and flux vector gives us the approximation of the available energy transformation to the generation of eddies. The equation for the variation of $EKE = \frac{1}{2}\rho_0(u'^2 + v'^2)$ is finally (given by (Masina et al. (1999)):

$$\frac{\delta K_e}{\delta t} + \vec{U} \cdot \vec{\nabla} K_e + \overline{W} K_{ez} + \vec{u'} \cdot \vec{\nabla} K_e + w' K_{ez} =$$

$$- \vec{u'} \cdot \vec{\nabla} p' + \rho_o [- \vec{u'} \cdot (\vec{u'} \cdot \nabla \vec{U}) - \vec{u'} \cdot (w' \vec{V_z})$$

$$+ \vec{u'} \cdot \overline{(\vec{u'} \cdot \vec{\nabla} \vec{u'})} + \vec{u'} \cdot \overline{w' \vec{u'}_z}$$

$$+ K_{Mh}(\vec{u'} \cdot \nabla^2 \vec{u'}) + \vec{u'} \cdot (K_{Mv} \vec{u'}_z)_z]$$

Where the velocity field is (u, v, w) and the density is ρ. The horizontal and vertical viscosity coefficients are K_{Mh} and K_{Mv}, respectively.

The averaging in time of the above equation yields the terms that contribute to the rate of change in mean EKE. Two main terms are usually considered:

- Barotropic conversion ($K_m K_e$) corresponds to the conversion of mean Kinetic energy (K_m) into EKE (K_e) when the horizontal deformation work terms are positives $K_m \rightarrow K_e$.

$$K_m K_e = < \frac{-1}{H} \int_H^0 (u'u' \frac{\delta \bar{u}}{\delta x} + u'v' \frac{\delta \bar{u}}{\delta y} + u'w' \frac{\delta \bar{u}}{\delta z} + v'u' \frac{\delta \bar{v}}{\delta x} + v'v' \frac{\delta \bar{v}}{\delta y} + v'w' \frac{\delta \bar{v}}{\delta z}) >$$

- Baroclinic conversion ($P_e K_e$) corresponds to the baroclinic conversion of the available eddy potential energy (P_e) of the mean state into EKE $P_e \rightarrow K_e$, when its value is positive.

$$P_e K_e = < \frac{-g}{H \rho_0} \int_H^0 (\rho' w') dz >$$

where the brackets here represent the mean during the IEKWs-TIWs interaction period of each event, i.e., 20 days (starting 6 days before the IEKWs-TIWs event). The $'$ are the perturbations, the overbar is the 30-day running mean to capture the transient effect of the passage of the IEKWs on the TIWs energetics. The vertical integration is from the surface to the depth H=100 m. The constant variables are the gravitational acceleration g = 9.8ms^{-2} and the reference water density ρ_o = 1025 km m^{-3}.

3. Validation of the long control run simulation

In this section, we assess the CR-long run using the in-situ, satellite and reanalysis data described previously with a specific focus on the mean thermal state and circulation, the intraseasonal variability related to both IEKWs and TIWs as well as the representation of the interactions between the two as described in Escobar-Franco et al. (2022).

a. Mean state

(i) Thermal state

Fig. 1a displays the long-term mean SST from the CR experiment, which shows the typical features of the tropical Pacific, in particular the presence of the cold tongue, a patch of cold upwelling water along the equator in the central and eastern Pacific and along the coasts of South America, the warm pool, characterized by water above 29°C in the western Pacific, and a meridionally asymmetric structure with warmer water in the northern hemisphere (Wang and Fiedler (2006)). Overall, the CR simulation is characterized by small negative SST biases, most pronounced in the central eastern equatorial Pacific and in the Peruvian upwelling system (see statistics in Table 1). These negative surface biases can originate from the direct SST response to a too shallow thermocline of about 30 meters as compared with SODA in the central eastern Pacific but also from a slight negative shortwave radiation bias, which can contribute to the SST excessive cooling. Note that we also observed a relatively strong sensitivity of the depth and slope of the mean equatorial thermocline to the position of the western boundary of the domain (not shown). This appears to be due to persistent aliasing between the model and GLORYS2V4 bathymetry, despite the mask applied, resulting in large differences in current strength and vertical structure in the Mindanao, Halmahera, and New Guinea gyres, and subsequent incorrect adjustment in the Western Pacific mean stratification. A similar problem was reported by Grenier et al. (2011), where the mean zonal currents were not well simulated at 147°E along the equator and the core of the EUC was following a shallower thermocline than in the observations. From the Taylor's diagram, even if the simulation exhibits a higher variability than the observations, the central and eastern Pacific show good correlations (>= 0.9) and small dispersion between the observed and simulated values of sea temperature, SSH, and thermocline's depth.

(ii) Mean equatorial circulation

The CR-long run mean equatorial circulation is now compared with the observations from Johnson's drifter-derived climatology, at four meridional sections at 170°W, 140°W, 125°W and 110°W in Fig. 1b. All four sections exhibit a good agreement for both the position and intensity of the main equatorial currents, namely, the NECC, SEC and EUC. In particular, the northern and southern branches of the SEC are well simulated with their maximum (roughly -0.5 and -0.6 m/s) between 2°S–5°N and 7°S–3°S respectively. The outcrop and intensification of the EUC in the eastern Pacific are also well reproduced by the model with velocities close to 1 m/s and depth of its core at 100m and 75m at the section 140°W and 125°W respectively. These patterns of the equatorial currents are also consistent with the

findings of Yang et al. (2022b); Kessler (2006a); Johnson et al. (2002) and Yu and McPhaden (1999).

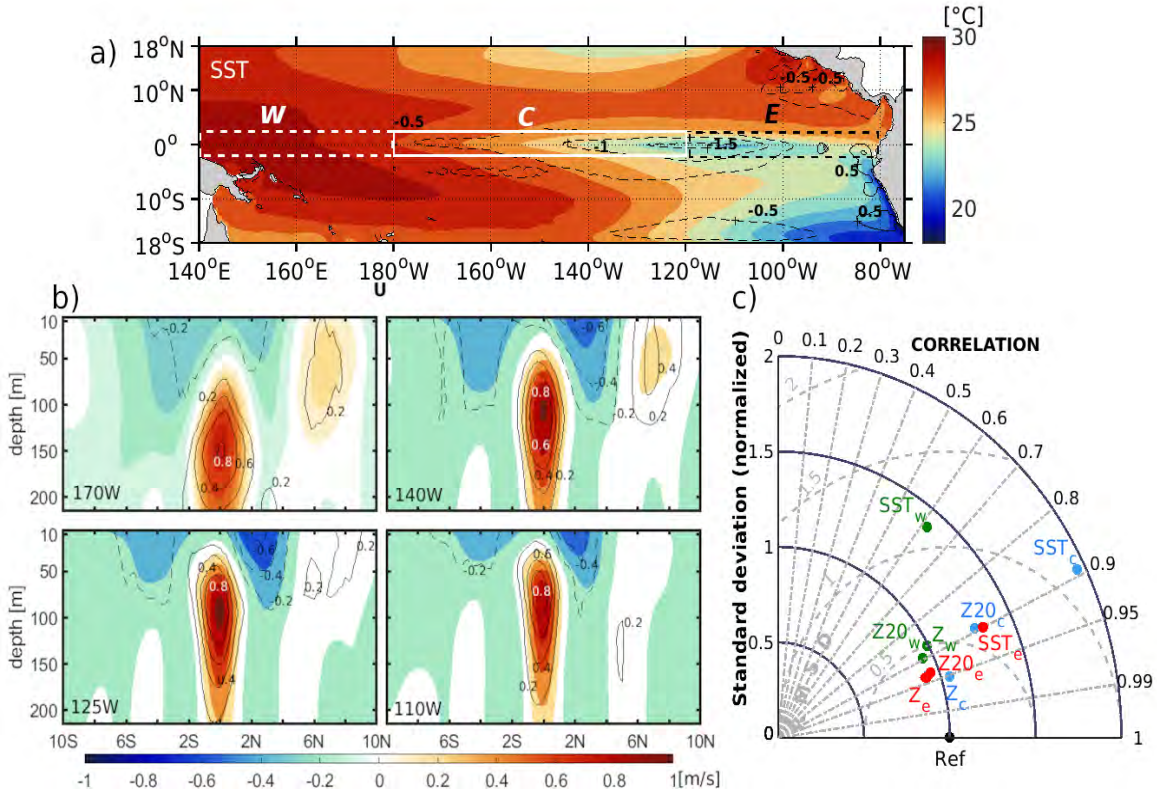

Fig. 1: (a) Mean sea surface temperature (SST) from the CR long simulation (shading) and biases between the model and OISST (dashed/plain black contours for negative/positive biases) for the total 1993-2019 period. (b) Depth–latitude section of zonal currents at four cross-sections: 175°W, 140°W, 125°W and 110°W for model (shading) and observations from Johnson's Climatology (contours). Eastward (westward) currents are shown with solid (dashed) lines. (c) Taylor diagram of SST, sea surface height (Z) and the depth of the isotherm 20°C (Z20) monthly time series averaged in three different equatorial (2.5°S-2.5°N) domains delineated in panel (a): the western (140°E-180°, variables indicated in green), central (180°-120°W, variables indicated in blue) and eastern (120°W-80°W, variables indicated in red) Pacific. On the Taylor diagram, the distance along the radius represents the ability to capture observed variability (standard deviation). The distance along the circumference depicts correlation with the observations, and gray inlaid dashed circles show unbiased root-mean-square-error.

Units	SSTw ◦ *C*	SSTc ◦ *C*	SSTe ◦ *C*	SSHw *m*	SSHc *m*	SSHe *m*	Z20w *m*	Z20c *m*	Z20e *m*
Obs	29.12	27.62	25.77	0.03	0.04	0.04	-172.35	-181.50	-51.97
CR	29.06	26.19	24.54	-0.001	-0.0018	-0.0003	-148.58	-151.16	-45.62
Bias (CR-obs)	-0.06	-1.43	-1.23	-0.03	-0.04	-0.04	23.84	30.35	6.35

Table 1: Long-term mean observed and simulated (CR-long run) values of all variables used in the Taylor Diagram from Fig. 1c (bottom panel) averaged in each of the three equatorial regions (W,C,E) delineated in Fig. 1a, along the mean bias (difference between observational products and the model).

a. TIWs mesoscale activity

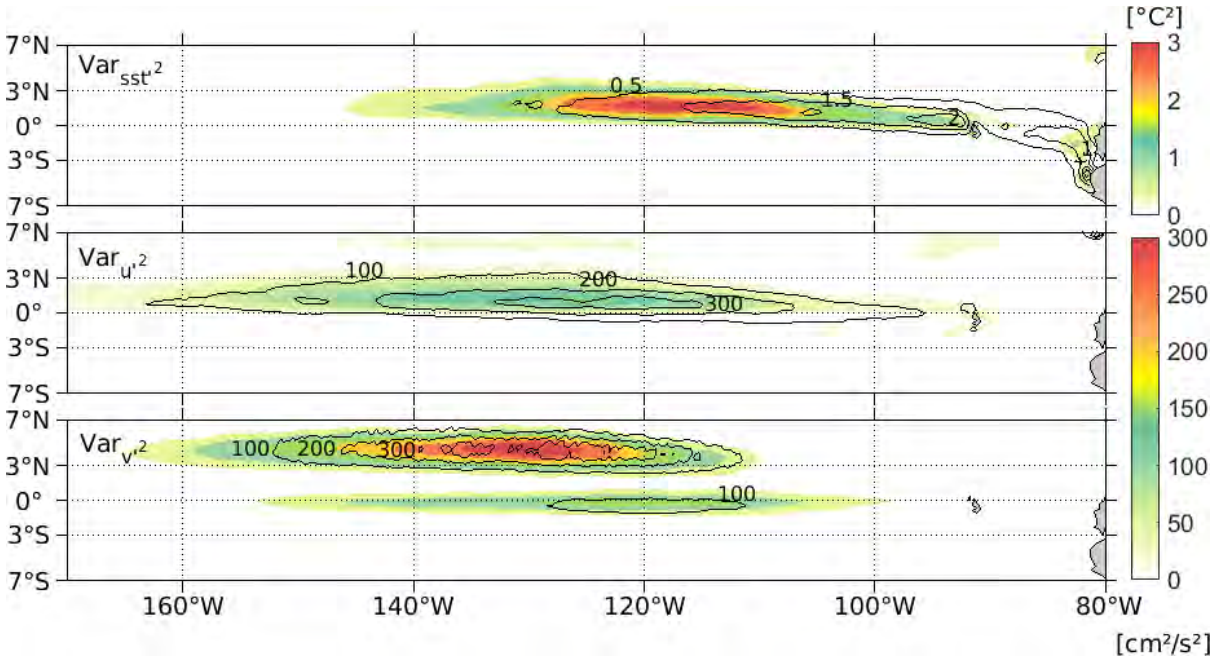

Fig. 2: Variance of simulated (shading) and observed (contours) sea surface temperature (a), zonal (b) and meridional currents (c) intraseasonal anomalies (as the departures from a 1-month running mean) averaged in the first 5 meters. Observed SST comes from OISST and horizontal currents from GLORYS2V4 reanalysis product.

To evaluate the ability of the CR to reproduce the intraseasonal variability associated with TIW activity, we show in Fig. 2 the simulated and observed variances of SST and horizontal currents intraseasonal anomalies. The spatial patterns of SST variability are similar to that of OISST with a maximum situated between 100°W and 130°W and between the Equator and 3°N (Fig. 2a), although the amplitude appears shifted west by ~ 15° relative to that of GLORYS2V4. The patterns of horizontal currents intraseasonal variance are also well simulated by the CR with a maximum shifted westward compared to that of SST between 120°W and 150°W consistently with GLORYS2V4 but further west than in the simulation

with the same model of Menkes et al. (2006). The variance of u' lies within the same latitudinal range as that of SST (Fig. 2b) but is slightly underestimated compared to GLORYS2V4, while the simulated variance of v' displays the observed dipole structure, yet with a stronger off-equatorial peak. It is worth mentioning that different reanalyses (e.g., GLORYS12, HYCOM, ECCO2 and GODAS) exhibit contrasted dipole patterns and intensities of v'^2 (Xue et al. (2023); Maillard et al. (2022b)). However, the pattern of intraseasonal variance of meridional currents remains consistent with most reanalysis products, as well as those obtained from altimeters (Wang et al. (2020)) and other modeling studies (e.g., Graham (2014)). Overall, the patterns of SST and horizontal velocity intraseasonal variances simulated are consistent with observations, even though there is a westward shift of the T and u variance relative to GLORYS2V4 (Fig. 2). The patterns are very similar to those in Menkes et al. (2006), Baturin and Niiler (1997), Graham (2014), and Shinoda et al. (2009), indicating that the model configuration used here is capable of realistically simulating TIW activity in terms of both spatial patterns and intensity.

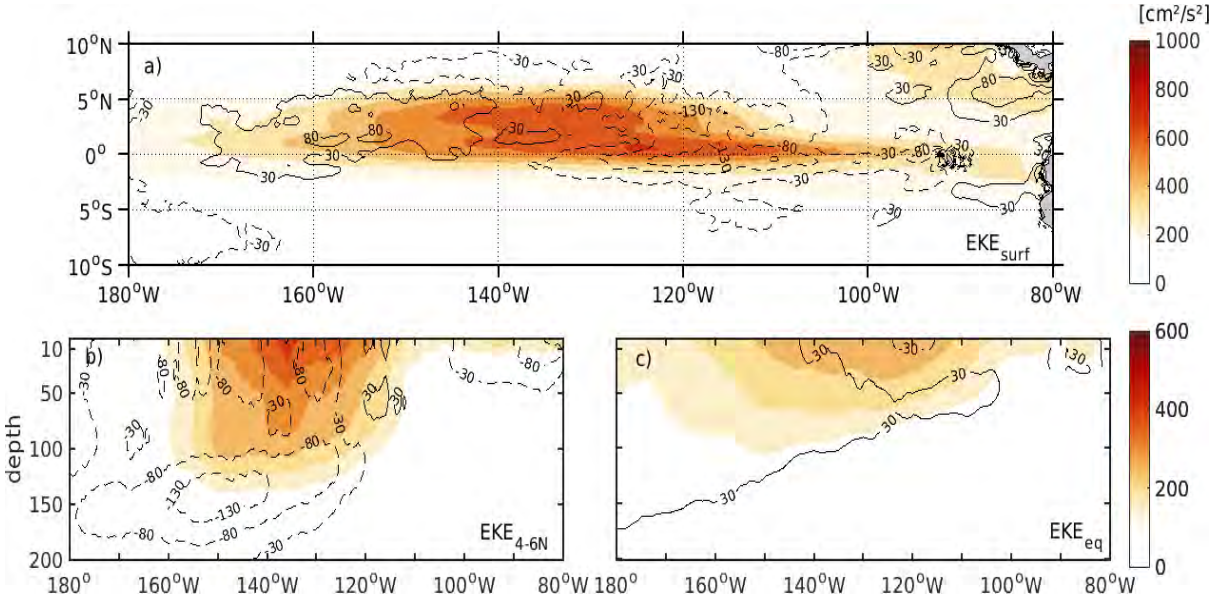

Fig. 3: Mean surface (a) and zonal sections averaged along the equator (2.5°N-2.5°S) (b) and over the TIWs region (3°N-5°N) (c) of EKE from the CR-long simulation (shading). Contours show the biases between the CR-long simulation and GLORYS2V4 (dashed/plain black contours for negative/positive biases) for the total 1993-2018 period.

To complement this evaluation of TIW features, the mean mesoscale activity is also evaluated using the mean eddy kinetic energy (*i.e.*, $EKE = \frac{1}{2}(\overline{u'^2 + v'^2})$) as a metric (Fig. 3). The highest values of EKE at the surface are found along the equator and in an off-equatorial band with a maximum centered around 3°N (Fig. 3a), and between 110°W and 160°W, the region where TIWs are indeed the most active (Fig. 1b). In addition, the EKE is found to be the strongest (~250–500 cm²s⁻²) between the surface and 100 m (Fig. 3b,c), dropping to almost zero below 200 m in the TIW active region. Overall, the levels and patterns of EKE are in good agreement with other modeling studies (Marchesiello et al. (2011)) even those at higher resolution (e.g., Maillard et al. (2022a) using CROCO at 1/12 degree horizontal resolution) indicating that the submesoscale dynamics associated with finer structures within TIWs main cusps (unresolved in the present modeling study) do not represent a large portion of the intraseasonal mesoscale activity in equatorial regions. This gives confidence in the

ability of our simulation at a 1/4 degree horizontal resolution to capture the salient features of the TIWs mesoscale dynamics and associated intraseasonal variability.

4. IEKWs-TIWs interaction energetics

a. Composite Analysis: EKWs-TIWs interaction

We now evaluate the ability of the CR-long simulation to capture the IEKWs-TIWs nonlinear interaction. We begin by characterizing the IEKWs-TIWs in a manner similar to Escobar et al. (2022). In particular, in order to capture the variability of TIWs and IEKWs with a period of ~30 days and 60-90 days respectively, we compute, similarly to Escobar-Franco et al. (2022), the intraseasonal anomalies of the detrended sea level from the CR-long simulation as the departure of the instantaneous daily data from the monthly mean following the method by Lin et al. (2000). Then a decomposition of the simulated sea level intraseasonal anomalies into Complex Empirical Orthogonal Functions (CEOF) is performed over the domain 160°E-90°W and 10°N-10°S. The reader is referred to Barnett (1983) for details on the CEOF analysis, a classic technique to evaluate propagating climate signals (e.g., Boucharel et al., 2013, 2016).

The first mode (CEOF1) is characterized by a pattern with a peak amplitude along the equator that is symmetric with respect to the equator (Fig. 4a), and thus captures the variability associated with IEKWs (with an explained variance of 16%) although some wavy patterns can also be observed toward the TIWs region indicating the interaction between the two types of waves. The second mode (CEOF2) has a peak loading at the center of action of TIW activity (Fig. 4b). Overall, the results are consistent with those obtained from the satellite altimeter data (Escobar-Franco et al. (2022)), although the order of the first two modes is reversed and the interaction is not as equally distributed between the two modes as in the observations, where a more mixed IEKW-TIW pattern was found for both CEOF1 and 2. From the CR simulation, the IEKWs-TIWs interaction is mainly captured by the first mode.

We then identify the intraseasonal events associated with the IEKWs-TIWs interaction in a similar manner than in Escobar-Franco et al. (2022), i.e., when the daily sea level anomalies reconstructed using CEOF1 and averaged in the region [2°S–2°N, 150–130°W] is above (downwelling events) or below (upwelling events) 1 standard deviation. We also require that the selected events approximately coincide with those identified from observations by Escobar-Franco et al. (2022) in order to ease the interpretation of the comparison between the model and observations. We found that 14 downwelling and 19 upwelling events met these conditions, which represent respectively ~56 % and 67% of the events identified in (Escobar-Franco et al. (2022)). We will use this subset of events to perform a composite evolution analysis of the eddy kinetic energy budget terms for the differences between the CR and LIN runs in order to infer processes at work during the IEKW-TIW interaction.

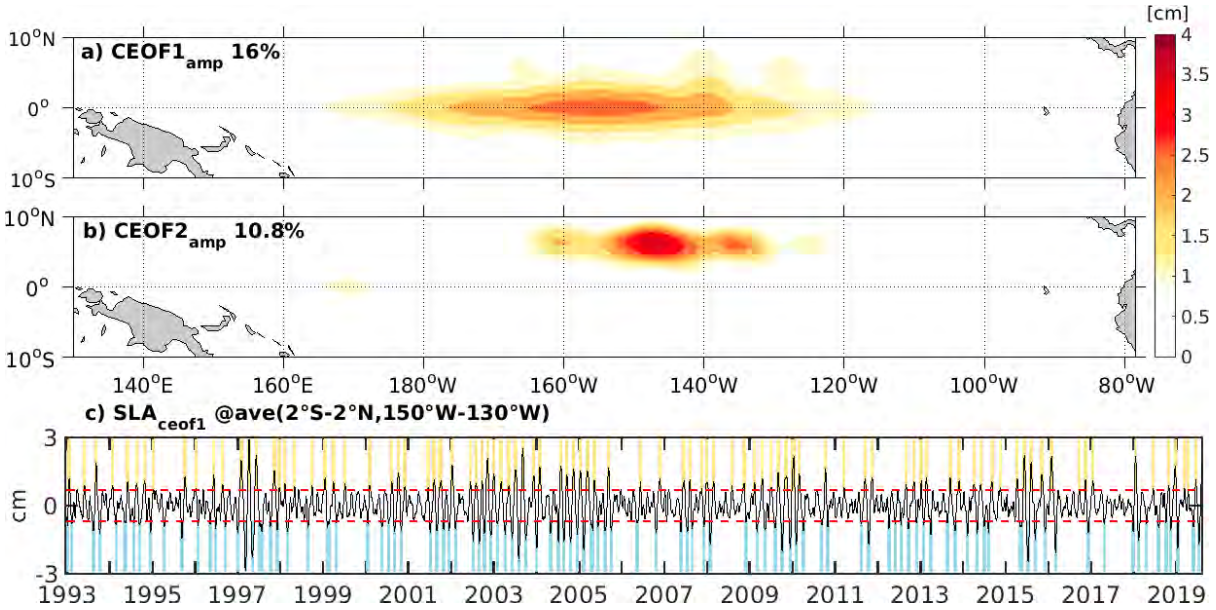

Fig. 4: Decomposition into Complex Empirical Orthogonal Functions (CEOF) of the intraseasonal sea level anomalies from the CR-long simulation. Spatial patterns of the amplitude of the (a) first (CEOF1) and (b) second (CEOF2) mode. (c) Reconstructed SLA from CEOF1 and averaged in the region (2°S–2°N, 150°W–130°W). SLA events with anomalies above (below) 1 standard deviation are highlighted in yellow (blue).

b.Eddy Kinetic Energy Budget

We now evaluate the changes in EKE associated with the passage of different phases of IEKWs. Fig. 5 shows the differences in surface EKE between the ensemble average of upwelling (Fig. 5a) or downwelling (Fig. 5b) IEKWs events of the selected TIW-IEKW events averaged over the first 20 days and the background EKE from CR (i.e., long-term mean). The averaging period of 20 days corresponds approximately to the time it takes for the wave to pass through the main region of TIWs activity. We observe an increase (decrease) in the EKE along the equator and in the region of TIW activity (140°W-100°W, 2°S-5°N) for the upwelling (downwelling) IEKWs compared to the long-term average EKE.

Similar, yet less patchy patterns are observed when the EKE is integrated in the 100-m upper-ocean layer (Fig. 5c and d). The fractions of EKE change relative to the long-term mean induced by the different phases of IEKWs are shown in Fig. 5e for the average over the volume (2°S-5°N; 140°W-100°W; 0-100m), indicating a marked asymmetric response of EKE change to IEKWs phase (upwelling versus downwelling). This is similar to studies focused on interannual timescales, which showed that the mean EKE associated with TIWs tends to increase significantly more during cold events than during warm events (Xue et al. 2020) due to increased SST meridional gradient. In particular, the upwelling IEKW enhances the volume-averaged EKE by 27% and the downwelling IEKW reduces it by 20% during the first 20 days, which implies a difference between upwelling and downwelling phases of 47% in terms of the total volume-averaged EKE. Note that this is in contrast to the idealized experiment of HT16, which found an asymmetry in mean EKE between upwelling and downwelling phrases that was about half weaker over almost the same volume (7°S-10°N; 150°W-110°W; 0-244m). We will see that such differences can be partly interpreted as resulting from the spread of IEKW amplitude within our ensemble, and also from the

different experimental setup. Overall, our results indicate that the passage of both IEKWs phases (upwelling and downwelling) are influential on the TIWs activity, being significant at the 95% confidence level.

While the previous analysis (Fig. 5) provides the overall integrated changes in EKE associated with the different phases of the IEKWs (i.e., the baseline is the mean EKE over the span of the simulation), we now analyze the changes in EKE between CR and LIN among the selected events (i.e., baseline is the mean EKE from the ensemble of selected events of the LIN simulations), which provides an estimate of the actual EKE changes induced by the interaction between the IEKWs and the TIWs. The difference between CR and LIN thus provides convenient access to the anomalous EKE budget associated with this interaction. Fig. 6 displays the differences between the CR and LIN experiments in surface and upper-ocean (averaged in the first 100m) EKE composite (i.e., ensemble average) for the different phases of IEKWs events. Concurrently, a large (small) increase in EKE can be observed in the dominant region of TIW activity (140°W-100°W, 2°S-5°N) during upwelling (downwelling) IEKWs events. These patterns of EKE change with a meridional dipole structure characterized by a large (small) transfer of EKE from the equatorial band to the off-equatorial TIWs region during the passage of an upwelling (downwelling) IEKW, are indicative of where variations in conversion terms between CR and LIN should occur.

We now document the energetics associated with the IEKWs-TIWs interaction based on the composite analysis of the difference in the conversion terms embedded in the EKE equation between the CR and LIN simulations. The focus is on the barotropic and baroclinic energy conversion terms that are the dominant processes to explain the rate of EKE changes.

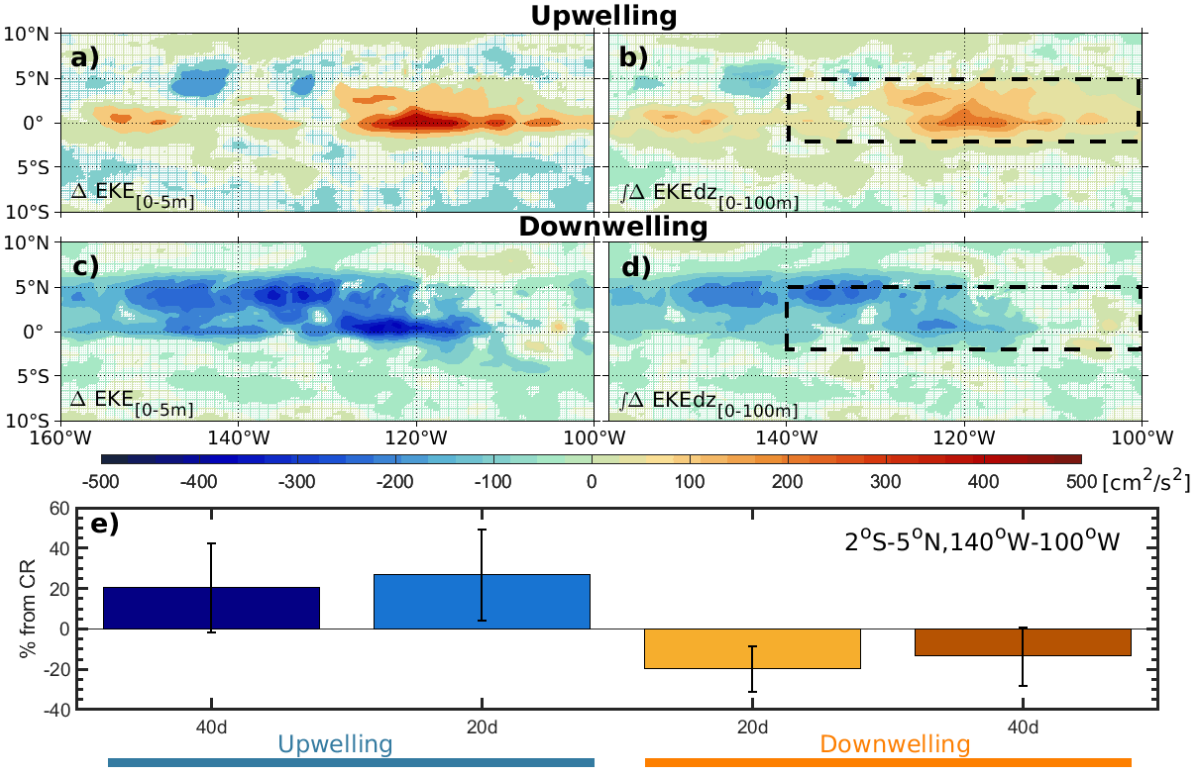

Fig. 5: Mean composite anomalies in surface EKE for upwelling (a) or downwelling (c) IEKWs events. Anomalies refer here as the difference between the mean over the first 20 days for the ensemble average of individual selected events and the long-term mean (1993-2018). (b, d) same as (a,c) but for the average quantities over the first 100m. The white dots denote areas where the difference does not exceed the 95% confidence level based on a

two-tailed Student's t-test. (e) Differences in upper-ocean EKE averaged in the region 2°S-5°N, 140°W-100°W for upwelling (blue bar) or downwelling (orange bar) IEKWs events and the long-term mean. EKE composites are averaged in the first 20 (blue/orange bar) or 40 days (dark blue/brown bar). Values are indicated in % of the CR-long run background EKE. The error bars denote the 95% confidence intervals based on a Student *t* test.

The differences in the EKE and conversion terms between the CR and LIN experiments' ensemble average are shown for both a latitude-depth and a longitude-depth section averaged in the region of TIWs activity in Fig. 7 and Fig. 8 respectively, in order to visualize details in their vertical structure. It indicates that the strong (small) increase in EKE in the TIWs region north of the equator extends down to 150m when upwelling (downwelling) IEKWs propagate in the presence of TIWs. This stronger EKE is associated with an increased TIWs activity triggered during the passage of upwelling IEKWs by a stronger barotropic conversion confined within the top 50 meters (Fig. 7c and Fig. 8c). The barotropic conversion is due to a stronger meridional shear and larger transfer of available potential energy from the equatorial zonal surface currents shear, in particular between the EUC and NECC (Fig. 7e and Fig. 8e). This increase in EKE also comes from baroclinic instabilities that occur mainly in the subsurface between 30 and 100m (Fig. 7b and Fig. 8b). Such baroclinic conversion arises from the increase in the meridional temperature gradient associated with the shoaling of the equatorial thermocline in the eastern equatorial Pacific induced by the passage of upwelling IEKWs (Fig. 7e and Fig. 8e). Conversely, because changes in equatorial stratification due to the passage of downwelling IEKWs do not lead to significant changes in either the zonal circulation or the meridional thermal structure, both energy conversion terms are much weaker when downwelling IEKWs propagate in the presence of TIWs, revealing only slightly altered TIW activity and a weak nonlinear interaction between the two waves. This asymmetry in the dynamical response is likely to convert in the heat budget over the central-eastern equatorial Pacific as will be seen later on (discussion section).

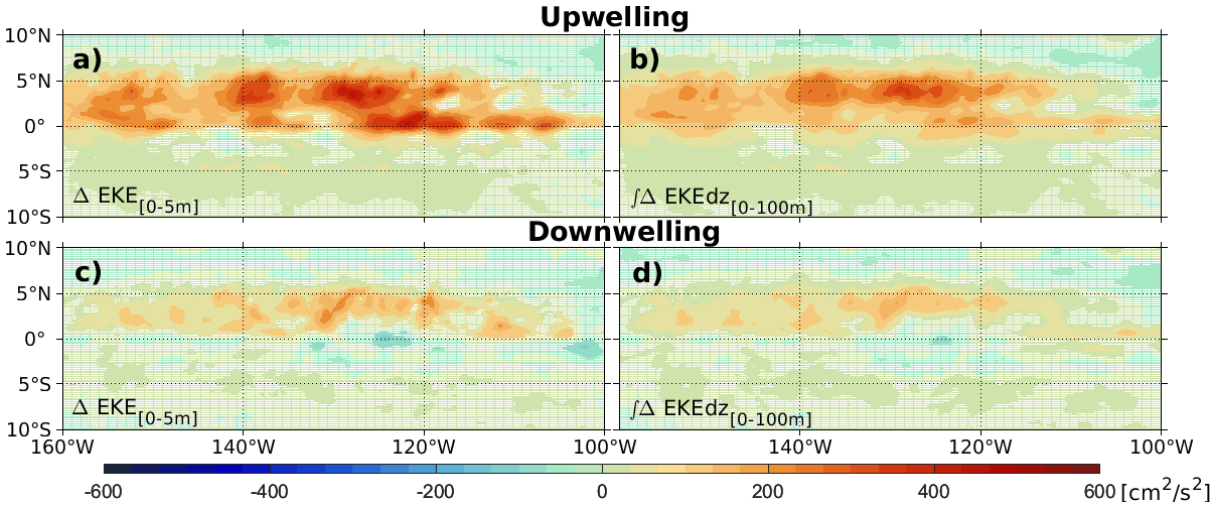

Fig. 6: Differences in surface (a) and upper-ocean (averaged in the first 100m) (b) EKE composite (i.e., ensemble average) during upwelling IEKWs events between the CR and LIN experiments (Δ=CR-LIN). (c) and (d) are the same respectively as (a) and (b) but for downwelling IEKWs events. Events composites are averaged during the first 20 days after the model is initialized. The white dots denote areas where the difference between the mean

values of the CR and LIN run does not exceed the 95% confidence level based on a two-tailed Student′s t-test.

To further quantify the asymmetry in the TIWs-IEKWs interaction between upwelling and downwelling IEKWs phases, we inspect the barotropic and baroclinic conversion rates as a function of the amplitude of the IEKWs. Fig. 9 presents scatter plots between the amplitude of IEKWs events along the equator and the changes in EKE, barotropic and baroclinic conversion rates in the regions where the peak anomalies are found (see rectangles in Fig. 8). Fig. 9a evidences the asymmetry in the response of changes in EKE to upwelling and downwelling IEKWs with a linear correlation of 0.77, reflecting the much stronger increase in EKE during upwelling events than during downwelling events. Notably, there is a tendency for a larger dispersion in the amplitude of ΔEKE in response to upwelling IEKWs, resulting in an approximate nonlinear relationship between the IEKWs amplitude and changes in EKE, with the second-order polynomial fit between ΔEKE and IEKWs strength reaching 0.81 (black line in Fig. 9a). This indicates a larger sensitivity of change in EKE to the characteristics of the IEKWs for the upwelling phase than for the downwelling phase. Interestingly, this asymmetry is due to the changes in the barotropic instabilities rather than the baroclinic instabilities induced by the presence of TIWs (Fig. 9b). In particular, there is no change in the correlation from the linear to the nonlinear regression between the IEKWs amplitude and the baroclinic conversion terms, while the correlation increases by ~14.4% for the barotropic conversion terms (see green and black lines in Fig. 9b). However, the standard error of the nonlinear regression model (Fig. 9) is larger for the barotropic instabilities than for the baroclinic instabilities. Nevertheless, this indicates a more nonlinear relationship between the amplitude of the passing IEKWs and the induced changes in the meridional shear of the background zonal flows $\delta U/\delta y$. On the other hand, the changes in the meridional temperature gradient $\delta T/\delta y$ (Fig. 7 d,e) associated with the baroclinic energy conversion involved in the TIWs-IEKWs interaction responds more linearly to the amplitude and phase of the passing IEKW.

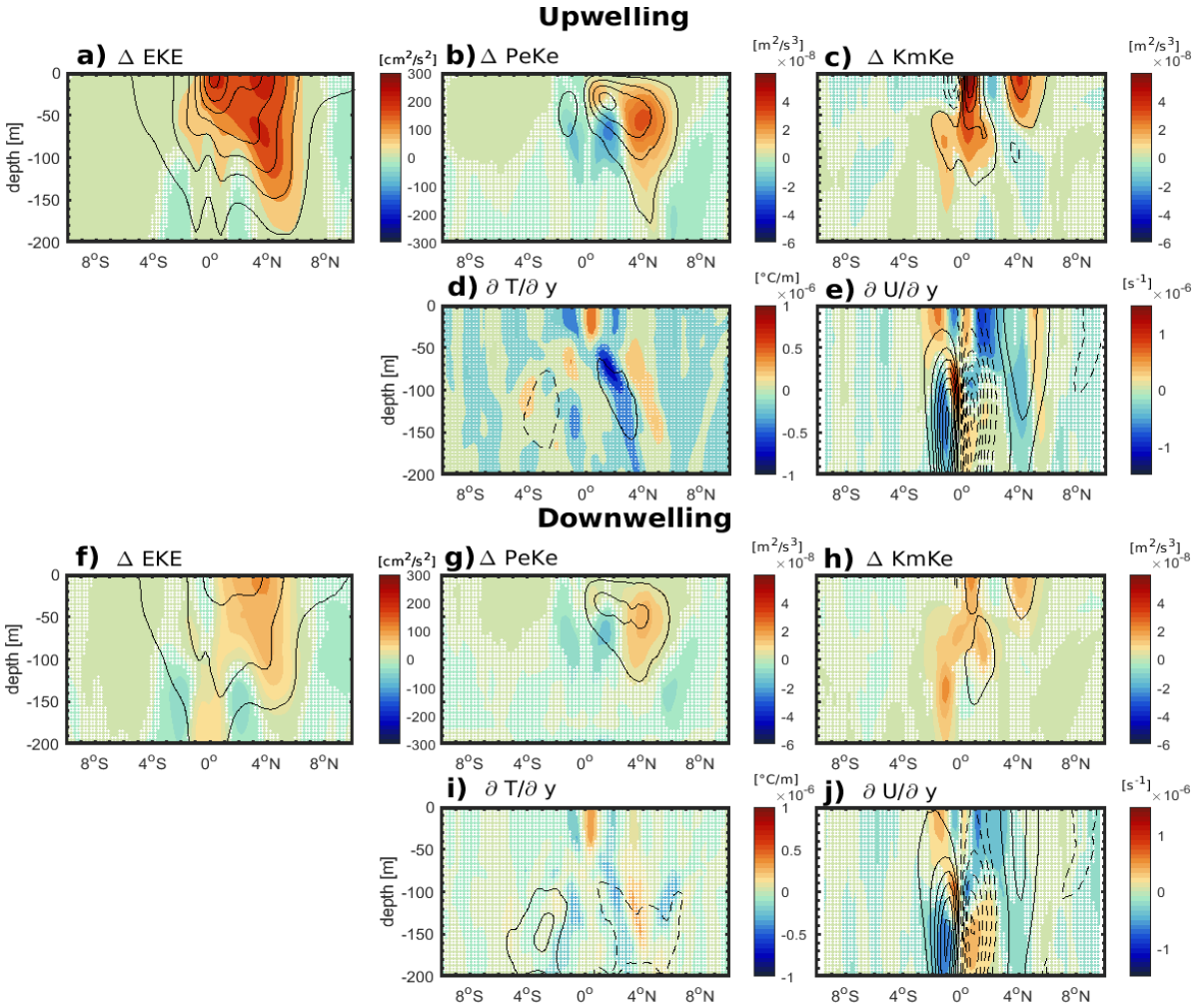

Fig. 7: Zonally averaged (between 160°W and 110°W) latitude-depth sections for the Upwelling/Downwelling phases (top panels/bottom panels) of the differences in ensemble-averaged (a/f) EKE, (b/g) baroclinic instability (PeKe), (c/h) barotropic instability (KmKe), (d/i) meridional temperature gradient (δT/δy) and (e/j) zonal current shear (δU/δy) during IEKWs upwelling events between the CR and LIN simulations (Δ=CR−LIN). The composites are averaged in the first 20 days after the events are identified (cf. section 2d). Contours in each panel show the mean values for the CR run ensemble average (EKE contours every 100cm²s⁻², PeKe and KmKe contours from $1x10^{-8}$m²s³ every $2x10^{-8}$ m²s³, δU/δy from $1x10^{-6}$s⁻¹ every $1x10^{-6}$s⁻¹ and δT/δy from $0.5x10^{-6}$ °Cm⁻¹ every $0.5x10^{-6}$ °Cm⁻¹). The white dots indicate the regions where the difference does not exceed the 95 % confidence level based on a two-tailed Student′s t-test.

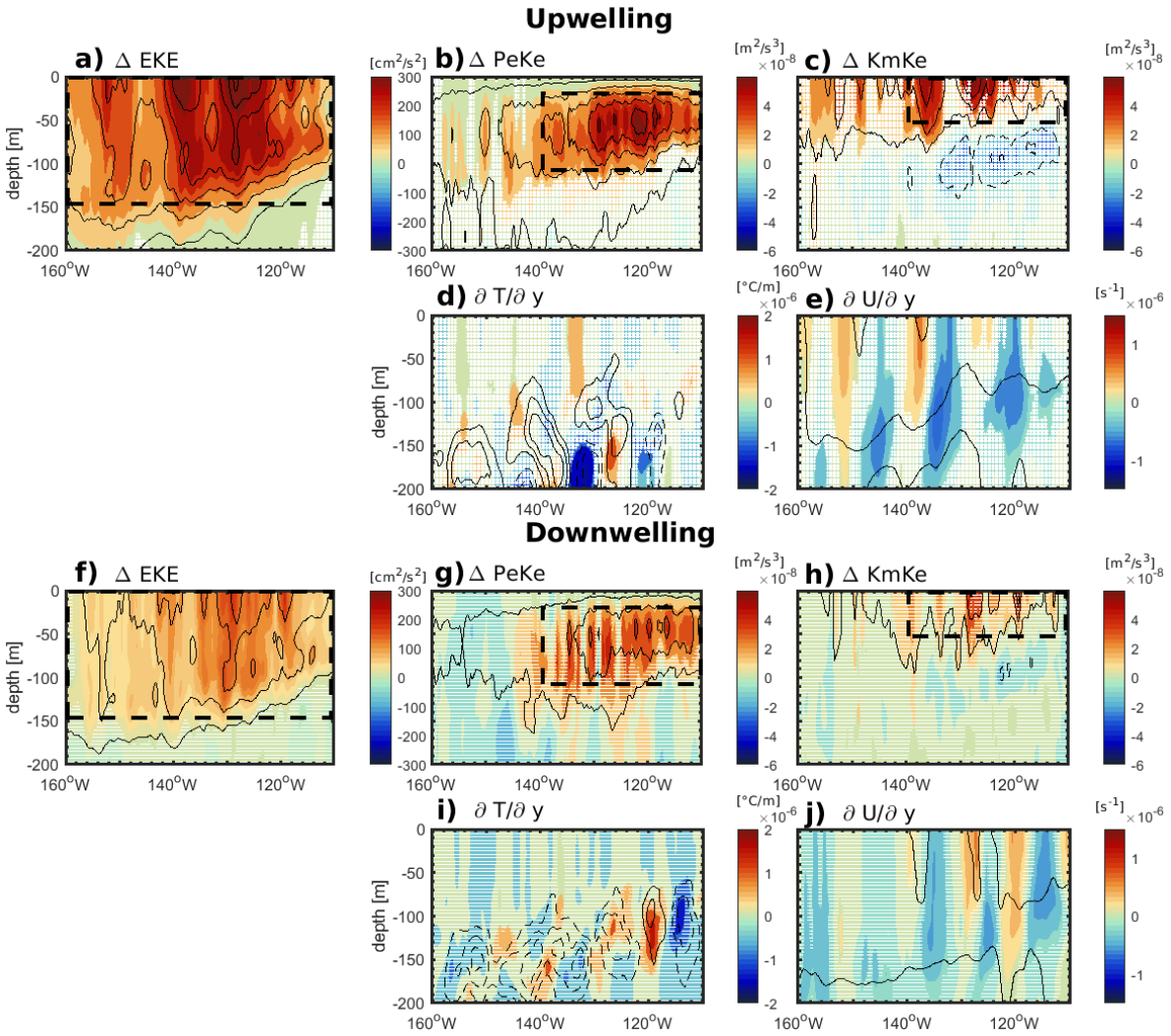

535

536 Fig. 8: Same as Fig. 7 but for Longitude-depth sections (averaged between 3°N and 5°N).

537

538 As an attempt to assess the temporal asymmetry in the response and dispersion among our
539 ensemble, we present in Fig. 10 the evolution of the differences between the CR and LIN
540 ensemble means in the cumulative EKE, baroclinic, and barotropic conversion terms
541 averaged over the regions delineated in Fig. 8 for upwelling and downwelling IEKWs events.
542 The reference time for the integration of quantities corresponds to the initial time of the LIN
543 simulations, which implies that the curves start from zero (except for the sea level). In order
544 to emphasize differences between the upwelling and downwelling phases, we select the most
545 energetic IEKWs events (i.e., cumulative EKE > 1*std for the upwelling events and < 1*std
546 for the downwelling events) for deriving the composite evolutions. First of all, we observe
547 more dispersion among the upwelling events than in the downwelling events, due to the
548 different characteristics of the IEKWs, consistently with results of Fig. 9. Fig. 10 also reveals
549 that the changes in EKE occur instantaneously, i.e., as soon as the upwelling IEKW reaches
550 the TIWs field, suggesting that both conversion terms of instability have a quick response,
551 likely once the changes in the meridional temperature and zonal current gradient are altered
552 by the interaction between TIWs and the propagation of upwelling IEKWs.

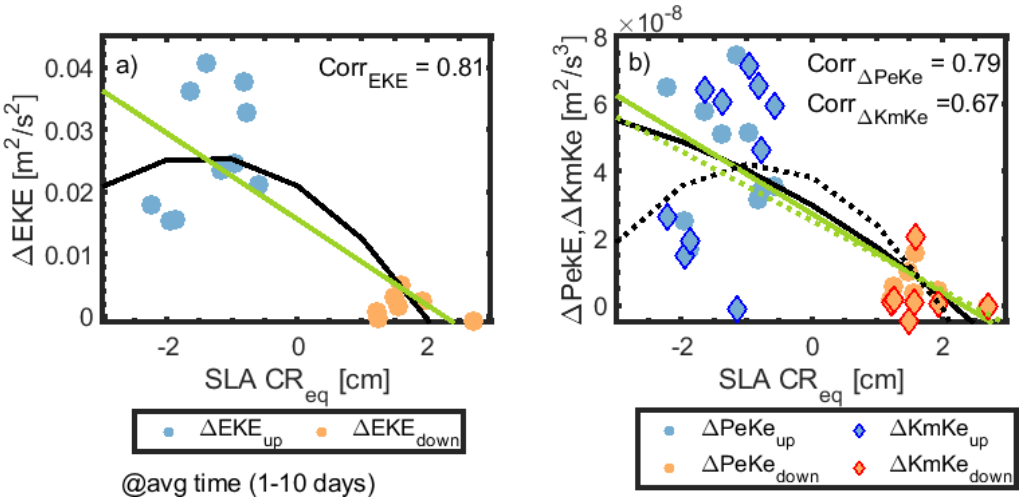

553

554 Fig. 9: Scatter diagrams between the sea level anomalies (SLA) averaged between
555 120°W-160°W and 2.5°N-2.5°S obtained from the CR simulation and the difference
556 (CR-LIN) of (a) EKE, (b) PeKe and KmKe averaged in the corresponding region indicated in
557 Fig. 8. The blue (orange) markers correspond to the instabilities values for the upwelling
558 (downwelling) phase of the Kelvin wave. The continuous black (green) line is the polynomial
559 (linear) curve fitting to the set of values of ΔEKE and ΔPeKe and the dotted line for the
560 ΔKmKe. Quantities are averaged for the first 10 days of the interaction. "Corr" refers to the
561 correlation between the time series of the instabilities terms and the SLA at the two phases of
562 the Kelvin wave based on the second-order polynomial fit.

563

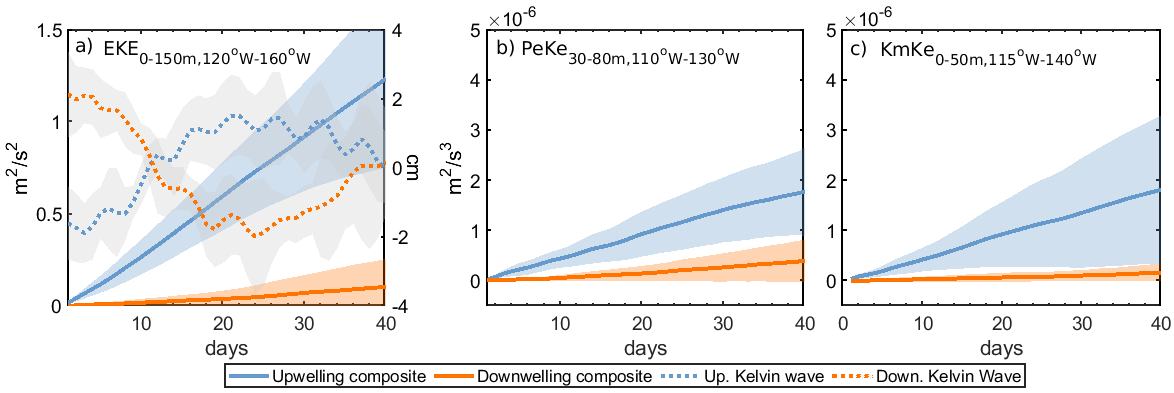

564

565 Fig. 10: Time evolution of the difference between the CR and LIN ensemble average in
566 cumulative (a) EKE, (b) baroclinic and (c) barotropic conversion terms averaged in regions
567 delineated in Fig. 8 (a), (b) and (c) respectively for upwelling (plain blue lines) and
568 downwelling (plain orange lines) IEKWs events. Composite sea surface height anomalies
569 (SSH) averaged in the equatorial region [120°W-160°W; 2.5°N-2.5°S] during upwelling
570 (dashed blue lines) and downwelling (dashed orange lines) IEKWs events are shown in (a),
571 where the IEKW has a symmetrical amplitude between both upwelling and downwelling
572 phases. The shading around the time series represents the +/-1 standard deviation of the
573 ensemble difference.

574

575

576

5. Discussion and conclusion

Observations suggest that IEKWs and TIWs interact nonlinearly (Escobar-Franco et al. (2022)), but the underlying mechanism remains unclear. In this study, our motivation was to gain insight into the mechanisms at work based on sensitivity experiments with a tropical Pacific ocean model, and to extend the study of HT16 in a more realistic setup (1993-2018) to allow a more direct comparison with observations. In particular, the activity of IEKWs and TIWs exhibits a pronounced seasonal cycle and interannual modulation, which must be taken into account to further advance the understanding of their interaction at intraseasonal timescales. IEKWs may also have different vertical structure variability that may be influential on this interaction. Our model setup is shown to be able to realistically reproduce most aspects of the mean and seasonal circulation in the equatorial Pacific, in particular a realistic mean thermocline and the mean vertical structure of the EUC and NEC. The model also simulates a fairly realistic pattern and amplitude of the mean EKE in the TIW region, resulting in a CEOF mode decomposition of sea level intraseasonal anomalies that is consistent with that of the observational study by Escobar-Franco et al. (2022), although the observations show a more mixed IEKW-TIW pattern than the model. In particular, the sea level intraseasonal variability projects onto two dominant CEOF modes that mix contributions of the IEKWs (i.e., peak loading along the equator with an approximate Gaussian meridional structure) and the TIWs (i.e., peak loading along ∼5°N in the central Pacific). Analysis of the changes in the mean EKE in the TIWs region during upwelling and downwelling IEKW events further shows that the latter is increased more during upwelling events than during downwelling events, indicating an asymmetry of the TIW-IEKW interaction with respect to the phase of the Kelvin wave (despite the symmetry in terms of equatorial SLA between the two phases). The propagation of upwelling IEKWs leads to a strong and rapid increase (about 27% of the background level) of the upper-ocean mesoscale activity north of the equator, whereas downwelling IEKWs trigger a barely significant decrease (20%) in the off-equatorial eddy activity. In order to gain insight into the processes at work in each of the individual events selected from the CEOF decomposition, we perform sensitivity experiments with the model, which consist in eliminating the nonlinear advection in the momentum equations. This provides simulations of the selected events in which TIWs activity is strongly damped without affecting the mean state that serve as a baseline for the estimation of anomalies in the variables and tendency terms of the EKE rate of change. The results indicate that both barotropic and baroclinic conversion terms contribute rather equally to the increase in the mean EKE during upwelling events, with corresponding changes in the meridional temperature gradient and meridional current shear between the EUC and NECC (stronger in Figs. 8 and 9 d,e for the upwelling panel). The dispersion among individual events is quite large, reflecting the diversity of IEKW characteristics. However there is a clear separation in the results between the ensemble of upwelling and downwelling events in terms of the cumulative tendency terms (Fig. 9), consistent with the net effect observed on the mean EKE (stronger mean EKE for upwelling versus downwelling events) with respect to the long-term mean. Overall our results indicate that the IEKWs alter the balance of the EKE budget in the TIWs activity region resulting in the growth and decay of their mesoscale activity. While these results are qualitatively consistent with the idealized modeling study from HT16, we observed two noticeable differences: 1) a much faster (almost instantaneous) adjustment in TIWs activity and 2) a more asymmetric TIWs response to the passage of different phases of IEKWs. These differences are interpreted as resulting from the more realistic modeling framework used here. In particular, in their sensitivity experiments, HT16 use a Kelvin forcing at 160°W with a prescribed vertical structure, while corresponding to the first baroclinic mode derived from their model stratification, causing this prescribed IEKW to

dynamically adjust to the mean state through modal dispersion as it propagates eastward into the region of TIWs (Busalacchi and Cane (1988); Dewitte et al. (1999)). In other word, the experiment of HT16 favors IEKWs with energy dominantly projecting on the first baroclinic mode (evidenced in their composite evolution of the SSH of their Figure 7), which is not the case in observations (Dewitte et al. (1999); Cravatte et al. (2003)) and our modeling framework. Noteworthy higher-order baroclinic modes IEKWs can more easily interact with TIWs due to their finer vertical scales and their tendency to trap more energy in the surface layer than the first baroclinic mode Kelvin wave. It is suggested here that details in IEKWs vertical structure may explain the large dispersion of the response of changes in EKE to upwelling waves. Upwelling IKEWs tend in particular to originate from a location along the equator to the east of that of downwelling IKEWs as a response to the forcing by wind bursts (Chiodi and Harrison (2015)), so that they tend to project more energy on high-order modes with a larger sensitivity to details in mean stratification. Figure S1 shows the equatorial section of the root-mean-square of the CR (full line) and LIN (dotted) composite of the sea level anomalies projected onto the Kelvin meridional mode (following the method by Cane and Sarachik (1976) and Boulanger and Menkes (1995)) during the first 20 days. We observe a peak in SLA variability in the western/central Pacific around 170°E/210°E for downwelling/upwelling Kelvin waves suggesting indeed that upwelling IEKWs tend to be generated more to the east than downwelling IEKWs.

This issue would deserve more investigations, which could be based on our model setup, but is beyond the scope of the present paper.

Because our experimental setup, unlike that of Maillard et al. (2022ab) for example, is designed so that the mean state is not affected by the presence of individual IEKWs-TIWs interaction events, we cannot directly quantify its potential rectifying effect on lower frequency variability. However, it remains possible to evaluate how the nonlinear interaction between TIWs and IEKWs in the CR run has the potential to impact the heat budget in the eastern equatorial Pacific. We focus on the non-linear dynamical heating (NDH) term of the heat budget because this term has been shown to be involved in the interaction between TIWs and IEKWs in a former study (Escobar et al., 2002) and is also known to vary significantly during ENSO-induced TIWs activity (Xue et al 2022, 2021), allowing for a qualitative comparison with former studies. The meridional component of this term, which is dominated by the contribution from anomalous meridional currents in this region (Xue et al., 2020), is calculated ($NDH = - v'\delta yT'$) and compared with the observational estimate of Escobar-Franco et al. (2022) based on geostrophic currents, see their Figure 5c, black line). While the model allows for the integration over the first 100m, the estimation from observations implicitly assumes that the vertical structure of the geostrophic current is homogeneous over the first 100m, which is equivalent to assuming an idealized structure of a first baroclinic mode for horizontal currents (i.e., a step function along the vertical with a value of 1 in the first 100m and zero below) and that the mixed layer extends down to 100m (which is not the case in this region). Fig. 11 shows the results for the zonal average between 150°W and 110°W of the NDH meridional component. It shows that there is a good qualitative agreement between the observations and the model, despite the assumptions used to derive the observational estimate. Both estimates tend to have a strong loading just north of the equator although the model has a peak that differs from the observations, peaking at 2-3°N. The meridional variability is comparable between the two estimates, which somehow represents an indirect validation of the model.

We now estimate the NDH induced by the interaction considering intraseasonal anomalies of velocity and temperature as the difference between CR and LIN for the individual events ensemble average. Fig. 12 shows the latitude-depth sections in the central Pacific (zonal average between 160°W and 110°W) of this "anomalous" NDH decomposed into zonal and meridional components, for the ensemble mean of upwelling and downwelling events (mean over the first 20-days from starting date). It indicates that the region of influence of the anomalous NDH is concentrated north of equator, consistently with the meridional profile of mean NDH (Fig. 11) and that the meridional contribution dominates over the zonal contribution. The vertical structure of this term is also quite complex, which indicates that it may not be estimated easily from surface observations. The results also reveals the asymmetric response between upwelling and downwelling, with a stronger warming north of equator (∼4°N) due to the meridional NDH during upwelling events extending from the surface up to 200m (see Fig. 13 for statistical significance of the difference between upwelling and downwelling events). The warming tendency due to meridional NDH during upwelling events reaches 0.5 and 1°C/month in the first 200 meters, which is quite significant and comparable to the estimate of TIWs-induced NHH during La Niña events (Xue et al. 2020). Although our experimental framework cannot directly inform us of the rectifying pathways, this suggests that, over time and a series of successive events of similar phase, the TIWs-IEKW interaction can potentially be as effective as the TIWs-ENSO interaction in modulating the mean state in this region. In particular because TIWs warm the equatorial cold tongue through meridional nonlinear dynamical heating (Graham (2014); Im et al. (2012); Menkes et al. (2006)) and reduce the zonal circulation, their enhanced activity during the propagation of the upwelling IEKWs would therefore counteract the cooling due to the shoaling of the equatorial thermocline and the strengthening of the EUC induced by IEKWs. Conversely, the equatorial warming and circulation reduction induced by downwelling IEKWs will not be offset by changes in eddy activity since TIWs features remain essentially unchanged by the propagation of downwelling IEKWs. Considering that the statistics (frequency of occurrence, amplitude) of the upwelling and downwelling IEKW are comparable (which is also reflected in the statistics of WWBs and EWBs (Chiodi and Harrison (2015); Puy et al. (2016)), the IEKWs-TIWs interaction represents a potentially effective conduit by which mean SST in the central and eastern equatorial Pacific can be modulated at seasonal to interannual timescales. We may in particular speculate that it could explain why EWBs are in general not effective in counteracting developing El Niño events. This hypothesis would be interesting to test from ocean-atmosphere coupled models that can realistically simulate TIWs activity,the mean state and ENSO cycle. This is planned for future work.

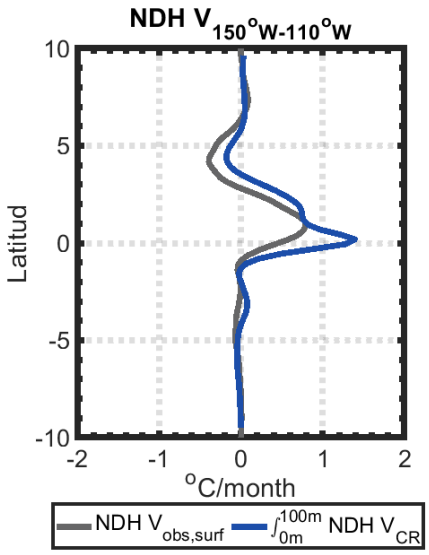

Fig. 11: Longitudinal average (between 150°W and 110°W) of intraseasonal NDH for the surface observations (gray line) and CR simulation (blue line) for the first 100m averaged and for the period 1993-2018.

The nonlinear effect of this interaction on intraseasonal equatorial variability also has implications for understanding the dissipation of IEKWs as they propagate in the far eastern Pacific. Previous studies have interpreted such a dissipation as resulting from either scattering of energy associated with the change in density along the sloping thermocline (Giese and Harrison (1991)), the vertical propagation of wave energy (Dewitte et al. (1999)), the loss in energy associated with the reflection of Rossby wave onto the density front near 120°W (Mosquera-Vásquez et al. (2014)), or Doppler shifting by the equatorial undercurrent (McPhaden (1986)). Our results suggest that the IEKWs-TIWs interaction could also participate in reducing the amplitude of the upwelling IEKWs in the far eastern Pacific since the peak amplitude at 90°W is smaller by 50% in LIN than in CR (not shown). Note that this is consistent with the La Niña events being of the Central Pacific type. Overall, there is a need to investigate to what extent such an interaction may contribute to the so-called ENSO diversity (Capotondi et al. (2020)), which refers to the existence of distinct ENSO patterns (Central Pacific vs. Eastern Pacific) of contrasting magnitude. This could be addressed by coupled model experiments based on the model setup developed here, coupled to an atmospheric model with reduced physics. This is also a plan for future work. Regardless, we believe that our study suggests that the IEKWs-TIWs interaction may represent another important facet of tropical Pacific system dynamics that needs to be considered in order to simulate and better understand the energy cascade between high and low frequency variability in this region.

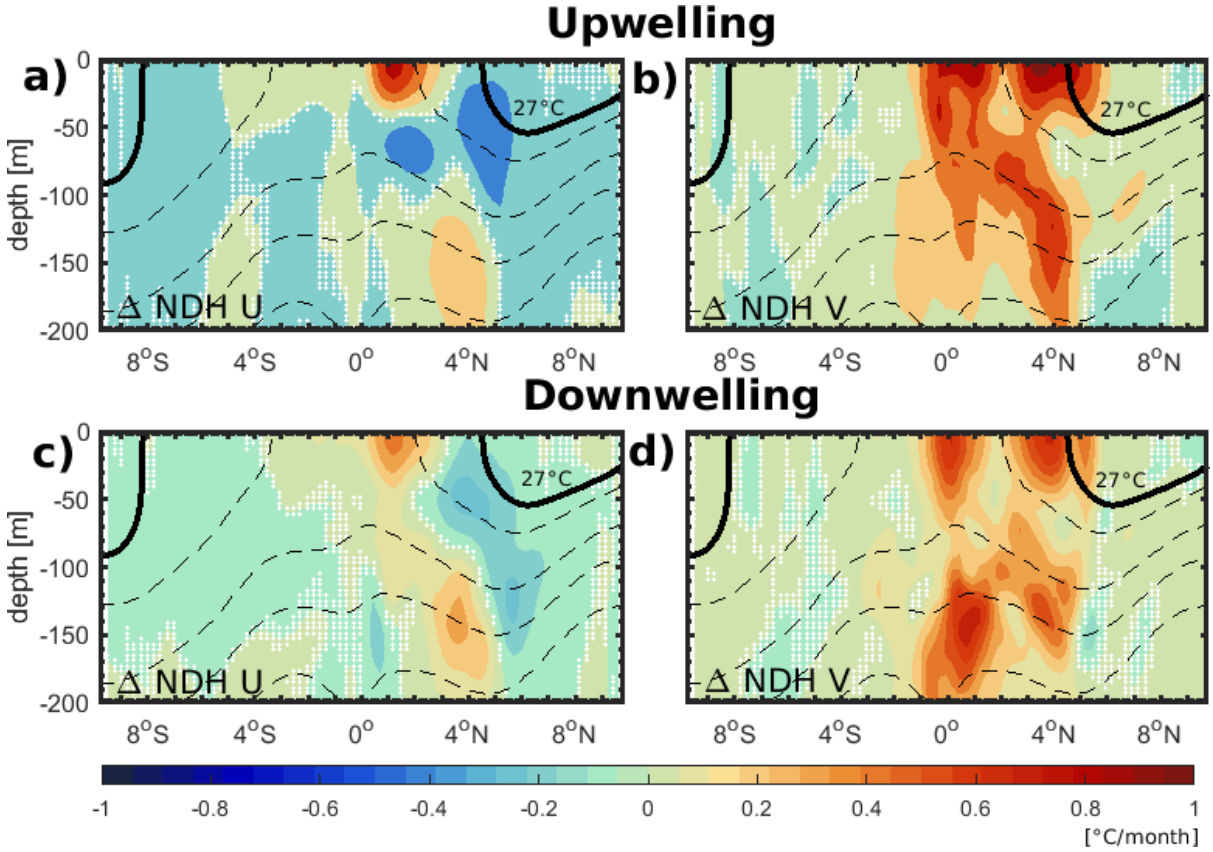

Fig. 12: Latitude-depth sections (averaged between 160°W and 110°W) of the differences in ensemble-average (a) Zonal NDH (ΔNDH U) and (b) Meridional NDH (ΔNDH V). The white dots indicate the regions where the difference does not exceed the 95 % confidence level based on a two-tailed Student's t-test. The black and dashed contours are the mean state of sea temperature from the CR (from 14°C every 4°C). The 27°C isotherm is denoted by the solid line.

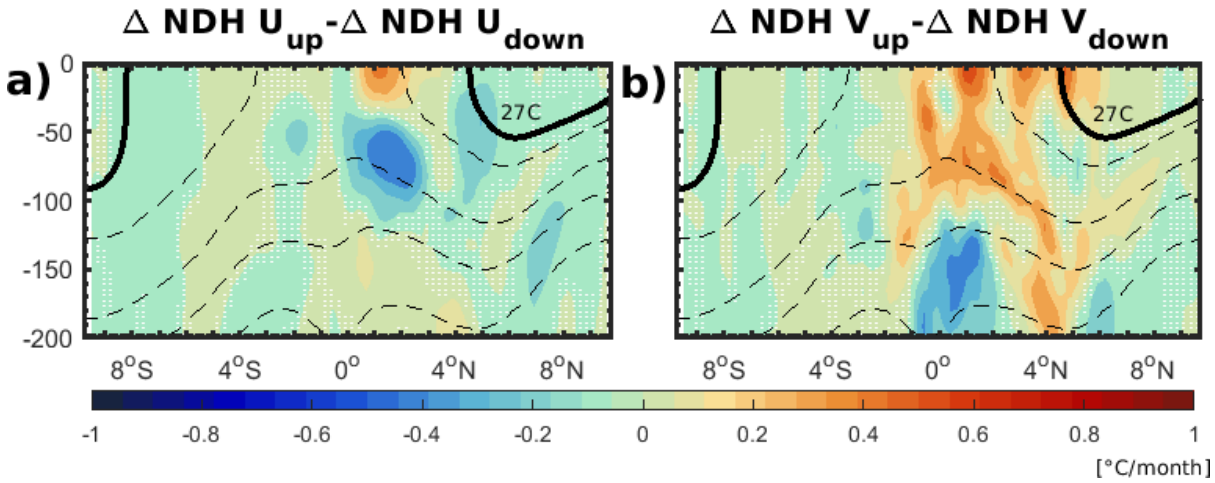

Fig. 13: Latitude-depth sections (averaged between 160°W and 110°W) of the differences between upwelling and downwelling (from ensemble-average) for (a) Zonal NDH (NDH U) and (b) Meridional NDH (NDH V). The white dots indicate the regions where the difference does not exceed the 95 % confidence level based on a two-tailed Student's t-test. The black and dashed contours are the mean state of sea temperature from the CR (from 14°C every 4°C). The 27°C isotherm is denoted by the solid line.

Acknowledgments.
BD acknowledges support from ANID (Concurso de Fortalecimiento al Desarrollo Científico de Centros Regionales 2020-R20F0008-CEAZA, Anillo Eclipse ACT210071 and Centro de Investigación Oceanográfica en el Pacífico Sur-Oriental COPAS COASTAL FB210021, Fondecyt Regular N°1231174) and Agence Nationale de la Recherche (grant ANR-18-CE01-0012). This project was also supported by the French Agence Nationale de la Recherche project MOPGA "TROCODYN" (Grant ANR-17-MPGA-0018). The authors would like to acknowledge the region Occitanie and the CALMIP center for providing access to their supercomputer Olympe.

Data Availability Statement.

All presented data are available at https://doi.org/10.6084/m9.figshare.24146691

Supplementary

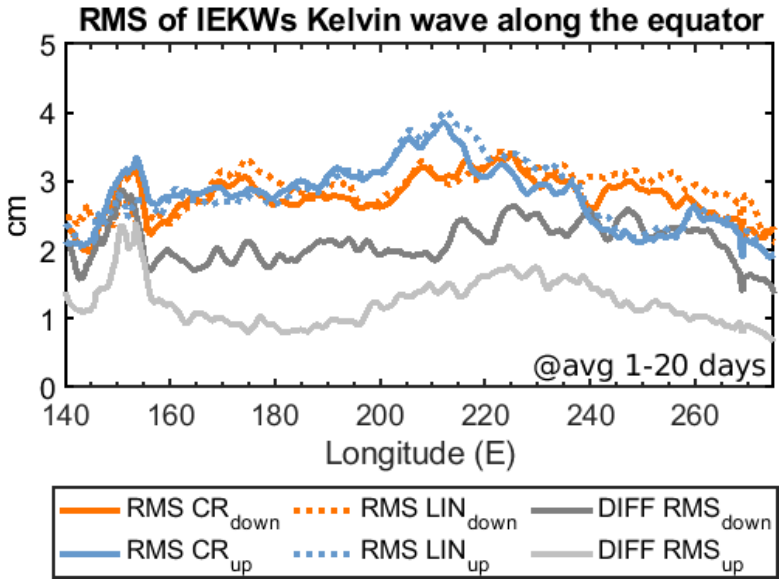

Fig. S1.- Plots of root-mean-square (RMS) of the SSH projected onto the first meridional Kelvin mode along the equator for the upwelling (blue lines) and downwelling (orange) events and their differences (CR-LIN, in gray lines) during the first 20 days. The full and dotted lines RMS from the CR and LIN simulation, respectively.

REFERENCES

Allen, M.R., Lawrence, S.P., Murray, M.J., Mutlow, C.T., Stockdale, T.N., Llewellyn-Jones, D.T., Anderson, D.L.T., 1995. Control of tropical instability waves in the pacific. Geophysical Research Letters 22, 2581–2584. URL: https://agupubs.onlinelibrary.wiley.com/doi/abs/10.1029/95GL02653, doi:https://doi.org/10.1029/95GL02653, arXiv:https://agupubs.onlinelibrary.wiley.com/doi/pdf/10.1029/95GL02653

An, S.I., 2004. Interdecadal changes in the el nino–la nina asymmetry. Geophysical Research Letters 31.

An, S.I., 2008. Interannual variations of the tropical ocean instability wave and enso. Journal of Climate 21, 3680–3686.

Angell, J., Robinson, T., Lawrence, S., 1998. Topex/poseidon observations of kelvin, rossby and tropical instability waves in the equatorial pacific ocean. Advances in Space Research 22, 1561–1565.

Barnett, T., 1983. Interaction of the monsoon and pacific trade wind system at interannual time scales part i: the equatorial zone. Monthly Weather Review 111, 756–773.

Baturin, N., Niiler, P., 1997. Effects of instability waves in the mixed layer of the equatorial pacific. Journal of Geophysical Research: Oceans 102, 27771–27793.

Boucharel, J., Jin, F.F., 2020. A simple theory for the modulation of tropical instability waves by enso and the annual cycle. Tellus A: Dynamic Meteorology and Oceanography 72, 1–14.

Boucharel, J., F.-F. Jin, M.E. England, B. Dewitte, I.-I. Lin, S.-C. Huang, and M. A. Balmaseda, Influence of intraseasonal oceanic Kelvin waves on the Eastern Pacific hurricane activity. J. Climate, doi:10.1175/JCLI-D-16-0112.1y, (2016).

Boucharel, J., A. Timmermann, and F.-F. Jin, Zonal phase propagation of ENSO SST anomalies – revisited. Geophys. Res. Lett. DOI: 10.1002/grl.50685 (2013).

Boulanger, J.-P., and Menkes, C. (1995). Propagation and reflection of long equatorial waves in the Pacific Ocean during the 1992–1993 El Niño. J. Geophys. Res. 100:25041. doi: 10.1029/95JC02956

Busalacchi, A.J., Cane, M.A., 1988. The effect of varying stratification on low-frequency equatorial motions. Journal of physical oceanography 18, 801–812.

Cane, M., and Sarachik, E. (1976). Forced Baroclinic Ocean Motions .1. Linear Equatorial Unbounded Case. J. Mar. Res. 34, 629–665.

Capotondi, A., Wittenberg, A.T., Kug, J.S., Takahashi, K., McPhaden, M.J., 2020. Enso diversity. El Niño Southern Oscillation in a changing climate , 65–86.

Carton, J.A., Giese, B.S., 2008. A reanalysis of ocean climate using simple ocean data assimilation (soda). Monthly weather review 136, 2999–3017.

Chiodi, A.M., Harrison, D., 2015. Equatorial pacific easterly wind surges and the onset of la niña events. Journal of Climate 28, 776–792.

Conejero, C., 2021. Impact du changement climatique sur la circulation océanique dans les systèmes d'upwelling de bord Est de l'hémisphère Sud. Ph.D. thesis. Toulouse 3.

Cox, M.D., 1980. Generation and propagation of 30-day waves in a numerical model of the pacific. Journal of Physical Oceanography 10, 1168–1186.

Cravatte, S., Picaut, J., Eldin, G., 2003. Second and first baroclinic kelvin modes in the equatorial pacific at intraseasonal timescales. Journal of Geophysical Research: Oceans 108.

Debreu, L., Marchesiello, P., Penven, P., Cambon, G., 2012. Two-way nesting in split-explicit ocean models: Algorithms, implementation and validation. Ocean Modelling 49, 1–21.

Dewitte, B., Reverdin, G., Maes, C., 1999. Vertical structure of an ogcm simulation of the equatorial pacific ocean in 1985–94. Journal of Physical Oceanography 29, 1542–1570.

Escobar-Franco, M.G., Boucharel, J., Dewitte, B., 2022. On the relationship between tropical instability waves and intraseasonal equatorial kelvin waves in the pacific from satellite observations (1993–2018). Frontiers in Marine Science .

Fairall, C.W., Bradley, E.F., Hare, J., Grachev, A.A., Edson, J.B., 2003. Bulk parameterization of air–sea fluxes: Updates and verification for the coare algorithm. Journal of climate 16, 571–591.

Giese, B.S., Harrison, D., 1991. Eastern equatorial pacific response to three composite westerly wind types. Journal of Geophysical Research: Oceans 96, 3239–3248.

Graham, T., 2014. The importance of eddy permitting model resolution for simulation of the heat budget of tropical instability waves. Ocean Modelling 79, 21–32. URL: https://www.sciencedirect.com/science/article/pii/S1463500314000535, doi:https://doi.org/10.1016/j.ocemod.2014.04.005.

Grenier, M., Cravatte, S., Blanke, B., Menkes, C., Koch-Larrouy, A., Durand, F., Melet, A., Jeandel, C., 2011. From the western boundary currents to the pacific equatorial undercurrent: Modeled pathways and water mass evolutions. Journal of Geophysical Research: Oceans 116.

Gruber, N., Lachkar, Z., Frenzel, H., Marchesiello, P., Münnich, M., McWilliams, J.C., Nagai, T., Plattner, G.K., 2011. Eddy-induced reduction of biological production in eastern boundary upwelling systems. Nature geoscience 4, 787–792.

Gushchina, D., Dewitte, B., 2012. Intraseasonal tropical atmospheric variability associated with the two flavors of el niño. Monthly Weather Review 140, 3669 – 3681. URL: https://journals.ametsoc.org/view/journals/mwre/140/11/mwr-d-11-00267.1.xml, doi:10.1175/MWR-D-11-00267.1.

Harrison, D., Giese, B.S., 1988. Remote westerly wind forcing of the eastern equatorial pacific; some model results. Geophysical research letters 15, 804–807.

Hendon, H.H., Wheeler, M.C., Zhang, C., 2007. Seasonal dependence of the mjo–enso relationship. Journal of climate 20, 531–543.

Holmes, R., Thomas, L., 2015. The modulation of equatorial turbulence by tropical instability waves in a regional ocean model. Journal of Physical Oceanography 45, 1155–1173.

Holmes, R., Thomas, L., 2016. Modulation of tropical instability wave intensity by equatorial kelvin waves. Journal of Physical Oceanography 46, 2623–2643.

Huang, B., Liu, C., Freeman, E., Graham, G., Smith, T., Zhang, H.M., 2021. Assessment

and intercomparison of noaa daily optimum interpolation sea surface temperature (doisst)

version 2.1. Journal of Climate 34, 7421–7441.

Huang, B., Xue, Y., Wang, H., Wang, W., Kumar, A., 2012. Mixed layer heat budget of the el niño in ncep climate forecast system. Climate dynamics 39, 365–381.

Huang, B., Xue, Y., Zhang, D., Kumar, A., McPhaden, M.J., 2010. The ncep godas ocean analysis of the tropical pacific mixed layer heat budget on seasonal to interannual time scales. Journal of Climate 23, 4901–4925.

Im, S.H., An, S.I., Kim, S.T., Jin, F.F., 2015. Feedback processes responsible for el niño-la niña amplitude asymmetry. Geophysical Research Letters 42, 5556–5563.

Im, S.H., An, S.I., Lengaigne, M., Noh, Y., 2012. Seasonality of tropical instability waves and its feedback to the seasonal cycle in the tropical eastern pacific. The Scientific World Journal 2012.

Jin, F.F., An, S.I., Timmermann, A., Zhao, J., 2003. Strong el niño events and nonlinear dynamical heating. Geophysical research letters 30, 20–1.

Johnson, G.C., Sloyan, B.M., Kessler, W.S., McTaggart, K.E., 2002. Direct measurements of upper ocean currents and water properties across the tropical pacific during the 1990s. Progress in Oceanography 52, 31–61.

Kessler, W.S., 2006. The circulation of the eastern tropical pacific: A review. Progress in Oceanography 69, 181–217.

Large, W.G., McWilliams, J.C., Doney, S.C., 1994. Oceanic vertical mixing: A review and a model with a nonlocal boundary layer parameterization. Reviews of geophysics 32, 363–403.

L'Heureux, M.L., Levine, A.F., Newman, M., Ganter, C., Luo, J.J., Tippett, M.K., Stockdale, T.N., 2020. Enso prediction. El Niño Southern Oscillation in a changing climate, 227–246.

Lin, J.W.B., Neelin, J.D., Zeng, N., 2000. Maintenance of tropical intraseasonal variability: Impact of evaporation–wind feedback and midlatitude storms. Journal of the Atmospheric Sciences 57, 2793–2823.

Madden, R.A., Julian, P.R., 1972. Description of global-scale circulation cells in the tropics with a 40–50 day period. Journal of Atmospheric Sciences 29, 1109–1123.

Maillard, L., Boucharel, J., Renault, L., 2022a. Direct and rectified effects of tropical instability waves on the eastern tropical pacific mean state in a regional ocean model. Journal of Physical Oceanography .

Maillard, L., Boucharel, J., Stuecker, M., Jin, F.F., Renault, L., 2022b. Modulation of the eastern equatorial pacific seasonal cycle by tropical instability waves. Geophysical Research Letters 49, e2022GL100991.

Marchesiello, P., Capet, X., Menkes, C., Kennan, S.C., 2011. Submesoscale dynamics in tropical instability waves. Ocean Modelling 39, 31–46.

Marchesiello, P., McWilliams, J.C., Shchepetkin, A., 2001. Open boundary conditions for long-term integration of regional oceanic models. Ocean modelling 3, 1–20.

Masina, S., Philander, S., Bush, A., 1999. An analysis of tropical instability waves in a numerical model of the pacific ocean: 2. generation and energetics of the waves. Journal of Geophysical Research: Oceans 104, 29637–29661.

McCreary, J. P., and Z. Yu, 1992: Equatorial dynamics in a 2 1/2-layer model. Prog. Oceanogr., 29, 61–132, https://doi.org/10.1016/0079-6611(92)90003-I.

McPhaden, M.J., 1986. The equatorial undercurrent: 100 years of discovery. Eos, Transactions American Geophysical Union 67, 762–765.

McPhaden, M.J., Zebiak, S.E., Glantz, M.H., 2006. Enso as an integrating concept in earth science. science 314, 1740–1745.

Menkes, C.E., Vialard, J.G., Kennan, S.C., Boulanger, J.P., Madec, G.V., 2006. A modeling study of the impact of tropical instability waves on the heat budget of the eastern equatorial pacific. Journal of Physical Oceanography 36, 847–865.

Mosquera-Vásquez, K., Dewitte, B., Illig, S., 2014. The central pacific el niño intraseasonal kelvin wave. Journal of Geophysical Research: Oceans 119, 6605–6621.

Mosquera-Vásquez, K., Dewitte, B., Illig, S., Takahashi, K., Garric, G., 2013. The 2002/2003 el niño: equatorial waves sequence and their impact on sea surface temperature. Journal of Geophysical Research: Oceans 118, 346–357.

Philander, S., 1978. Forced oceanic waves. Reviews of Geophysics 16, 15–46.

Philander, S., Hurlin, W., 1988. The heat budget of the tropical pacific ocean in a simulation of the 1982–83 el niño. Journal of physical oceanography 18, 926–931.

Praveen Kumar, B., Vialard, J., Lengaigne, M., Murty, V., Mcphaden, M.J., 2012. Tropflux: Air-sea fluxes for the global tropical oceans—description and evaluation. Climate dynamics 38, 1521–1543.

Puy, M., Vialard, J., Lengaigne, M., Guilyardi, E., 2016. Modulation of equatorial pacific westerly/easterly wind events by the madden–julian oscillation and convectively-coupled rossby waves. Climate dynamics 46, 2155–2178.

Qiao, L., Weisberg, R.H., 1998. Tropical instability wave energetics: Observations from the tropical instability wave experiment. Journal of Physical Oceanography 28, 345–360.

Renault, L., Masson, S., Arsouze, T., Madec, G., Mcwilliams, J.C., 2020. Recipes for how to force oceanic model dynamics. Journal of Advances in Modeling Earth Systems 12, e2019MS001715.

Renault, L., Molemaker, M.J., McWilliams, J.C., Shchepetkin, A.F., Lemarié, F., Chelton, D., Illig, S., Hall, A., 2016. Modulation of wind work by oceanic current interaction with the atmosphere. Journal of Physical Oceanography 46, 1685–1704.

Roundy, P.E., 2006. The role of equatorial rossby waves in westerly wind bursts, in: 27th Conference on Hurricanes and Tropical Meteorology.

Seiki, A., Takayabu, Y.N., 2007. Westerly wind bursts and their relationship with intraseasonal variations and enso. part i: Statistics. Monthly Weather Review 135, 3325–3345.

Shchepetkin, A.F., McWilliams, J.C., 2005. The regional oceanic modeling system (roms): a split-explicit, free-surface, topography-following-coordinate oceanic model. Ocean modelling 9, 347–404.

Shinoda, T., Kiladis, G.N., Roundy, P.E., 2009. Statistical representation of equatorial waves and tropical instability waves in the pacific ocean. Atmospheric research 94, 37–44.

Vergara, O., Dewitte, B., Ramos, M., Pizarro, O., 2017. Vertical energy flux at enso time scales in the subthermocline of the southeastern pacific. Journal of Geophysical Research: Oceans 122, 6011–6038.

Wang, C., Fiedler, P.C., 2006. Enso variability and the eastern tropical pacific: A review. Progress in oceanography 69, 239–266.

955 Wang, M., Xie, S.P., Shen, S.S., Du, Y., 2020. Rossby and yanai modes of tropical instability
956 waves in the equatorial pacific ocean and a diagnostic model for surface currents. Journal
957 of Physical Oceanography 50, 3009–3024.

958 Wengel, C., Lee, S.S., Stuecker, M.F., Timmermann, A., Chu, J.E., Schloesser, F., 2021.
959 Future high-resolution el niño/southern oscillation dynamics. Nature Climate Change 11,
960 758–765.

961 Wheeler, M., Kiladis, G.N., 1999. Convectively coupled equatorial waves: Analysis of clouds
962 and temperature in the wavenumber–frequency domain. Journal of the Atmospheric
963 Sciences 56, 374–399.

964 Xue, A., F.-F. Jin, W. Zhang, J. Boucharel, and J.-S. Kug, Parameterizing the nonlinear
965 feedback on ENSO from Tropical Instability Waves (TIWs) by Nonlinear Eddy Thermal
966 Diffusivity. Climate Dynamics, https://doi.org/10.1007/s00382-023-06744-4, (2023).

967 Xue, A., Zhang, W., Boucharel, J., Jin, F.F., 2021. Anomalous tropical instability wave
968 activity hindered the development of the 2016/17 la niña. Journal of Climate 34,
969 5583–5600.

970 Xue, A., F.-F. Jin, W. Zhang, J. Boucharel, S. Zhao, and X. Yuan, Delineating the seasonally
971 modulated feedback onto ENSO from the Tropical Instability Wave activity. Geophys.
972 Res. Lett.,47, e2019GL085863.https://doi.org/10.1029/2019GL085863, (2020).

973 Yang, L., Murtugudde, R., Zheng, S., Liang, P., Tan, W., Wang, L., Feng, B., Zhang, T., 2022.
974 Seasonal variability of the pacific south equatorial current during the argo era. Journal of
975 Physical Oceanography 52, 2289–2304.

976 Yu, Z., J. P. McCreary, and J. A. Proehl, 1995: Meridional asymmetry and energetics of
977 tropical instability waves. J. Phys. Oceanogr., 25, 2997–3007,
978 https://doi.org/10.1175/1520-0485(1995)025,2997:MAAEOT.2.0.CO;2.

979 Yu, X., McPhaden, M.J., 1999. Seasonal variability in the equatorial pacific. Journal of
980 Physical Oceanography 29, 925–947.

981 Zhang, C., 2005. Madden-julian oscillation. Reviews of Geophysics 43.

Conclusion and perspectives

In this thesis, we have investigated the interaction between the two major sources of intraseasonal oceanic variability in the equatorial Pacific: the Intraseasonal Equatorial Kelvin Waves (IEKWs) and the Tropical Instabilities Waves (TIWs). In particular, the IEKW is an integral part of both El Niño and La Niña events as the main conduit by which WWBs and EWBs transfer momentum flux from the atmosphere to the ocean during their developments. On the other hand, TIWs, with a strong activity during the boreal fall, modulate seasonally the cold tongue, driving its warming through eddy mixing and the meridional non-linear dynamic heating, and thus also modulate the ENSO cycle.

Both IEKWs and the TIWs have thus an impact on the ocean mean state in the Eastern Equatorial Pacific ocean, and their interaction has been previously studied with observations and modeling approaches. However, previous studies are either mostly based on case studies or on model experimentation within an idealized framework. In addition there is still no consensus on the existence of a dominant process to explain this interaction and even on the "efficiency" of this interaction (i.e. whether it yields to a significant redistribution of heat and energy within the equatorial Pacific system). For instance, Holmes and Thomas (2016) (hereinafter HT16), in their idealized model experiments, find a weak asymmetry in the response of mean EKE in the TIWs region to the Kelvin wave between upwelling and downwelling events, which is counterintuitive with respect to what take place during ENSO (i.e. enhancement of TIWs activity during La Niña versus damping during El Niño).

The general objective of this thesis was to gain insights on this issue and extent the previous studies taking into account the diversity in IEKWs in the observational record, as well as overcoming limitations of the previous modeling experimental setup.

In the first part of this work, we have analyzed almost 30 years (1993-2018) of altimetric data to document both types of waves and their interaction. In this analysis, we applied the complex empirical orthogonal functions (CEOF) to the sea level intraseasonal anomalies (SLA) in order to capture the propagation characteristic of both waves.

- The CEOF method provided the spatial pattern of the interaction between both waves with the first two CEOF modes which grasp 21% of the explained variance: *(i)* the first order CEOF exhibits the strong amplitude at the TIWs cusps, between the 3°N-7°N and 120°-165°W (region documented of the TIWs activity) and less signal of the IEKW. *(ii)* The second CEOF mode displays mainly the signature of the IEKW and also the TIWs cusps but with less amplitude. The sum-up contribution of the sea level anomalies reconstructed from both CEOF 1 and CEOF2 explain the 42% of the variance of the total sea level between 2°N-2°S, 170°W-120°W.
- From the CEOF modes, we could determine peak events with strongest interactions between the IEKW and TIWs by reconstructing the SLA from CEOF 2, in total 25 downwelling and 28 upwelling events. These events were analyzed with lagged-composites of

zonal wind stress (Tx), sea level (SLA), meridional currents and sea surface temperature intraseasonal anomalies. We have also projected the SLA and the zonal wind stress (Tx) onto the theoretical Kelvin wave meridional structure to document how EWEs (WWEs) triggers an upwelling (downwelling) IEKW and therefore modifies the TIWs amplitude.

- We evidenced the asymmetry previously suggested by HT16, but with a faster response on the TIWs amplitude. From our methodological approach, the upwelling IEKWs tend to promote a larger TIWs amplitude than downwelling IEKWs by $\sim 15\%$ and the modulation occurs almost instantaneously.

- TIWs have been shown to warm the Cold Tongue via direct meridional non-linear dynamical heating (NDH). We were also interested in the contribution of these events to the TIWs-induced NDH at intraseasonal time scales. The result showed that the meridional NDH associated to these interaction events can be as large as that for interannual time scales, inducing a warming to the cold tongue of about 0.8 °C/month in both IEKW phases.

- Our study was restricted by using observational data, however we also approximated the TIWs kinetic energy from the geostrophic currents of AVISO, in the same domain as HT16 (150°W-110°W, 7°S-10°N), in order to compare our results of asymmetry between the two phases of the IEKWs and the TIWs response. Even if our methodological approach do not permit to separate the Kelvin phases, we could observe that the TIWs kinetic energy increases (decreases) 20 days after the interaction event, a faster TIWs response that what was suggested by HT16 (45-60 days). This result motivated the second part of this research.

In the second part of this work, we studied more deeply the TIWs energetic during the passage of the upwelling or downwelling IEKW phases. We developed a grid configuration of a high-resolution, *i.e.*, eddy-resolving, regional oceanic model (CROCO) at 1/4° of horizontal resolution. As a first step, the simulation was validated based on satellite observations, in-situ observations and reanalysis products, indicating a realistic representation of the spatial and temporal variability of the oceanic variables. Here, we performed two types of simulations: the so-called "Control Run (CR-Run)" and another without non-linear terms in the momentum equation "Linear Run (LIN-Run)", as a way to reduce the generation of mesoscale variations. The sensitivity experiments (LIN-Run) were started with the conditions of the CR-RUN 6 days before the onset of each upwelling or downwelling IEKWs events. Then, the LIN-RUN were rerun for 90 days in order to minimize changes in the mean state over the course of the events.

- As a first step, in order to follow the same line than in the first part of this research, we applied the same CEOF methodological approach to the modeled sea level intraseasonal anomalies from (CR-Run) to identify the interaction events. We selected 19 upwelling and 14 downwelling IEKWs events corresponding to the events also identified with the satellite observation in the first part of this research.

- We examined the TIWs kinetic energy (TIWKE), as a measure of the intensity of TIWs mesoscale activity, for the two phases of the IEKW. We set our analysis to the first 20 days, the time it takes for the wave to pass through the main region of TIWs activity. We compared the EKE integrated in the upper ocean (0-100 meters) from the CR-RUN (20 days of composite events, restarted 6 days before the peak) and the EKE from the long-term run (1993-2018). We observed an EKE reduction in the TIWs region during the passage of downwelling IEKWs and an slightly EKE increase (110°W-130°W) in the TIWs region during the passage of upwelling IEKWs. This suggests an asymmetry in the TIWs response to the IEKWs phases, with an increase about 27% and reduction of 20% during the upwelling and downwelling phases of the IEKWs, respectively. Additionally, we compared the EKE from the CR-RUN and the LIN-RUN during the first 20 days of each run, which grasp the net change in mesoscale activity solely due to the passage of Kelvin waves. The results evidenced a large (small) increase of the EKE upper-ocean integrated during the upwelling (downwelling) events.

- We also studied the eddy kinetic energy (EKE) and the principal terms contributing to the rate of change in TIWKE: barotropic (conversion of the mean Kinetic energy into EKE) and baroclinic (baroclinic conversion of the available eddy potential energy into EKE) conversion terms. Our results demonstrate the EKE associated to the TIWs activity is strengthened primarily during the passage of upwelling IEKWs: first, via barotropic conversion (confined to the first 50 meters), and later with less magnitude via baroclinic conversion (peaking between 30 and 70 meters). These results confirm that IEKWs disrupt the background circulation and contribute to the surface zonal current shear between the EUC and the SEC, and between the SEC and NECC, transferring the kinetic and potential energy into the eddy kinetic energy that generates the TIWs.

- Like in the observations, we observe a faster TIWs response to the IEKW than in the numerical study of HT16. We attribute this difference to a limitation of the experimental setup of HT16. In particular, their IEKW forcing consists in a sea level perturbation at 160°W with a prescribed vertical structure corresponding to the first baroclinic mode. This approach omits the fact that at this longitude, the Kelvin wave projects more energy on the higher-order baroclinic modes, resulting in a dynamical inconsistency and certainly in a transient dynamical adjustment that has not counterpart in the observations. We thus suggest that the difference between both numerical approaches may explain the difference in both the timing of the TIWs response and the amplitude of the asymmetry of the response between upwelling and downwelling events.

- Along the equator, we observe a reduction of mean EKE during the passage of the downwelling IEKWs, which implies a reduction in the transfer of EKE from the equator region band to the off-equatorial TIWs region.

We now briefly review the main limitations of our first study:

While altimetric data can provide real cases of interaction between the TIWs and IEKWs, we were limited to the surface data. We exploited all the data available to identify not only the interaction events for the two phases of the IEKWs, but also to evaluate the asymmetry

previously suggested by HT16. While the CEOF decomposition technique has been shown to be skillful in capturing conjointly the dominant propagating features of IEKWs and TIWs in the sea level data, it yields two dominant modes mixing both signals in a way that is not straightforward to interpret. In particular because there are periods when there is no interaction between IEKWs and TIWs, the orthogonality condition between the PC timeseries may produce a spurious variability that has no physical interpretation. As a consequence, the mode patterns may also reflect this spurious variability and may be sensitive to the period under investigation. This could in particular explain why the CEOF decomposition applied to the modeled sea level anomalies yields a different variance and pattern of the two dominant modes compared to the results from altimetry, despite the good model skill in simulating the sea level anomalies. Also, the CEOF decomposition, as a linear technique, has inherent limitations for capturing the asymmetry of the IEKWs-TIWs interaction. Nevertheless the CEOF technique appears as the most appropriate statistical tool for documenting this interaction considering the propagating nature of the phenomena under interest, and we think there is the possibility to improve this approach through, for instance, carrying the CEOF decomposition over running temporal windows to better grasp periods when the interaction is the strongest. We could also have thought of reducing the dimension of the system to be analyzed through carrying the CEOF decomposition along the sole latitudes of maximum variance of TIWs and IEKWs. Sensitivity tests that were done at the early stage of the study (*e.g.*, domain over which the CEOF analysis is done, normalization of sea level anomalies, filtering method, etc) suggest however that the selection of the events would have been only marginally impacted.

Regarding our modeling set up, we believe there is room for improvements to simulate more realistically the mean circulation considering that we noted a sensitivity of the model solution to details in the way the western boundary conditions are prescribed in the model. In particular, there is not a perfect match of the complicated bathymetry and topography at the western boundary between the GLORYS2V4 grid and the final CROCO grid due to the smoothing procedure used to generate the CROCO grid. This may generate spurious recirculation pattern in the model that could explain the cold bias and a shallower thermocline depth compared to the observations, evidenced in the CR-RUN simulations. We could evidence that reducing the domain or masking the western islands improved the performance of our simulations. Nevertheless, we end up with a model configuration that was considered sufficiently realistic to address intraseasonal variability.

Despite the limitations mentioned above, our results have opened perspectives for further advancing the understanding of the interaction between these two waves, and its influence on tropical climate variability. We list below some directions that we think are of interest:

Relationship between the wind events in the western-central Pacific and the impact on the TIWKE through the propagation of IEKWs. Although the upwelling IEKWs can yield a significant increase in TIWKE, we have noted a non-linear relationship between the two quantities with also a significant dispersion. It questions the extent to which such a non-linearity is tied to the characteristics of the IEKWs (*i.e.*, propagation speed, vertical structure, peak longitude), the latter being determined by the characteristics of the wind

stress forcing (*i.e.*, EWBs or EWEs). Chiodi et al. (2014) and Puy et al. (2019) showed that there is a significant diversity in EWBs in terms of their amplitude, peak location and association with the convective phase of the MJO. A relationship between the MJO and the second PC from the sea level intraseasonal anomalies calculated in Chapter 3 is evident in Figure 4.1. The higher correlations are observed in the first semester, supporting the hypothesis that the MJO can modulate the EWBs and WWBs and therefore the IEKWs-TIWs interaction. It thus calls to examine if the IEKWs-TIWs interaction documented here could be somehow constrained by the characteristics of the "type" of EWBs. This has practical interest since it would allow for a more direct prediction of the magnitude of the IEKWs-TIWs interaction. This could be examined based on sensitivity experiments with the model as well as a vertical mode decomposition of the model's variability to infer the details of the IEKWs (*i.e.*, energy according to the different baroclinic modes) and its relationship with the EWBs. In this line it would be also interesting to further document the low-level atmospheric response to the IEKWs-TIWs, observing that it is apparently not confined to the region of TIWs activity. This would be the starting point for addressing the rectified effect of this oceanic process on the tropical climate variability (see below).

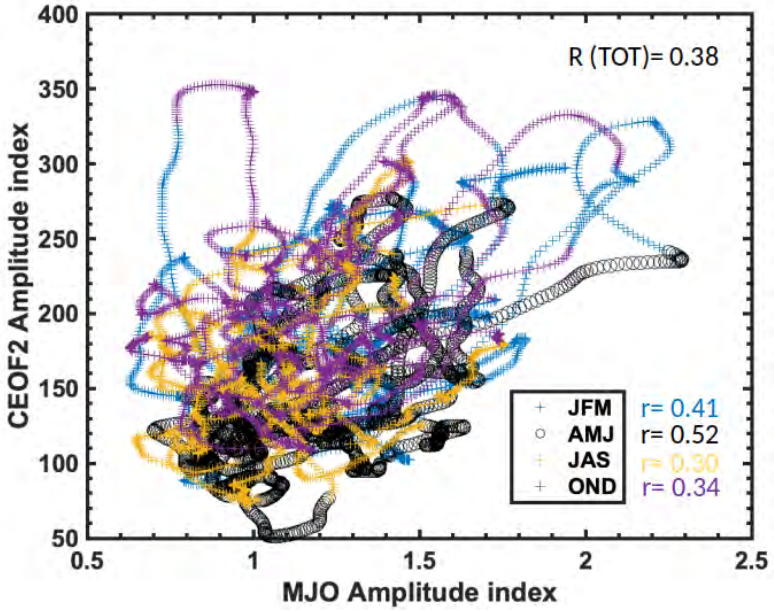

Figure 4.1: Relationship between MJO and PC2 (1993-2018). MJO amplitude index is the projection of 20-96 days filtered OLR including all eastward and westward wave numbers onto the daily spatial EOF patterns of 30-96 day eastward filtered OLR (Kiladis et al. (2014))

Quantifying the dissipation of the IEKWs due to the interaction with the TIWs
We have investigated the interaction between TIWs and IEKWs with a focus on the changes in TIWKE. However, the IEKWs also experience fluctuations in energy due to this interaction, which may constrain its characteristics further east of the TIWs region. The dissipation of the IEKW in the far eastern Pacific is an important question considering the strong oceanic teleconnection along the west coast of South America influential on the productive ecosystems

there (Sprintall et al. (2020)). A number of processes has been proposed to explain the IEKW dissipation in the far eastern Pacific, and there is no consensus on a prevailing one or if all of them contribute with comparable efficiency. The study presented here proposes another candidate for the dissipation process. In the chapter 4, we note that in our control experiment that the downwelling IEKW has a significantly weaker amplitude east of 120°W in the "linear" version of the model, suggesting that the TIWs-IEKWs interaction is an effective process to dissipate the IEKWs. However the model incorporates other dissipation processes documented in the literature.

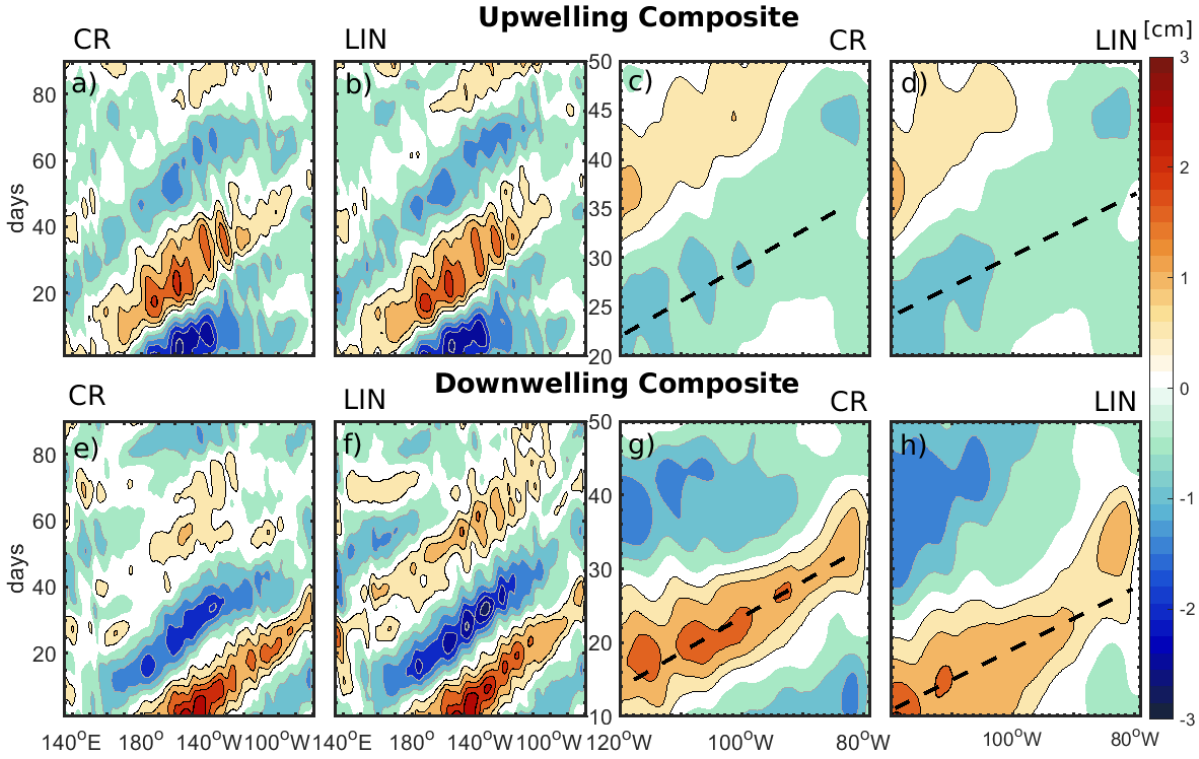

Figure 4.2: SSH anomalies from Upwelling (top panel) and Downwelling (bottom panel) composites and from (a,c,e,f) CR simulation and (b, d, f, h) LIN simulation. SSH anomalies are filtered with a 30-day moving average in time. SSH anomalies data is averaged between ± 2.5° latitude in the first 90 days from model initialization.

However the model incorporates other dissipation processes documented in the literature. For instance, Mosquera-Vásquez et al. (2014) has evidenced a partial reflection of the IEKWs as Rossby waves near 120°W, as well as vertical propagation of energy from the forcing region, processes that also contribute to the energy damping of the IEKWs. Scattering of energy (Busalacchi and Cane (1988); Giese and Harrison (1991)) is also taking place in the model due to the varying stratification. TIWs induce turbulent mixing in the thermocline (Tanaka et al. (2015)) that has the potential to alter the IEKW characteristics. A clearer picture on how all these processes relate to each other and influence the IEKW in the far eastern Pacific would be valuable for improving our predictive capabilities of the oceanic teleconnection at intraseasonal timescales in the far eastern Pacific, with here again a practical benefit for the

economy of the surrounding countries (Ecuador, Peru, Panama, Chile). This issue could be here also tackled with the model through in particular refining the grid (through nesting to resolve the coastal upwelling dynamics) in the far eastern Pacific to better take into account mixing processes due to submesoscale activity. This would also require tuning the model in terms of its representation of mean EKE through the parameterization of air-sea interaction at mesoscale (see Renault et al. (2020), e.g. coefficient to parameterize of air-sea coupling effect at mesoscale) or through coupling with a Marine Boundary Layer model to better represent atmospheric forcing at fine scale (both momentum and heat). Sensitivity experiments consisting in modulating the magnitude of the mean trade winds would allow constraining the mean thermocline slope and circulation, which would allow documenting the sensitivity of the aforementioned processes to the mean state and thereby map the conditions that favor one or the other. Comparison to the results of "linear" simulations would complement this analysis.

The IEKWs-TIWs interaction and ENSO. As it was discussed, the IEKWs and the TIWs are essential component of the tropical Pacific variability, while the downwelling IEKWs (forced by stochastic winds) are essential to the onset of the warm phase of ENSO (in particular during strong Eastern Pacific El Niño events) (McPhaden and Yu (1999); Gushchina and Dewitte (2012)), TIWs are more active during La Niña conditions (Yu and Liu (2003); Philander (1990); Vialard et al. (2001)) and can contribute to the ENSO asymmetry being more enhanced during La Niña than they are reduced during El Niño, by warming the cold tongue. Since we have evidenced that the upwelling IEKW can increase TIWs activity and thus alter the heat budget in the far eastern Pacific, it questions the extent to which the IEKWs-TIWs interaction can modulate the tropical Pacific variability. In particular, strong El Niño events are generally followed by multi-year La Niña events (Okumura and Deser (2010)) during which EWBs are favored (Chiodi et al. (2014). The amplitude and duration of these La Niña events have impacts on climate conditions over South America (Cai et al. (2020), which calls for better understanding the conditions that may favor their persistence or decay. We may hypothesize that the IEKWs-TIWs interaction during these prolonged cold events may act as a negative feedback through accumulating residual warming by the enhanced TIWs activity. This could be tested based on experiments with an hybrid coupled model. This model could consist in the tropical ocean model configuration used in this study coupled to a simplified atmospheric model (*e.g.*, statistical model), in which EWBs are prescribed during La Niña periods. Comparison of experiments with and without EWBs would diagnose the residual effect of the IEKWs-TIWs events on the mean state. A comprehensive heat budget would allow inferring the thermodynamical processes that are the most impacted by this interaction. This would allow in particular estimating the role of heat flux forcing and entrainment and their sensitivity to the TIWs-IEKWs interaction, which has been disregarded in our study although they can potentially contribute to the rectified effect suggested by the analysis of NDH. An extension of this coupled modeling work would be also to evaluate the role of this TIWs-IEKWs interaction on ENSO diversity.

It would be also interesting to further document the atmospheric response associated to the TIWs-IEKWs interactions since it may help better understand how it can modulate lower

frequency coupled mode in the tropical Pacific basin. While we noted that the observed pattern of low-level atmospheric circulation during episode of TIWs-IEKWs coupling exhibited features indicative of air-sea coupling at mesoscales, we did not investigate if there was a change in some aspect of the ITV (e.g. convective waves). This issue would represent a key step to address the role of the TIWs-IEKWs interaction on the tropical Pacific system.

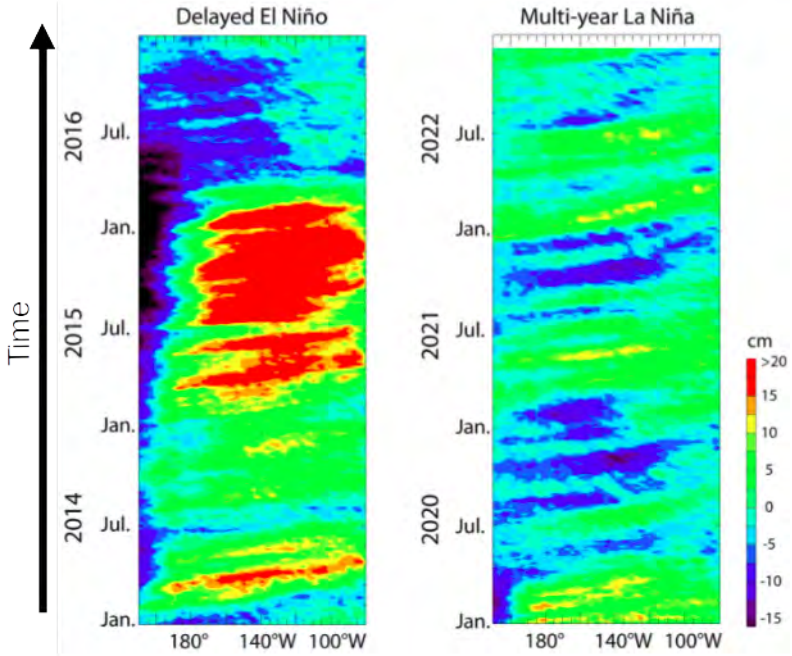

Figure 4.3: Time-longitude of the intraseasonal sea level anomalies along the equator (2.5°N-2.5°S) from (a) January-2014 to December-2016 and (b) January-2020 to December-2022.

4.2 Conclusion and perspectives

Dans cette thèse, nous avons étudié l'interaction entre les deux sources majeures de la variabilité océanique intrasaisonnière dans le Pacifique équatorial qui ont un impact sur l'état moyen de l'océan Pacifique tropical : les ondes Kelvin équatoriales intrasaisonnières (IEKWs) et les ondes d'instabilité tropicales (TIWs). En particulier, l'IEKW fait partie intégrante des événements El Niño et La Niña en tant que principal conduit par lequel les WWBs (or WWEs) et EWBs (or WWEs) transfèrent le flux de quantité de mouvement de l'atmosphère à l'océan pendant leur développement. D'autre part, les TIWs, avec une forte activité pendant l'automne boréal, modulent de manière saisonnière la cold tongue, entraînant son réchauffement par le biais du mélange tourbillonnaire et du chauffage dynamique non linéaire méridional, et modulent donc également le cycle ENSO.

Les IEKWs et les TIWs ont donc un impact sur l'état moyen de l'océan dans l'est du Pacifique équatorial et leur interaction a été précédemment étudiée dans des études observationnelles et de modélisation numérique. Cependant, les études précédentes sont principalement basées sur des études de cas ou sur l'expérimentation de modèles dans un cadre idéalisé. En outre, il n'y a toujours pas de consensus sur l'existence d'un processus dominant pour expliquer cette interaction et même sur l'"efficacité" de cette interaction (c'est-à-dire si elle conduit à une redistribution significative de la chaleur et de l'énergie dans le Pacifique équatorial). Par exemple, dans leurs expériences de modèle idéalisé, Holmes and Thomas (2016) trouvent une faible asymétrie dans la réponse de l'EKE moyenne dans la région TIWs à l'onde Kelvin entre les événements d' "upwelling" et de "downwelling", ce qui est contre-intuitif par rapport à ce qui se passe pendant ENSO (c'est-à-dire l'augmentation de l'activité des TIW pendant La Niña et diminution pendant El Niño).

L'objectif général de cette thèse était d'obtenir un aperçu de cette question et d'étendre les études précédentes en prenant en compte la diversité des IEKWs dans des observations longues, ainsi que de surmonter les limitations des configurations expérimentales de modélisation précédentes.

Dans la première partie de ce travail, nous avons analysé près de 30 ans (1993-2018) de données altimétriques pour documenter les deux types d'ondes et leur interaction. Dans cette analyse, nous avons appliqué les fonctions orthogonales empiriques complexes (CEOF) aux anomalies intrasaisonnières du niveau de la mer (SLA) afin de capturer la caractéristique de propagation des deux ondes.

- La méthode CEOF a fourni la structure spatiale de l'interaction entre les deux ondes avec les deux premiers modes CEOF qui capturent 21% la variance expliquée : (i) le premier mode CEOF présente une forte amplitude au niveau des méandres des TIWs, entre 3°N-7°N (région documentée de l'activité TIWs) et un signal moindre de l'IEKW. (ii) Le second mode CEOF présente principalement la signature des IEKWs et également des TIW mais avec une amplitude moindre. La contribution cumulée des anomalies du niveau de la mer reconstituées à partir des deux CEOF 1 et CEOF2 explique 42% de la variance du niveau total de la mer entre 2°N-2°S, 170°W-120°W.

- A partir des modes CEOF, nous avons pu déterminer les pics d'interaction entre les deux ondes en reconstruisant le SLA à partir du CEOF2, au total 25 événements de downwelling et 28 de upwelling. Ces événements ont été analysés avec des composites "laggués" de la tension de vent zonal (Tx), du niveau de la mer (SLA), des courants méridiens et des anomalies intrasaisonnières de la température de surface de la mer. Nous avons également projeté la SLA et la tension de vent zonal sur la structure méridienne théorique de l'onde de Kelvin pour documenter comment les EWEs (WWEs) déclenchent une IEKW d'upwelling (de downwelling) et modifient ainsi l'amplitude des TIWs.

- Nous avons mis en évidence l'asymétrie précédemment suggérée par HT16, mais avec une réponse plus rapide de l'amplitude des TIWs. D'après notre approche méthodologique, les IEKWs d'upwellings ont tendance à promouvoir une plus grande amplitude des TIWs que les IEKWs de downwelling d'environ $\sim 15\%$ et la modulation se produit presque instantanément.

- Il a été démontré que les TIWs réchauffent la cold tongue par le biais d'un chauffage dynamique non linéaire (NDH) méridional direct. Nous nous sommes également intéressés à la contribution de ces événements au NDH induit par les TIWs à des échelles de temps intrasaisonnières. Les résultats ont montré que le NDH méridien méridional associé à ces événements d'interaction peut être aussi important que celui aux échelles de temps interannuelles, induisant un réchauffement de la cold tongue d'environ 0.8 $^\circ C/mois$ dans les deux phases IEKW.

- Notre étude a été limitée par l'utilisation de données d'observation, cependant nous avons aussi approximé l'énergie cinétique des TIWs à partir des courants géostrophiques d'AVISO, sur le même domaine que HT16 (150°W-110°W, 7°S-10°N), afin de comparer nos résultats d'asymétrie entre les deux phases des IEKWs. Même si notre approche méthodologique méthodologique ne permet pas de séparer les phases de l'onde de Kelvin, nous avons pu observer que l'énergie cinétique du TIWs augmente (diminue) 20 jours après l'événement d'interaction, une réponse plus rapide des TIWs que ce qui était suggéré par HT16 (45-60 jours). Ce résultat a motivé la deuxième partie de ce travail de thèse.

Dans la deuxième partie, nous avons étudié plus profondément les TIWs énergétiques lors du passage des phases d'upwelling ou de downwelling IEKW. Nous avons développé une configuration d'un modèle océanique régional à haute résolution (CROCO) à 1/4° de résolution horizontale. Dans un premier temps, la simulation a été validée sur la base d'observations satellitaires, d'observations in-situ et de produits de réanalyse, indiquant une représentation réaliste de la variabilité spatiale et temporelle des variables océaniques. Ici, nous avons réalisé deux types de simulations, la soi-disant « Control Run (CR-Run) » et une autre sans termes non linéaires dans l'équation de moment « Linear Run (LIN-Run) », afin de réduire la génération de variations mésoéchelles. Les expériences de sensibilité (LIN-Run) ont commencé avec les conditions du CR-RUN 6 jours avant le début de chaque événement de IEKWs upwelling ou downwelling. Ensuite, les expériences LIN-RUN ont tourné pendant 90 jours afin de minimiser les changements d'état moyen au cours des événements.

- Dans un premier temps, afin de suivre la même ligne de la première partie de cette recherche, nous avons appliqué la même approche méthodologique CEOF aux anomalies simulées du niveau de la mer intrasaisonnier (CR-Run) pour identifier les événements d'interaction. Nous avons identifié 19 événements d'upwelling et 14 événements de downwelling correspondant aux événements également identifiés dans les observations satellites dans la première partie de cette recherche.

- Nous avons examiné l'énergie cinétique des TIWs (TIWKE), comme mesure de l'intensité de l'activité mésoéchelle des TIWs pour les deux phases de l'IEKW. Nous avons fixé notre analyse aux 20 premiers jours, soit le temps nécessaire à l'onde IEKW pour traverser la principale région d'activité des TIWs. Nous avons comparé l'EKE intégrée dans la partie supérieure de l'océan (0-100 mètres) à partir du CR-RUN (20 jours d'événements composites, redémarré 6 jours avant le pic) et l'EKE du run long (1993-2018). Nous avons observé une réduction de l'EKE dans la région des TIWs lors du passage des IEKWs de downwelling et une légère augmentation de l'EKE (110°W-130°W) lors du passage des IEKWs d'upwelling. Cela suggère une asymétrie dans la réponse des TIWs aux phases de l'IEKWs, avec une augmentation d'environ 16% et une réduction de 4,6% pendant les phases d'upwelling et de downwelling de l'IEKWs, respectivement. De plus, nous avons comparé l'EKE du CR-RUN et du LIN-RUN pendant les 20 premiers jours de chaque run, ce qui permet de saisir le changement net de l'activité mésoéchelle uniquement dû au passage des ondes de Kelvin. Les résultats ont mis en évidence une forte (faible) augmentation de l'EKE intégré (premières 100 mètres) pendant les événements de upwelling (downwelling).

- Nous avons également étudié l'énergie cinétique tourbillonnaire (EKE) et les principaux termes contribuant au taux de variation de TIWKE: barotrope (conversion de l'énergie cinétique moyenne en EKE) et baroclinique (conversion baroclinique de l'énergie potentielle de tourbillon disponible en EKE). Nos résultats démontrent que l'EKE associée à l'activité des TIWs est renforcée principalement pendant le passage des IEKWs d'upwelling: d'abord, via la conversion barotrope (confinée aux 50 premiers mètres), puis avec une magnitude moindre via la conversion barocline (pic entre 30 et 70 mètres). Ces résultats confirment que Les IEKWs perturbent la circulation moyenne et contribuent au cisaillement du courant zonal de surface entre l'EUC et le SEC et entre le SEC et le NECC, en transférant l'énergie cinétique et potentielle dans l'énergie cinétique tourbillonnaire qui génère les TIWs.

- Comme dans les observations, nous observons une réponse plus rapide des TIWs à l'IEKW que dans l'étude numérique de HT16. En particulier, leur forçage de l'IEKW consiste en une perturbation du niveau de la mer à 160°W avec une structure verticale prescrite correspondant au premier mode barocline. Cette approche omet le fait qu'à cette longitude, l'onde de Kelvin projette plus d'énergie sur les modes baroclines d'ordre supérieur, ce qui entraîne une incohérence dynamique et certainement un ajustement dynamique transitoire qui ne se retrouve pas dans les observations. Nous suggérons donc que la différence entre les deux approches numériques peut expliquer la différence à la fois dans le timing de la réponse des TIWs et l'amplitude de l'asymétrie de la réponse entre les événements de upwelling et de downwelling.

- Le long de l'équateur, on observe une réduction de l'EKE moyenne lors du passage des IEKWs de downwelling, ce qui implique une réduction du transfert de l'EKE de la bande de la région équatoriale vers la région hors équateur des TIWs.

Nous allons maintenant passer brièvement en revue les principales limitations de notre première étude : Alors que les données altimétriques peuvent fournir des cas réels d'interaction entre les TIWs et les IEKWs, nous nous sommes limités aux données de surface. Nous avons exploité toutes les données disponibles pour identifier non seulement les événements d'interaction aux deux phases des IEKWs, mais aussi pour évaluer l'asymétrie précédemment suggérée par HT16. Bien que la technique de décomposition CEOF se soit avérée utile pour capturer les caractéristiques dominantes de propagation des IEKW et des TIWs dans les données de niveau de la mer, elle produit deux modes dominants mélangeant les deux signaux d'une manière qui n'est pas simple à interpréter. En particulier parce qu'il y a des périodes où il n'y a pas d'interaction entre les IEKWs et les TIWs, la condition d'orthogonalité entre les séries temporelles PC peut produire une variabilité fallacieuse qui n'a pas d'interprétation physique. Par conséquent, les structures spatiales du mode peuvent également refléter cette variabilité fallacieuse et peuvent être sensibles à la période étudiée. Cela pourrait notamment expliquer pourquoi la décomposition CEOF appliquée aux anomalies simulées du niveau de la mer produit une variance et une configuration différentes de celles de l'altimétrie, malgré la bonne capacité du modèle à simuler les anomalies de hauteur de mer. De plus, la décomposition CEOF, en tant que technique linéaire, a des limites inhérentes pour capturer l'asymétrie de l'interaction IEKWs-TIWs. Néanmoins, la technique CEOF apparaît comme l'outil outil statistique le plus approprié pour documenter cette interaction compte tenu de la nature propagatrice, et nous pensons qu'il est possible d'améliorer cette approche en effectuant, par exemple, la décomposition CEOF sur des fenêtres temporelles glissantes afin de mieux saisir les périodes où l'interaction est la plus forte. Nous aurions également pu penser à réduire la dimension du système à analyser en portant la décomposition CEOF le long des seules latitudes de variance maximale des TIWs et IEKWs.Les tests de sensibilité qui ont été effectués au début de l'étude (par exemple, le domaine sur lequel l'analyse CEOF, la normalisation des anomalies du niveau de la mer, la méthode de filtrage, etc.) suggèrent cependant que la sélection des événements n'aurait été que marginalement impactée.

En ce qui concerne la mise en place de notre modélisation, nous pensons qu'il est possible d'améliorer de façon plus réaliste la circulation moyenne, étant donné que nous avons noté une sensibilité de la solution du modèle aux détails dans la façon dont les conditions aux limites ouest sont prescrites dans le modèle. En particulier, il n'y a pas une correspondance parfaite de la bathymétrie et de la topographie complexes à la frontière ouest entre la grille GLORYS2V4 et la grille CROCO finale en raison de la procédure de lissage utilisée pour générer la grille CROCO. Cela peut générer une recirculation irréaliste dans le modèle qui pourrait expliquer le biais froid et une profondeur de thermocline plus faible par rapport aux observations, mises en évidence dans les simulations CR-RUN. Nous avons pu constater que la réduction du domaine ou le masquage des îles dans l'ouest du bassin améliorait les performances de nos simulations. Néanmoins, nous nous retrouvons avec une configuration de modèle qui a été jugée suffisamment réaliste pour aborder la variabilité intrasaisonnière.

Malgré les limites mentionnées ci-dessus, nos résultats ont ouvert des perspectives pour continuer à améliorer la compréhension de l'interaction entre ces deux ondes et son rôle sur la variabilité du climat tropical. Nous énumérons ci-dessous quelques orientations qui nous semblent intéressantes:

Relation entre les événements de vent dans le Pacifique centre-ouest et l'impact sur le TIWKE par la propagation des IEKWs. Bien que les IEKWs upwelling peuvent produire une augmentation significative de TIWKE, nous avons noté une relation non linéaire entre les deux quantités avec également une dispersion significative. Il s'agit de savoir dans quelle mesure une telle non-linéarité est liée aux caractéristiques des IEKWs (i.e. vitesse de propagation, structure verticale, longitude du pic), ces dernières étant déterminées par les caractéristiques du forçage du vent (*i.e.* WWBs ou EWBs). Chiodi et al. (2014) et Puy et al. (2019) ont montré qu'il existe une diversité significative dans les EWBs en termes d'amplitude, de localisation des pics et d'association avec la phase convective de la MJO. Il convient donc d'examiner si l'interaction IEKWs-TIWs documentée ici pourrait être en quelque sorte limitée par les caractéristiques du "type" EWBs. Ceci a un intérêt pratique car cela permettrait une prédiction plus directe de l'amplitude de l'interaction IEKWs-TIWs. Cela pourrait être examiné sur la base d'expériences de sensibilité du modèle ainsi que sur une décomposition en mode vertical du modèle afin de déduire les détails des IEKWs (i.e. l'énergie selon les différents modes baroclinques) et leur relation avec les EWBs. Dans cette veine, il serait également intéressant de documenter davantage la réponse atmosphérique de surface au mode d'intération IEKWs-TIWs, en observant qu'elle n'est apparemment pas confinée à la région d'activité des TIWs. Cela pourrait être le point de départ pour aborder l'effet rectifié de ce processus océanique sur la variabilité du climat tropical (voir ci-dessous).

Quantifier la dissipation des IEKWs due à l'interaction avec les TIWs Nous avons étudié l'interaction entre les TIWs et les IEKWs en mettant l'accent sur les changements dans les TIWKE. Cependant, les IEKWs connaissent également des fluctuations d'énergie dues à cette interaction, ce qui peut limiter leurs caractéristiques plus à l'est de la région des TIWs. La dissipation de l'IEKW dans le Pacifique oriental est une question importante compte tenu de la forte téléconnexion océanique le long de la côte ouest de l'Amérique du Sud influençant les écosystèmes productifs de cette région (Sprintall et al. (2020)). Un certain nombre de processus ont été proposés pour expliquer la dissipation des IEKWs dans le Pacifique oriental, et il n'existe pas de consensus sur celui qui prévaut ou si tous d'entre eux contribuent avec une efficacité comparable. L'étude présentée ici propose un autre candidat pour le processus de dissipation. Dans le chapitre 4, nous notons que sur notre expérience du modèle de contrôle que les IEKWs d'upwelling ont une amplitude significativement plus faible à l'est de 120°W que dans la la version "linéaire" du modèle, ce qui suggère que l'interaction TIWs-IEKWs constitue un moyen efficace pour dissiper les IEKWs. La diffusion de l'énergie (Busalacchi and Cane (1988); Giese and Harrison (1991)) a également lieu dans le modèle en raison de la stratification variable. Les TIWs induisent un mélange turbulent dans la thermocline (Tanaka et al. (2015)) qui a le potentiel de modifier les caractéristiques des IEKWs. Une vision plus claire de la manière dont tous ces processus sont liés les uns aux autres et influencent

l'IEKW dans le Pacifique oriental serait utile pour améliorer nos capacités de prédiction de la téléconnexion océanique à l'échelle intrasaisonnière dans cette région, avec là encore, des avantages pratiques pour l'économie des pays environnants (Équateur, Pérou, Panama, Chili). Cette question pourrait également être abordée avec le modèle, notamment en affinant la grille dans le Pacifique extrême-oriental afin de mieux prendre en compte les processus de mélange dus à l'activité sub-mésoéchelle. Cela nécessiterait également d'ajuster le modèle en termes de représentation de l'EKE moyenne par la paramétrisation de l'interaction air-mer à mésoéchelle (voir Renault et al. (2020)) ou par le biais d'un couplage avec un modèle de couche limite marine pour mieux représenter le forçage atmosphérique à fine échelle (à la fois la quantité de mouvement et la chaleur). Les expériences de sensibilité consistant à moduler l'amplitude des alizés moyens permettraient de contraindre la pente de la thermocline moyenne et la circulation, ce qui permettrait de documenter la sensibilité des processus susmentionnés à l'état moyen et ainsi de cartographier les conditions qui favorisent l'un ou l'autre. Une comparaison avec les résultats des simulations "linéaires" compléterait cette analyse.

L'interaction IEKWs-TIWs et ENSO Comme on l'a vu, les IEKWs et les TIWs sont des composantes essentielles de la variabilité du Pacifique tropical, tandis que les IEKWs downwelling (forcés par des vents stochastiques) sont essentielles pour le début de la phase chaude d'ENSO (en particulier pendant les événements El Niño du Pacifique Est) (McPhaden and Yu (1999); Gushchina and Dewitte (2012)), les TIWs sont plus actives pendant les conditions La Niña (Yu and Liu (2003); Philander (1990); Vialard et al. (2001)) et peuvent contribuer à l'asymétrie ENSO en réchauffant la cold tongue. Puisque nous avons prouvé que les IEKWs upwellings peuvent augmenter l'activité des TIWs et donc modifier le bilan thermique dans le Pacifique extrême-oriental, on peut se demander dans quelle mesure l'interaction IEKWs-TIWs peut moduler la variabilité du Pacifique tropical. En particulier, les forts événements El Niño sont généralement suivis d'événements La Niña pluriannuels (Okumura and Deser (2010)) au cours desquels les EWBs sont favorisés (Chiodi et al. (2014)). L'amplitude et la durée de ces événements La Niña ont des impacts sur les conditions climatiques au-dessus de l'Amérique du Sud (Cai et al. (2020)), ce qui nécessite de mieux comprendre les conditions qui peuvent favoriser leur persistance ou leur déclin. Nous pouvons émettre l'hypothèse que l'interaction IEKWs-TIWs au cours de ces événements froids prolongés peut agir comme une rétroaction négative en accumulant le réchauffement résiduel par l'activité accrue des TIWs. Cela pourrait être testé sur la base d'expériences avec un modèle hybride couplé. Ce modèle pourrait consister en la configuration du modèle d'océan tropical utilisé dans cette étude, couplée à un modèle atmosphérique simplifié (par exemple, un modèle statistique). La comparaison des expériences avec et sans EWBs permettrait de diagnostiquer l'effet résiduel des événements IEKWs-TIWs sur l'état moyen. Un bilan thermique complet permettrait de déduire les processus thermodynamiques les plus touchés par cette interaction. Cela permettrait notamment d'estimer le rôle du forçage du flux thermique et de l'entraînement et leur sensibilité à l'interaction TIWs-IEKWs, qui n'a pas été pris en compte dans notre étude bien qu'ils puissent potentiellement contribuer à l'effet rectifié suggéré par l'analyse du NDH. Une extension de ce travail de modélisation couplée serait également d'évaluer le rôle de cette interaction TIWs-IEKWs sur la diversité ENSO.

Il serait également intéressant de documenter plus précisément la réponse atmosphérique associée aux interactions TIWs-IEKWs, car cela pourrait aider à mieux comprendre comment elle peut moduler le mode couplé à plus basse fréquence dans le bassin tropical du Pacifique. Bien que nous ayons noté que le pattern observé de la circulation atmosphérique pendant l'épisode de couplage TIWs-IEKWs présentait des caractéristiques indiquant un couplage air-mer à méso-échelle, nous n'avons pas cherché à savoir s'il y avait un changement dans un aspect de l'ITV (par exemple les ondes convectives). Cette question représente une étape clé pour aborder le rôle de l'interaction TIWs-IEKWs sur le système tropical du Pacifique.

Appendix A

.1 Supplementary Material

On the Relationship Between Tropical Instability Waves and Intraseasonal Equatorial Kelvin Waves in the Pacific From Satellite Observations (1993–2018) `https://www.frontiersin.org/articles/10.3389/fmars.2022.788908/full#supplementary-material`

Article published in *Frontiers in Marine Science.*

Article edited by: Frédéric Cyr, Northwest Atlantic Fisheries Centre, Fisheries and Oceans Canada, Canada

Article reviewed by: - Ryan Holmes, The University of Sydney, Australia - Tong Lee, NASA Jet Propulsion Laboratory (JPL), United States

Supplementary Material

1. Supplementary Figures

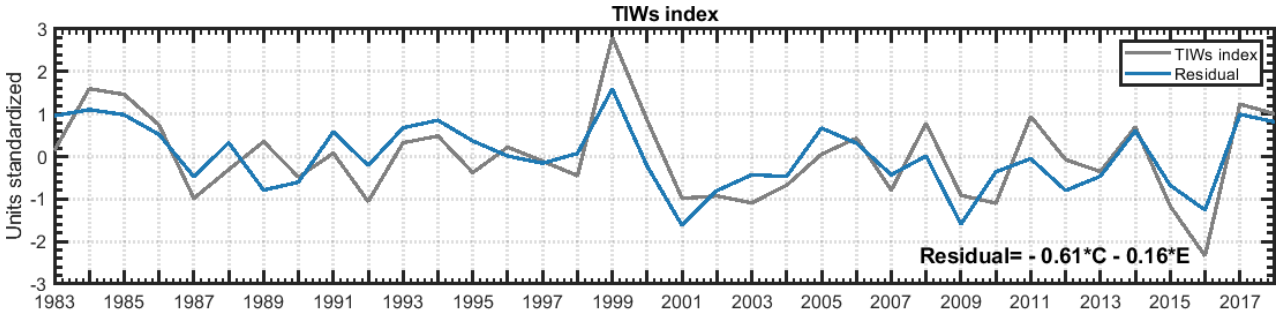

Supplementary Figure 1. Evolution of the TIWs activity index (blue line) and its residual with respect to ENSO variability (gray line) between 1982 and 2018. The TIWs activity index is defined based on SST data following An (2008). The residual consists in the difference between the TIWs activity index (yearly mean may-april) and its bilinear regression onto the E and C indices defined as in Takahashi et al. (2011). E anc C index were calculated from the yearly mean of the monthly anomalies of the SST.

Supplementary Material

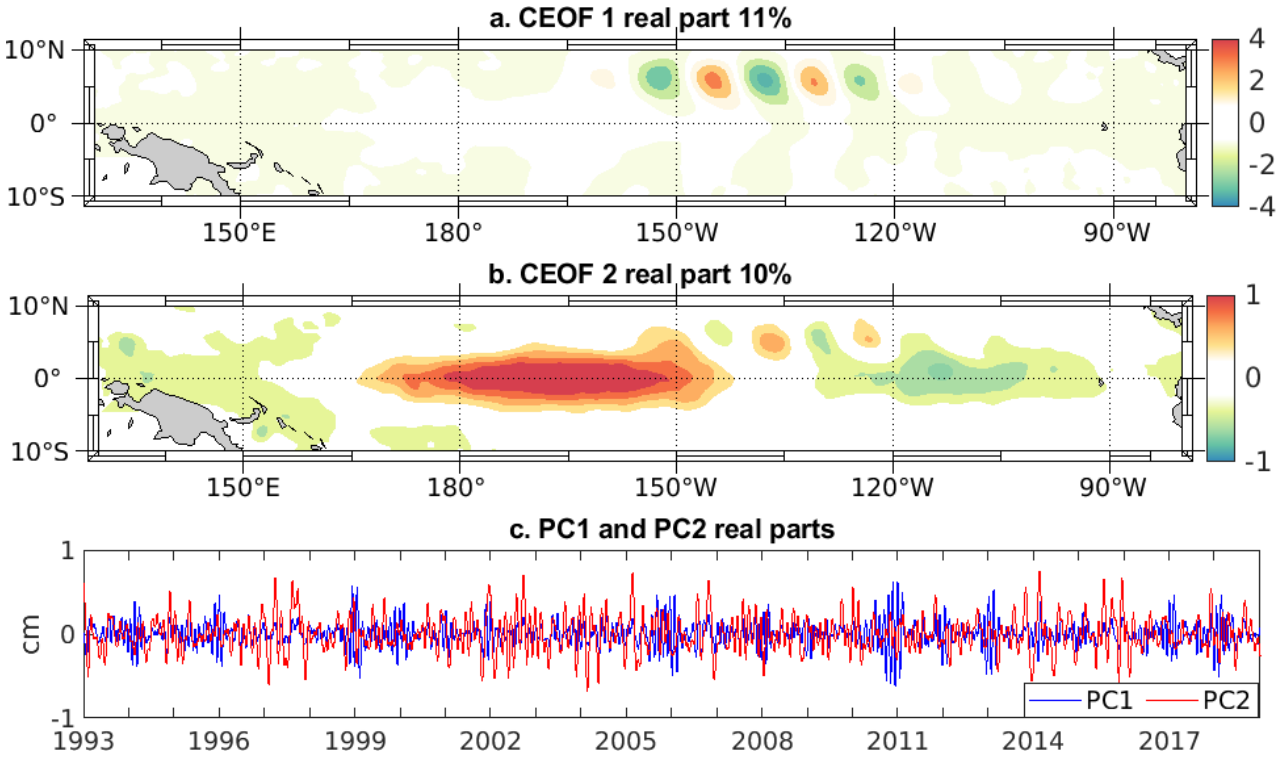

Supplementary Figure 2. CEOF decomposition of intraseasonal sea level anomalies: real part of (a) first and (b) second mode. (c) 30-days smoothed real part of the first and second PC.

Supplementary Material

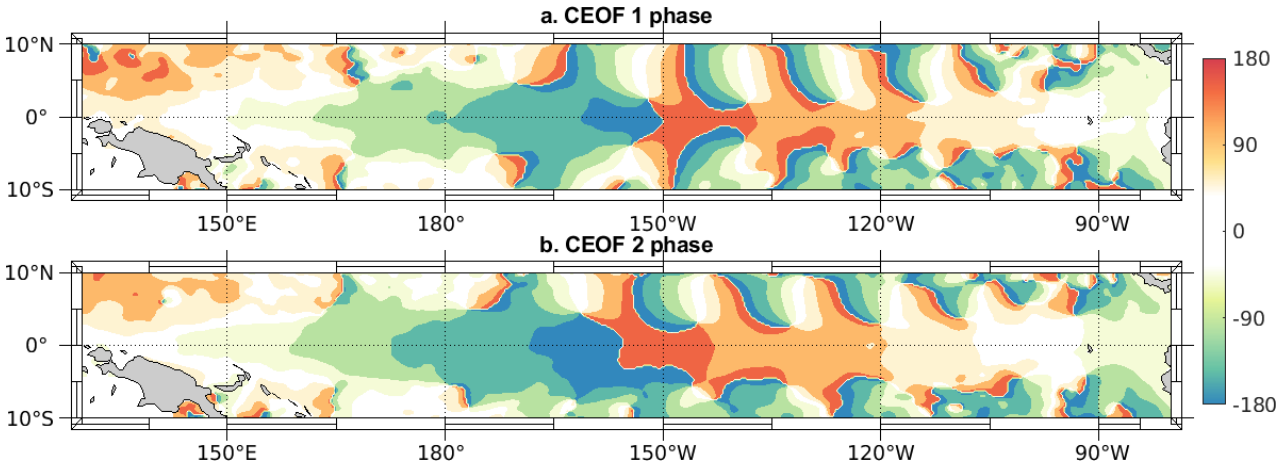

Supplementary Figure 3. CEOF decomposition of intraseasonal sea level anomalies: phase of (a) first and (b) second mode.

Supplementary Material

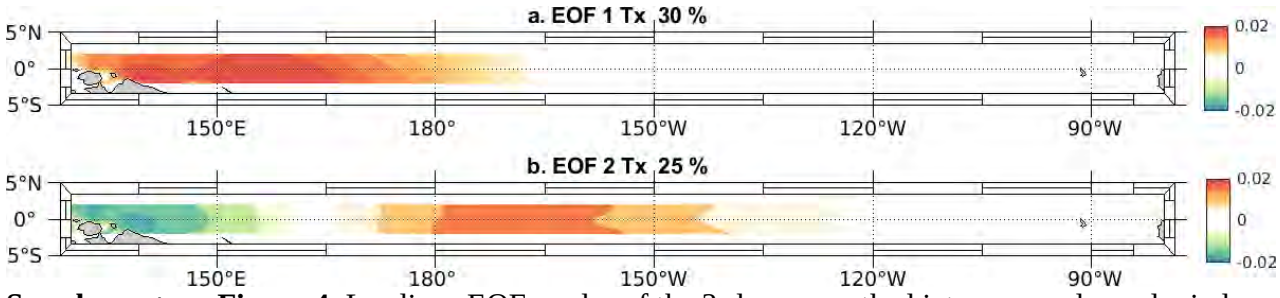

Supplementary Figure 4. Leadings EOF modes of the 3-days smoothed intraseasonal zonal wind stress anomalies (Tx) in the equatorial region (2.5°S-2.5°N).

Supplementary Material

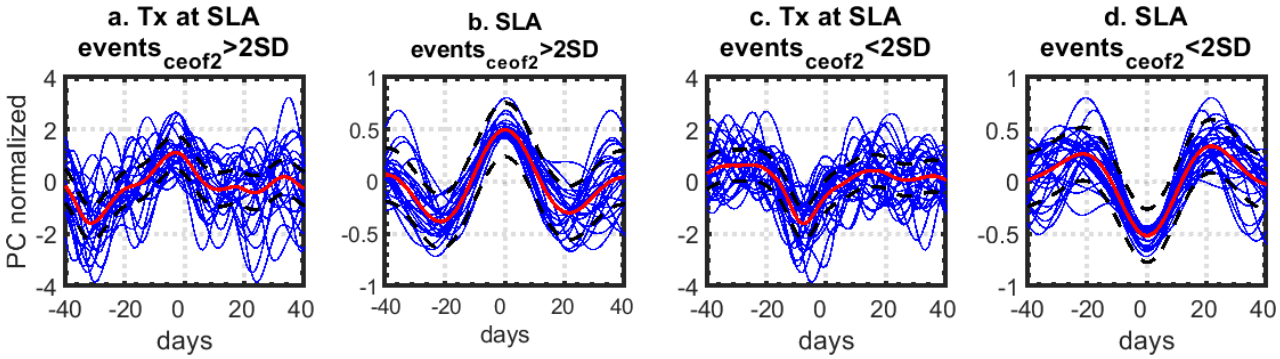

Supplementary Figure 5. (a) Plume (thin blue lines) and composite average (thick red line) of the 25 positive events of zonal wind stress PC1 time series centered at lag 0 of the corresponding SLA positive events. (b) plume (thin blue lines) and composite average (thick red line) of the sea level anomalies reconstructed from PC2 (lag 0 at the SLA peak). (c) and (d) are the same as (a) and (b) for the SLA negative events but for zonal wind stress (Tx) anomalies (PC1).

Supplementary Material

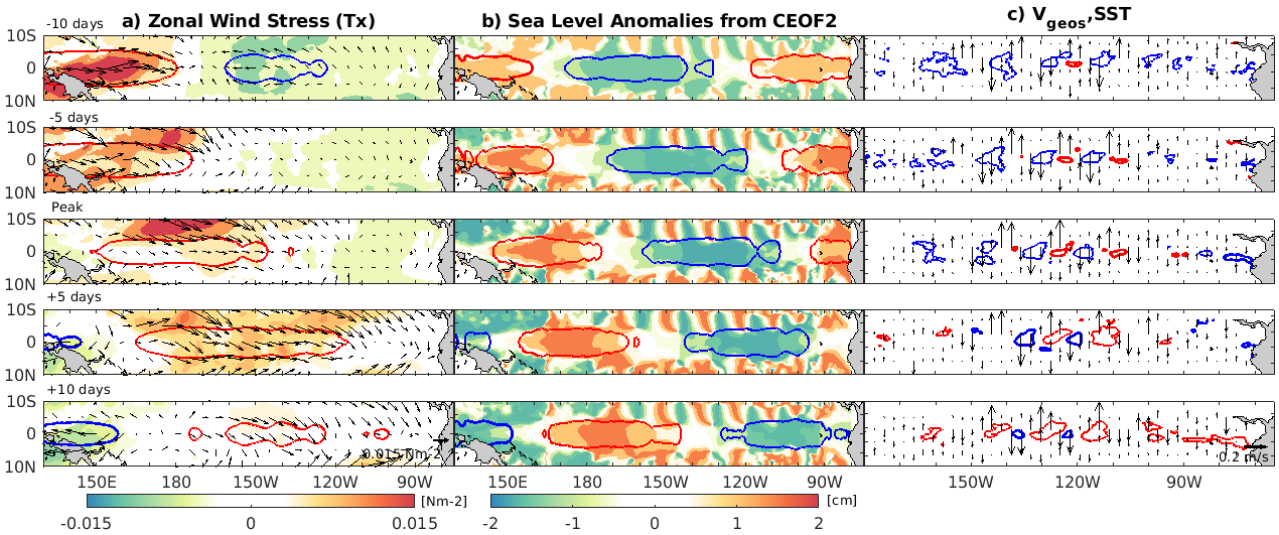

Supplementary Figure 6. Same as Figure 2 but lead/lag composites are for the strong negative equatorial SLA events identified in Figure 2a (i.e. the IKW upwelling phases).

Bibliography

Allen, M.R., Lawrence, S.P., Murray, M.J., Mutlow, C.T., Stockdale, T.N., Llewellyn-Jones, D.T., Anderson, D.L.T., 1995. Control of tropical instability waves in the pacific. Geophysical Research Letters 22, 2581–2584. URL: https://agupubs.onlinelibrary.wiley.com/doi/abs/10.1029/95GL02653, doi:https://doi.org/10.1029/95GL02653, arXiv:https://agupubs.onlinelibrary.wiley.com/doi/pdf/10.1029/95GL02653.

Amedo, C., Villanoy, C., Udarbe-Walker, M., 2002. Indicators of upwelling at the northern bicol shelf. UPV J. Nat. Sci 7, 42–52.

An, S.I., 2004. Interdecadal changes in the el nino–la nina asymmetry. Geophysical Research Letters 31.

An, S.I., 2008. Interannual variations of the tropical ocean instability wave and enso. Journal of Climate 21, 3680–3686.

An, S.I., Jin, F.F., 2004. Nonlinearity and asymmetry of enso. Journal of Climate 17, 2399–2412.

An, S.I., Wang, B., 2000. Interdecadal change of the structure of the enso mode and its impact on the enso frequency. Journal of Climate 13, 2044–2055.

Angell, J., Robinson, T., Lawrence, S., 1998. Topex/poseidon observations of kelvin, rossby and tropical instability waves in the equatorial pacific ocean. Advances in Space Research 22, 1561–1565.

Barnett, T., 1983. Interaction of the monsoon and pacific trade wind system at interannual time scales part i: the equatorial zone. Monthly Weather Review 111, 756–773.

Baturin, N., Niiler, P., 1997. Effects of instability waves in the mixed layer of the equatorial pacific. Journal of Geophysical Research: Oceans 102, 27771–27793.

Benestad, R., Sutton, R., Allen, M., Anderson, D., 2001. The influence of subseasonal wind variability on tropical instability waves in the pacific. Geophysical research letters 28, 2041–2044.

Benestad, R.E., Sutton, R.T., Anderson, D.L., 2002. The effect of el niño on intraseasonal kelvin waves. Quarterly Journal of the Royal Meteorological Society: A journal of the atmospheric sciences, applied meteorology and physical oceanography 128, 1277–1291.

Bergman, J.W., Hendon, H.H., Weickmann, K.M., 2001. Intraseasonal air–sea interactions at the onset of el niño. Journal of Climate 14, 1702–1719.

Betts, A.K., Ridgway, W., 1988. Coupling of the radiative, convective, and surface fluxes over the equatorial pacific. Journal of Atmospheric Sciences 45, 522–536.

Bjerknes, J., 1969. Atmospheric teleconnections from the equatorial pacific. Monthly weather review 97, 163–172.

Boucharel, J., 2010. Modes de variabilité climatique dans l'océan Pacifique tropical: quantification des non-linéarités et rôle sur les changements de régimes climatiques. Ph.D. thesis. Université Paul Sabatier-Toulouse III.

Boucharel, J., Almar, R., Kestenare, E., Jin, F.F., 2021. On the influence of enso complexity on pan-pacific coastal wave extremes. Proceedings of the National Academy of Sciences 118, e2115599118.

Boucharel, J., Dewitte, B., Garel, B., Du Penhoat, Y., 2009. Enso's non-stationary and non-gaussian character: The role of climate shifts. Nonlinear Processes in Geophysics 16, 453–473.

Boucharel, J., Jin, F.F., 2020. A simple theory for the modulation of tropical instability waves by enso and the annual cycle. Tellus A: Dynamic Meteorology and Oceanography 72, 1–14.

Boucharel, J., Jin, F.F., England, M.H., Dewitte, B., Lin, I., Huang, H.C., Balmaseda, M.A., 2016a. Influence of oceanic intraseasonal kelvin waves on eastern pacific hurricane activity. Journal of Climate 29, 7941–7955.

Boucharel, J., Jin, F.F., England, M.H., Lin, I., 2016b. Modes of hurricane activity variability in the eastern pacific: Implications for the 2016 season. Geophysical Research Letters 43, 11–358.

Boucharel, J., Timmermann, A., Jin, F.F., 2013. Zonal phase propagation of enso sea surface temperature anomalies: Revisited. Geophysical Research Letters 40, 4048–4053.

Boulanger, J.P., Cravatte, S., Menkes, C., 2003. Reflected and locally wind-forced interannual equatorial kelvin waves in the western pacific ocean. Journal of Geophysical Research: Oceans 108.

Boulanger, J.P., Menkes, C., 1995. Propagation and reflection of long equatorial waves in the pacific ocean during the 1992–1993 el nino. Journal of Geophysical Research: Oceans 100, 25041–25059.

Boulanger, J.P., Menkes, C., 1999. Long equatorial wave reflection in the pacific ocean from topex/poseidon data during the 1992–1998 period. Climate dynamics 15, 205–225.

Bryden, H.L., Brady, E.C., 1985. Diagnostic model of the three-dimensional circulation in the upper equatorial pacific ocean. Journal of Physical Oceanography 15, 1255–1273.

Busalacchi, A.J., Cane, M.A., 1988. The effect of varying stratification on low-frequency equatorial motions. Journal of physical oceanography 18, 801–812.

Busalacchi, A.J., Takeuchi, K., O'Brien, J.J., 1983. Interannual variability of the equatorial pacific—revisited. Journal of Geophysical Research: Oceans 88, 7551–7562.

Busecke, J.J., Resplandy, L., Dunne, J.P., 2019. The equatorial undercurrent and the oxygen minimum zone in the pacific. Geophysical Research Letters 46, 6716–6725.

Cai, W., McPhaden, M.J., Grimm, A.M., Rodrigues, R.R., Taschetto, A.S., Garreaud, R.D., Dewitte, B., Poveda, G., Ham, Y.G., Santoso, A., et al., 2020. Climate impacts of the el niño–southern oscillation on south america. Nature Reviews Earth & Environment 1, 215–231.

Cane, M.A., Sarachik, E., 1976. Forced baroclinic ocean motions. i. the linear equatorial unbounded case. J. Mar. Res. 34, 629–665.

Cane, M.A., Sarachik, E., Moore, D., Sarachik, E., 1981. The response of a linear baroclinic equatorial ocean to periodic forcing. Journal of Marine Research 39, 651–693.

Capotondi, A., Wittenberg, A.T., Newman, M., Di Lorenzo, E., Yu, J.Y., Braconnot, P., Cole, J., Dewitte, B., Giese, B., Guilyardi, E., et al., 2015. Understanding enso diversity. Bulletin of the American Meteorological Society 96, 921–938.

Carton, J.A., Giese, B.S., 2008. A reanalysis of ocean climate using simple ocean data assimilation (soda). Monthly weather review 136, 2999–3017.

Chelton, D.B., Esbensen, S.K., Schlax, M.G., Thum, N., Freilich, M.H., Wentz, F.J., Gentemann, C.L., McPhaden, M.J., Schopf, P.S., 2001. Observations of coupling between surface wind stress and sea surface temperature in the eastern tropical pacific. Journal of Climate 14, 1479–1498.

Chiodi, A.M., Harrison, D.E., Vecchi, G.A., 2014. Subseasonal atmospheric variability and el niño waveguide warming: Observed effects of the madden–julian oscillation and westerly wind events. Journal of Climate 27, 3619–3642.

Choi, J., An, S.I., Kug, J.S., Yeh, S.W., 2011. The role of mean state on changes in el niño's flavor. Climate Dynamics 37, 1205–1215.

Clarke, A.J., 2008. An introduction to the dynamics of El Niño and the Southern Oscillation. Elsevier.

Clement, A.C., Seager, R., Murtugudde, R., 2005. Why are there tropical warm pools? Journal of Climate 18, 5294–5311.

Collins, M., An, S.I., Cai, W., Ganachaud, A., Guilyardi, E., Jin, F.F., Jochum, M., Lengaigne, M., Power, S., Timmermann, A., et al., 2010. The impact of global warming on the tropical pacific ocean and el niño. Nature Geoscience 3, 391–397.

Conejero, C., 2021. Impact du changement climatique sur la circulation océanique dans les systèmes d'upwelling de bord Est de l'hémisphère Sud. Ph.D. thesis. Toulouse 3.

Contreras, R.F., 2002. Long-term observations of tropical instability waves. Journal of Physical Oceanography 32, 2715–2722.

Cox, M.D., 1980. Generation and propagation of 30-day waves in a numerical model of the pacific. Journal of Physical Oceanography 10, 1168–1186.

Cravatte, S., Picaut, J., Eldin, G., 2003. Second and first baroclinic kelvin modes in the equatorial pacific at intraseasonal timescales. Journal of Geophysical Research: Oceans 108.

Davis, R.E., Kessler, W.S., Sherman, J.T., 2012. Gliders measure western boundary current transport from the south pacific to the equator. Journal of Physical Oceanography 42, 2001–2013.

Debreu, L., Marchesiello, P., Penven, P., Cambon, G., 2012. Two-way nesting in split-explicit ocean models: Algorithms, implementation and validation. Ocean Modelling 49, 1–21.

Dee, D.P., Uppala, S.M., Simmons, A.J., Berrisford, P., Poli, P., Kobayashi, S., Andrae, U., Balmaseda, M., Balsamo, G., Bauer, d.P., et al., 2011. The era-interim reanalysis: Configuration and performance of the data assimilation system. Quarterly Journal of the royal meteorological society 137, 553–597.

Delcroix, T., Boulanger, J.P., Masia, F., Menkes, C., 1994. Geosat-derived sea level and surface current anomalies in the equatorial pacific during the 1986–1989 el niño and la niña. Journal of Geophysical Research: Oceans 99, 25093–25107.

Delpech, A., Cravatte, S., Marin, F., Ménesguen, C., Morel, Y., 2020. Deep eddy kinetic energy in the tropical pacific from lagrangian floats. Journal of Geophysical Research: Oceans 125, e2020JC016313.

DeMott, C.A., Stan, C., Randall, D.A., Kinter, J.L., Khairoutdinov, M., 2011. The asian monsoon in the superparameterized ccsm and its relationship to tropical wave activity. Journal of Climate 24, 5134–5156.

Dewitte, B., Illig, S., Renault, L., Goubanova, K., Takahashi, K., Gushchina, D., Mosquera, K., Purca, S., 2011. Modes of covariability between sea surface temperature and wind stress intraseasonal anomalies along the coast of peru from satellite observations (2000–2008). Journal of Geophysical Research: Oceans 116.

Dewitte, B., Reverdin, G., Maes, C., 1999. Vertical structure of an ogcm simulation of the equatorial pacific ocean in 1985–94. Journal of Physical Oceanography 29, 1542–1570.

Dewitte, B., Takahashi, K., 2019. Diversity of moderate el niño events evolution: role of air–sea interactions in the eastern tropical pacific. Climate Dynamics 52, 7455–7476.

Dewitte, B., Vazquez-Cuervo, J., Goubanova, K., Illig, S., Takahashi, K., Cambon, G., Purca, S., Correa, D., Gutiérrez, D., Sifeddine, A., et al., 2012. Change in el niño flavours over 1958–2008: Implications for the long-term trend of the upwelling off peru. Deep Sea Research Part II: Topical Studies in Oceanography 77, 143–156.

Dewitte, B., Yeh, S.W., Moon, B.K., Cibot, C., Terray, L., 2007. Rectification of enso variability by interdecadal changes in the equatorial background mean state in a cgcm simulation. Journal of climate 20, 2002–2021.

Donguy, J.R., Meyers, G., 1996. Mean annual variation of transport of major currents in the tropical pacific ocean. Deep Sea Research Part I: Oceanographic Research Papers 43, 1105–1122.

Enfield, D.B., 1987. The intraseasonal oscillation in eastern pacific sea levels: How is it forced? Journal of Physical Oceanography 17, 1860–1876.

Escobar-Franco, M.G., Boucharel, J., Dewitte, B., 2022. On the relationship between tropical instability waves and intraseasonal equatorial kelvin waves in the pacific from satellite observations (1993–2018). Frontiers in Marine Science .

Evans, W., Strutton, P.G., Chavez, F.P., 2009. Impact of tropical instability waves on nutrient and chlorophyll distributions in the equatorial pacific. Deep Sea Research Part I: Oceanographic Research Papers 56, 178–188.

Fairall, C.W., Bradley, E.F., Hare, J., Grachev, A.A., Edson, J.B., 2003. Bulk parameterization of air–sea fluxes: Updates and verification for the coare algorithm. Journal of climate 16, 571–591.

Fedorov, A., Harper, S., Philander, S., Winter, B., Wittenberg, A., 2003. How predictable is el niño? Bulletin of the American Meteorological Society 84, 911–920.

Fedorov, A.V., 2002. The response of the coupled tropical ocean–atmosphere to westerly wind bursts. Quarterly Journal of the Royal Meteorological Society: A journal of the atmospheric sciences, applied meteorology and physical oceanography 128, 1–23.

Fiedler, P.C., Talley, L.D., 2006. Hydrography of the eastern tropical pacific: A review. Progress in Oceanography 69, 143–180.

Fine, R.A., Lukas, R., Bingham, F.M., Warner, M.J., Gammon, R.H., 1994. The western equatorial pacific: A water mass crossroads. Journal of Geophysical Research: Oceans 99, 25063–25080.

Flament, P.J., Kennan, S.C., Knox, R.A., Niiler, P.P., Bernstein, R.L., 1996. The three-dimensional structure of an upper ocean vortex in the tropical pacific ocean. Nature 383, 610–613.

Galanti, E., Tziperman, E., 2000. Enso's phase locking to the seasonal cycle in the fast-sst, fast-wave, and mixed-mode regimes. Journal of the atmospheric sciences 57, 2936–2950.

Ganachaud, A., Cravatte, S., Melet, A., Schiller, A., Holbrook, N., Sloyan, B., Widlansky, M., Bowen, M., Verron, J., Wiles, P., et al., 2014. The s outhwest p acific o cean circulation and climate experiment (spice). Journal of Geophysical Research: Oceans 119, 7660–7686.

Garric, G., Parent, L., Greiner, E., Drévillon, M., Hamon, M., Lellouche, J.M., Régnier, C., Desportes, C., Le Galloudec, O., Bricaud, C., et al., 2017. Performance and quality assessment of the global ocean eddy-permitting physical reanalysis glorys2v4., in: EGU General Assembly Conference Abstracts, p. 18776.

Gasparin, F., Ganachaud, A., Maes, C., Marin, F., Eldin, G., 2012. Oceanic transports through the solomon sea: The bend of the new guinea coastal undercurrent. Geophysical Research Letters 39.

Giese, B.S., Harrison, D., 1991. Eastern equatorial pacific response to three composite westerly wind types. Journal of Geophysical Research: Oceans 96, 3239–3248.

Gordon, A.L., 1986. Is there a global scale ocean circulation? Eos, Transactions American Geophysical Union 67, 109–110.

Gouriou, Y., Toole, J., 1993. Mean circulation of the upper layers of the western equatorial pacific ocean. Journal of Geophysical Research: Oceans 98, 22495–22520.

Graham, T., 2014. The importance of eddy permitting model resolution for simulation of the heat budget of tropical instability waves. Ocean Modelling 79, 21–32. URL: https://www.sciencedirect.com/science/article/pii/S1463500314000535, doi:https://doi.org/10.1016/j.ocemod.2014.04.005.

Grenier, M., Cravatte, S., Blanke, B., Menkes, C., Koch-Larrouy, A., Durand, F., Melet, A., Jeandel, C., 2011. From the western boundary currents to the pacific equatorial undercurrent: Modeled pathways and water mass evolutions. Journal of Geophysical Research: Oceans 116.

Gushchina, D., Dewitte, B., 2012. Intraseasonal tropical atmospheric variability associated with the two flavors of el niño. Monthly Weather Review 140, 3669 – 3681. URL: https://journals.ametsoc.org/view/journals/mwre/140/11/mwr-d-11-00267.1.xml, doi:10.1175/MWR-D-11-00267.1.

Gushchina, D., Dewitte, B., 2019. Decadal modulation of the relationship between intraseasonal tropical variability and enso. Climate Dynamics 52, 2091–2103.

Hansen, D.V., Paul, C.A., 1984. Genesis and effects of long waves in the equatorial pacific. Journal of Geophysical Research: Oceans 89, 10431–10440.

Harrison, D., Giese, B.S., 1988. Remote westerly wind forcing of the eastern equatorial pacific; some model results. Geophysical research letters 15, 804–807.

Harrison, D., Vecchi, G.A., 1997. Westerly wind events in the tropical pacific, 1986–95. Journal of climate 10, 3131–3156.

Hashizume, H., Xie, S.P., Liu, W.T., Takeuchi, K., 2001. Local and remote atmospheric response to tropical instability waves: A global view from space. Journal of Geophysical Research: Atmospheres 106, 10173–10185.

Hayes, S., Mangum, L., Picaut, J., Sumi, A., Takeuchi, K., 1991. Toga-tao: A moored array for real-time measurements in the tropical pacific ocean. Bulletin of the American Meteorological Society 72, 339–347.

Hendon, H.H., Liebmann, B., Glick, J.D., 1998. Oceanic kelvin waves and the madden–julian oscillation. Journal of the Atmospheric Sciences 55, 88–101.

Hendon, H.H., Zhang, C., Glick, J.D., 1999. Interannual variation of the madden–julian oscillation during austral summer. Journal of Climate 12, 2538–2550.

Hersbach, H., Bell, B., Berrisford, P., Hirahara, S., Horányi, A., Muñoz-Sabater, J., Nicolas, J., Peubey, C., Radu, R., Schepers, D., et al., 2020. The era5 global reanalysis. Quarterly Journal of the Royal Meteorological Society 146, 1999–2049.

Holmes, R., Thomas, L., 2015. The modulation of equatorial turbulence by tropical instability waves in a regional ocean model. Journal of Physical Oceanography 45, 1155–1173.

Holmes, R., Thomas, L., 2016. Modulation of tropical instability wave intensity by equatorial kelvin waves. Journal of Physical Oceanography 46, 2623–2643.

Horel, J.D., 1982. On the annual cycle of the tropical pacific atmosphere and ocean. Monthly Weather Review 110, 1863–1878.

Houze Jr, R.A., 2004. Mesoscale convective systems. Reviews of Geophysics 42.

Hsin, Y.C., Qiu, B., 2012. Seasonal fluctuations of the surface north equatorial countercurrent (necc) across the pacific basin. Journal of Geophysical Research: Oceans 117.

Hu, D., Wu, L., Cai, W., Gupta, A.S., Ganachaud, A., Qiu, B., Gordon, A.L., Lin, X., Chen, Z., Hu, S., et al., 2015. Pacific western boundary currents and their roles in climate. Nature 522, 299–308.

Hu, S., Fedorov, A.V., Lengaigne, M., Guilyardi, É., 2014. The impact of westerly wind bursts on the diversity and predictability of el niño events: An ocean energetics perspective. Geophysical research letters 41, 4654–4663.

Hu, Z.Z., Kumar, A., Huang, B., 2016. Spatial distribution and the interdecadal change of leading modes of heat budget of the mixed-layer in the tropical pacific and the association with enso. Climate dynamics 46, 1753–1768.

Huang, B., Liu, C., Banzon, V., Freeman, E., Graham, G., Hankins, B., Smith, T., Zhang, H., 2020. Noaa 0.25-degree daily optimum interpolation sea surface temperature (oisst), version 2.1. NOAA National Centers for Environmental Information .

Im, S.H., An, S.I., Kim, S.T., Jin, F.F., 2015. Feedback processes responsible for el niño-la niña amplitude asymmetry. Geophysical Research Letters 42, 5556–5563.

Im, S.H., An, S.I., Lengaigne, M., Noh, Y., 2012. Seasonality of tropical instability waves and its feedback to the seasonal cycle in the tropical eastern pacific. The Scientific World Journal 2012.

Inoue, R., Lien, R.C., Moum, J., 2012. Modulation of equatorial turbulence by a tropical instability wave. Journal of Geophysical Research: Oceans 117.

Jakoboski, J., Todd, R.E., Owens, W.B., Karnauskas, K.B., Rudnick, D.L., 2020. Bifurcation and upwelling of the equatorial undercurrent west of the galapagos archipelago. Journal of Physical Oceanography 50, 887–905.

Janicot, S., Mounier, F., Gervois, S., Sultan, B., Kiladis, G.N., 2010. The dynamics of the west african monsoon. part v: The detection and role of the dominant modes of convectively coupled equatorial rossby waves. Journal of Climate 23, 4005–4024.

Jean-Michel, L., Eric, G., Romain, B.B., Gilles, G., Angélique, M., Marie, D., Clement, B., Mathieu, H., Olivier, L.G., Charly, R., et al., 2021. The copernicus global 1/12 oceanic and sea ice glorys12 reanalysis. Frontiers in Earth Science 9, 698876.

Jin, F.F., An, S.I., Timmermann, A., Zhao, J., 2003. Strong el niño events and nonlinear dynamical heating. Geophysical research letters 30, 20–1.

Jin, F.F., Lin, L., Timmermann, A., Zhao, J., 2007. Ensemble-mean dynamics of the enso recharge oscillator under state-dependent stochastic forcing. Geophysical research letters 34.

Jin, F.F., Neelin, J.D., Ghil, M., 1994. El niño on the devil's staircase: Annual subharmonic steps to chaos. Science 264, 70–72.

Jin, F.F., Neelin, J.D., Ghil, M., 1996. El niño/southern oscillation and the annual cycle: Subharmonic frequency-locking and aperiodicity. Physica D: Nonlinear Phenomena 98, 442–465.

Johnson, E.S., Proehl, J.A., 2004. Tropical instability wave variability in the pacific and its relation to large-scale currents. Journal of physical oceanography 34, 2121–2147.

Johnson, G.C., Sloyan, B.M., Kessler, W.S., McTaggart, K.E., 2002. Direct measurements of upper ocean currents and water properties across the tropical pacific during the 1990s. Progress in Oceanography 52, 31–61.

Kang, I.S., Kug, J.S., 2002. El niño and la niña sea surface temperature anomalies: Asymmetry characteristics associated with their wind stress anomalies. Journal of Geophysical Research: Atmospheres 107, ACL–1.

Kao, H.Y., Yu, J.Y., 2009. Contrasting eastern-pacific and central-pacific types of enso. Journal of Climate 22, 615–632.

Keenlyside, N., Kleeman, R., 2002. Annual cycle of equatorial zonal currents in the pacific. Journal of Geophysical Research: Oceans 107, 8–1.

Kennan, S.C., Flament, P.J., 2000. Observations of a tropical instability vortex. Journal of Physical Oceanography 30, 2277–2301.

Kessler, W.S., 2001. Eof representations of the madden–julian oscillation and its connection with enso. Journal of Climate 14, 3055–3061.

Kessler, W.S., 2002. Is enso a cycle or a series of events? Geophysical Research Letters 29, 40–1.

Kessler, W.S., 2006a. The circulation of the eastern tropical pacific: A review. Progress in Oceanography 69, 181–217.

Kessler, W.S., 2006b. The circulation of the eastern tropical pacific: A review. Progress in Oceanography 69, 181–217.

Kessler, W.S., McPhaden, M.J., 1995. Oceanic equatorial waves and the 1991–93 el niño. Journal of Climate 8, 1757–1774.

Kessler, W.S., McPhaden, M.J., Weickmann, K.M., 1995. Forcing of intraseasonal kelvin waves in the equatorial pacific. Journal of Geophysical Research: Oceans 100, 10613–10631.

Kiladis, G.N., Dias, J., Straub, K.H., Wheeler, M.C., Tulich, S.N., Kikuchi, K., Weickmann, K.M., Ventrice, M.J., 2014. A comparison of olr and circulation-based indices for tracking the mjo. Monthly Weather Review 142, 1697–1715.

Kiladis, G.N., Wheeler, M.C., Haertel, P.T., Straub, K.H., Roundy, P.E., 2009. Convectively coupled equatorial waves. Reviews of Geophysics 47.

Kim, D., Sobel, A.H., Maloney, E.D., Frierson, D.M., Kang, I.S., 2011. A systematic relationship between intraseasonal variability and mean state bias in agcm simulations. Journal of Climate 24, 5506–5520.

Kim, S.T., Jin, F.F., 2011a. An enso stability analysis. part i: Results from a hybrid coupled model. Climate dynamics 36, 1593–1607.

Kim, S.T., Jin, F.F., 2011b. An enso stability analysis. part ii: Results from the twentieth and twenty-first century simulations of the cmip3 models. Climate Dynamics 36, 1609–1627.

Kimura, S., Inoue, T., Sugimoto, T., 2001. Fluctuation in the distribution of low-salinity water in the north equatorial current and its effect on the larval transport of the japanese eel. Fisheries Oceanography 10, 51–60.

Klein, S.A., Hartmann, D.L., 1993. The seasonal cycle of low stratiform clouds. Journal of Climate 6, 1587–1606.

Knauss, J.A., 1959. Measurements of the cromwell current. Deep Sea Research (1953) 6, 265–286.

Knauss, J.A., 1966. Further measurements and observations on the cromwell current. J. marine Res. 24, 205–240.

Knauss, J.A., KING, J.E., 1958. Observations of the pacific equatorial undercurrent. Nature 182, 601–602.

Knox, R., Halpern, D., 1982. Long range kelvin wave propagation of transport variations in pacific ocean equatorial currents. J. Mar. Res 40, 39.

Knutson, T.R., Weickmann, K.M., 1987. 30–60 day atmospheric oscillations: Composite life cycles of convection and circulation anomalies. Monthly Weather Review 115, 1407–1436.

Kug, J.S., Jin, F.F., An, S.I., 2009. Two types of el niño events: Cold tongue el niño and warm pool el niño. Journal of Climate 22, 1499 – 1515. URL: `https://journals.ametsoc.org/view/journals/clim/22/6/2008jcli2624.1.xml`, doi:`10.1175/2008JCLI2624.1`.

Kutsuwada, K., McPhaden, M., 2002. Intraseasonal variations in the upper equatorial pacific ocean prior to and during the 1997–98 el niño. Journal of physical oceanography 32, 1133–1149.

Large, W.G., McWilliams, J.C., Doney, S.C., 1994. Oceanic vertical mixing: A review and a model with a nonlocal boundary layer parameterization. Reviews of geophysics 32, 363–403.

Lawrence, S., Angell, J., 2000. Evidence for rossby wave control of tropical instability waves in the pacific ocean. Geophysical research letters 27, 2257–2260.

Lawrence, S.P., Allen, M.R., Anderson, D.L., Llewellyn-Jones, D.T., 1998. Effects of subsurface ocean dynamics on instability waves in the tropical pacific. Journal of Geophysical Research: Oceans 103, 18649–18663.

Lee, T., Lagerloef, G., Gierach, M.M., Kao, H.Y., Yueh, S., Dohan, K., 2012. Aquarius reveals salinity structure of tropical instability waves. Geophysical Research Letters 39.

Legeckis, R., 1977. Long waves in the eastern equatorial pacific ocean: A view from a geostationary satellite. Science 197, 1179–1181.

Legeckis, R., Brown, C.W., Bonjean, F., Johnson, E.S., 2004. The influence of tropical instability waves on phytoplankton blooms in the wake of the marquesas islands during 1998 and on the currents observed during the drift of the kon-tiki in 1947. Geophysical Research Letters 31.

Lellouche, J.M., Greiner, E., Le Galloudec, O., Garric, G., Regnier, C., Drevillon, M., Benkiran, M., Testut, C.E., Bourdalle-Badie, R., Gasparin, F., et al., 2018. Recent updates to the copernicus marine service global ocean monitoring and forecasting real-time 1/ 12 high-resolution system. Ocean Science 14, 1093–1126.

Lellouche, J.M., Le Galloudec, O., Drévillon, M., Régnier, C., Greiner, E., Garric, G., Ferry, N., Desportes, C., Testut, C.E., Bricaud, C., et al., 2013. Evaluation of global monitoring and forecasting systems at mercator océan. Ocean Science 9, 57–81.

Lengaigne, M., Boulanger, J.P., Menkes, C., Delecluse, P., Slingo, J., 2004a. Westerly wind events in the tropical pacific and their influence on the coupled ocean-atmosphere system. Earth Climate: The Ocean-Atmosphere Interaction, Geophys. Monogr 147, 49–69.

Lengaigne, M., Boulanger, J.P., Menkes, C., Masson, S., Madec, G., Delecluse, P., 2002. Ocean response to the march 1997 westerly wind event. Journal of Geophysical Research: Oceans 107, SRF–16.

Lengaigne, M., Guilyardi, E., Boulanger, J.P., Menkes, C., Delecluse, P., Inness, P., Cole, J., Slingo, J., 2004b. Triggering of el niño by westerly wind events in a coupled general circulation model. Climate Dynamics 23, 601–620.

Lien, R.C., Caldwell, D.R., Gregg, M., Moum, J.N., 1995. Turbulence variability at the equator in the central pacific at the beginning of the 1991–1993 el nino. Journal of Geophysical Research: Oceans 100, 6881–6898.

Lin, I.I., Camargo, S.J., Patricola, C.M., Boucharel, J., Chand, S., Klotzbach, P., Chan, J.C., Wang, B., Chang, P., Li, T., et al., 2020. Enso and tropical cyclones. El Niño Southern Oscillation in a Changing Climate , 377–408.

Lin, J.W.B., Neelin, J.D., Zeng, N., 2000. Maintenance of tropical intraseasonal variability: Impact of evaporation–wind feedback and midlatitude storms. Journal of the Atmospheric Sciences 57, 2793–2823.

Lin, Y.L., 2007. Mesoscale dynamics. volume 630. Cambridge University Press Cambridge.

Liu, F., Huang, G., Feng, L., 2012. Critical roles of convective momentum transfer in sustaining the multi-scale madden–julian oscillation. Theoretical and Applied Climatology 108, 471–477.

Liu, F., Wang, B., 2012. A model for the interaction between 2-day waves and moist kelvin waves. Journal of the atmospheric sciences 69, 611–625.

Liu, F., Wang, B., 2013. Impacts of upscale heat and momentum transfer by moist kelvin waves on the madden–julian oscillation: A theoretical model study. Climate dynamics 40, 213–224.

Liu, H., Zhou, H., Yang, W., Liu, X., Li, Y., Yang, Y., Chen, X., Li, X., 2021. A three-dimensional gravest empirical mode determined from hydrographic observations in the western equatorial pacific ocean. Journal of Marine Systems 214, 103487.

Liu, X., Zhou, H., 2020. Seasonal variations of the north equatorial current across the pacific ocean. Journal of Geophysical Research: Oceans 125, e2019JC015895.

Lukas, R., 1986. The termination of the equatorial undercurrent in the eastern pacific. Progress in Oceanography 16, 63–90.

Lukas, R., Firing, E., 1984. The geostrophic balance of the pacific equatorial undercurrent. Deep Sea Research Part A. Oceanographic Research Papers 31, 61–66.

Lyman, J.M., Chelton, D.B., DeSzoeke, R.A., Samelson, R.M., 2005. Tropical instability waves as a resonance between equatorial rossby waves. Journal of physical oceanography 35, 232–254.

Lyman, J.M., Johnson, G.C., Kessler, W.S., 2007. Distinct 17-and 33-day tropical instability waves in subsurface observations. Journal of physical oceanography 37, 855–872.

Madden, R.A., Julian, P.R., 1971. Detection of a 40–50 day oscillation in the zonal wind in the tropical pacific. Journal of Atmospheric Sciences 28, 702–708.

Madden, R.A., Julian, P.R., 1972. Description of global-scale circulation cells in the tropics with a 40–50 day period. Journal of Atmospheric Sciences 29, 1109–1123.

Madec, G., Delecluse, P., Imbard, M., Levy, C., 1997. Ocean general circulation model reference manual. Note du Pôle de modélisation .

Maillard, L., 2023. Influence des ondes tropicales d'instabilité sur la variabilité climatique du Pacifique tropical Est. Ph.D. thesis. Université Paul Sabatier-Toulouse III.

Maillard, L., Boucharel, J., Renault, L., 2022a. Direct and rectified effects of tropical instability waves on the eastern tropical pacific mean state in a regional ocean model. Journal of Physical Oceanography .

Maillard, L., Boucharel, J., Stuecker, M., Jin, F.F., Renault, L., 2022b. Modulation of the eastern equatorial pacific seasonal cycle by tropical instability waves. Geophysical Research Letters 49, e2022GL100991.

Marzeion, B., Timmermann, A., Murtugudde, R., Jin, F.F., 2005. Biophysical feedbacks in the tropical pacific. Journal of Climate 18, 58–70.

Masina, S., Philander, S., Bush, A., 1999. An analysis of tropical instability waves in a numerical model of the pacific ocean: 2. generation and energetics of the waves. Journal of Geophysical Research: Oceans 104, 29637–29661.

Matsuno, T., 1966. Quasi-geostrophic motions in the equatorial area. Journal of the Meteorological Society of Japan. Ser. II 44, 25–43.

McClain, C.R., Christian, J.R., Signorini, S.R., Lewis, M.R., Asanuma, I., Turk, D., Dupouy-Douchement, C., 2002. Satellite ocean-color observations of the tropical pacific ocean. Deep Sea Research Part II: Topical Studies in Oceanography 49, 2533–2560.

McCreary Jr, J.P., 1984. Equatorial beams. Journal of Marine Research 42, 395–430.

McCreary Jr, J.P., Yu, Z., 1992. Equatorial dynamics in a 212-layer model. Progress in Oceanography 29, 61–132.

McPhaden, M.J., 1986. The equatorial undercurrent: 100 years of discovery. Eos, Transactions American Geophysical Union 67, 762–765.

McPhaden, M.J., 1996. Monthly period oscillations in the pacific north equatorial countercurrent. Journal of Geophysical Research: Oceans 101, 6337–6359.

McPhaden, M.J., 1999. Genesis and evolution of the 1997-98 el niño. Science 283, 950–954.

McPhaden, M.J., 2002a. El nino, la nina, and the climate swings of 1997–98: A review. La Niña and its impacts. Facts and speculation , 25–30.

McPhaden, M.J., 2002b. Mixed layer temperature balance on intraseasonal timescales in the equatorial pacific ocean. Journal of climate 15, 2632–2647.

McPhaden, M.J., Santoso, A., Cai, W., 2020. Introduction to el niño southern oscillation in a changing climate. El Niño Southern Oscillation in a Changing Climate , 1–19.

McPhaden, M.J., Taft, B.A., 1988. Dynamics of seasonal and intraseasonal variability in the eastern equatorial pacific. Journal of Physical Oceanography 18, 1713–1732.

McPhaden, M.J., Yu, X., 1999. Equatorial waves and the 1997–98 el niño. Geophysical Research Letters 26, 2961–2964.

McPhaden, M.J., Zebiak, S.E., Glantz, M.H., 2006. Enso as an integrating concept in earth science. science 314, 1740–1745.

Meehl, G., Lukas, R., Kiladis, G., Weickmann, K., Matthews, A., Wheeler, M., 2001. A conceptual framework for time and space scale interactions in the climate system. Climate Dynamics 17, 753.

Menkes, C.E., Vialard, J.G., Kennan, S.C., Boulanger, J.P., Madec, G.V., 2006. A modeling study of the impact of tropical instability waves on the heat budget of the eastern equatorial pacific. Journal of Physical Oceanography 36, 847–865.

Meyers, G., Donguy, J.R., 1984. The north equatorial countercurrent and heat storage in the western pacific ocean during 1982–83. Nature 312, 258–260.

Mitchell, T.P., Wallace, J.M., 1992. The annual cycle in equatorial convection and sea surface temperature. Journal of Climate 5, 1140–1156.

Mosquera-Vásquez, K., Dewitte, B., Illig, S., 2014. The central p acific e l n iño intraseasonal k elvin wave. Journal of Geophysical Research: Oceans 119, 6605–6621.

Musman, S., 1989. Sea height wave form in equatorial waves and its interpretation. Journal of Geophysical Research: Oceans 94, 3303–3309.

Neelin, J.D., Jin, F.F., Syu, H.H., 2000. Variations in enso phase locking. Journal of Climate 13, 2570–2590.

Okumura, Y.M., Deser, C., 2010. Asymmetry in the duration of el niño and la niña. Journal of Climate 23, 5826–5843.

Perigaud, C., Dewitte, B., 1996. El niño–la niña events simulated with cane and zebiak's model and observed with satellite or in situ data. part i: Model data comparison. Journal of climate 9, 66–84.

Philander, S., 1973. Equatorial undercurrent: Measurements and theories. Reviews of Geophysics 11, 513–570.

Philander, S., 1976. Instabilities of zonal equatorial currents. Journal of Geophysical Research 81, 3725–3735.

Philander, S., 1978. Forced oceanic waves. Reviews of Geophysics 16, 15–46.

Philander, S., 1990. El niño, la niña, and the southern oscillation, 293 pp.

Philander, S., Pacanowski, R., 1981. The oceanic response to cross-equatorial winds (with application to coastal upwelling in low latitudes). Tellus 33, 201–210.

Picaut, J., Delcroix, T., 1995. Equatorial wave sequence associated with warm pool displacements during the 1986–1989 el niño-la niña. Journal of Geophysical Research: Oceans 100, 18393–18408.

Picaut, J., Masia, F., Du Penhoat, Y., 1997. An advective-reflective conceptual model for the oscillatory nature of the enso. Science 277, 663–666.

Picaut, J., Sombardier, L., 1993. Influence of density stratification and bottom depth on vertical mode structure functions in the tropical pacific. Journal of Geophysical Research: Oceans 98, 14727–14737.

Polito, P.S., Ryan, J.P., Liu, W.T., Chavez, F.P., 2001. Oceanic and atmospheric anomalies of tropical instability waves. Geophysical Research Letters 28, 2233–2236.

Praveen Kumar, B., Vialard, J., Lengaigne, M., Murty, V., Mcphaden, M.J., 2012. Tropflux: Air-sea fluxes for the global tropical oceans—description and evaluation. Climate dynamics 38, 1521–1543.

Puy, M., Vialard, J., Lengaigne, M., Guilyardi, E., 2016. Modulation of equatorial pacific westerly/easterly wind events by the madden–julian oscillation and convectively-coupled rossby waves. Climate dynamics 46, 2155–2178.

Puy, M., Vialard, J., Lengaigne, M., Guilyardi, E., DiNezio, P.N., Voldoire, A., Balmaseda, M., Madec, G., Menkes, C., Mcphaden, M.J., 2019. Influence of westerly wind events stochasticity on el niño amplitude: The case of 2014 vs. 2015. Climate Dynamics 52, 7435–7454.

Qiao, L., Weisberg, R.H., 1995. Tropical instability wave kinematics: Observations from the tropical instability wave experiment. Journal of Geophysical Research: Oceans 100, 8677–8693.

Qiao, L., Weisberg, R.H., 1997. The zonal momentum balance of the equatorial undercurrent in the central pacific. Journal of physical oceanography 27, 1094–1119.

Qiao, L., Weisberg, R.H., 1998. Tropical instability wave energetics: Observations from the tropical instability wave experiment. Journal of Physical Oceanography 28, 345–360.

Qiu, B., Joyce, T.M., 1992. Interannual variability in the mid-and low-latitude western north pacific. Journal of Physical Oceanography 22, 1062–1079.

Qiu, B., Koh, D.A., Lumpkin, C., Flament, P., 1997. Existence and formation mechanism of the north hawaiian ridge current. Journal of Physical Oceanography 27, 431–444.

Qiu, B., Lukas, R., 1996. Seasonal and interannual variability of the north equatorial current, the mindanao current, and the kuroshio along the pacific western boundary. Journal of Geophysical Research: Oceans 101, 12315–12330.

Qu, T., Mitsudera, H., Yamagata, T., 1998. On the western boundary currents in the philippine sea. Journal of Geophysical Research: Oceans 103, 7537–7548.

Rebert, J.P., Donguy, J.R., Eldin, G., Wyrtki, K., 1985. Relations between sea level, thermocline depth, heat content, and dynamic height in the tropical pacific ocean. Journal of Geophysical Research: Oceans 90, 11719–11725.

Renault, L., Masson, S., Arsouze, T., Madec, G., Mcwilliams, J.C., 2020. Recipes for how to force oceanic model dynamics. Journal of Advances in Modeling Earth Systems 12, e2019MS001715.

Renault, L., Molemaker, M.J., McWilliams, J.C., Shchepetkin, A.F., Lemarié, F., Chelton, D., Illig, S., Hall, A., 2016. Modulation of wind work by oceanic current interaction with the atmosphere. Journal of Physical Oceanography 46, 1685–1704.

Roundy, P.E., Kiladis, G.N., 2006. Observed relationships between oceanic kelvin waves and atmospheric forcing. Journal of Climate 19, 5253–5272.

Roundy, P.E., Schreck, C.J., Janiga, M.A., 2009. Contributions of convectively coupled equatorial rossby waves and kelvin waves to the real-time multivariate mjo indices. Monthly Weather Review 137, 469–478.

Rudnick, D.L., Owens, W.B., Johnston, T.S., Karnauskas, K.B., Jakoboski, J., Todd, R.E., 2021. The equatorial current system west of the galápagos islands during the 2014–16 el niño as observed by underwater gliders. Journal of Physical Oceanography 51, 3–17.

Rydbeck, A., Jensen, T., Flatau, M., 2019. Characterization of intraseasonal kelvin waves in the equatorial pacific ocean. Journal of Geophysical Research: Oceans 124, 2028–2053.

Setoh, T., Imawaki, S., Ostrovskii, A., Umatani, S.I., 1999. Interdecadal variations of enso signals and annual cycles revealed by wavelet analysis. Journal of Oceanography 55, 385–394.

Shchepetkin, A.F., McWilliams, J.C., 2005. The regional oceanic modeling system (roms): a split-explicit, free-surface, topography-following-coordinate oceanic model. Ocean modelling 9, 347–404.

Shinoda, T., Kiladis, G.N., Roundy, P.E., 2009. Statistical representation of equatorial waves and tropical instability waves in the pacific ocean. Atmospheric research 94, 37–44.

Sprintall, J., Cravatte, S., Dewitte, B., Du, Y., Gupta, A.S., 2020. Enso oceanic teleconnections. El Niño Southern Oscillation in a changing climate , 337–359.

Stein, K., Timmermann, A., Schneider, N., 2011. Phase synchronization of the el niño-southern oscillation with the annual cycle. Physical review letters 107, 128501.

Stevenson, M.R., Taft, B.A., 1971. New evidence of the equatorial undercurrent east of the galapagos islands. J. Mar. Res 29, 103–115.

Straub, K.H., Kiladis, G.N., Ciesielski, P.E., 2006. The role of equatorial waves in the onset of the south china sea summer monsoon and the demise of el niño during 1998. Dynamics of Atmospheres and Oceans 42, 216–238.

Strutton, P.G., Ryan, J.P., Chavez, F.P., 2001. Enhanced chlorophyll associated with tropical instability waves in the equatorial pacific. Geophysical Research Letters 28, 2005–2008.

Stuecker, M.F., Timmermann, A., Jin, F.F., Chikamoto, Y., Zhang, W., Wittenberg, A.T., Widiasih, E., Zhao, S., 2017. Revisiting enso/indian ocean dipole phase relationships. Geophysical Research Letters 44, 2481–2492.

Stuecker, M.F., Timmermann, A., Jin, F.F., McGregor, S., Ren, H.L., 2013. A combination mode of the annual cycle and the el niño/southern oscillation. Nature Geoscience 6, 540–544.

Suarez, M.J., Schopf, P.S., 1988. A delayed action oscillator for enso. Journal of Atmospheric Sciences 45, 3283–3287.

Sun, D.Z., Zhang, T., Sun, Y., Yu, Y., 2014. Rectification of el niño–southern oscillation into climate anomalies of decadal and longer time scales: Results from forced ocean gcm experiments. Journal of Climate 27, 2545–2561.

Sverdrup, H.U., 1947. Wind-driven currents in a baroclinic ocean; with application to the equatorial currents of the eastern pacific. Proceedings of the National Academy of Sciences 33, 318–326.

Taburet, G., Sanchez-Roman, A., Ballarotta, M., Pujol, M.I., Legeais, J.F., Fournier, F., Faugere, Y., Dibarboure, G., 2019. Duacs dt2018: 25 years of reprocessed sea level altimetry products. Ocean Science 15, 1207–1224.

Takayabu, Y.N., Iguchi, T., Kachi, M., Shibata, A., Kanzawa, H., 1999. Abrupt termination of the 1997–98 el niño in response to a madden–julian oscillation. Nature 402, 279–282.

Tanaka, Y., Hibiya, T., Sasaki, H., 2015. Downward lee wave radiation from tropical instability waves in the central equatorial p acific o cean: A possible energy pathway to turbulent mixing. Journal of Geophysical Research: Oceans 120, 7137–7149.

Taschetto, A.S., Ummenhofer, C.C., Stuecker, M.F., Dommenget, D., Ashok, K., Rodrigues, R.R., Yeh, S.W., 2020. Enso atmospheric teleconnections. El Niño southern oscillation in a changing climate , 309–335.

Timmermann, A., An, S.I., Kug, J.S., Jin, F.F., Cai, W., Capotondi, A., Cobb, K.M., Lengaigne, M., McPhaden, M.J., Stuecker, M.F., et al., 2018. El niño–southern oscillation complexity. Nature 559, 535–545.

Tuchen, F.P., Brandt, P., Claus, M., Hummels, R., 2018. Deep intraseasonal variability in the central equatorial atlantic. Journal of Physical Oceanography 48, 2851–2865.

Tziperman, E., Stone, L., Cane, M.A., Jarosh, H., 1994. El niño chaos: Overlapping of resonances between the seasonal cycle and the pacific ocean-atmosphere oscillator. Science 264, 72–74.

Ventrice, M.J., Thorncroft, C.D., Janiga, M.A., 2012a. Atlantic tropical cyclogenesis: A three-way interaction between an african easterly wave, diurnally varying convection, and a convectively coupled atmospheric kelvin wave. Monthly weather review 140, 1108–1124.

Ventrice, M.J., Thorncroft, C.D., Schreck III, C.J., 2012b. Impacts of convectively coupled kelvin waves on environmental conditions for atlantic tropical cyclogenesis. Monthly weather review 140, 2198–2214.

Vialard, J., Menkes, C., Boulanger, J.P., Delecluse, P., Guilyardi, E., McPhaden, M.J., Madec, G., 2001. A model study of oceanic mechanisms affecting equatorial pacific sea surface temperature during the 1997–98 el niño. Journal of Physical Oceanography 31, 1649 – 1675. URL: https://journals.ametsoc.org/view/journals/phoc/31/7/1520-0485_2001_031_1649_amsoom_2.0.co_2.xml, doi:10.1175/1520-0485(2001)031<1649:AMSOOM>2.0.CO;2.

Von Schuckmann, K., Brandt, P., Eden, C., 2008. Generation of tropical instability waves in the atlantic ocean. Journal of Geophysical Research: Oceans 113.

Von Schuckmann, K., Le Traon, P.Y., Alvarez-Fanjul, E., Axell, L., Balmaseda, M., Breivik, L.A., Brewin, R.J., Bricaud, C., Drevillon, M., Drillet, Y., et al., 2016. The copernicus marine environment monitoring service ocean state report. Journal of Operational Oceanography 9, s235–s320.

Walker, G.T., 1923. Correlation in seasonal variation of weather. viii: A preliminary study of world weather. Memoires of India Meteorological Department 24, 75–131.

Walker, G.T., 1924. Correlations in seasonal variations of weather. i. a further study of world weather. Memoires Indian Meteorol. Dep. 24, 275–332.

Walker, G.T., Bliss, E., 1928. World weather iii. Memoires of the Royal Meteorological Society 2, 97–106.

Walker, G.T., Bliss, E., 1932. World weather v. Memoires of the Royal Meteorological Society 4, 53–84.

Wallace, J.M., Mitchell, T., Deser, C., 1989. The influence of sea-surface temperature on surface wind in the eastern equatorial pacific: Seasonal and interannual variability. Journal of Climate 2, 1492–1499.

Wang, B., Liu, F., 2011. A model for scale interaction in the madden–julian oscillation. Journal of the atmospheric sciences 68, 2524–2536.

Wang, B., Wang, Y., 1996. Temporal structure of the southern oscillation as revealed by waveform and wavelet analysis. Journal of Climate 9, 1586–1598.

Wang, M., Du, Y., Qiu, B., Cheng, X., Luo, Y., Chen, X., Feng, M., 2017. Mechanism of seasonal eddy kinetic energy variability in the eastern equatorial p acific o cean. Journal of Geophysical Research: Oceans 122, 3240–3252.

Wang, M., Du, Y., Qiu, B., Xie, S.P., Feng, M., 2019. Dynamics on seasonal variability of eke associated with tiws in the eastern equatorial pacific ocean. Journal of Physical Oceanography 49, 1503–1519.

Wang, Y., Gozolchiani, A., Ashkenazy, Y., Havlin, S., 2016. Oceanic el-niño wave dynamics and climate networks. New Journal of Physics 18, 033021.

Warner, S.J., Holmes, R.M., Hawkins, E.H., Hoecker-Martinez, M.S., Savage, A.C., Moum, J.N., 2018. Buoyant gravity currents released from tropical instability waves. Journal of Physical Oceanography 48, 361–382.

Weickmann, K.M., Lussky, G.R., Kutzbach, J.E., 1985. Intraseasonal (30–60 day) fluctuations of outgoing longwave radiation and 250 mb streamfunction during northern winter. Monthly Weather Review 113, 941–961.

Weidman, P., Mickler, D.L., Dayyani, B., Born, G., 1999. Analysis of legeckis eddies in the near-equatorial pacific. Journal of Geophysical Research: Oceans 104, 7865–7887.

Wheeler, M., Kiladis, G.N., 1999. Convectively coupled equatorial waves: Analysis of clouds and temperature in the wavenumber–frequency domain. Journal of the Atmospheric Sciences 56, 374–399.

Wyrtki, K., 1974a. Equatorial currents in the pacific 1950 to 1970 and their relations to the trade winds. Journal of Physical Oceanography 4, 372–380.

Wyrtki, K., 1974b. Sea level and the seasonal fluctuations of the equatorial currents in the western pacific ocean. Journal of Physical Oceanography 4, 91–103.

Wyrtki, K., 1974c. Sea level and the seasonal fluctuations of the equatorial currents in the western pacific ocean. Journal of Physical Oceanography 4, 91–103.

Wyrtki, K., Bennett, E.B., 1963. Vertical eddy viscosity in the pacific equatorial undercurrent, in: Deep Sea Research and Oceanographic Abstracts, Elsevier. pp. 449–455.

Wyrtki, K., Kendall, R., 1967. Transports of the pacific equatorial countercurrent. Journal of Geophysical Research 72, 2073–2076.

Wyrtki, K., Kilonsky, B., 1984. Mean water and current structure during the hawaii-to-tahiti shuttle experiment. Journal of Physical Oceanography 14, 242–254.

Xie, S.P., Ishiwatari, M., Hashizume, H., Takeuchi, K., 1998. Coupled ocean-atmospheric waves on the equatorial front. Geophysical Research Letters 25, 3863–3866.

Xue, A., Jin, F.F., Zhang, W., Boucharel, J., Kug, J.S., 2023. Parameterizing the nonlinear feedback on enso from tropical instability waves (tiws) by nonlinear eddy thermal diffusivity. Climate Dynamics , 1–16.

Xue, A., Jin, F.F., Zhang, W., Boucharel, J., Zhao, S., Yuan, X., 2020. Delineating the seasonally modulated nonlinear feedback onto enso from tropical instability waves. Geophysical Research Letters 47, e2019GL085863.

Xue, A., Zhang, W., Boucharel, J., Jin, F.F., 2021. Anomalous tropical instability wave activity hindered the development of the 2016/17 la niña. Journal of Climate 34, 5583–5600.

Yang, L., Murtugudde, R., Zheng, S., Liang, P., Tan, W., Wang, L., Feng, B., Zhang, T., 2022. Seasonal variability of the pacific south equatorial current during the argo era. Journal of Physical Oceanography .

Yoder, J.A., Ackleson, S.G., Barber, R.T., Flament, P., Balch, W.M., 1994. A line in the sea. Nature 371, 689–692.

Yu, J.Y., Liu, W.T., 2003. A linear relationship between enso intensity and tropical instability wave activity in the eastern pacific ocean. Geophysical Research Letters 30. URL: https://agupubs.onlinelibrary.wiley.com/doi/abs/10.1029/2003GL017176, doi:https://doi.org/10.1029/2003GL017176, arXiv:https://agupubs.onlinelibrary.wiley.com/doi/pdf/10.1029/2003GL017176.

Yu, Z., McCreary Jr, J.P., Proehl, J.A., 1995. Meridional asymmetry and energetics of tropical instability waves. Journal of Physical Oceanography 25, 2997–3007.

Zhang, C., 2001. Intraseasonal perturbations in sea surface temperatures of the equatorial eastern pacific and their association with the madden–julian oscillation. Journal of climate 14, 1309–1322.

Zhang, C., 2005. Madden-julian oscillation. Reviews of Geophysics 43.